KYOTO UNIVERSITY

DOCTORAL THESIS

Decoupling Interdependent Cytoskeletal Processes to Control Cell Adhesion Dynamics

Author:
Ian Torao HOFFECKER

Supervisor:
Dr. Hiroo IWATA

A thesis submitted in partial fulfilment of the requirements for the degree of Doctor of Philosophy

in the

Reparative Materials Group
Department of Polymer Science

October 2014

"...the interfaces between two bulk forms of matter are responsible for some of the most unexpected actions"

Pierre Gilles de Gennes
1994 Dirac Memorial Lecture

KYOTO UNIVERSITY

Abstract

Graduate School of Engineering
Department of Polymer Science

Doctor of Philosophy

Decoupling Interdependent Cytoskeletal Processes to Control Cell Adhesion Dynamics

by Ian Torao HOFFECKER

The cytoskeleton is a dynamic, self-organizing system composed of multiple interacting modular elements, spanning the molecular to the cellular scale, and capable of responding adaptively to stimuli serving multiple purposes. A consequence of the adaptive, multifunctionality of the cytoskeleton is that many processes of interest, for example migration, adhesion, and traction force, are fundamentally linked to each other. As an illustrative example, it is not trivial to target migration for modulation while fixing adhesion and traction force as constant variables. Traction forces are generated by stress fibers, filamentous actin bundles that undergo ratchet-like tension via the action of myosin motor proteins; the tension is then transmitted through focal adhesions to the exterior of the cell. Resistance to this tension triggers enhanced formation of stress fibers and the growth of the focal adhesions. Migration is accomplished by these same forces with direction determined by the net force formed by multiple tensile stress fibers distributed across the body of the cell and anchored to focal adhesions. This interconnectedness poses obstacles for designing experiments in cell biology and also technology for tissue engineering, either of which may call for precision control of a single variable.

This thesis describes the development of experimental strategies for controlling cellular behaviors related to cytoskeletal processes in ways that are outside the range of normal cytoskeletal responses to environmental stimuli. The underlying principle behind these strategies is the concept of decoupling or bypassing interdependent cytoskeletal variables. Three approaches can be described generally as: 1) Applying a priori theories of the cytoskeleton to design environments (eg: patterned substrates) that elicit unique cell behaviors within the limits of nominal cellular responses to external stimuli. 2) Treating cells with drugs to influence cytoskeletal processes directly, altering their response to a given environmental stimulus. 3) Bypassing the cytoskeleton altogether by engineering mechanisms that accomplish the target behavior without direct involvement of cytoskeletal elements.

In Chapter 2, "Assessing the spatial resolution of cellular rigidity sensing using a micropatterned hydrogel-photoresist composite," a patterned substrate is designed with the purpose of eliminating hypothetical models of cellular rigidity sensing mechanics. Cells are able to exert traction forces on their underlying substrates, and the rigidity of these substrates has increasingly been shown to have a major impact on connected cellular responses such as differentiation and apoptosis. The cellular response to substrate rigidity involves the deformation of substrates in response to exerted cellular traction forces, however little is known of how a cell is able to measure or respond to that deformation. Competing theories involving intra-focal adhesion mechanisms, force measurement occurring between local focal adhesion clusters, and large scale mechanisms requiring the stress fibers formed across the length of the cell have all been proposed. To narrow the range of possible explanations, the size scale of rigidity sensing, if determined, can identify which category of mechanisms is more probable. Composite substrates composed of elastic polyacrylamide hydrogel of controlled elastic properties were patterned using photolithography to support grafted arrays of SU-8 photoresist 6.5 micrometer-long square islands. The instrinsic rigidity of the islands is such that a cell on a uniformly coated SU-8 surface would respond by expressing large traction forces, mature focal adhesions, and well-defined stress fibers. However the rigidity of the islands, if sheared relative to the underlying gel, would comply according to the rigidity of the much softer elastic hydrogel mechanics. The size of the islands is such that a single cell, when fully spread, would span several islands, but they are large enough to support the formation of multiple mature focal adhesions. ECM ligand coating was restricted to the islands by the hydrophilic property of the gel, thus limiting direct cell contact to the rigid islands.

The results showed that cells on patterns of rigid islands grafted to soft gels responded as though adhered to uniformly soft gels, ie: by exerting small traction forces, un-matured focal contacts, and weakly organized actin fibers. This indicates that in spite of the direct contact of cells to intrinsically rigid SU-8 islands, the long range deformations

across the body of the cell served as the metric for determining response to rigidity. The spatial resolution, in other words, of cellular rigidity sensing is limited to a cell-scale rather than depending on sub or intra-molecular details occurring at the scale of focal adhesions or even between local clusters of focal adhesions, as this too would have been permitted by 6.5 micrometer sized islands.

In Chapter 3, "Manipulation of cell sorting within mesenchymal stromal cell-islet cell multicellular spheroids," the collective dynamics of islet cells aggregated with mesenchymal stromal cells (MSCs) are controlled using pharmacological agents to produce relative changes in cytoskeletal processes. Initially, MSC-islet-cell multicellular spheroids were formed and observed, exhibiting collective sorting into minimally contacting spheroidal compartments of MSCs and islet cells. When the spheroids were formed in the presence of ROCK inhibitor, a drug known to partially disrupt actin networks while simultaneously stabilizing cadherin localization at the cell periphery, the spheroids again underwent cell sorting but assumed core-shell architectures with islets occupying the exterior and MSCs at the core. The MSCs were shown to have upregulated expression of E-cadherin when treated with ROCK inhibitor, and pan-cadherin staining of non-ROCK inhibitor aggregates showed that cadherins in MSCs were chaotically distributed rather than occupying the borders between cells. The relative change in cadherin organization suggests that ROCK inhibitor treatment resulted in increased cohesive interaction between islet cells and MSCs, causing the convergence to organization with greater adhesive contact between the two cell types.

In Chapter 4, "Long term culture of cells patterned on glass via membrane-tethered oligonucleotides," cells bearing membrane-inserted single stranded DNA (ssDNA) conjugates are attached to glass substrates patterned by inkjet printer with complementary ssDNA. Unlike integrins, which transmit external forces directly to the interior actin network and associated cytoskeletal modules, ssDNA-conjugated phospholipids associate only with the lipid membrane. Therefore, cell attachment to ssDNA patterned substrates is rapid and limited by the rate of cell convection or contact with the surface rather than the kinetics of DNA hybridization which is comparatively fast and also occurs on faster timescales than integrin-ECM mediate adhesion and spreading. Adherent-type cells that were patterned on glass substrates with both ssDNA and adsorbed fibronectin exhibited competition between the migratory forces of the natural cytoskeleton and the artificial attachment due to ssDNA. Migration was slowed relative to normal migration, and traces of membrane components torn from the escaping cell could be observed at the initial contact points.

In Chapter 5 "Sequence-specific nuclease-mediated release of cells tethered by oligonucleotide phospholipids," nucleases are used to sever the connections formed by ssDNA-PEG-lipid bonds. ssDNA-PEG-lipids are employed to pattern cells on 2D glass substrates and form multicellular aggregates through heterotypic complementary DNA hybridization. By exposing the DNA bonds to restriction endonucleases specific to the sequence contained in the DNA sequence, the bonds can be severed. In addition, nonspecific nuclease can be used to digest DNA irrespective of the contained sequence. Both treatment approaches were used to detach cells sequestered to 2D glass substrates, and brief flushing in a flow chamber was sufficient to selectively separate cells of interest. Likewise, multicellular aggregates held together by DNA bonds could be dispersed with the same sequence specificity by brief incubation with restriction endonucleases, and conversely digestion of bonds with nonspecific nucleases could nonspecifically disperse the aggregates.

In Chapter 6, "Estimation of Cell-Cell Adhesion Energy Mediated by DNA-Lipid Bonds", the Hertz contact model is employed in order to estimate the strength of ssDNA-PEG-lipid adhesion between cells. The estimation works by measuring the deformation of cell membranes when adhesive contacts are formed. With this information and by knowing the elastic properties of cells, the adhesion energy and adhesion energy per unit area of cell surface can be inferred. Average measurements of the adhesion energy were taken for cells modified with ssDNA-PEG-lipids and compared with cells modified with 10:1 methoxy-PEG-lipid : ssDNA-PEG-lipid testing the hypothesis that adding neutral membrane inserts to reduce the adhesion between cells could be reflected in the Hertz model estimates used. It is demonstrated here as well that average adhesion energy per unit area can be used to numerically predict the size of the contact area formed for cells of given dimensions.

In summary, the thesis explores three types of cytoskeletal manipulation which can be used to constrain the behavior of cells in different contexts. By separating normally coupled cytoskeletal variables such as adhesion vs migration or traction force vs rigidity sensing, a variety of unique forms of cellular behavior can be controlled.

Contents

List of Figures

List of Tables

Dedicated to my family Adam, John, and Lilian...

Chapter 1

Background

1.1 Introduction

1.1.1 Engineering Control in the Face of Complex Processes

Obtaining precision control of the position, internal processes, migratory patterns, and group behavior of cells is a key requisite for designing experiments in cell biology or therapies in tissue engineering. Major advancements have been made in uncovering the internal workings of cells, however their behavior is still dependent on too many state variables for the high level prediction and control required for the level of engineering possible with many other physical problems. Consider, as an example, industrial scale chemical reactions. Though any physical system must exist in a greater context and is subject to the fluctuations of innumerable variables, it is nevertheless possible to allocate attention to only those variables which influence the designer's goals of such a system. In industrial scale chemical reactions, the exact velocities and momenta of individual molecules are ignored by aggregating them into statistical thermodynamic variables which can be measured and tuned. Simulations can be used reliably to design industrial processes without the need for a detailed molecular level description.

One must be cautious not to characterize nature itself as either simple or complex in these instances. This error, coined by E.T. Jaynes as the "Mind Projection Fallacy"[1] occurs when one infers an ontological generality from one's internal perceptions. Predictability in chemical process engineering is possible because the standard of accuracy for adequate prediction allows for insensitivity to sufficiently small changes in most variables such that the information required to meet those standards is limited to a finite resolution. The simplicity is contrived and not inherent in nature. Atomic fluctuations are still occurring

[1] Edwin T Jaynes. *Probability theory: the logic of science*. Cambridge university press, 2003.

in reality, and an immensely powerful computer would still be required to simulate the movements of all atoms in the chemical process, though little practical utility would be gained in exchange for that power as far as improving the process is concerned.

In contrast to the often sufficiently descriptive variables relevant to predicting and designing large scale chemical processes, the resolution of information required to predict important changes in the cytoskeleton, or cell behavior generally, is still poorly defined and varies greatly depending on the application. As with chemical process engineering, the information required for cytoskeletal prediction also depends on the strictness of accuracy. To determine the position of a migrating cell 30 seconds from the present at an accuracy of $<\pm$ 5 μm might require only empirical data of the average persistence length of similar cells migrating under sufficiently similar environmental conditions. However, if that prediction were instead to require that the cell's position be known 1 hour from the present at an accuracy of $<\pm$ 5 μm, the information needed to define the system may be far more challenging to obtain and could come at great cost. Indeed, knowledge of the cell's unique individual history could be needed to determine quantitatively the status of cytoskeletally relevant gene regulation, its position in the cell cycle, the spatial mapping of focal adhesions and stress fibers. Precise data about the nutrients in the surrounding medium and predictive models of a cell's response to small variations in those nutrients might be needed to predict its metabolic output. Such a model would be computationally expensive in the way that an atomic-resolution industrial chemical process simulation might be. Yet unlike the chemical process simulation, it is conceivable that a tissue engineering therapy with the goal of regenerating functional pancreatic tissue or a simulation attempting to predict the movement of metastatic cancer cells might realistically require control at the level of individual cell movements over long timescales, and a level of prediction falling short of this may offer little or no practical value.

1.1.2 The Central Problem of this Thesis: Dimensionality Reduction in Cytoskeletal Processes

Suppose now that rather than a cell migrating arbitrarily in 2 dimensions, we instead choose to exploit the *a priori* empirical model of "contact guidance"[2] which permits us to constrain the probability density function of anticipated outcomes by designing a substrate with longitudinal grooves known to result in guided migration in most cell types. The cell can now move forward or backward along the groove, and we thus reduce the dimensions of the problem (in this case, these are spatial dimensions) increasing

[2]Graham A Dunn and Julian P Heath. "A new hypothesis of contact guidance in tissue cells". In: *Experimental cell research* 101.1 (1976), pp. 1–14.

our precision when it comes to predicting where the cell might be in 1 hour. Spatial dimensionality reduction has been applied in several instances to improve cell position and movement control[3].

Consider an alternative approach to reducing the number of relevant variables in the problem. The cytoskeletal inhibiting agent, Cytochalasin D, is known to inhibit actin polymerization and the force-generating machinery responsible for cell migration[4]. In this case, prediction of the cell's position 1 hour from the present is trivial. However, one can see here that utility may have been sacrificed for the sake of accurate prediction. In the limited context of a problem where the goal is knowing the cell's position, the Cytochalasin D strategy may suffice. However, realistically we must often consider how to reduce the dimensions of a biological system under a number of other constraints. These constraints include the obvious, such as cell viability, but we may for instance wish to direct cell movement without 1 dimensional contact guidance tracks or predict the positions of many healthy, randomly migrating cells in a 3D scaffold for a tissue engineering therapy. It may not contribute to the goal of engineering functional tissue to inhibit the migration of all cells within the scaffold, and we may wish to have predictive control over cell position 1 hour from the present.

This thesis is concerned with the elimination and decoupling of interdependent variables involved in output cell mechanical behaviors. This includes cell adhesion, cortical tension, actomyosin contractile force, traction forces, environmental rigidity sensing, migration, cell-cell cohesive interaction, and the mesenchymal-epithelial transition. This list is far from exhaustive, although it covers many of the key themes explored herein. The research presented is experimental, rather than theoretical, and the methods explored are a sample, fitting into representative classes of general strategies for dimensionality reduction in cytoskeletal processes. In the following sections of this chapter, the interdependencies of cytoskeletal variables will be explored along with approaches for isolating, removing, and bypassing variables for the purposes of simplification, improved prediction, and control of macroscopic cell behavior.

1.1.3 Interdependencies within the Cytoskeleton

Central to decomposing the complex cytoskeletal system into manipulable variables are the ideas of scale and hierarchical reduction. The higher order behaviors of cells related to movement and shape arise out of the interactions between polymeric protein

[3]Stephanie S Chang et al. "Guidance of cell migration by substrate dimension". In: *Biophysical journal* 104.2 (2013), pp. 313–321.

[4]Mary L Stracke et al. "Cytoskeletal agents inhibit motility and adherence of human tumor cells". In: *Kidney international* 43 (1993), pp. 151–151.

filaments, ATP-catalyzed force generating molecular motors, adhesion molecules, and the complex interactions of adapter and cross-linking proteins. These many elements and their diverse functions comprise the cytoskeleton, yet there exists no central controller responsible for the structural patterns or global force vectors; rather, innumerable interconnected algorithms taking place in parallel are responsible for the higher order observable traits such as the direction a cell moves: determined by the resultant force of many force vectors of varying magnitudes and directions. A global characteristic such as migration velocity may require examination at a finer level of hierarchical reduction, and likewise a multicellular phenomenon such as cell sorting could require an understanding of cell-scale details. A notable feature of the cytosketon is the transduction of forces from outside a cell to inside a cell, with internal components participating in force generation applied externally, mediated through trans-membrane proteins. This inside-to-outside characteristic leads to complex patterns at the multicellular level, as forces are transmitted from one corner of a cell through nearest-neighbor interactions to more distant cells. Major cell behaviors such as apoptosis, division, or differentiation which may seem superficially unrelated in fact have a deep connection to the cytoskeleton[5]. Control of cytoskeletal processes is central to several practical issues in biomedicine, for example cancer therapeutics[6], regenerative medicine[7], stem cell differentiation and iPS induction[8]. For thorough review on interdependencies and multitasking in the cytoskeleton, see Huber et al[9].

The cytoskeleton is composed of 3 major classes of macromolecular filaments (actin, microtubules, and intermediate filaments). This review will focus on actin, which is particularly relevant to this thesis. Actin is a globular protein which polymerizes to form a variety of structural patterns serving various mechanical and biochemical roles in the cell. Different actin isoforms, β and γ, are expressed in non-muscle cells, while α and β forms occur in muscle cells. β actin tends to concentrate at the leading edge of cells, and γ actin is found in stress fibers that are responsible for contractile force generation. Actin forms linear semi-flexible filaments through nucleation and growth kinetics where nucleation is energetically unfavorable compared to growth of pre-established filaments. Actin filaments are dynamic, and compression forces exerted on the cell leading edge can be driven by the rapid assembly of actin at the boundary in parallel with disassembly

[5]Francis J Alenghat and Donald E Ingber. "Mechanotransduction: all signals point to cytoskeleton, matrix, and integrins". In: *Science Signaling* 2002.119 (2002), pe6.

[6]Dmitriy Kedrin et al. "Cell motility and cytoskeletal regulation in invasion and metastasis". In: *Journal of mammary gland biology and neoplasia* 12.2-3 (2007), pp. 143–152.

[7]Michael P Sheetz. "Cell control by membrane–cytoskeleton adhesion". In: *Nature Reviews Molecular Cell Biology* 2.5 (2001), pp. 392–396.

[8]Nikolce Gjorevski, Eline Boghaert, and Celeste M Nelson. "Regulation of epithelial-mesenchymal transition by transmission of mechanical stress through epithelial tissues". In: *Cancer Microenvironment* 5.1 (2012), pp. 29–38.

[9]F Huber et al. "Emergent complexity of the cytoskeleton: from single filaments to tissue". In: *Advances in Physics* 62.1 (2013), pp. 1–112.

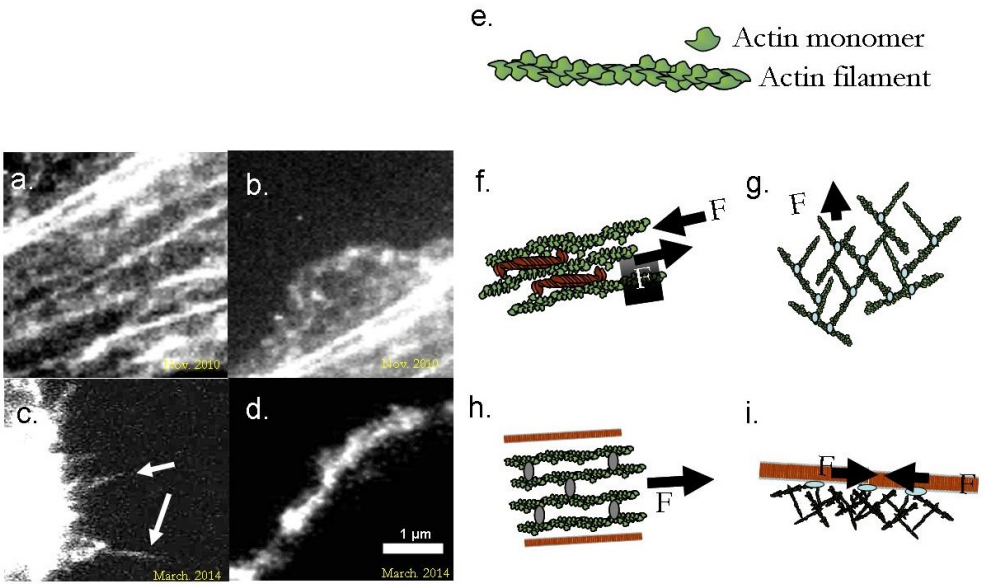

FIGURE 1.1: The multiple roles of actin. (a, f) Stress fibers on an NIH 3T3 fibroblast formed from bundles of actin cross-linked with myosin motors responsible for generating ratchet-like tension. (b, g) Lamellipodium of an NIH 3T3 fibroblast protruding outward from the mobile edge and composed of actin network. (c, h) Filopodia (white arrows) on a CCRF-CEM lymphoblast-like cell - thin projections of cross-linked actin bundles extending from the surface of the cell. (d, i) The actin cortex of a CCRF-CEM cell - a thin layer of actin mesh just beneath the phospholipid membrane that generates surface tension. (e) The basic unit of many cytoskeletal structures is the globular actin monomer which forms filaments by linking to other actin monomers.

in other parts of the cell, a process known as treadmilling. Other structural motifs are based on actin filaments such as the cortex that supports cell membranes, contractile stress fibers, muscle filaments, and protrusions such as lamellipodia and filopodia. While multiple actin isoforms are included in this list, this alone is not enough to account for the incredible variability in function, for example compression versus tension (Fig. 1.1).

The interactions between actin filaments governed by cross-linking proteins and molecular motors such as myosin II are a major contributor to structural and functional diversity. Modulating cross-linking density of the static cross-linker protein scruin in actin solutions was sufficient to increase the elastic modulus of the actin-scruin networks by orders of magnitude, and the application of stresses was shown to affect modulus as well, indicating a nonlinear, multi-domain mechanical state space for even such a simple, two-component system[10]. Actin can also form bundles, anisotropic structures consisting of parallel actin filaments stacked together by actin binding proteins[11], leading to entirely different mechanical characteristics compared to actin networks. Actin filaments within

[10] Margaret L Gardel et al. "Elastic behavior of cross-linked and bundled actin networks". In: *Science* 304.5675 (2004), pp. 1301–1305.

[11] Mireille MAE Claessens et al. "Actin-binding proteins sensitively mediate F-actin bundle stiffness". In: *Nature materials* 5.9 (2006), pp. 748–753.

stress fibers are cross-linked laterally by myosin II motors forming contractile, tension-generating fibers used by the cell to exert forces on the external environment. Structure dynamics are important as well, and the on and off rates of actin binding proteins, the hysteresis of macroscopic actin structures, the diffusion of monomer subunits, the availability of latent subunits such as profilin-capped actin are also determinants of actin structures[12]. Structures formed from actin, along those formed from microtubules and intermediate filaments, occur through a process of self-organization.

Adherent cell types such as epithelial cells and mesenchymal cells can attach to extracellular matrix proteins through adhesion proteins called integrins[13]. Integrins straddle the phospholipid membrane with both extracellular and intracellular domains. Integrins bind to external ligands contained in ECM proteins such as laminin, vitronectin, fibronectin, and collagen, and they intracellularly interface with adapter proteins linked to cytoskeletal filaments, bridging exterior and interior mechanical environments[14]. Integrins are composed of two subunits: α and β which each come in several types. The particular combination of α and β subunits determines which ligands that integrin can bind to extracellularly. Integrin attachment occurs in large molecular complexes called focal complexes or focal adhesions (Fig. 1.2a). On the cytoplasmic side, these complexes consist of integrins spanning the transmembrane region, and several cytoplasmic proteins that serve as adapters and regulators of cytoskeletal attachment such as paxillin and talin. These adhesion sites are dynamic: the size of focal adhesions is regulated by the application of force actuated by stress fibers, and the distinction between focal complexes, small nucleation sites of adhesion proteins less than a single micrometer in diameter[15], and mature focal adhesions is often ambiguous. Focal adhesion proteins talin, paxillin, α-actinin, filamin, and focal adhesion kinase (FAK) form an adapter complex that interfaces with actin stress fibers (Fig. 1.2c). Stress fibers are filamentous super-structures composed of multiple actin subunits, and are significant for their role in generating tension across the cell.

In addition to interacting with extracellular matrix, cells also mechanically interact with neighboring cells. In 1978, George Bell published a monograph "Models for the

[12] Thomas D Pollard and Gary G Borisy. "Cellular motility driven by assembly and disassembly of actin filaments". In: *Cell* 112.4 (2003), pp. 453–465; Tatyana M Svitkina and Gary G Borisy. "Arp2/3 complex and actin depolymerizing factor/cofilin in dendritic organization and treadmilling of actin filament array in lamellipodia". In: *The Journal of cell biology* 145.5 (1999), pp. 1009–1026; Michiki Kasai, Hirotaka Kawashima, and Fumio Oosawa. "Structure of F–actin solutions". In: *Journal of Polymer Science* 44.143 (1960), pp. 51–69.

[13] David A. Cheresh and R.P. Mecham. *Integrins: Molecular and Biological Responses to the Extracellular Matrix*. Biology of extracellular matrix. Academic Press, 1994. ISBN: 9780121711603.

[14] S.C. Froehner and V. Bennett. *Cytoskeletal Regulation of Membrane Function: Society of General Physiologists 50th Annual Symposium, Marine Biological Laboratory, Woods Hole, Massachusetts, 5-7 September 1996*. Annual symposium. Rockefeller University Press, 1997. ISBN: 9780874700596.

[15] Catherine G Galbraith, Kenneth M Yamada, and Michael P Sheetz. "The relationship between force and focal complex development". In: *The Journal of cell biology* 159.4 (2002), pp. 695–705.

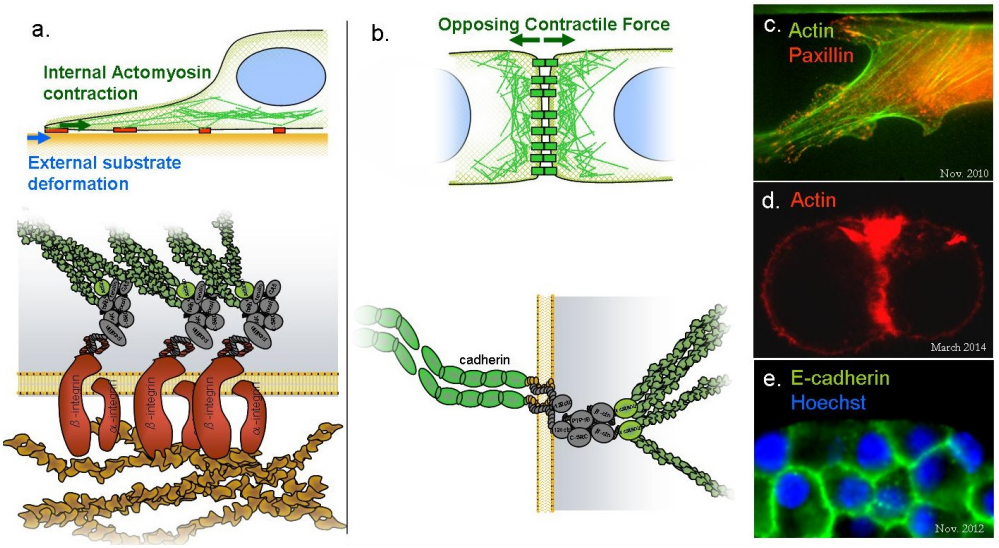

FIGURE 1.2: (a) The external environment of an adherent cell and its internal cytoskeleton are mechanically linked through focal adhesions - clusters of membrane-spanning integrins (red) that bind on the outside to extracellular matrix (brown) while connected internally to adaptor proteins (gray) linked with the actin cytoskeleton (green). (b) Adherens junctions link the internal actin cytoskeleton (green) through adaptor proteins (gray) to other cells through homotypic cadherin bonds.(c) A spread NIH 3T3 fibroblast displaying stress fibers identified by fluorescent phalloidin bound to actin (green) and focal adhesions labeled with antibodies specific to the focal adhesion protein paxillin (red). (d) Fluorescent phalloidin bound to actin (red) localized near the interface of two cohering HEK293 cells mediated by adherens junctions. (e) Pancreatic beta cells expressing E-cadherin (green) localized at cell-cell boundaries.

Specific Adhesion of Cells to Cells"[16] in which he described how cell adhesion could occur through thermodynamic coupling of macromolecules extending from the surface of cells. At the time, limited information as to the identity of the major adhesion molecules was unknown, yet the mechanisms of possible intercellular adhesion laid out by Bell proved to be insightful. Today cell adhesion molecules, referred to as CAMs, consist of a large group of integral membrane proteins responsible for mediating adhesion, signaling, and various functional roles between adjacent cells.

Among the adhesion mechanisms Bell proposed was that of a homotypic adhesion molecule such that it would bind when adjacent to another molecule of its kind. This was later shown by Takeichi and coworkers[17] to be the mechanism governing the function of cadherins (Fig. 1.2e), a class of calcium-dependent cell-cell adhesion molecules that mediate adherens junctions (Fig. 1.2b) and desmosomes. Because of their nature as homotypic adhesion molecules, cadherins are important for selective interactions between

[16] George I Bell. "Models for the specific adhesion of cells to cells". In: *Science* 200.4342 (1978), pp. 618–627.

[17] Masatoshi Takeichi. "The cadherins: cell-cell adhesion molecules controlling animal morphogenesis". In: *Development* 102.4 (1988), pp. 639–655.

"like" cells[18], and this property has been shown to be central to many multicellular processes including the regulation of morphogenesis and development[19], the progression of cancer and metastasis[20], as well as pluripotency and stem cell differentiation[21]. Several classes of cadherin have been identified such the Classical Type I cadherins which include E-cadherin, also known as cdh1 or epithelial cadherin, and N-cadherin, also known as cdh2 or neural cadherin. Additionally, there are desmosomal cadherins, protocadherins, and a variety of unclassified cadherins[22]. The large diversity in cadherin types and sub-types as well as their critical role in multicellular processes has stimulated extensive investigation into their mechanisms and functions. A result of this has been the growing consensus that cadherins are not entirely selective adhesion mediators, and that cross-reactivity between different cadherin molecules can occur[23].

To complicate matters, cadherins are far from being the only mediators of intercellular adhesion. In addition to homotypic adhesion molecules, cell surfaces can present a variety of heterotypic adhesion receptors such as the Intercellular Adhesion Molecules (ICAMs) and Vascular Cell Adhesion Molecule-1 (VCAM-1), members of the immunoglobulin superfamily which recognize and bind to specific surface antigens[24]. On top of this, selectins are another class of intercellular adhesion mediators that mediate the interactions of leukocytes and other cells[25]. Homotypic binding mediated by crosslinking of complementary glycoproteins may also occur under certain circumstances as with the binding via galectin-3 (Gal-3)[26]. In Chapter 3, in which changes in the sorting behavior

[18] Masatoshi Takeichi. "Cadherins: a molecular family important in selective cell-cell adhesion". In: *Annual review of biochemistry* 59.1 (1990), pp. 237–252.

[19] Masatoshi Takeichi. "Cadherin cell adhesion receptors as a morphogenetic regulator". In: *Science* 251.5000 (1991), pp. 1451–1455; Jennifer M Halbleib and W James Nelson. "Cadherins in development: cell adhesion, sorting, and tissue morphogenesis". In: *Genes & development* 20.23 (2006), pp. 3199–3214.

[20] Jiirgen Behrens et al. "Loss of epithelial differentiation and gain of invasiveness correlates with tyrosine phosphorylation of the E-cadherin/beta-catenin complex in cells transformed with a temperature-sensitive v-SRC gene." In: *The Journal of cell biology* 120.3 (1993), pp. 757–766.

[21] Torben Redmer et al. "E-cadherin is crucial for embryonic stem cell pluripotency and can replace OCT4 during somatic cell reprogramming". In: *EMBO reports* 12.7 (2011), pp. 720–726.

[22] Sabine Pokutta and William I Weis. "Structure and mechanism of cadherins and catenins in cell-cell contacts". In: *Annu. Rev. Cell Dev. Biol.* 23 (2007), pp. 237–261.

[23] Deborah Leckband and Anil Prakasam. "Mechanism and dynamics of cadherin adhesion". In: *Annu. Rev. Biomed. Eng.* 8 (2006), pp. 259–287.

[24] Steven D Marlin and Timothy A Springer. "Purified intercellular adhesion molecule-1 (ICAM-1) is a ligand for lymphocyte function-associated antigen 1 (LFA-1)". In: *Cell* 51.5 (1987), pp. 813–819; Michael L Dustin et al. "Induction by IL 1 and interferon-gamma: tissue distribution, biochemistry, and function of a natural adherence molecule (ICAM-1)." In: *The Journal of Immunology* 137.1 (1986), pp. 245–254; Mariano J Elices et al. "VCAM-1 on activated endothelium interacts with the leukocyte integrin VLA-4 at a site distinct from the VLA-4/fibronectin binding site". In: *Cell* 60.4 (1990), pp. 577–584.

[25] Michael B Lawrence and Timothy A Springer. "Leukocytes roll on a selectin at physiologic flow rates: distinction from and prerequisite for adhesion through integrins". In: *Cell* 65.5 (1991), pp. 859–873; Frank Austrup et al. "P-and E-selectin mediate recruitment of T-helper-1 but not T-helper-2 cells into inflamed tissues". In: (1997).

[26] Hidenori Inohara and Avraham Raz. "Functional evidence that cell surface galectin-3 mediates homotypic cell adhesion". In: *Cancer research* 55.15 (1995), pp. 3267–3271.

of multicellular aggregates integrated by cell-cell adhesion molecules, we will see how the identification of cell adhesion molecules becomes important for drawing conclusions about the mechanisms of multicellular organization. Here the potential for multiple cell adhesion molecules contributing simultaneously to interactions becomes a confounding factor that must be overcome.

A large body of evidence indicates that focal adhesions, focal complexes, and stress fibers are regulated by positive and negative feedback signals involving physical force[27]. Actin is recruited to nascent focal complexes, and this allocation leads to the establishment actin filaments and the beginnings of stress fibers, generating tensile force on the adhesion complex. Tensile force actuated by stress fibers is transmitted through the focal complex into integrins and finally to the external ECM to which the integrin is bound to. Though the mechanisms are not fully understood, it is recognized that the actuation of tensile force through focal complexes coupled with the resistance to that force from the external environment promotes the recruitment of additional focal adhesion proteins, the enlargement of the focal complex, and positive reinforcement through additional stress fiber formation, and that this positive feedback leads to further enlargement and maturation of the focal complex into focal adhesions, the reinforcement of filamentous actin into large cell-spanning stress fibers, and actuation of larger tensile forces. In the case where tensile force is met by low resistance, transient focal complexes fail to mature into large focal adhesions, and stress fibers fail to surpass the barriers to nucleation and sustained maintenance[28]. This regulatory system is constantly dissipating energy to adapt to chemical and mechanical signals from the environment. Conversely, cadherin mediated adherens junctions are also connected to the actin cytoskeleton and force sensing machinery. Actin can be observed localized at cell-cell boundaries mediated by adherens junctions (Fig. 1.2d). A study by Engl et al shows that manipulating contractile forces in cell-cell doublets with cytoskeletal inhibitors has a profound effect on the distribution and expression level of cadherins in adherens junctions[29]. It is this self-organizing aspect which makes examining any one variable in isolation difficult, as many of the observable functional characteristics of the cytoskeleton like migration emerge from the collective interactions of modular components of a highly interconnected system.

[27] Daniel Riveline et al. "Focal contacts as mechanosensors externally applied local mechanical force induces growth of focal contacts by an mdia1-dependent and rock-independent mechanism". In: *The Journal of cell biology* 153.6 (2001), pp. 1175–1186; Boris Hinz and Giulio Gabbiani. "Mechanisms of force generation and transmission by myofibroblasts". In: *Current opinion in biotechnology* 14.5 (2003), pp. 538–546; Magdalena Chrzanowska-Wodnicka and Keith Burridge. "Rho-stimulated contractility drives the formation of stress fibers and focal adhesions." In: *The Journal of cell biology* 133.6 (1996), pp. 1403–1415.

[28] Nathalie Q Balaban et al. "Force and focal adhesion assembly: a close relationship studied using elastic micropatterned substrates". In: *Nature cell biology* 3.5 (2001), pp. 466–472; L. Lu and Washington University in St. Louis. *Mechanical Properties of Actin Stress Fibers*. Washington University in St. Louis, 2008. ISBN: 9780549646426.

[29] W Engl et al. "Actin dynamics modulate mechanosensitive immobilization of E-cadherin at adherens junctions". In: *Nature cell biology* 16.6 (2014), pp. 587–594.

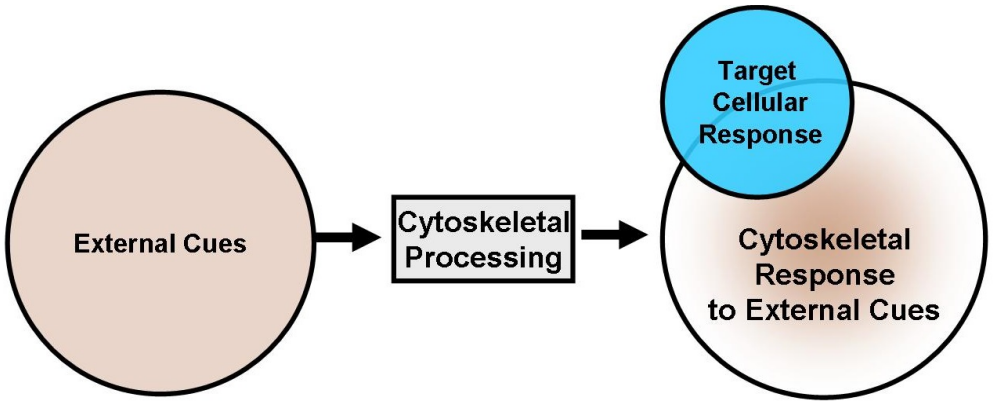

FIGURE 1.3: The space of all possible environmental stimuli corresponds to a finite distribution of cell behaviors, some of which may have desirable biotechnological applications or may shed light on the cytoskeletal mechanisms leading to those behaviors.

1.2 Control of Cytoskeletal Processes with Engineered Environments

Strategies for controlling cell spatial position, migration, and interaction can be divided roughly into three categories: those that harness the normal cell responses to physical environmental characteristics, those that manipulate the processes of force generation and sensing internally through genetic or pharmacological means, and a third category which we shall refer to as bypassing the cytoskeleton or, in other words, engineering alternative methods for achieving some effective cell behavior that do not rely directly on the cytoskeletal algorithms that process external cues.

Consider the highly simplified diagram shown in Fig. 1.3, which illustrates the base-case scenario of a normal cell, the input variables represented by the space of potential environmental stimuli. For example, the porosity of a 3D scaffold supporting cell attachment could be one of many parameters in this space. The output behavior of the the cell is represented as a probability distribution. A single point in behavior space represents the many dimensions needed to define the characteristics of a given cell's behavior such as migration speed, the distribution of adhesive ligands, the exact mapping of tensile forces due to stress fibers, or the cell's unique state of gene regulation. Points close to the periphery of the distribution can be thought of those behaviors which are unusual given the space of possible environmental inputs, for example a cell occupying the shape of a square or a cell that exhibits persistent unidirectional migration for 1 hour on an unconstrained 2D substrate would each have low, though non-zero, probabilities of occurring in a population of cells.

Intersecting the distribution of output behaviors is a category we shall refer to as target cellular response, or the output behaviors of interest. The overlapping region corresponds

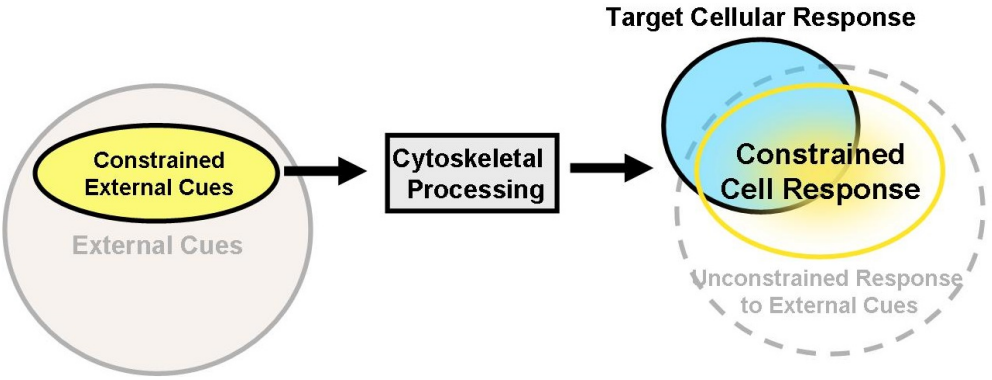

FIGURE 1.4: Careful engineering of substrates, scaffolds, or other physical environments can constrain the behavior of cells leading to desired behavioral characteristics such as directed migration or predictable cell geometry.

to desirable output behaviors that are conceivable based on the normal cytoskeletal algorithm's capability of processing external cues. Given the correct external cues, the cytoskeletal machinery is sufficient to achieve certain target behaviors. Target behaviors which lie outside this region however, are effectively not possible given the normal physical limitations of the cell. For example, a cell which attaches with a particular minimum separation force to a surface on a timescale less than one second might conceivably serve a purpose in the design of some engineering application. However, within the limits of natural cell biology, this might not be possible.

Fig. 1.4 shows how careful control of environmental input signals can narrow the distribution of behaviors significantly. An instance of this approach was described earlier with the concept of a 1D contact guidance track designed to narrow the distribution of potential cell migratory behaviors. Though the dimensions involved need not necessarily be spatial. In Chapter 2, a composite substrate is designed to elicit highly specific behavior based on natural cell mechanics in order to test hypothetical models of cell rigidity sensing. In this instance, the goal of the experiment was not only to narrow the distribution of possible output cell behaviors by designing a unique environmental input signal, but to eliminate contending models of what is possible given normal cell mechanics and thus clarify our understanding of the output probability distribution of normal cell behavior illustrated in Fig. 1.3 and 1.4.

Controlling aspects of cell adhesion has historically been and remains today the most versatile and widely utilized method to manipulate cytoskeletal processes. Controlling cell adhesion is most commonly approached by modulating the density or type of protein attached to 2D substrates. Proteins such as fibronectin and collagen which contain cell surface receptor-binding domains can be immobilized on surfaces. The dimensions of adhesive proteins are much smaller than the cell (the hydrodynamic radius of fibronectin

is 8.7 nm[30]), and surfaces with grafted or adsorbed adhesion proteins are often thought of as continuously adhesive substrates. Modulation of bulk adhesion protein density has major consequences on the migration speed of cells. Cell migration is fastest at intermediate surface fibronectin concentrations and slower for low and high concentrations, and the sensitivity to differences in fibronectin concentration have been shown to be dependent on integrin expression levels[31]. A similar dependence of motility on type 1 collagen surface density has been demonstrated[32], and cell spread area has also been shown to depend on ligand density[33].

The dependence of numerous cellular processes on cytoskeletal dynamics and therefore adhesion makes control of adhesion protein density an important aspect of any experiment. Bitterman et al showed that fibronectin acts as a growth factor for fibroblasts in the presence of other soluble factors[34]. Fibronectin present in serum permits adhesion of cells on cell culture dishes by adsorbing onto the surface[35]. The thermodynamic properties of the culture substrate have a major impact on fibronectin adsorption and thus cell adhesion, spreading, and migration. Polystyrene culture dishes treated with plasma differ from non-treated dishes by the wettability of their surfaces, resulting in better adsorption of fibronectin and subsequent cell attachment. The effect of surface wettability and the presence of certain surface functional groups on the adsorption of serum proteins were studied extensively by Arima and Iwata who showed that highly hydrophobic surfaces and highly hydrophilic surfaces alike supported limited adhesion protein adsorption compared to intermediate wettabilities[36]. The differential adhesion strength of bone marrow cell cultures is used to separate bone marrow stromal cells/stem cells (MSCs) from other adherent and nonadherent cell types such as hematopoietic stem cells by utilizing hydrophobic non-treated tissue culture dishes with limited capacity for adsorbed fibronectin[37]. While bulk surface concentration has often been employed as

[30] Valentin Nelea, Yukiko Nakano, and Mari T Kaartinen. "Size distribution and molecular associations of plasma fibronectin and fibronectin crosslinked by transglutaminase 2". In: *The protein journal* 27.4 (2008), pp. 223–233.

[31] Sean P Palecek et al. "Integrin-ligand binding properties govern cell migration speed through cell-substratum adhesiveness". In: *Nature* 385.6616 (1997), pp. 537–540.

[32] Christianne Gaudet et al. "Influence of type I collagen surface density on fibroblast spreading, motility, and contractility". In: *Biophysical journal* 85.5 (2003), pp. 3329–3335.

[33] Padmavathy Rajagopalan et al. "Direct comparison of the spread area, contractility, and migration of balb/c 3T3 fibroblasts adhered to fibronectin-and RGD-modified substrata". In: *Biophysical journal* 87.4 (2004), pp. 2818–2827.

[34] Peter B Bitterman et al. "Role of fibronectin as a growth factor for fibroblasts." In: *The Journal of cell biology* 97.6 (1983), pp. 1925–1932.

[35] Frederick Grinnell and Marian K Feld. "Fibronectin adsorption on hydrophilic and hydrophobic surfaces detected by antibody binding and analyzed during cell adhesion in serum-containing medium." In: *Journal of Biological Chemistry* 257.9 (1982), pp. 4888–4893.

[36] Yusuke Arima and Hiroo Iwata. "Effect of wettability and surface functional groups on protein adsorption and cell adhesion using well-defined mixed self-assembled monolayers". In: *Biomaterials* 28.20 (2007), pp. 3074–3082.

[37] Melody Baddoo et al. "Characterization of mesenchymal stem cells isolated from murine bone marrow by negative selection". In: *Journal of cellular biochemistry* 89.6 (2003), pp. 1235–1249.

a control parameter for cytoskeletal processes, the nanoscale organization of adhesion proteins has been shown to be equally important as the bulk density, with processes as major as differentiation depending on the clustering of adjacent ligands[38]. A form of essential symmetry breaking in cell migration patterns can be engineered by preparing substrates with adhesive ligand gradients. This phenomenon, known as haptotaxis, occurs as a result of migration forces exerted by cells which are positively dependent on the coupling between integrins and adhesive ligands[39]. Fibronectin is a multifunctional cross-linking molecule with binding domains specific to the integrin family on cell surfaces[40] as well as several components of the extracellular matrix such as collagen and heparin[41]. The cell-binding characteristic of fibronectin is importantly not limited to an emergent specificity derived from quaternary or tertiary structure, and although the molecular weight of fibronectin is approximately 440 kDa, the small peptide argenine-glycine-aspartic acid (RGD) contained within fibronectin has repeatedly been shown to possess similar integrin-specific adhesive properties as the complete protein[42].

While the assumption of bulk, uniform adhesiveness is often assumed for fibronectin or RGD-coated substrates, the mesoscale distribution of binding sites plays an important role. Meheshwari et al showed that the clustering of RGD fragments is key to the adhesion and migration of cells[43]. One advantage of the RGD peptide is its small size which enables different chemical modifications from that of whole fibronectin. It has been shown that multivalent RGD-bearing polymers are more effective than single RGD substrates[44].

In addition to fibronectin and collagen, other adhesive proteins have been used to control adhesion and subsequent cytoskeletal processes of different cell types. One of these is laminin which, like fibronectin and collagen, binds with integrins on the cell surface. However, laminins have been shown to be specific to integrins present on epithelial cells and may play an important role in the maintenence of epithelial cell layers polarity where the use of fibronectin or collagen might disrupt these traits[45].

[38] Kuen Yong Lee et al. "Nanoscale adhesion ligand organization regulates osteoblast proliferation and differentiation". In: *Nano Letters* 4.8 (2004), pp. 1501–1506.

[39] Stephen B Carter. "Haptotaxis and the mechanism of cell motility". In: *Nature* 213 (1967), pp. 256–260.

[40] Edward F Plow et al. "Ligand binding to integrins". In: *Journal of Biological Chemistry* 275.29 (2000), pp. 21785–21788.

[41] Richard O Hynes and Kenneth M Yamada. "Fibronectins: multifunctional modular glycoproteins." In: *The Journal of cell biology* 95.2 (1982), pp. 369–377.

[42] Roumen Pankov and Kenneth M Yamada. "Fibronectin at a glance". In: *Journal of cell science* 115.20 (2002), pp. 3861–3863.

[43] Gargi Maheshwari et al. "Cell adhesion and motility depend on nanoscale RGD clustering". In: *Journal of cell science* 113.10 (2000), pp. 1677–1686.

[44] Elisabeth Garanger et al. "Multivalent RGD synthetic peptides as potent α V β 3 integrin ligands". In: *Organic & biomolecular chemistry* 4.10 (2006), pp. 1958–1965.

[45] Victor P Terranova, David H Rohrbach, and George R Martin. "Role of laminin in the attachment of PAM 212 (epithelial) cells to basement membrane collagen". In: *Cell* 22.3 (1980), pp. 719–726.

Besides bulk adsorption and immobilization of adhesive ligands, much effort has gone into the development of microscale resolution patterning techniques used to control the spatial properties of cells on 2D substrates. Here, the wide variety of surface patterning techniques used to control cell cytoskeletal processes and behavior will be reviewed. Adhesive ligand patterning to create geometries of limited traction available to cells is a powerful tool in controlling many different cell behaviors coupled to the cytoskeleton, the most basic of these being shape and position[46]. However these same geometric restrictions have been used to control the cell cycle including cell death[47], proliferation, and growth[48].

The mechanical properties of substrates supporting cell adhesion have increasingly been implicated as critical factors for affecting force-generating components of the cytoskeletal system responsible for phenomena such as migration, persistence, and shape. Elastic polyacrylamide hydrogel substrates of controlled mechanical rigidity, an attribute which can be controlled by the concentrations of monomers and crosslinking reagents used during gel synthesis[49], have been a major tool for exploring mechanical forces and their connection to cell behavior. By measuring local elastic deformations of hydrogels in response to forces exerted by cells, it is possible to obtain a detailed sub-cellular resolution mapping of cell-generated forces, a technique known as traction force microscopy[50]. Traction force microscopy revealing gradients in force generation across the body of the cell have been used to explain how migration occurs as a result of net tensile forces resultant from an asymmetrical force distribution, allowing for the design of substrates with gradients in material rigidity used to guide the movement of cells (referred to as durotaxis)[51]. Combinations of adhesion patterning and controlled material rigidity have allowed for detailed explorations of force generation and sensing under spatial dimensionality constraints[52].

More broadly, substrate preparation techniques have had a significant impact on establishing the field of cell mechanics, leading to various discoveries related to cell force generation and sensing and subsequently causing a field-wide recognition in cell biology

[46] Christopher S Chen et al. "Micropatterned surfaces for control of cell shape, position, and function". In: *Biotechnology Progress* 14.3 (1998), pp. 356–363.

[47] Christopher S Chen et al. "Geometric control of cell life and death". In: *Science* 276.5317 (1997), pp. 1425–1428.

[48] Sui Huang and Donald E Ingber. "Shape-dependent control of cell growth, differentiation, and apoptosis: switching between attractors in cell regulatory networks". In: *Experimental cell research* 261.1 (2000), pp. 91–103.

[49] Robert J Pelham and Yu-li Wang. "Cell locomotion and focal adhesions are regulated by substrate flexibility". In: *Proceedings of the National Academy of Sciences* 94.25 (1997), pp. 13661–13665.

[50] Micah Dembo and Yu-Li Wang. "Stresses at the cell-to-substrate interface during locomotion of fibroblasts". In: *Biophysical journal* 76.4 (1999), pp. 2307–2316.

[51] Chun-Min Lo et al. "Cell movement is guided by the rigidity of the substrate". In: *Biophysical journal* 79.1 (2000), pp. 144–152.

[52] Chang et al., "Guidance of cell migration by substrate dimension".

of the importance of mechanical forces for determining cell behavior. Supported lipid membranes have been used to control the presentation of adhesive ligands for cell attachment[53]. Surfaces designed to respond to electrical stimulation in order to activate cell adhesion have been explored. Yousaf et al used an electrically-triggered activation of hydroquinone and a subsequent Diels-Alder reaction couple RGD peptides in situ, effectively activating the surface for cell adhesion thus permitting the modification of substrates with two different groups of cells[54].

This section has explored a variety of engineered environments used for controlling migration, adhesion, and other cytoskeletal processes. However, it should be mentioned here that the dimensionality reduction that permits controlled cellular behaviors such as the persistence of cells on 1D tracks[55], applies also to the ubiquitous use of 2D substrates instead of 3D environments, which offer technical challenges, for instance in imaging, despite being arguably more relevant to in vivo environments. However, a field-wide shift towards 3D environment design is underway. Notable examples of 3D cell environment design include the development of techniques to measure traction forces in 3D or account for normal traction forces on 2D substrates[56] as well as the loading of cells into hydrogels for tissue engineering[57].

1.3 Internal Manipulation of Cytoskeletal Processing

In the previous section, a number of techniques for tuning input stimuli to elicit specific cellular behaviors were covered. In this section, techniques for manipulating the internal cellular algorithms responsible for processing environmental input signals will be covered.

[53] Jay T Groves, Lara K Mahal, and Carolyn R Bertozzi. "Control of cell adhesion and growth with micropatterned supported lipid membranes". In: *Langmuir* 17.17 (2001), pp. 5129–5133.

[54] Muhammad N Yousaf, Benjamin T Houseman, and Milan Mrksich. "Using electroactive substrates to pattern the attachment of two different cell populations". In: *Proceedings of the National Academy of Sciences* 98.11 (2001), pp. 5992–5996.

[55] Chang et al., "Guidance of cell migration by substrate dimension".

[56] Christian Franck et al. "Three-dimensional traction force microscopy: a new tool for quantifying cell-matrix interactions". In: *PLoS One* 6.3 (2011), e17833; H Delanoë-Ayari, JP Rieu, and M Sano. "4D traction force microscopy reveals asymmetric cortical forces in migrating Dictyostelium cells". In: *Physical review letters* 105.24 (2010), p. 248103; Thorsten M Koch et al. "3D Traction forces in cancer cell invasion". In: *PLoS One* 7.3 (2012), e33476; Wesley R Legant et al. "Multidimensional traction force microscopy reveals out-of-plane rotational moments about focal adhesions". In: *Proceedings of the National Academy of Sciences* 110.3 (2013), pp. 881–886.

[57] Mark W Tibbitt and Kristi S Anseth. "Hydrogels as extracellular matrix mimics for 3D cell culture". In: *Biotechnology and bioengineering* 103.4 (2009), pp. 655–663; Liora Almany and Dror Seliktar. "Biosynthetic hydrogel scaffolds made from fibrinogen and polyethylene glycol for 3D cell cultures". In: *Biomaterials* 26.15 (2005), pp. 2467–2477; George P Dillon et al. "The influence of physical structure and charge on neurite extension in a 3D hydrogel scaffold". In: *Journal of Biomaterials Science, Polymer Edition* 9.10 (1998), pp. 1049–1069.

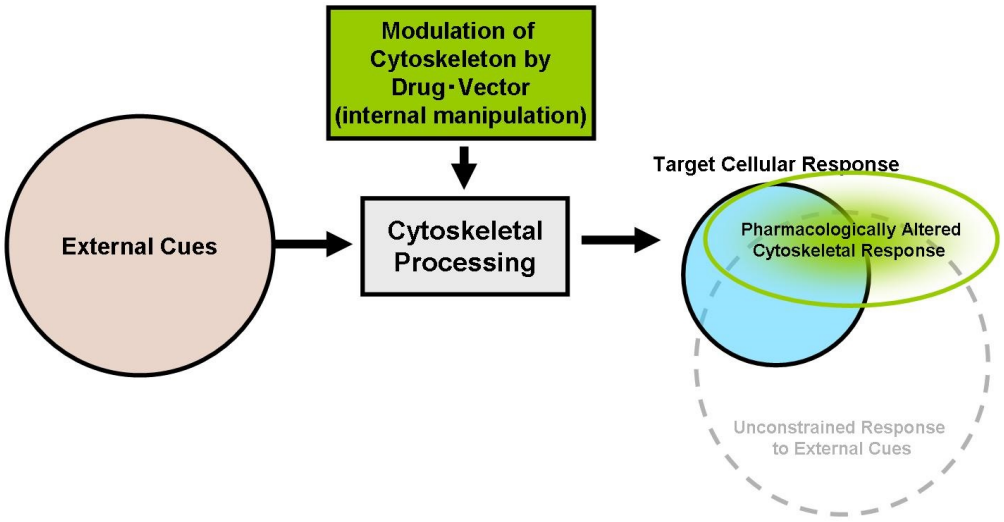

FIGURE 1.5: Genetic and pharmacological manipulation of cytoskeletal processes can influence how input signals are processed leading to novel behavior.

Consider Fig. 1.5, in which the cytoskeletal processing module is internally influenced, leading to a new output behavior probability distribution. The boundaries of this distribution may be different from a normal cell even given the same set of external cues. The modification may extend further into the range of interesting and useful target cell behaviors, but it may also extend outside that category as well.

The cytoskeleton is robust enough that removing certain elements from it does not necessarily lead to death of the organism. For example, null mutant mouse models for the intermediate filaments vimentin, neurofilament NFL, and GFAP are all viable[58]. Mice lacking gelsolin, a regulator of actin assembly and disassembly, exhibited slowed inflammatory, fibroblast, and hemostatic activity but were nonetheless viable[59]. This property exemplifies the multifunctionality and of cytoskeletal components which can fulfill or assist adaptively in the roles of other components.

Signaling networks are necessarily interconnected, thus the relevance of a particular protein or pathway to the cytoskeleton, an already broadly inclusive system, is semantically challenging. Pathways most closely associated with adhesion, force generation, and force sensing will be considered here. Key to understanding these phenomena has been the elucidation of regulatory pathways via genetic knockout of specific cytoskeletal proteins such as filaments, focal adhesion proteins, filament-associated proteins, and molecular

[58]M Bishr Omary, Pierre A Coulombe, and WH Irwin McLean. "Intermediate filament proteins and their associated diseases". In: *New England Journal of Medicine* 351.20 (2004), pp. 2087–2100; Thomas D Pollard, William C Earnshaw, and Jennifer Lippincott-Schwartz. *Cell biology*. Elsevier Health Sciences, 2007.

[59]Walter Witke et al. "Hemostatic, inflammatory, and fibroblast responses are blunted in mice lacking gelsolin". In: *Cell* 81.1 (1995), pp. 41–51.

motor proteins. Knocking out specific proteins is the most direct way to decouple variables experimentally. In a study by Gregor et al, the role of vimentin in force sensing through focal adhesions was investigated by decoupling vimentin from focal adhesions via knockout of vimentin or the cytolinker protein plectin. The knockout fibroblasts in this study had attenuated FAK activation, decreased focal adhesion turnover, high affinity elongated focal adhesions, and decreased cellular tension[60]. Palazzo et al used FAK knockout fibroblasts to determine the role that focal adhesions play in stabilizing microtubules. Comparison of FAK knockout mice to Src-Yes-Fyn, Paxillin, and Cas knockouts was used to narrow the possible pathways involved in local microtubule stabilization[61].

In addition to knockdown, experiments involving the artificial introduction of cytoskeletal proteins have been used in a number of cell biological experiments. Transfected L-cells, which when unmodified do not express cadherins and thus do not form tight intercellular junctions, were used by Nose et al in the discovery of cadherins as cell-cell adhesion-mediating molecules[62]. The transfectants were able to form tight intercellular junctions and multicellular aggregates. The experiment demonstrated, in addition to the natural role of cadherins, that entirely novel intercellular interactions could be engineered through this method.

While the above examples are almost exclusively related to experimental cell biology, manipulating cytoskeletal pathways genetically has practical applications as well. Cytoskeletal irregularities are commonly associated with cancer, and potential therapeutic targets. Epithelial cell adhesion molecule (EpCAM), for example is over expressed in breast cancer and has been identified as a potential gene therapy target[63]. When over expressed, EpCAM leads to attenuated association of the cadherin/catenin complex[64], having an indirect impact on cytoskeletal forces involved in cell-cell cohesion.

The epithelial to mesenchymal transition (EMT) and mesenchymal to epithelial transition (MET) are major shifts in cell phenotype with consequences for cytoskeletal force generation, sensing, adhesion. These phenomena are also causal regulators of EMT and MET. Cancer metastasis has been connected with EMT and MET-related mutations[65].

[60] Markus Schober et al. "Focal adhesion kinase modulates tension signaling to control actin and focal adhesion dynamics". In: *The Journal of cell biology* 176.5 (2007), pp. 667–680.

[61] Alexander F Palazzo et al. "Localized stabilization of microtubules by integrin-and FAK-facilitated Rho signaling". In: *Science* 303.5659 (2004), pp. 836–839.

[62] Akinao Nose, Akira Nagafuchi, and Masatoshi Takeichi. "Expressed recombinant cadherins mediate cell sorting in model systems". In: *Cell* 54.7 (1988), pp. 993–1001.

[63] Walid A Osta et al. "EpCAM is overexpressed in breast cancer and is a potential target for breast cancer gene therapy". In: *Cancer research* 64.16 (2004), pp. 5818–5824.

[64] Sergey V Litvinov et al. "Epithelial cell adhesion molecule (Ep-CAM) modulates cell–cell interactions mediated by classic cadherins". In: *The Journal of cell biology* 139.5 (1997), pp. 1337–1348.

[65] Mahmut Yilmaz and Gerhard Christofori. "EMT, the cytoskeleton, and cancer cell invasion". In: *Cancer and Metastasis Reviews* 28.1-2 (2009), pp. 15–33.

TABLE 1.1: List of common cytoskeletally active drugs.

Drug Name	Effect on Cytoskeleton
Cytochalasin D	Distrupts actin filaments by preventing polymerization
Latrunculin	Distrupts actin filaments by preventing polymerization
Nocodazole	Depolymerizes microtubules
Y-27632	Inhibits myosin contraction while allowing adherens junction formation
Blebbistatin	Inhibits myosin-driven contraction

For this reason, EMT-associated genes have been explored as possible targets for gene therapy such as with hepatocyte growth factor gene therapy[66]. There may be potential in regenerative medicine to exploit EMT pathways to control cell plasticity, as has been proposed for diabetes-related gene therapy induction of endocrine differentiation in adult pancreatic tissue[67].

Though the distinction from environmental stimuli becomes less clear, cytoskeleton-influencing small molecule inhibitors and growth factor proteins are yet another approach to manipulating cytoskeletal processes. Table 1.1[68] shows a list of small molecule inhibitors and their known effects.

Similar experiments can be designed using cytoskeletal inhibitors as with gene knockout, allowing one to isolate particular nodes or connections in a signaling pathway. Rape et al investigated the pathway-dependent increase of traction forces after depolymerization of microtubules by examining the effects of pharmacological inhibitors of myosin II and FAK[69]. McBeath et al used cytochalasin D and Y-27632 to demonstrate the connection between cell shape-dependent lineage commitment of mesenchymal stem cells and the cytoskeleton[70].

[66] Junwei Yang, Chunsun Dai, and Youhua Liu. "Hepatocyte growth factor gene therapy and angiotensin II blockade synergistically attenuate renal interstitial fibrosis in mice". In: *Journal of the American Society of Nephrology* 13.10 (2002), pp. 2464–2477.

[67] Susan L Samson and Lawrence Chan. "Gene therapy for diabetes: reinventing the islet". In: *Trends in Endocrinology & Metabolism* 17.3 (2006), pp. 92–100.

[68] Manfred Schliwa. "Action of cytochalasin D on cytoskeletal networks." In: *The Journal of cell biology* 92.1 (1982), pp. 79–91; Walter M Morton, Kathryn R Ayscough, and Paul J McLaughlin. "Latrunculin alters the actin-monomer subunit interface to prevent polymerization". In: *Nature cell biology* 2.6 (2000), pp. 376–378; B Herman, MA Langevin, and DF Albertini. "The effects of taxol on the organization of the cytoskeleton in cultured ovarian granulosa cells." In: *European journal of cell biology* 31.1 (1983), pp. 34–45; Tomoyo Koga et al. "Rho-associated protein kinase inhibitor, Y-27632, induces alterations in adhesion, contraction and motility in cultured human trabecular meshwork cells". In: *Experimental eye research* 82.3 (2006), pp. 362–370; Mihály Kovács et al. "Mechanism of blebbistatin inhibition of myosin II". in: *Journal of Biological Chemistry* 279.34 (2004), pp. 35557–35563.

[69] Andrew Rape, Wei-hui Guo, and Yu-li Wang. "Microtubule depolymerization induces traction force increase through two distinct pathways". In: *Journal of cell science* 124.24 (2011), pp. 4233–4240.

[70] Rowena McBeath et al. "Cell shape, cytoskeletal tension, and RhoA regulate stem cell lineage commitment". In: *Developmental cell* 6.4 (2004), pp. 483–495.

Analogous to genetic manipulation, many cytoskeletally active drugs have deleterious effects on cell function and health, a property which is exploited in cancer therapeutics such as the case with the microtubule-disrupting drug taxol used commonly for chemotherapy[71]. However, examples of positive uses of cytoskeletally active drugs can be found as well. ROCK inhibitor Y-27632, is used in the culture of epithelial and stem cells for its utility in preserving epithelial characteristics and preventing apoptosis[72]. Growth factors in combination with substrate physical constraints (eg: mechanical rigidity, spatial geometry, ECM ligand density) can be used to impact cell processes such as differentiation[73].

1.4 Cytoskeleton-Independent Methods for Controlling Cell Behavior

This section covers physical/mechanical methods for achieving some of the same functionality that the cytoskeleton provides. Though there are many pharmacological and genetic tools for manipulating cell behavior that are not directly tied to cytoskeletal processes, this section will mainly discuss external modifications of the cell membrane to induce artifical cell attachment or artificial adhesion. Fig. 1.6 shows how a process designed to occur in parallel with cytoskeletal processes can be used to explore different behaviors normally outside the bounds of possible responses to environmental stimuli without and with pharmacological or genetic manipulation of cytoskeletal pathways.

Antibodies, ubiquitous in biosciences and highly target-specific, can be used to mediate the attachment of cells to surfaces independently of cytoskeletally-linked cell adhesion molecules. Shin et al used antibodies specific to CD4 to attach cells to substrates. In their design, antibodies were tethered via biotin-avidin coupling chemistry involving a UV-cleavable crosslinker, allowing for CD4-bearing cells to be captured and subsequently released after UV exposure[74], and Zhu et al demonstrated a similar concept with electrically-stimulated release of cells attached through antibodies[75].

[71] Maurie Markman and Tarek M Mekhail. "Paclitaxel in cancer therapy". In: *Expert opinion on pharmacotherapy* 3.6 (2002), pp. 755–766.

[72] Xiangyun Li et al. "The ROCK inhibitor Y-27632 enhances the survival rate of human embryonic stem cells following cryopreservation". In: *Stem cells and development* 17.6 (2008), pp. 1079–1086; Fumitaka Osakada et al. "Stepwise differentiation of pluripotent stem cells into retinal cells". In: *Nature protocols* 4.6 (2009), pp. 811–824.

[73] Murat Guvendiren and Jason A Burdick. "The control of stem cell morphology and differentiation by hydrogel surface wrinkles". In: *Biomaterials* 31.25 (2010), pp. 6511–6518.

[74] Dong-Sik Shin et al. "Photolabile micropatterned surfaces for cell capture and release". In: *Chemical Communications* 47.43 (2011), pp. 11942–11944.

[75] He Zhu, Jun Yan, and Alexander Revzin. "Catch and release cell sorting: Electrochemical desorption of T-cells from antibody-modified microelectrodes". In: *Colloids and Surfaces B: Biointerfaces* 64.2 (2008), pp. 260–268.

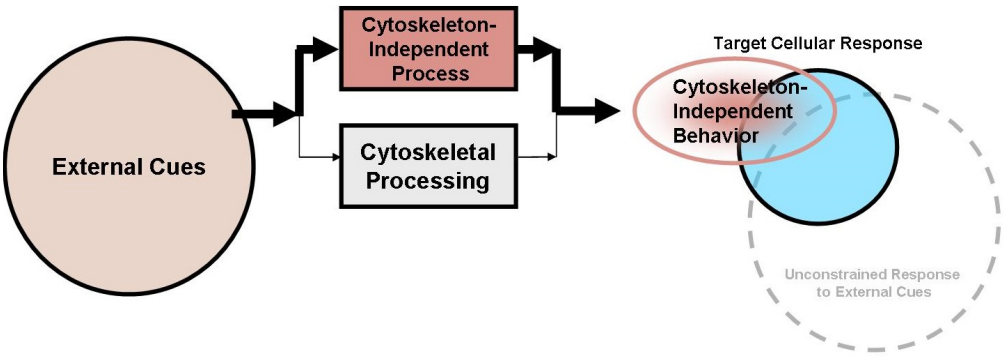

FIGURE 1.6: Modification in parallel with cytoskeletal processes can introduce novel cell behaviors such as order of magnitude-accelerated cell attachment to surfaces occurring through the kinetics of DNA hybridization as opposed to focal adhesion assembly.

Work by Bertozzi and colleagues on the modification of glycans present on cell surfaces has proven to be a means to introducing novel adhesive functionality to cells even without the use of transfected cDNA or natural proteins. For example, Chandra et al exposed azide-modified surface glycans with phosphine-functionalized oligonucleotides, introducing the heterotypic hybridization specificity of ssDNA to cell surfaces[76]. This method is distinct from the use of ECM proteins and integrins to program cell adhesion since surface glycans are largely independent of the actin cytoskeleton, meaning that the adhesive functionality introduced is superficial, and decoupled from cytoskeletal processes. Cells such as jurkat cells used in the study, a cell line of lymphocyte origin, which do not possess the normal adhesion machinery required of adherent cells like fibroblasts or epithelial cells can still be modified and attached to surfaces bearing the complementary DNA.

An alternative method for engineering novel cell surface chemistry, which does not involve direct covalent bond-mediated chemical modification of cell surface molecules, is to synthesize phospholipid-based nanotechnologies capable of associating with the cell membrane through non-covalent thermodynamic interactions. Iwata and Teramura originally used this technique to achieve novel cell surface attributes, for example by imparting immuno-compatibility to cells via membrane modification with hydrophilic polymers[77]. An additional level of functionality can be achieved by conjugating hydrophilic membrane inserts to single stranded DNA (ssDNA) which can hybridize to

[76]Ravi A Chandra et al. "Programmable cell adhesion encoded by DNA hybridization". In: *Angewandte Chemie* 118.6 (2006), pp. 910–915.

[77]Yuji Teramura, Yoshihiro Kaneda, and Hiroo Iwata. "Islet-encapsulation in ultra-thin layer-by-layer membranes of poly (vinyl alcohol) anchored to poly (ethylene glycol)–lipids in the cell membrane". In: *Biomaterials* 28.32 (2007), pp. 4818–4825; Suguru Miura, Yuji Teramura, and Hiroo Iwata. "Encapsulation of islets with ultra-thin polyion complex membrane through poly (ethylene glycol)-phospholipids anchored to cell membrane". In: *Biomaterials* 27.34 (2006), pp. 5828–5835; Yuji Teramura and Hiroo Iwata. "Bioartificial pancreas: microencapsulation and conformal coating of islet of Langerhans". In: *Advanced drug delivery reviews* 62.7 (2010), pp. 827–840; Yuji Teramura et al. "Behavior of synthetic polymers immobilized on a cell membrane". In: *Biomaterials* 29.10 (2008), pp. 1345–1355; Yuji Teramura and Hiroo Iwata. "Islets surface modification prevents blood-mediated inflammatory responses".

complementary ssDNA thus permitting the design of artificial attachment schemes mediated via the cell membrane[78]. This technique is explored in Chapter 4 with respect to the decoupling of lipid insert-mediated attachment of cells to surfaces from cytoskeletal, integrin/focal adhesion-mediated adhesion. Referring back to Fig. 1.6, the presence of ssDNA-PEG-lipids on the surface of cells means that parallel attachment processes can occur. Because of the major difference in time scales of DNA hybridization, which occurs on the order of seconds or less, versus integrin-mediated adhesion, which occurs on the order of minutes to hours, is comparable to an analogous electronic circuit with parallel processes of unequal resistances. It is more probable that cell convection or the rate of physical exposure of the membrane to its complementary ssDNA-bearing counterpart surface is the rate-determining step for DNA-mediated attachment rather than the hybridization reaction of adjacent ssDNA complement pairs, in contrast to integrin-mediated attachment in which the settling of cells is typically faster than the kinetics of adhesion. This property enables the design of systems that require some form of cell adhesion that would otherwise be prevented or limited by the restrictions of natural cell adhesion.

ssDNA-PEG-lipid-based attachment schemes come with other freedoms afforded by the departure from directly cytoskeletally-linked adhesion. In Chapter 5, restriction endonucleases and nonspecific nucleases are used to uncouple adhesive connections formed via ssDNA-modified cells and 2D substrates as well as other ssDNA-modified cells. In Chapter 6, the cohesion due to ssDNA-PEG-lipid cell-cell adhesion is estimated based on the deformation of cell membranes, demonstrating that quantitative modulation of adhesive properties may be possible in a way that would be complicated when working with natural cell adhesion regulatory pathways that are interconnected with other cell behaviors such like apoptosis, proliferation, and differentiation.

In: *Bioconjugate chemistry* 19.7 (2008), pp. 1389–1395; Yuji Teramura and Hiroo Iwata. "Surface modification of islets with PEG-lipid for improvement of graft survival in intraportal transplantation". In: *Transplantation* 88.5 (2009), pp. 624–630.

[78]Naohiro Takemoto, Yuji Teramura, and Hiroo Iwata. "Islet surface modification with urokinase through DNA hybridization". In: *Bioconjugate chemistry* 22.4 (2011), pp. 673–678; Kengo Sakurai, Yuji Teramura, and Hiroo Iwata. "Cells immobilized on patterns printed in DNA by an inkjet printer". In: *Biomaterials* 32.14 (2011), pp. 3596–3602; Yuji Teramura et al. "Control of cell attachment through polyDNA hybridization". In: *Biomaterials* 31.8 (2010), pp. 2229–2235; Yuji Teramura et al. "Microencapsulation of islets with living cells using polyDNA-PEG-lipid conjugate". In: *Bioconjugate chemistry* 21.4 (2010), pp. 792–796; Hao Chen, Yuji Teramura, and Hiroo Iwata. "Immobilization of anticoagulant-loaded liposomes on cell surfaces by DNA hybridization". In: *Biomaterials* 32.31 (2011), pp. 7971–7977; Hiroo Iwata. "Cell LEGO". in: *Optical MEMS and Nanophotonics (OMN), 2013 International Conference on*. IEEE. 2013, pp. 75–76.

1.5 Controlling Multicellular Dynamics

1.5.1 Collective Cell Adhesion Dynamics

The tools discussed in this thesis are relevant not only to cell-substrate adhesive interactions but also to cell-cell cohesive interactions. To understand why controlling artificial cell-cell interactions might be a useful capability, it is helpful to first understand the importance of cell-cell adhesion in a variety of biomedical problems, and where artificial tools may be used to overcome some of the limitations inherent in nature.

The integrity of tissues can partially be attributed to the strength of neighbor interactions in networks of connected cells. Multiple factors contribute to the mechanical integrity of tissues such as the compressive mechanics of cells and cytoskeletal filaments, the tensile mechanics of large interconnected ECM networks, and the propagation of forces through soft/stiff composite tissue architectures[79]. A major factor in tissue integrity is the mechanical coupling between cells and the propagation of forces over large sheets and 3-dimensional networks of interconnected cells. These connections are mediated by some of the cell-cell adhesion molecules discussed above, and by junctions such as desmosomes and adherens junctions which serve to link the cytoskeletons and intracellular force-generating machinery of each cell to neighboring cells creating a large mechanical network[80].

In addition to tissue integrity, however, the constraints on cell movement caused by cell-cell connections give rise to collective multicellular migratory patterns, or migratory behavior that emerges from the constraints imposed on cells by their interaction with the greater network. Among these patterns are synchronized migration, turbulent and laminar-like flows, vortices and coherent angular motion.[81]. These patterns arise from the propagation of adhesive interactions and forces between cells, restricting migratory movements to those compatible with the movements of nearest neighbors. In some cases,

[79] Karol Miller et al. "Mechanical properties of brain tissue in-vivo: experiment and computer simulation". In: *Journal of biomechanics* 33.11 (2000), pp. 1369–1376; Blayne A Roeder et al. "Tensile mechanical properties of three-dimensional type I collagen extracellular matrices with varied microstructure". In: *Journal of biomechanical engineering* 124.2 (2002), pp. 214–222; Chikayoshi Sumi, Akifumi Suzuki, and Kiyoshi Nakayama. "Estimation of shear modulus distribution in soft tissue from strain distribution". In: *Biomedical Engineering, IEEE Transactions on* 42.2 (1995), pp. 193–202.

[80] Kathleen J Green and Cory L Simpson. "Desmosomes: new perspectives on a classic". In: *Journal of Investigative Dermatology* 127.11 (2007), pp. 2499–2515; Mirna Perez-Moreno, Colin Jamora, and Elaine Fuchs. "Sticky business: orchestrating cellular signals at adherens junctions". In: *Cell* 112.4 (2003), pp. 535–548.

[81] Kevin Doxzen et al. "Guidance of collective cell migration by substrate geometry". In: *Integrative Biology* 5.8 (2013), pp. 1026–1035; Kandice Tanner et al. "Coherent angular motion in the establishment of multicellular architecture of glandular tissues". In: *Proceedings of the National Academy of Sciences* 109.6 (2012), pp. 1973–1978; Sri Ram Krishna Vedula et al. "Emerging modes of collective cell migration induced by geometrical constraints". In: *Proceedings of the National Academy of Sciences* 109.32 (2012), pp. 12974–12979.

tools from statistical physics used to study phase transitions have been imported to study collective motion[82]. These patterns hold relevance to cancer biology due to the asocial and subsequently social nature required for cancer cells undergoing both metastasis to escape their tissues of origin as well as reintegration with new tissues[83]. Additionally, controlling the collective action of groups of cells is a necessary quality for next generation tissue engineering constructs designed to replace complex, inhomogeneous, and non-equilibrium regenerative targets.

As discussed in the previous sections, we will consider how it might be possible to control certain aspects of collective migration by isolating variables of interest, focusing particularly on the adhesion and force-generating processes that are central to collective cell movements. Due to the distributed nature of collective cell movement, pattern control depends on either manipulating the strength of interactions between constituents whether they be cells or lattice points on a magnet or the global structure defining how those interaction propagate over larger distances. Doxzen et al used geometric boundary constraints as a control parameter to trigger and un-trigger synchronized rotational motion of cells patterned in circles. In the same study, different cell lines such as cells that had undergone the epithelial to mesenchymal transition (EMT) and cancer cell lines were also shown to have a diminished capacity for persistent synchronized migration. In the former case global boundary conditions were used to control the emergence of ordered migration, whereas in the latter case constituent interactions built into the system were exchanged.

While the choice of adhesive boundary constraints may indeed be used to modulate the global alignment of collective cell motion, this procedure is not easily adapted to 3D or tissue engineering applications. Therefore, a better understanding of and a capacity to manipulate the cell-cell adhesive interactions remains a major goal in collective migration work today. One avenue of investigation is the mechanism of the kinetics of cadherin coupling and decoupling. For cells to migrate relative to one another, adhesions between cells must be transiently stable, weak, or in some other way permissive to cell movement. Peglion et al recently contributed a report related to cell-cell dynamics in which they show that retrograde flow of cadherins occurs during migration of cells, and that a form of treadmilling similar to that which occurs on 2D substrates drives migration in a collective environment[84]. Polarized migrating cells in this case express cadherins at the leading edge of the cell and endocytose them when they reach the trailing edge. They

[82] Doxzen et al., "Guidance of collective cell migration by substrate geometry"; Balint Szabo et al. "Phase transition in the collective migration of tissue cells: experiment and model". In: *Physical Review E* 74.6 (2006), p. 061908.

[83] Peter Friedl and Darren Gilmour. "Collective cell migration in morphogenesis, regeneration and cancer". In: *Nature reviews Molecular cell biology* 10.7 (2009), pp. 445–457.

[84] Florent Peglion, Flora Llense, and Sandrine Etienne-Manneville. "Adherens junction treadmilling during collective migration". In: *Nature cell biology* 16.7 (2014), pp. 639–651.

also showed that the polarized distribution of adherens junctions were controlled by a front-to-rear gradient of catenin phosphorylation.

The cell-cell adhesion-mediating molecules and junctions in multicellular networks are critical for the propagation of interactions, however equally as critical is the cytoskeletal network that transmits forces intracellularly and from one face of the cell surface to another. Keratin, a type of intermediate filament, interfaces with desmosomes while actin networks are connected to adherens junctions. Evidence from Huen et al suggests that intermediate filaments and actin networks act synergistically to regulate the strength of cell-cell adhesions[85]. Huen et al also showed that strain-sensitive reinforcement of the cytoskeleton similar to that of integrin-actin regulation occurs in intercellular junctions. Work by Russel et al suggests that desmosome maintenance may in fact be regulated by tensile force sensing and subsequent intermediate filament network organization[86]. Vasioukhin et al showed that severing the link between intracellular keratin and desmosomes reduced the strength of intercellular adhesion[87], however contrary to this, a recent report by Harris et al suggests that the tissue-scale stiffness of epithelial cell sheets is more dependent on the formation of adherens junctions, and an experiment involving the decoupling of keratin and desmosomes did not yield a significant change in sheet integrity[88].

Harris et al found that the disruption of adherens junctions formation and maintenance by E-cadherin antibodies, ROCK-inhibition with the drug Y-27632, actomyosin contraction inhibition with Blebbistatin, formin inhibition with SMIFH2, and lamellipodial extension inhibition (prior to sheet confluency) via CK666 all resulted in significant reductions in the tensile integrity of large epithelial sheets, suggesting a major role for cytoskeletal elements in the maintenance and formation of intercellular cohesion. Actin remodeling and tensile force generation may play a major role in transmitting long range forces across multiple cells. Inoue et al showed that actomyosin tension is required for the recruitment and organization of adherens junctions as well as the formation of zona occludens[89].

[85] Arthur C Huen et al. "Intermediate filament–membrane attachments function synergistically with actin-dependent contacts to regulate intercellular adhesive strength". In: *The Journal of cell biology* 159.6 (2002), pp. 1005–1017.

[86] David Russell et al. "Mechanical stress induces profound remodelling of keratin filaments and cell junctions in epidermolysis bullosa simplex keratinocytes". In: *Journal of cell science* 117.22 (2004), pp. 5233–5243.

[87] Valeri Vasioukhin et al. "Desmoplakin is essential in epidermal sheet formation". In: *Nature cell biology* 3.12 (2001), pp. 1076–1085.

[88] Andrew R Harris, Alicia Daeden, and Guillaume T Charras. "Formation of adherens junctions leads to the emergence of a tissue-level tension in epithelial monolayers". In: *Journal of cell science* 127.11 (2014), pp. 2507–2517.

[89] Yuka Miyake et al. "Actomyosin tension is required for correct recruitment of adherens junction components and zonula occludens formation". In: *Experimental cell research* 312.9 (2006), pp. 1637–1650.

The cytoskeleton, far from being a passive medium, is capable of generating force as well as sensing forces to the extent that resistances or external forces exerted upon a cell can be responded to in turn. This role of force sensing and response adds a new dimension to be considered in collective migration problems. In examining the propagation of apical junctions in epithelial cell sheets, Revenu et al showed that microtubules are essential for the establishment of epithelial cell polarity but unnecessary for their maintenance[90]. In a recent report by Plestant et al, adhesive interactions mediated by N-cadherin were shown to limit the recruitment of microtubules, which approached the junctions but were prevented from reaching junction boundaries by the presence of acto-myosin contractile machinery[91]. An emerging theme of competing forces arises here, as we see that microtubules, typically responsible for the extension of membrane boundaries and a source of outward compressive force, are opposed by acto-myosin tension from stable junction formation.

Considering the goal of harnessing and controlling emergent collective dynamics, and acknowledging that intercellular adhesion is pivotal to the outcomes of collective cell dynamics, we now cover some of the work that has been done on engineering adhesion between cells through artificial means.

In many cases, the identification and isolation of adhesion proteins can be used to introduce the adhesive functionality observed naturally in one cell type to another cell type thus evoking behavior not ordinarily exhibited. This was done with cadherins by Tekeichi et al with L-cells, which normally do not express cadherins and possess no native capacity to aggregate, yet after being transfected with cadherin-encoding plasmids were able to aggregate spontaneously[92]. Berendt et al demonstrated this procedure with ICAM-1 by transfecting COS cells, introducing novel interaction between the COS cells and plasmodium falciparum[93]. Similarly, in order to demonstrate the existence of a novel class of adhesion molecules associated with tight junctions, Martin et al transfected CHO cells with cDNA encoding for the JAM protein thus introducing homotypic JAM-forming capacity to the CHO cells[94]. In previous sections we discussed the various

[90] Céline Revenu et al. "Quantitative cell polarity imaging defines leader-to-follower transitions during collective migration and the key role of microtubule-dependent adherens junction formation". In: *Development* 141.6 (2014), pp. 1282–1291.

[91] Charlotte Plestant et al. "Adhesive interactions of N-cadherin limit the recruitment of microtubules to cell–cell contacts through organization of actomyosin". In: *Journal of cell science* 127.8 (2014), pp. 1660–1671.

[92] Kohei Hatta et al. "Cloning and expression of cDNA encoding a neural calcium-dependent cell adhesion molecule: its identity in the cadherin gene family." In: *The Journal of cell biology* 106.3 (1988), pp. 873–881.

[93] AR Berendt et al. "Intercellular adhesion molecule-1 is an endothelial cell adhesion receptor for Plasmodium falciparum". In: *Nature* 341.6237 (1989), pp. 57–59.

[94] Inés Martìn-Padura et al. "Junctional adhesion molecule, a novel member of the immunoglobulin superfamily that distributes at intercellular junctions and modulates monocyte transmigration". In: *The Journal of cell biology* 142.1 (1998), pp. 117–127.

strategies that can be employed to impart unique behavior characteristics on cells via cytoskeletal manipulation by controlling environmental input signals with engineered substrates, by manipulating cytoskeletal regulatory pathways pharmacologically or genetically, and finally by bypassing cytoskeletal pathways like adhesion using engineered artificial alternatives like ssDNA-PEG-lipids.

Many of the techniques used to modify cells for specific functionality and binding to surfaces have been adapted for aggregation and artificial intercellular adhesion. The most prominent example again is glycan-modification. De Bank et al used periodate oxidation of sialic acid residues to generate aldehyde functional groups on cell surfaces, followed by exposure to biotin-hydrazide. The biotin-avidin relationship was then exploited by adding crosslinking avidin to biotin-bearing cells leading to precipitation of cellular aggregates[95]. This method was shown later to be useful for the co-culturing of unlike cell types, facilitating differentiation of embryonic stem cells, and accelerating the engraftment of keratinocytes onto a dermal skin layer model[96].

DNA aptamers optimized for specific affinities comparable to those of antibodies and chosen through the SELEX method have also been used to engineer specific cell-cell interactions. Altman et al used protein-specific aptamers to engineer artificial cell-cell adhesion schemes such as the binding between cells via avidin-recognizing aptamers and biotin-conjugated aptamers specific to cell surface proteins present on other cells[97]. Indeed, the selection process used to identify aptamers is powerful enough that it has been used to determine cell-specific aptamers, bypassing the need to identify particular proteins or glycans of interest, a process referred to as Cell-SELEX[98].

Lipid-conjugates for cell surface modification have proven to be versatile tools for bestowing specific adhesive functionality on cells while remaining decoupled from the cytoskeleton. Many of the receptor-ligand targeting schemes used for glycan-mediated artificial cell-cell adhesion can be applied to lipid conjugation schemes. Xiong et al used cell-specific aptamers conjugated to phospholipids and were able to generate specific heterotypic cellular aggregates and further demonstrated the technique could be used to program cytotoxic T-cells to target tumor cells with sufficient specificity[99]. ssDNA-PEG-lipids are explored in Chapters 5 and 6 for manipulating cell-cell adhesion. By limiting

[95] Paul A De Bank et al. "Surface engineering of living myoblasts via selective periodate oxidation". In: *Biotechnology and bioengineering* 81.7 (2003), pp. 800–808.

[96] Paul A De Bank et al. "Accelerated formation of multicellular 3-D structures by cell-to-cell crosslinking". In: *Biotechnology and bioengineering* 97.6 (2007), pp. 1617–1625.

[97] Meghan O Altman et al. "Modifying cellular properties using artificial aptamer-lipid receptors". In: *Scientific reports* 3 (2013).

[98] Kwame Sefah et al. "Development of DNA aptamers using Cell-SELEX". in: *Nature protocols* 5.6 (2010), pp. 1169–1185.

[99] Xiangling Xiong et al. "DNA Aptamer-Mediated Cell Targeting". In: *Angewandte Chemie International Edition* 52.5 (2013), pp. 1472–1476.

adhesion to membrane-associated tethers, multicellular aggregates of non-adherent, non-cohesive CCRF-CEM cells could be achieved in the absence of cadherins or other natural cell-cell adhesion molecules.

Methods to disrupt cell-cell adhesion have also been developed, many of which make use of the bio-intert characteristics of certain hydrophilic polymers such as polyethylene glycol (PEG). Teramura and Iwata used PEG-conjugated phospholipids to impart biocompatible characteristics on islets for improved islet transplantation therapy[100]. Small molecule inhibitors, growth factors, cytokines, EMT/MET switches, and genetic knockout strategies discussed in Section 1.3, can also be used to influence collective cell dynamics, though these will not be discussed in detail here.

[100]Teramura, Kaneda, and Iwata, "Islet-encapsulation in ultra-thin layer-by-layer membranes of poly (vinyl alcohol) anchored to poly (ethylene glycol)–lipids in the cell membrane"; Miura, Teramura, and Iwata, "Encapsulation of islets with ultra-thin polyion complex membrane through poly (ethylene glycol)-phospholipids anchored to cell membrane"; Teramura and Iwata, "Bioartificial pancreas: microencapsulation and conformal coating of islet of Langerhans"; Teramura et al., "Behavior of synthetic polymers immobilized on a cell membrane"; Teramura and Iwata, "Islets surface modification prevents blood-mediated inflammatory responses"; Teramura and Iwata, "Surface modification of islets with PEG-lipid for improvement of graft survival in intraportal transplantation".

Chapter 2

Assessing the spatial resolution of cellular rigidity sensing using a micropatterned hydrogel-photoresist composite

---

"Practical areas like percolation, frost heaving, crack propagation in metals, and the metallurgical quench all involve very complex microscopic physics underlying macroscopic effects, and most likely yield a mixture of some problems exhibiting fluctuations on all length scales and other problems which become simpler classical problems without fluctuations in larger scales."

Kenneth Wilson
Renormalization Group and Critical Phenomena
Reviews of Modern Physics, Vol. 55, No. 3, July 1983

2.1 Introduction

The rigidity of cell substrates dictates the deformation in response to traction forces applied by adhered cells and has a profound impact on cellular processes like migration, spreading, structural organization, growth, and differentiation[1]. Such influence has become an important consideration in both understanding pathological conditions particularly cancer metastasis[2] and in the design of scaffold materials for supporting regenerative therapies such as wound healing and tissue engineering[3]. Rigidity is measured by detecting material strain in response to applied mechanical forces[4]. For adherent cells like fibroblasts, the sensing involves focal adhesions, which transmit cytoskeletal contractile forces to the substrates and likely detect the strain through associated signal transduction enzymes and mechanosensitive components[5]. However, an important question is whether rigidity detection is confined locally to areas near individual focal adhesions, or is dependent on the strain across the length of the cell as implicated by wrinkling films[6].

Previous observations may be interpreted as supporting either a short- or long-range mechanism of rigidity sensing (Appendix Fig. A.1). The protein composition of focal adhesions, including components for both force transmission and sensing, appears self-sufficient for localized rigidity sensing as is supported by studies employing sub-micron beads. The effective rigidity of microscopic adherent beads, controlled by applying mechanical forces using either optical traps or magnets to counter traction forces exerted on the beads, was sufficient to affect local assembly of focal adhesions and actin filament bundles[7]. In addition, the turnover and density of integrins inside single focal adhesions appeared sufficient for sensing the spacing of adhesive ligands and substrate rigidity[8]. Other studies have suggested the existence of contraction dipoles or lateral

[1] Dennis E Discher, Paul Janmey, and Yu-li Wang. "Tissue cells feel and respond to the stiffness of their substrate". In: *Science* 310.5751 (2005), pp. 1139–1143.

[2] Matthew J PaszeK et al. "Tensional homeostasis and the malignant phenotype". In: *Cancer cell* 8.3 (2005), pp. 241–254; Robert W Tilghman et al. "Matrix rigidity regulates cancer cell growth and cellular phenotype". In: *PLoS One* 5.9 (2010), e12905.

[3] Stephanie J Bryant et al. "Crosslinking density influences chondrocyte metabolism in dynamically loaded photocrosslinked poly (ethylene glycol) hydrogels". In: *Annals of biomedical engineering* 32.3 (2004), pp. 407–417.

[4] Paul A Janmey, Penelope C Georges, and Søren Hvidt. "Basic rheology for biologists". In: *Methods in cell biology* 83 (2007), pp. 1–27.

[5] Discher, Janmey, and Wang, "Tissue cells feel and respond to the stiffness of their substrate"; Cindy K Miranti and Joan S Brugge. "Sensing the environment: a historical perspective on integrin signal transduction". In: *Nature cell biology* 4.4 (2002), E83–E90.

[6] Albert K Harris, Patricia Wild, and David Stopak. "Silicone rubber substrata: a new wrinkle in the study of cell locomotion". In: *Science* 208.4440 (1980), pp. 177–179.

[7] Daniel Choquet, Dan P Felsenfeld, and Michael P Sheetz. "Extracellular matrix rigidity causes strengthening of integrin–cytoskeleton linkages". In: *Cell* 88.1 (1997), pp. 39–48; Ning Wang and Donald E Ingber. "Control of cytoskeletal mechanics by extracellular matrix, cell shape, and mechanical tension". In: *Biophysical journal* 66.6 (1994), pp. 2181–2189.

[8] Bernhard Wehrle-Haller and Beat A Imhof. "The inner lives of focal adhesions". In: *Trends in cell biology* 12.8 (2002), pp. 382–389.

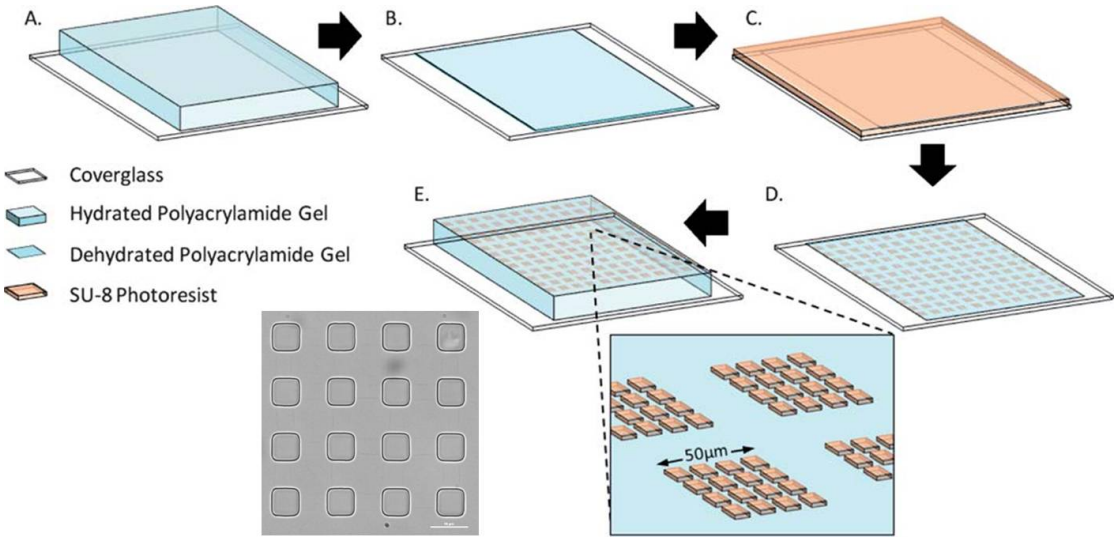

FIGURE 2.1: Schematic representation of the island patterning procedure. A sheet of polyacrylamide hydrogels is first polymerized on top of a bind-silane activated coverglass (A). The hydrogel is air dried causing the hydrogel to collapse down against the coverglass (B). A thin layer of the SU-8 photoresist is then applied to the dried hydrogel viaspin coating (C), followed by UV exposure through a photomask containing the pattern and development in the SU-8 developer to dissolve away unexposed regions of SU-8, leaving behind arrays of SU-8 islands (D). Immersion in PBS then allows the collapsed hydrogel to re-swell while maintaining the grafted SU-8 islands on the surface (E).

forces around single focal adhesions, which may be used for sensing rigidity in a local region of several focal adhesions[9]. However, the opposite conclusion may be reached from experiments with adherent cells placed on flexible pillars composed of relatively rigid polydimethylsiloxane (PDMS)[10], where cells responded not to the inherent rigidity of the materials but to the bending flexibility of the pillars, analogous to responses to homogeneous soft materials[11]. This suggests that the domain for rigidity sensing must be larger than the area of the pillars (1-2 μm in diameter). Herein, we report a novel technique for micropatterning substrate rigidity, with the goal of distinguishing cellular sensitivity to micro-scale rigidity from cell-scale rigidity (Appendix Fig. A.2). This method was used to generate an elastic hydrogel base with arrays of stiff islands grafted onto the surface. While a previous study has micropatterned islands of the photoresist on elastic materials for the purpose of measuring traction forces[12], the elastic material

[9] Ulrich S Schwarz et al. "Calculation of forces at focal adhesions from elastic substrate data: the effect of localized force and the need for regularization". In: *Biophysical journal* 83.3 (2002), pp. 1380–1394; James P Butler et al. "Traction fields, moments, and strain energy that cells exert on their surroundings". In: *American Journal of Physiology-Cell Physiology* 282.3 (2002), pp. C595–C605.

[10] John L Tan et al. "Cells lying on a bed of microneedles: an approach to isolate mechanical force". In: *Proceedings of the National Academy of Sciences* 100.4 (2003), pp. 1484–1489; Olivia Du Roure et al. "Force mapping in epithelial cell migration". In: *Proceedings of the National Academy of Sciences of the United States of America* 102.7 (2005), pp. 2390–2395.

[11] Alexandre Saez et al. "Is the mechanical activity of epithelial cells controlled by deformations or forces?" In: *Biophysical journal* 89.6 (2005), pp. L52–L54.

[12] Balaban et al., "Force and focal adhesion assembly: a close relationship studied using elastic micropatterned substrates".

used (polydimethylsilane) was too stiff for the present purpose. Using our method, the islands may move either easily (with a G' <500 Pa) or hardly (with a G' >10000 Pa) relative to each other upon the application of shear forces, while the islands themselves remain intrinsically rigid. This material allowed us to determine whether adhesive fibroblasts reacted to the intrinsic rigidity of the islands or to the bulk rigidity of the base hydrogel with cellular focal adhesions restricted to the rigid islands only.

2.2 Results and discussion

Reversible dehydration and rehydration of polyacrylamide hydrogels were exploited to allow for islands of the SU-8 photoresist to be cast over the surface in its dehydrated state. Patterns can be produced by tailoring the photomask used in selective exposure of the SU-8 photoresist (Fig. 2.1). The resolution allowed the generation of 4 x 4 arrays of 6.5 μm x 6.5 μm square islands separated by an edge-to-edge distance of 8 μm to cover an area of 50 μm x 50 μm, which is close to the average spread area of NIH 3T3 cells on unpatterned surfaces of the SU-8 photoresist[13]. This design was chosen in order to allow spreading fibroblasts to reach out and straddle multiple islands[14] while individually large enough to permit formation of multiple focal adhesions per island. By varying the concentration of acrylamide and bis-acrylamide, the rigidity of the base layer hydrogel may be controlled over a wide range. Control substrates of solid 50 μm x 50 μm SU-8 islands were also fabricated according to the same procedure.

This composite material was designed to possess two size scales of rigidity. The rigidity of SU-8 itself is high with a shear modulus of approximately 1-2 GPa[15]. In contrast, the hydrogels underlying these rigid islands may be as soft as several hundred Pa, which allowed the islands to move easily upon the exertion of traction forces. The results obtained with a soft hydrogel (G' $\approx 290 \pm 14$ Pa; triplicate samples, 4 measurements per sample) were then compared with those with a stiff hydrogel (G' $\approx 10.4 \pm 1.8$ kPa; triplicate samples, 4 measurements per sample). Similar shear moduli were obtained before and after exposing the gels to the micropatterning procedure, indicating that the grafting of the photoresist and the associated dehydration-rehydration did not significantly change the mechanical properties of the hydrogel (see the Experimental section). To test whether adherent cells respond either to the short-range rigidity within the stiff islands

[13]Christopher C Mader, Edward H Hinchcliffe, and Yu-li Wang. "Probing cell shape regulation with patterned substratum: requirement of myosin II-mediated contractility". In: *Soft Matter* 3.3 (2007), pp. 357–363.

[14]Dirk Lehnert et al. "Cell behaviour on micropatterned substrata: limits of extracellular matrix geometry for spreading and adhesion". In: *Journal of cell science* 117.1 (2004), pp. 41–52.

[15]Takayuki Fujita, Kazusuke Maenaka, and Yoichiro Takayama. "Dual-axis MEMS mirror for large deflection-angle using SU-8 soft torsion beam". In: *Sensors and Actuators A: Physical* 121.1 (2005), pp. 16–21.

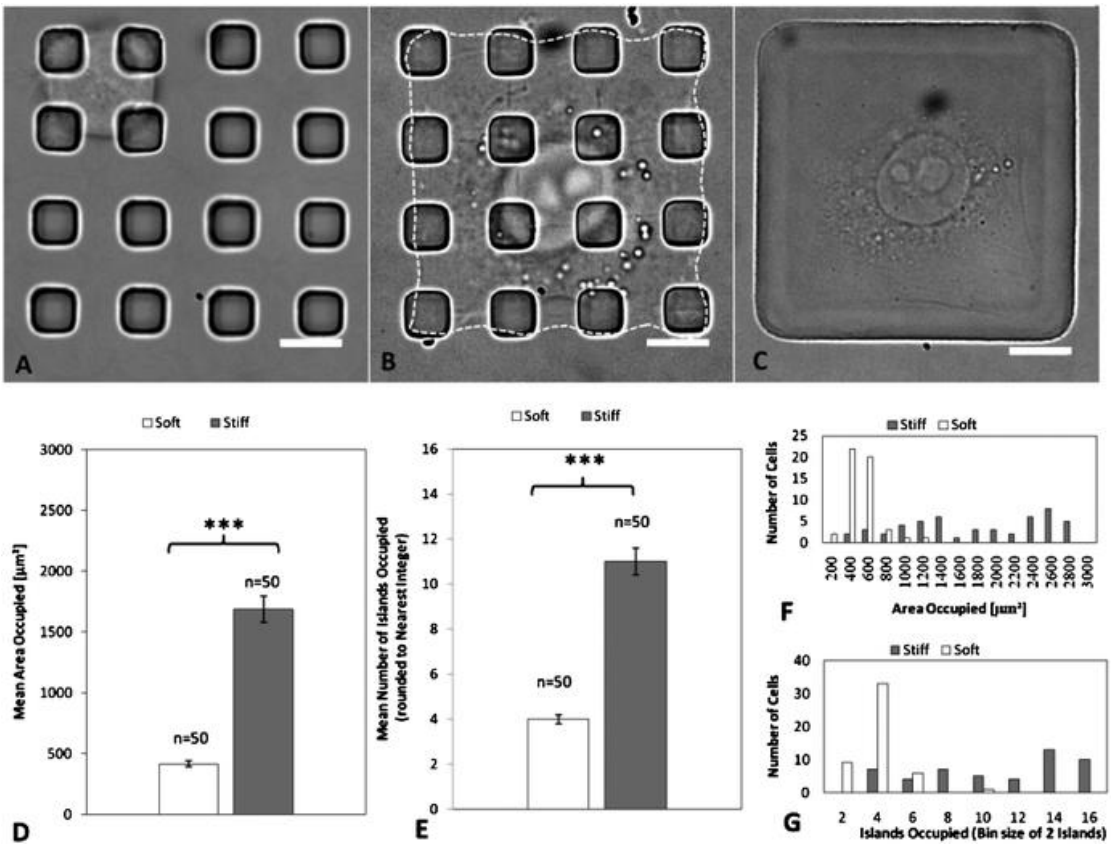

FIGURE 2.2: Cell spreading on composite substrates. NIH 3T3 cells on composite substrates with a soft base and rigid islands assume a minimally spread morphology consistent with those on uniformly soft substrates (A). Cells on composite substrates with a rigid base and rigid islands show a highly spread morphology consistent with those on uniformly stiff substrates (B), as do cells on control substrates made from soft hydrogels patterned with 50 x 50 μm solid squares (C). Scale bars, 10 μm. Measurements of mean spread area (D), and mean number of islands covered (E) 18 hr after seeding show striking differences ($p < 10^{-12}$ and $< 10^{-11}$ respectively) between cells on islands with soft (3% acrylamide, 0.08% bisacrylamide: white bars) and stiff (12% acrylamide, 0.2% bisacrylamide: gray bars) hydrogel bases. Bars represent standard error of the mean. Histogram of the spreading area (F), and number of islands covered (G) 18 hr after seeding show that the great majority cells on islands with a soft base are able to cover only four islands, while those on islands with a stiff base are more variable in spreading area with a peak covering all the islands in the 2D array.

or to the long-range rigidity of the underlying hydrogel, NIH 3T3 cells were cultured overnight on the patterned substrates with either soft (∼290 Pa) or rigid (∼10.4 kPa) hydrogel bases with identically patterned arrays of SU-8 islands. Clear differences in spreading behavior were observed between the two conditions (Fig. 2.2a and b). Cells on substrates with soft bases typically spanned no more than a 2 x 2 portion of the available islands (average total number of islands occupied n = 3.8 ± 0.2, n = 50; Fig. 2.2e and g), whereas substrates made from stiff hydrogel bases allowed many cells to spread over the entire 4 x 4 array (average total number of islands occupied n = 10.6 ± 0.6, n = 50; $p < 10^{-11}$; Fig. 2.2e and g). Measurements of spreading area indicated an average of 417 ± 23 μm^2 (n = 50) on soft hydrogel bases (Fig. 2.2d and f), but 1680 ±

100 μm^2 (n = 50) on stiff bases (Fig. 2.2d and f; p $<10^{-12}$). Control patterns of 50 μm x 50 μm solid SU-8 squares were covered entirely by cells (Fig. 2.2c). These responses were similar to those seen on uniformly soft or stiff materials[16].

In addition to the spreading area, both focal adhesions and stress fibers are known to increase in size with increasing substrate rigidity[17]. As expected, focal adhesions were restricted to the adhesive islands (Fig. 2.3). Composite substrates with rigid hydrogel bases induced the formation of large focal adhesions (Fig. 2.3a and the inset), which showed the typical elongated morphology aligned with adjoining stress fibers. Focal adhesions were typically located along outer edges and particularly at the four corners of each array (Fig. 2.3a and the inset), but were generally absent on islands in the interior of the arrays. The distribution is consistent with that observed and reported on solid square islands (Fig. 2.3d)[18]. The average area of focal adhesions on these substrates was 1.7 $\pm$ 0.1 μm^2 (Fig. 2.3e). Stress fibers in these cells were similarly well formed as a network throughout the cell.

In contrast, cells plated on composite substrates with soft hydrogel bases displayed only small focal contacts with no visible elongation, organization, or alignment (Fig. 2.3b). These focal contacts appeared randomly distributed as in cells during early stages of spreading. The average area occupied by each focal adhesion was much smaller than that on substrates with a stiff base (0.27 $\pm$ 0.01 μm^2; p $<10^{-28}$; Fig. 2.3e), and each island contained multiple focal contacts (insets of Fig. 2.3a and b). Similarly, only a few small, poorly organized stress fibers were found in these cells (Fig. 2.3e), analogous to those seen on homogeneous soft hydrogels.[19] Control cells on 50 μm x 50 μm solid squares or broad areas of SU-8 on soft hydrogels showed prominent focal adhesions and well-defined stress fibers (Fig. 2.3c and d). The contrasting results on stiff and soft hydrogel bases indicate that NIH 3T3 cells responded to the long-range rigidity even though the short-range rigidity was maintained at a constant high level.

Equally important is that the stiff islands were large enough to support the formation of multiple focal adhesions, indicating that short range rigidity between neighboring focal adhesions is insufficient to stimulate the formation of large focal adhesions as seen on uniformly stiff substrates. Alternatively, a large amount of slack anywhere along an axis of the cell may be sufficient to trigger dominant negative responses to prevent the formation of large stress fibers, focal adhesions, and spreading area, as suggested by the

[16] Tony Yeung et al. "Effects of substrate stiffness on cell morphology, cytoskeletal structure, and adhesion". In: *Cell motility and the cytoskeleton* 60.1 (2005), pp. 24–34; Lo et al., "Cell movement is guided by the rigidity of the substrate".

[17] Discher, Janmey, and Wang, "Tissue cells feel and respond to the stiffness of their substrate".

[18] Kevin Kit Parker et al. "Directional control of lamellipodia extension by constraining cell shape and orienting cell tractional forces". In: *The FASEB Journal* 16.10 (2002), pp. 1195–1204.

[19] Discher, Janmey, and Wang, "Tissue cells feel and respond to the stiffness of their substrate".

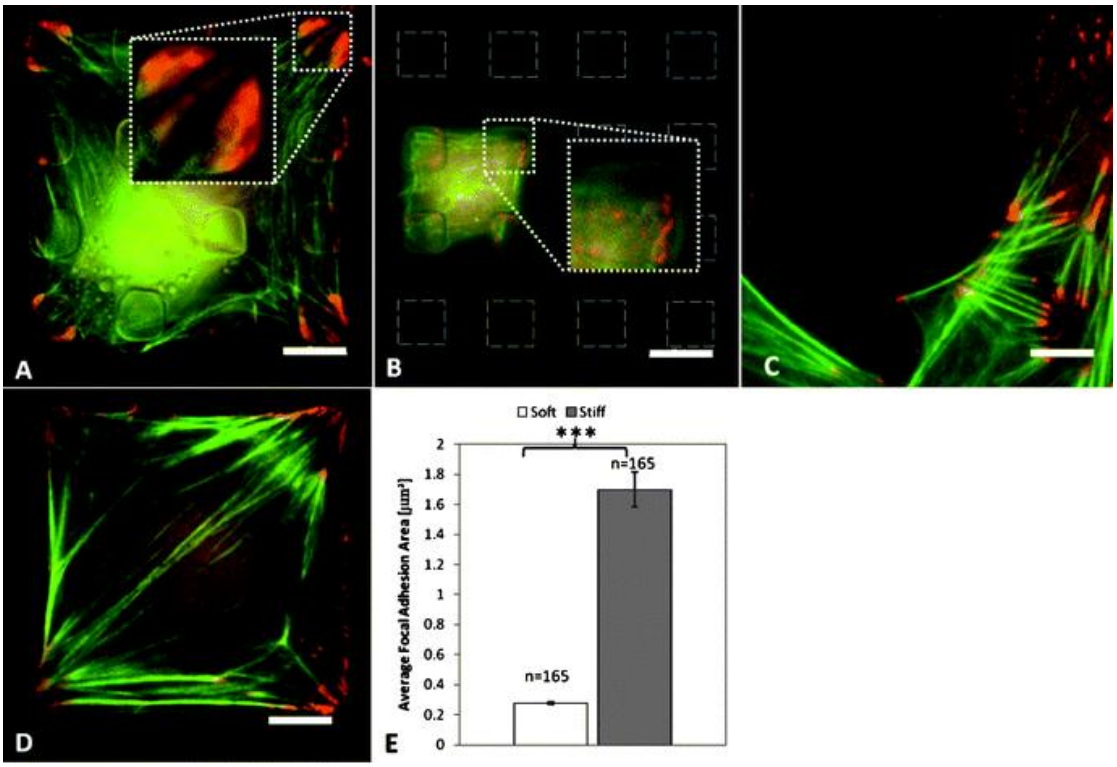

FIGURE 2.3: Organization of F-actin (green) and paxillin (red) in cells on composite substrates. Cells on islands with a stiff hydrogel base exhibit clearly defined stress fibers and multiple, well elongated focal adhesions at the corners and aligned towards the cell center (A). The inset shows an enlarged view of focal adhesions. In contrast, cells on islands with a soft hydrogel base exhibit poorly defined stress fibers with multiple small, poorly organized focal contacts on each covered island (B). The inset shows an enlarged view of these small focal contacts. Control cells seeded on large strips of SU-8 spread freely over the surface and form well defined stress fibers and focal adhesions (C), as do cells seeded over 50 μm x 50 μm solid squares on soft gels (D). Bars, 10 μm. Measurements of average focal adhesion areas show a large, significant ($p < 10^{-28}$) difference between cells on substrates with a soft base ($0.28 \pm 0.01\ \mu m^2$) and those on a stiff base ($1.7 \pm 0.1\ \mu m^2$; E). Error bars represent standard error of the mean, from 165 focal adhesions in five cells for each condition.

inability of cells to span more than two islands on soft bases. The present results may be explained by a positive feedback mechanism that drives cell spreading and cytoskeletal organization. Newly plated cells show a limited spreading area, small scattered focal contacts, and fine, poorly organized actin filament bundles. The resistance of substrates to probing traction forces across the cell length was determined during spreading, such that strong resistance triggers strong positive feedback responses including the formation of progressively larger stress fibers, activation of actin flux at focal adhesions, and growth of focal adhesions that drive the increase in traction forces and spreading area[20]. This

[20]Parker et al., "Directional control of lamellipodia extension by constraining cell shape and orienting cell tractional forces"; Cynthia A Reinhart-King, Micah Dembo, and Daniel A Hammer. "The dynamics and mechanics of endothelial cell spreading". In: *Biophysical journal* 89.1 (2005), pp. 676–689; Andrew D Rape, Wei-hui Guo, and Yu-li Wang. "The regulation of traction force in relation to cell shape and focal adhesions". In: *Biomaterials* 32.8 (2011), pp. 2043–2051.

process continues until the cell reaches the limit of spreading. In contrast, the lack of such feedback on soft substrates would keep cells in a poorly organized and poorly spread state. The results with stiff islands on the soft base further suggest that large amounts of slack during the course of spreading is sufficient to inhibit the positive feedback and the progress of spreading reactions.

It is important to note that the present study probes the scale of rigidity sensing without addressing the minimal adhesion area required to trigger the responses to stiff substrates. As long as adhesion sites are well-anchored to resist traction forces and tension is maintained between the two ends of a spreading cell, the area of adhesion may be as small as what is required to support the formation of a focal adhesion. This is consistent with previous findings that cells are able to spread over a matrix of small islands[21]. In addition, it explains why localized forces applied through sub-micron sized beads were able to elicit responses similar to those caused by long-range rigidity. As long as the cell is strongly adhered to the substrate, external forces exerted through micron-sized adhesive beads would generate sufficient tension to stimulate local responses. The present finding is significant both for understanding cellular behavior under physiological conditions and for designing materials for clinical treatments. For example, physiological environments are rarely chemically nor mechanically homogeneous. The present study suggests that the mechanical environment of a long-range soft scaffold may be maintained even if it is dotted with subcellular domains of rigid materials. Conversely, it implies that the mechanical stimulus of a long range rigid scaffold may be maintained despite the presence of subcellular domains of soft materials. In addition, the guidance of cell migration by substrate rigidity, known as durotaxis[22], may be determined by gradients over the cellular scale and unaffected by subcellular-scale variability in rigidity.

2.3 Experimental

2.3.1 Hydrogel preparation

The general procedure for patterning hydrogels with arrays of photoresist islands is outlined schematically in Fig. 2.1. This procedure allows for patterning of 1-2 μm features on either soft or stiff hydrogels. First, a coverglass was activated with 3 $\mu L\ mL^{-1}$ bind-silane (GE Healthcare, Waukesha, WI) in a solution of 95% ethanol and 5% glacial acetic

[21] Chen et al., "Geometric control of cell life and death".
[22] Lo et al., "Cell movement is guided by the rigidity of the substrate".

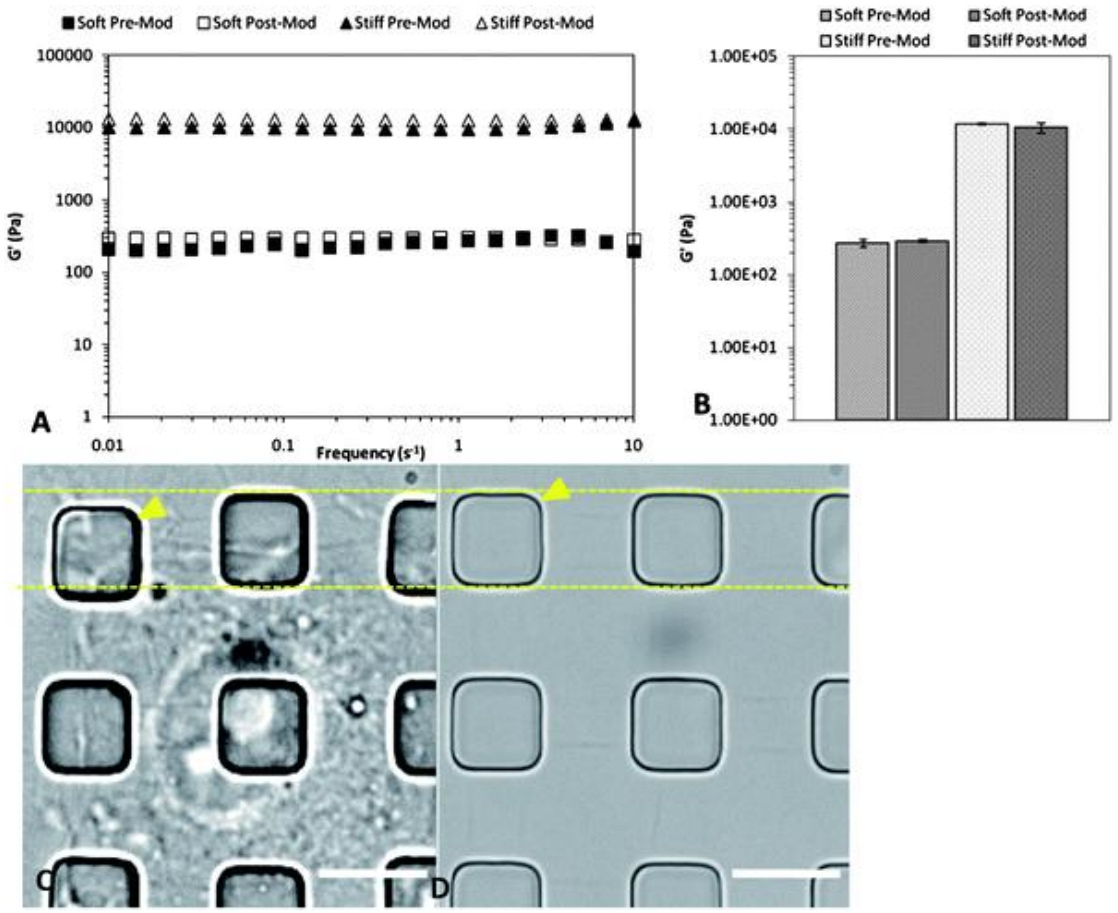

FIGURE 2.4: Characterization of substrate elasticity. Mechanical properties of the polyacrylamide base layer are measured before and after over-layering with SU-8 using parallel plate rheometry (A). Graph shows representative measurements of the elastic shear modulus G' [Pa] at a constant strain of 0.01 as a function of shear frequency taken before and after hydrogel modification, for both soft (3% acrylamide, 0.08% bisacrylamide) and stiff (12% acrylamide, 0.2% bisacrylamide) hydrogels. Note the horizontal trends of G' as a function of frequency, which indicate the elastic quality of the samples. The average values of G' from multiple measurements of triplicate samples before and after the modification for micropatterning show no change in elasticity after drying and reswelling in the procedure for SU-8 overlay (B). Error bars represent the standard error of the mean. To verify the elastic recovery of hydrogels with SU-8 islands on the surface, cells are allowed to adhere to the islands and exert traction forces overnight (C). Strain of the hydrogel is evident (C, lines and arrows). Upon removal of the cells with trypsin, the displaced islands return to their initial positions to restore the regularity of the pattern, illustrating elastic properties of the gel and no slippage between island and hydrogel (D, lines and arrows). Scale bars, 10 μm.

acid to allow the grafting of polyacrylamide hydrogels during polymerization. Polyacrylamide hydrogels were then prepared as previously described[23]. Precursor solutions were made by mixing stock solutions of N,N'-methylenebisacrylamide (bisacrylamide) (2% bisacrylamide; Bio-Rad, Hercules, CA) and acrylamide monomers (40% acrylamide; Bio-Rad, Hercules, CA) (Appendix Fig. A.3). The amount of acrylamide and the ratio of bisacrylamide to acrylamide control the rigidity of the hydrogela mixture of 3% acrylamide and 0.08% bisacrylamide was used for soft gels and a mixture of 12% acrylamide and 0.2% bisacrylamide was used for stiff gels. These solutions were degassed for 30 minutes before the initiation of polymerization with ammonium sulfate and N,N,N',N'-tetramethylenediamine (TEMED) at concentrations of 0.06% (w/v) and 0.04% (v/v), respectively. A 20 μL drop was pipetted onto the activated coverglass and then covered with a 25 x 25 mm square coverglass (No. 1, 25 mm x 25 mm; Corning Life Sciences) pretreated with hydrophobic RAIN-X (SOPUS Products, Houston, TX) to facilitate subsequent removal. The reaction was allowed to proceed for 1 hr at 25°C, and the resulting hydrogels were air dried vertically for 1 hr after removing the top coverslip (Fig. 2.1a and b).

2.3.2 Micropatterning

Arrays of rigid islands were created on dried hydrogels using the epoxy-based negative photoresist SU-8 2000 (Microchem, Newton, MA) (Appendix Fig. A.4). Micropatterning was conducted according to the protocol of the manufacturer to produce features <3 μm in height. Coverslips with dried hydrogel were baked at 95°C for 1 min before and after coating with 300 μL of SU-8 with a spin coater at 5000 rpm for 20 sec (WS-6505-6NPP-LITE, Laurell Technologies, North Wales, PA; Fig. 2.1c). The coverslips were then exposed to ultraviolet light (360 nm, 100 $mJcm^{-2}$) underneath a photomask with designed patterns (HTA Photomask, San Jose, CA), then baked for another 1 min at 95°C before immersion in the SU-8 developer (Microchem, Newton, MA, USA) for 90 sec to yield the pattern (Fig. 2.1d). Developed coverslips were rinsed twice with 95% ethanol (Pharmaco-AAPER, Sherlbyville, KY, USA), and baked at 95°C for 4 hr to ensure removal of any residual developer and mitigation of potential risk of cytotoxicity. Finally, the hydrogel was allowed to rehydrate in phosphate buffered saline (PBS; Fig. 2.1e) for 1 hr. Binding between the hydrogel and islands was stable enough such that the composite substrates lasted for at least three weeks upon storage.

[23]Karen A Beningo, Chun-Min Lo, and Yu-Li Wang. "Flexible polyacrylamide substrata for the analysis of mechanical interactions at cell-substratum adhesions". In: *Methods in cell biology* 69 (2002), pp. 325–339.

2.3.3 Cell culture

NIH 3T3 mouse fibroblasts (ATCC, Rockville, MA, USA) were incubated at 37°C in Dulbecco's Modified Eagle Medium (DMEM; Invitrogen) containing 10% donor adult bovine serum (Thermo-scientific), 2 mM L-glutamine, 50 $\mu g\ mL^{-1}$ streptomycin, and 50 $\mu g\ mL^{-1}$penicillin (Gibco BRL, Gaithersburg, MA, USA), under humidified atmosphere composed of 95% air and 5% carbon dioxide. Prior to plating cells, substrates were sterilized for 20 min under the germicidal lamp of a tissue culture cabinet. PBS was removed and replaced with cell culture media and allowed to equilibrate with the hydrogel. These media were then replaced with fresh media and incubated for 1 hr prior to cell plating, in order to allow passive adsorption of serum proteins to the SU-8 islands[24]. Plated cells were allowed to spread for 18 hr before observation or fixation. While the SU-8 photoresist most likely allowed cell adhesion by adsorbing extracellular matrix proteins, improved control of cell adhesion may be achieved in future studies through surface activation with agents such as sulfo-SANPAH and conjugation with a defined matrix protein[25]. This would also allow adhesion to take place over the entire surface rather than confined to stiff islands.

2.3.4 Fixation and fluorescent labeling

Cells were rinsed with 37°C PBS then fixed for 10 minutes. Fixation solution consisted of 4% formaldehyde (from 16% stock solution, Thermo-Scientific, Rockford, IL) in PBS with 0.1% Triton X-100 (Sigma-Aldrich). Immunofluorescence staining for paxillin was performed using 1:200 dilution of anti-paxillin polyclonal rabbit antibody (SC-5574, IgG, Santa Cruz Biotechnology, CA), and 1:200 fluorescent anti-rabbit antibody (Alexa Fluor 546, goat anti-rabbit, IgG (H + L) 2 $mg\ mL^{-1}$, Invitrogen) following the standard procedure. Actin stress fibers were counter-stained with fluorescein phalloidin (F-432, Molecular Probes, Eugene, OR).

2.3.5 Microscopy and image analysis

Images were taken using a Nikon Eclipse Ti inverted microscope (Nikon Instruments Inc., Melville, NY) with an Andor iXON EM charged coupled device camera (Andor Technologies, Belfast, North Ireland). Bright field images and fluorescence images were acquired using a Nikon 100x, 1.49 NA oil immersion objective lens. ImageJ software was

[24] Tiina Sikanen et al. "Dynamic coating of SU-8 microfluidic chips with phospholipid disks". In: *Electrophoresis* 31.15 (2010), pp. 2566–2574.

[25] Pelham and Wang, "Cell locomotion and focal adhesions are regulated by substrate flexibility".

used to measure the cell spreading area and focal adhesion area after manually tracing the areas of interest.

2.3.6 Rheological characterization

Rheological studies of the hydrogel were conducted using a Bohlin Gemini Advanced Rheometer (Malvern Instruments Inc., NJ). The gel was prepared on small circular coverslips following the same procedure as for cell culture, except that the gel was at a thickness of 500 μm. After zeroing the rheometer with a dummy coverslip, the hydrogel sample on a coverslip was loaded onto the rheometer and frequency sweeps at 25°C were conducted in the hydrogel's elastic regime from 10 Hz to 0.1 Hz at a constant strain of 0.01 using parallel plate geometry. For each sample, 4 frequency sweeps were conducted to obtain an average shear modulus (Fig. 2.4a and b). To test the rheological properties of the hydrogel after micropatterning, the patterning procedure was applied to circular 500 μm thick gels but without UV exposure, which caused the entire layer of the SU-8 photoresist to be removed during development. The processed hydrogels were then allowed to swell before testing under the same conditions as for control samples.

To assess elastic recovery of the hydrogel upon prolonged exertion of traction forces, cells were cultured overnight on a composite substrate with a soft base (Fig. 2.4c). Island displacement was visible compared to arrays without cells. Upon removal of the cells with trypsin, all the islands returned to their original positions as indicated by the restoration of the distance between islands to that of arrays without cells, suggesting that the hydrogels maintained their elasticity and that there was no slippage of the islands on the hydrogel surface (Fig. 2.4d) and (Appendix Fig. A.5).

2.4 Conclusions

In summary, we developed a new photoresist-hydrogel composite material with micropatterned rigidity dependent on the location and size scale of measurements. NIH 3T3 cells seeded on this material with a soft base were able to span only a limited distance and number of islands despite the adhesive contact with intrinsically rigid photoresist islands. Likewise, focal adhesions and stress fibers were small and unorganized as opposed to those on stiff bases, or in cells on uniformly stiff substrates. Our observations suggest that cells sense rigidity across the entire length of the cell body rather than in small domains within or between single focal adhesions. This principle may allow composite materials with distinct domains of chemical and physical properties to be designed for optimal clinical treatments. Future studies using this material with different cell types

such as epithelial and endothelial cells, myocytes, chondrocytes, or stem cells may reveal whether the present results represent a universal principle of mechanosensing for adhesive cells.

Chapter 3

Manipulation of cell sorting within mesenchymal stromal cell-islet cell multicellular spheroids

---

"A symmetry allows some freedom of action to each of them but the interaction among them forces them, figuratively speaking, to line up like a crowd of people looking into the same direction...So the symmetry appears to be lost. It is still possible to recover the lost symmetry by a global operation, but it would amount to a kind of phase transition."

Yoichiro Nambu
2008 Nobel Lecture

3.1 Introduction

Cotransplantation of islets with immunoprivileged cell types is a potential strategy for the protection of grafts to treat type I diabetes. Immunoprivileged cell types, such as Sertoli[1] and placenta-derived cells[2], have been shown to bestow immunoprotective benefits on islets.

Among the candidates for immunoprotective cells are mesenchymal stromal cells (MSCs) that are attractive for their practicality as autologous and allogenic donor sources and for the high yield that can be obtained compared with cells from other immune-privileged sites like the testes or fetus[3]. MSCs exhibit anti-inflammatory properties[4] that occur through a variety of pathways, such as proliferation inhibition of T-lymphocytes through direct contact[5] and secreted anti-inflammatory soluble factors[6] in response to proinflammatory stimuli.

Transplantation of MSCs for immunoprotection has met with success in several applications[7], and multiple studies have demonstrated successful cotransplantation of islets with MSCs under various conditions including xenotransplantation[8]. MSCs have also

[1] Gregory S Korbutt, John F Elliott, and Ray V Rajotte. "Cotransplantation of allogeneic islets with allogeneic testicular cell aggregates allows long-term graft survival without systemic immunosuppression". In: *Diabetes* 46.2 (1997), pp. 317–322; Hua Yang and James R Wright Jr. "Co-Encapsulation of Sertoli Enriched Testicular Cell Fractions Further Prolongs Fish-to-Mouse Islet Xenograft Survival1". In: *Transplantation* 67.6 (1999), pp. 815–820.

[2] Khalid M Qureshi et al. "Human amniotic epithelial cells induce localized cell-mediated immune privilege in vitro: implications for pancreatic islet transplantation". In: *Cell transplantation* 20.4 (2011), pp. 523–534.

[3] Lindolfo da Silva Meirelles, Pedro Cesar Chagastelles, and Nance Beyer Nardi. "Mesenchymal stem cells reside in virtually all post-natal organs and tissues". In: *Journal of cell science* 119.11 (2006), pp. 2204–2213.

[4] William T Tse et al. "Suppression of allogeneic T-cell proliferation by human marrow stromal cells: implications in transplantation". In: *TRANSPLANTATION-BALTIMORE-* 75.3 (2003), pp. 389–397; Amelia Bartholomew et al. "Mesenchymal stem cells suppress lymphocyte proliferation in vitro and prolong skin graft survival in vivo". In: *Experimental hematology* 30.1 (2002), pp. 42–48.

[5] Andrea Augello et al. "Bone marrow mesenchymal progenitor cells inhibit lymphocyte proliferation by activation of the programmed death 1 pathway". In: *European journal of immunology* 35.5 (2005), pp. 1482–1490.

[6] Roland Meisel et al. "Human bone marrow stromal cells inhibit allogeneic T-cell responses by indoleamine 2, 3-dioxygenase–mediated tryptophan degradation". In: *Blood* 103.12 (2004), pp. 4619–4621; Kazuya Sato et al. "Nitric oxide plays a critical role in suppression of T-cell proliferation by mesenchymal stem cells". In: *Blood* 109.1 (2007), pp. 228–234.

[7] Lynne M Ball et al. "Cotransplantation of ex vivo–expanded mesenchymal stem cells accelerates lymphocyte recovery and may reduce the risk of graft failure in haploidentical hematopoietic stem-cell transplantation". In: *Blood* 110.7 (2007), pp. 2764–2767; Andrea Augello et al. "Cell therapy using allogeneic bone marrow mesenchymal stem cells prevents tissue damage in collagen-induced arthritis". In: *Arthritis & Rheumatism* 56.4 (2007), pp. 1175–1186.

[8] Mario G Solari et al. "Marginal mass islet transplantation with autologous mesenchymal stem cells promotes long-term islet allograft survival and sustained normoglycemia". In: *Journal of autoimmunity* 32.2 (2009), pp. 116–124; Dora M Berman et al. "Mesenchymal stem cells enhance allogeneic islet engraftment in nonhuman primates". In: *Diabetes* 59.10 (2010), pp. 2558–2568.

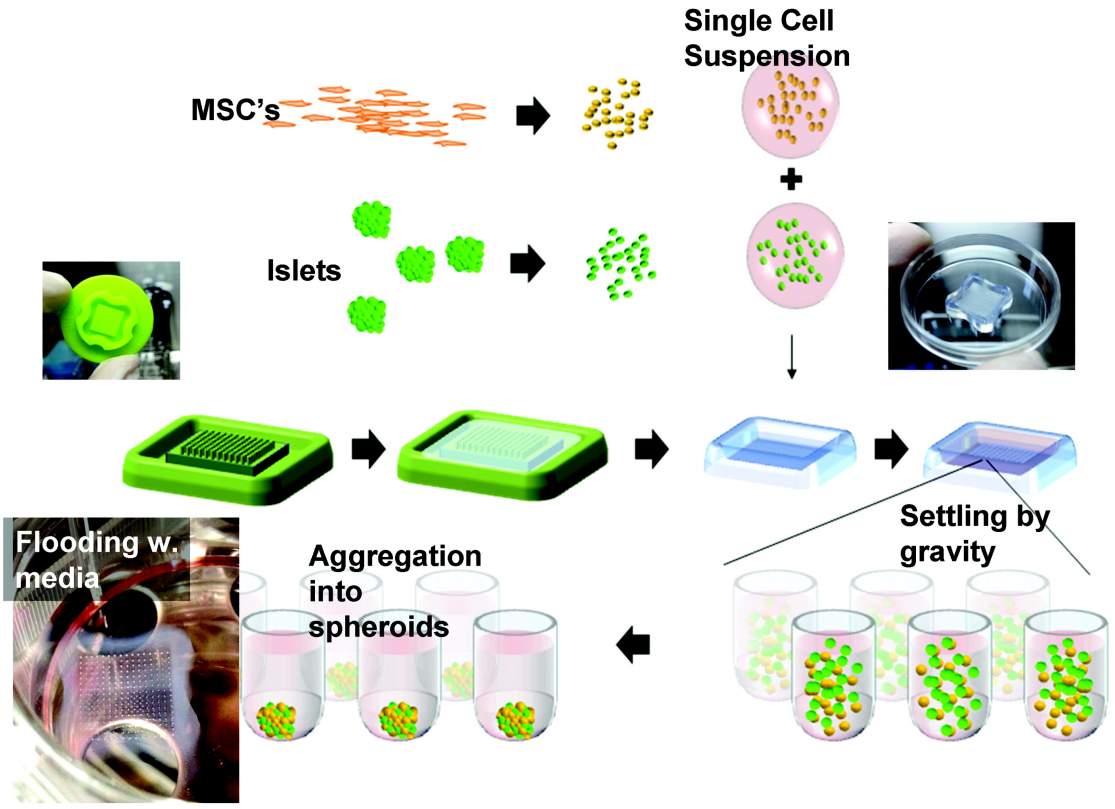

FIGURE 3.1: Agarose well array method for coaggregation of mesenchymal stromal cells (MSCs) and islet cells. A micromold is used to create agarose hydrogel arrays of 16x16 round-bottomed wells each 250μm in diameter. MSCs are detached from culture dishes and suspended in medium as single cells. Meanwhile, islets are also dissociated into a single-celled suspension to then be mixed with the MSC suspension in the desired proportions. The mixed suspension is then pipetted over the agarose array and allowed to settle by gravity for 24h. During this period, stable aggregates form after which media can be flooded over the array for long-term culture.

been shown to thrive in hypoxic conditions[9] and mitigate damage to islets subjected to hypoxia[10]. Evidence suggests that colocalization of MSCs and islets may improve the chances of graft success[11]. Intraportal islet transplantations like those carried out according to the Edmonton protocol[12] are subjected to size-exclusion filtering of injected particles caused by the branching and successive narrowing of blood vessels in the liver. Single cells thus penetrate further into the liver than islets, effectively delocalizing the two and potentially mitigating the protective benefits that MSCs bestow on islets. Immunoprotection of islets may depend on close proximity or direct contact with protector

[9]Yonghui Jin et al. "Mesenchymal stem cells cultured under hypoxia escape from senescence¡ i¿ via¡/i¿ down-regulation of p16 and extracellular signal regulated kinase". In: *Biochemical and biophysical research communications* 391.3 (2010), pp. 1471–1476.

[10]Yanrong Lu et al. "Mesenchymal stem cells protect islets from hypoxia/reoxygenation-induced injury". In: *Cell biochemistry and function* 28.8 (2010), pp. 637–643.

[11]Valeria Sordi and Lorenzo Piemonti. "Mesenchymal stem cells as feeder cells for pancreatic islet transplants". In: *The review of diabetic studies: RDS* 7.2 (2010), p. 132.

[12]AM James Shapiro et al. "Islet transplantation in seven patients with type 1 diabetes mellitus using a glucocorticoid-free immunosuppressive regimen". In: *New England Journal of Medicine* 343.4 (2000), pp. 230–238.

cells. However, no study has yet provided an approach for uniformly coaggregated, temporally stable, and clearly integrated composites of MSCs and islets.

In this study, we examined coaggregation of MSCs with cells of dissociated islets. Clear separation of islet-derived cells from MSCs into different spheroidal domains was observed by microscopy. Beta-cells and alpha-cells that comprise the majority of cells in islets are known to maintain cohesive integrity largely through intercellular bonds mediated by cadherins, such as E-cadherin[13], while the adhesion profile of MSCs has been shown to be dominated by members of the integrin and immunoglobulin family[14]. We hypothesized that cell sorting through differential cell-cell adhesion occurred; that is, coaggregation of islet-derived cells and MSCs leads to separation due to disagreement between adhesion modes[15]. An inhibitor of Rho Associated Kinase (ROCKi), Y-27632, is known to stabilize intercellular adherens junctions, reduce matrix-mediated migratory behavior, and promote cellular cohesion through cadherin expression[16]. We anticipated therefore that coaggregation of MSCs with islet cells in the presence of Y-27632 would enhance intercellular cohesion and colocalization.

3.2 Materials & Methods

For explanations of primary cell isolation and culture, purchased reagents, antibodies used, the immunostaining procedure, and timelapse confocal microscopy see Supplementary Materials and Methods (Appendix).

3.2.1 Preparation of islet/MSC coaggregates with gels

MSC/islet coaggregates were prepared by creating gel arrays containing many round-bottomed wells. A mold was used to create a well array of 256 (16x16) wells each of 250 μm in diameter (Microtissues, Inc., Providence, RI) by injecting hot 2.5% agarose (SeaKem GTG Agarose; Camrex Bio Science Rockland, Inc., Rockland, ME) in HBSS

[13] Domenico Bosco, Dominique G Rouiller, and Philippe A Halban. "Differential expression of E-cadherin at the surface of rat β-cells as a marker of functional heterogeneity". In: *Journal of endocrinology* 194.1 (2007), pp. 21–29; Géraldine Parnaud et al. "Cadherin engagement protects human β-cells from apoptosis". In: *Endocrinology* 152.12 (2011), pp. 4601–4609.

[14] Christian Niehage et al. "The cell surface proteome of human mesenchymal stromal cells". In: *PLoS One* 6.5 (2011), e20399.

[15] Ramsey A Foty and Malcolm S Steinberg. "The differential adhesion hypothesis: a direct evaluation". In: *Developmental biology* 278.1 (2005), pp. 255–263; Malcolm S Steinberg and Masatoshi Takeichi. "Experimental specification of cell sorting, tissue spreading, and specific spatial patterning by quantitative differences in cadherin expression". In: *Proceedings of the National Academy of Sciences* 91.1 (1994), pp. 206–209.

[16] Sven Kroening et al. "Matrix-independent stimulation of human tubular epithelial cell migration by Rho kinase inhibitors". In: *Journal of cellular physiology* 223.3 (2010), pp. 703–712.

solution (50-90°C) and chilling it to form a gel. The gel was kept sterile by storing it in ethanol until use at which point it was equilibrated in RPMI containing 20% FBS, 100 U/mL penicillin, and 100 $\mu g/mL$ streptomycin. MSCs were detached from their culture plates using 0.25% trypsin-EDTA solution and suspended in 100 μL of RPMI containing 20% FBS, 100 U/mL penicillin, and 100 $\mu g/mL$ streptomycin at a density of 3.8x10^6 $cells/mL$ to achieve a concentration of 1500 cells per well. Islets were dissociated into single-celled suspensions by incubation in 0.05% trypsin-EDTA solution for 1 min at 37°C. Islet cells were suspended in the same density as MSCs so that they could be mixed in a 1:1 ratio to achieve a final concentration of ≈3000 cells per well to be delivered to gels by pipetting 200 μL of cell suspension over a single gel. Settling by gravity was permitted for 24 hr in humidified conditions, 37°C, and 5% CO2. After 24 hr, aggregates could be identified within each well, and gels were perfused with extra media to provide long-term nutrient supply.

3.2.2 Characterization by cross-sectional contact ratio

Laser scanning confocal microscopy images were taken using an Olympus IX81 confocal microscope (Olympus, Tokyo, Japan). To differentiate between islet-derived cells and MSCs, islets were isolated from GFP-expressing mice (C57BL/6-Tg CAG-EGFP; Japan SLC, Inc., Shizuoka, Japan). Coaggregates were imaged with confocal microscopy to obtain cross-sectional images. Image analysis was conducted using ImageJ that was used to manually trace the perimeter of non-GFP-expressing domains of MSCs as well as the perimeter of contacting GFP and non-GFP domains. The ratio of contact perimeter to the MSC perimeter was determined for each condition to yield the cross-sectional contact ratio α.

3.2.3 Aggregate fragmentation with laminar fluid shear

An apparatus for exerting controlled fluid shear was constructed by connecting two 1-mL syringes of 5-mm ID with polyethylene HPLC tubing 3 m in length and of 400-μm ID. Before use, the syringe and tubing was cleaned by flushing once with 7:3 ethanol water, once with PBS, and once with RPMI containing 10% FBS to coat the walls with protein and prevent aggregates from adhering. Forty-eight aggregates were first imaged with phase contrast in a dish and subsequently loaded into syringes with 1 mL PBS and either coaggregates or islets. The loaded syringe was then placed in a syringe pump (PHD 2000; Harvard Apparatus, Holliston, MA) and pressed at constant flow rate. The laminar state of fluid flow was confirmed by estimating the Reynolds number using the 400-μm ID of the tubing, flow rate as determined in each experiment, and by assuming

density and viscosity to be those of water. Aggregates were recovered in a dish and reimaged after exposure to fluid shear. Mean shear rates were determined from the ratio of average velocity (flow rate divided by cross-sectional area) to the average tube radius (tube radius divided by two).

3.2.4 Image and statistical analysis of coaggregate response to fluid shear

The ratio of projected areas of islet domains to GFP-MSC domains (isolated from GFP-expressing mice; C57BL/6-Tg CAG-EGFP; Japan SLC, Inc., Shizuoka, Japan) was determined for each aggregate in ImageJ using color thresholding (red to magenta: 0-256) to separate islets (yellow: shades 0-50) from GFP-MSCs (green: shades 50-100) and the background (blue: shades 120-200). Image analysis of non-GFP aggregate area projections was done in ImageJ using brightness thresholding to eliminate the large background peak between 180 and 230 (black to white: 0-256). Thresholded areas of each coaggregate or islet were manually selected and compiled for statistical analysis. Because recovery of single cells and small particles was less reliable than that of larger particles, size distribution analysis of aggregates was accomplished by using the area-weighted mean of measured coaggregate areas (the sum of squares of areas divided by the sum of areas) in order to favor size changes of larger particles thus eliminating the need to account for every single cell or debris detached from sheared coaggregates.

3.2.5 Insulin secretion from islet/MSC coaggregates

Static insulin secretion assays were conducted by first rinsing 50 MSC/islet coaggregates (or 50 control islets) in HBSS to remove any traces of glucose-containing media. The size distribution and number of islets used to prepare coaggregates were the same as the control islet group to ensure that approximately equal numbers of beta cells would be assessed. Aggregates were first exposed to a solution of glucose-containing Krebs-Ringer's buffer (KRB) at a concentration of 0.1 g/dL. After 1 hr of exposure at 37°C, aggregates were then rinsed and transferred to KRB with 0.3 g/dL glucose for 1 hr (37°C), and finally rinsed and transferred to 0.1 g/dL glucose-containing KRB for 1 hr (37°C). Samples of the buffer solutions after each incubation period were collected and analyzed for insulin content using ELISA (Shibayagi Co Ltd., Gunma, Japan) according to the manufacturer's instructions.

3.2.6 Splenocyte proliferation measurement

Ninety-six-well plates with nontreated surfaces (IWAKI AGT, Tokyo, Japan) were used to culture 100 μL of RPMI with 10% FBS, 50 μM 2-β-mercaptoethanol (Sigma-Aldrich, St Louis, MO), 100 U/mL penicillin, and 100 $\mu g/mL$ streptomycin containing 1.5x10^5 BALB/c splenocytes per well alongside 50 C57BL/6 stimulator islets/coaggregates. Upon mixing, splenocytes were inoculated with anti-mouse CD3 antibodies at a concentration of 1.25 $\mu g/mL$ to stimulate T-cell activation and proliferation. Wells were agitated prior to taking 10 μL of samples for cell counting and replaced with fresh media each time. Cell counting was performed by taking images of cells at 20x magnification on a hemacytometer, and viability was accounted for using trypan blue exclusion (Life technologies Corporation, Grand Island, NY). Flow cytometry was used to verify that activated splenocytes proliferate more than unactivated or mitomycin C-inhibited splenocytes (SFig. A.12).

3.2.7 Immune cell stimulation index assessment by spectrophotometry

Immune cell proliferation was evaluated by measuring the absorbance due to turbidity at 750 nm of suspensions of splenocytes. Aggregates or islets contained within wells of 96-well plates undergoing immune reactions were manually removed by pipetting to leave only single-celled suspensions. Single-celled suspensions were agitated by pipetting until homogenous and then subjected to spectrophotometric analysis. Absorbance measurements were carried out using a Spectramax M1 spectrophotometer (Molecular Devices, San Jose, CA) at 750 nm. The stimulation index for splenocytes undergoing immune reactions was estimated by dividing the absorbance value for each condition by the absorbance value of unstimulated splenocytes. Islets were omitted from statistical comparison due to the high turbidity caused by islet-derived debris.

3.2.8 Statistical analysis

Statistical comparisons were performed with ANOVA followed by Tukey-Kramer post hoc test for multiple comparisons. Statistical significance was considered for either $p<0.05$ or $p<0.005$. Error bars represent the standard error of the mean unless otherwise indicated. Replicates were performed in triplicate unless otherwise indicated.

3.3 Results

Using the procedure outlined in Figure 3.1, we first formed aggregates without ROCK inhibitor Y-27632 to determine whether natural cohesive interaction between islet-derived cells and MSCs was permissive to the formation of stable spheroids. Islets were dissociated, and single-celled suspensions of MSCs and islet cells could be obtained quickly without leaving either cell type in a suspended state for more than an hour. Agarose well arrays were seeded with single-celled suspensions of islets and MSCs mixed in a 1:1 proportion and allowed to settle over a period of 24 hr (Fig. 3.2a). Solid aggregates steadily became more compact over the following 24 hr. However, within 72 hr, separation of cells into clearly defined spherical domains was observed (Fig. 3.2b). The heterogeneity of cell types was confirmed qualitatively by the difference in color of transmitted light as observed using phase-contrast microscopy. This phenomenon was highly reproducible and was observed in the majority of aggregates formed (Fig. 3.2c). Coaggregation of MSCs with islets isolated from GFP-expressing mice was used to track cell types in aggregates (Fig. 3.2d). Clear separation of GFP-expressing islet-derived cells from non-GFP-expressing MSCs into separate spheroidal domains could be observed by confocal laser scanning microscopy.

To influence the sorting behavior of cells within coaggregates, Y-27632, the small-molecule inhibitor of ROCKi, was included at a concentration of 30 μM with MSC/islet cell suspensions during the process of aggregation. The resulting coaggregates (hereafter referred to as ROCKi$^{[+]}$ coaggregates) after 72 hr were monospheroidal (Fig. 3.3a). The phenomenon was highly reproducible with the majority of coaggregates displaying similar monospheroidal characteristics (Fig. 3.3b). At higher magnifications of phase-contrast imaging with enhanced contrast, color heterogeneity could be observed between the outer shell of the coaggregates and the inner core (Fig. 3.3c). Confocal imaging of ROCKi$^{[+]}$ coaggregates formed with GFP-expressing islets and MSCs confirmed the core-shell nature of the coaggregates with islet-derived cells occupying the outer shell of the aggregate and non-GFP-expressing MSC-derived cells occupying the core (Fig. 3.3d).

We analyzed insulin secretion to assess the function of beta cells contained within coaggregates as well as to identify their relative localization and distribution. Immunostaining with anti-insulin antibodies was performed on cryosections of ROCKi$^{[+]}$ coaggregates (Fig. 3.4a) and those formed without Y-27632 (ROCKi$^{[-]}$ coaggregates) (Fig. 3.4b). ROCKi$^{[+]}$ coaggregates exhibited rings of insulin expression on the exteriors of sectioned aggregates while concentric nonexpressing regions of Hoechst-positive nuclei were contained within it. Separate domains of insulin-negative and insulin-positive cells were observed in the case of ROCKi$^{[-]}$ coaggregates. Insulin secretory function of beta

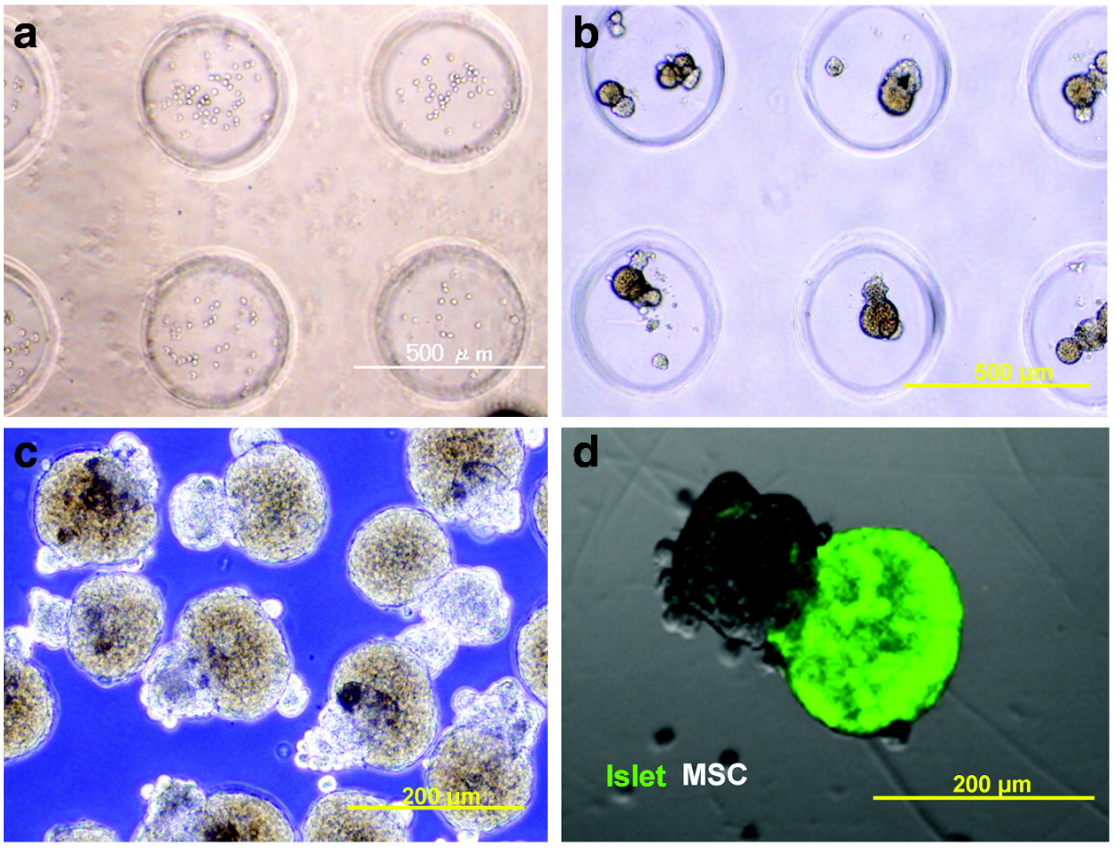

FIGURE 3.2: Coaggregation of MSCs and islets in agarose wells resulted in cell sorting into separate spherical domains. (a) Agarose well array immediately after addition of a single-celled suspension of MSCs and dissociated islet cells (4x magnification). (b) Coaggregates within their respective wells after 3 days of culture (10x magnification). (c) Coaggregates harvested from agarose well array and maintained on nontreated polystyrene (10x magnification). (d) Confocal imaging of day-3 coaggregates with islet cells from GFP-positive mice was used to identify islet-derived cells and revealed that islet-derived cells were localized within single spherical domains and that the domains of unlabeled MSCs contained few or no islet-derived cells (cropped from 10x magnification image).

cells contained within ROCKi$^{[+]}$ coaggregates in response to static stimulation with glucose was assessed and compared with unmodified islets (Fig. 3.4c). Neither insulin secretory response to high-glucose stimulation nor recovery to low insulin secretion levels upon exposure to low-glucose stimulation was significantly affected ($p>0.05$ in both cases) compared with unmodified islets. It should be noted that this assay did not account for differences in glucose/insulin diffusion due to differences in surface area to volume ratio or for differences in diffusion due to the monodispersity of coaggregate size versus the much broader size distribution of unmodified islets.

To provide an assessment of the immune-protective potential of MSCs aggregated with islets, an in vitro splenocyte proliferation assay was employed whereby anti-CD3-activated splenocytes were mixed in a 1:1 (cell:cell) ratio with allogenic coaggregates, islets, and aggregates composed solely of MSCs. Cell counts were taken regularly over the course

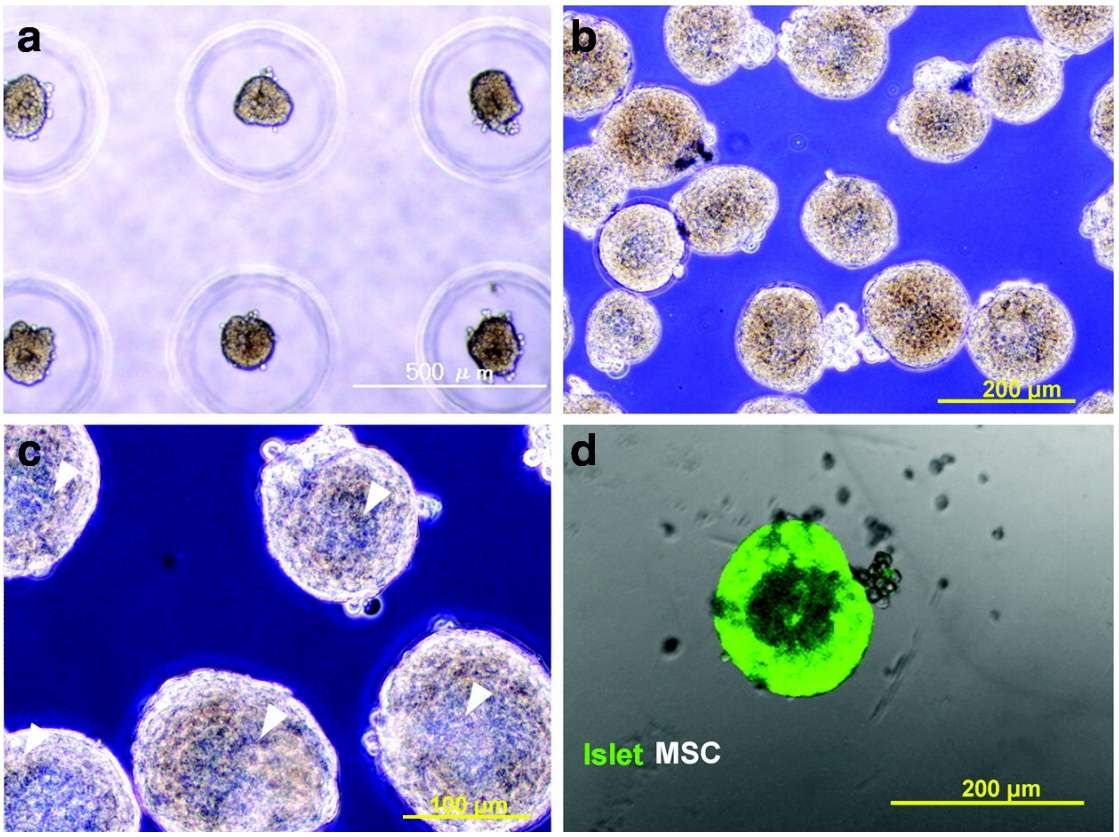

FIGURE 3.3: ROCKi$^{[+]}$ coaggregates exhibited core-shell single-sphere configurations. (a) ROCKi$^{[+]}$ coaggregates assumed clear single-sphere configurations after 3 days of culture in agarose well arrays and media containing Y-27632 (4x magnification). (b) Phase-contrast image of ROCKi$^{[+]}$ coaggregates harvested from agarose well arrays at day 3 (10x magnification). (c) Phase-contrast image of ROCKi$^{[+]}$ coaggregates reveals heterogeneity in color between the central core and outer shell of each spheroid (20x magnification). Arrowheads indicate core regions. (d) Confocal imaging of day-3 ROCKi$^{[+]}$ coaggregates with islet cells from GFP-positive mice was used to identify islet-derived cells and revealed that islet-derived cells localized within an outer shell domain of each spheroid while few GFP-positive cells could be seen in the central core (cropped from 10x magnification image).

of 5 days to track the proliferation of splenocytes for each condition (Fig. 3.5a). MSC-only aggregates were the superior suppressor of splenocyte proliferation with cell counts ($2x10^6$ on day 5) comparable to the unactivated splenocyte control condition ($1x10^6$ on day 5). Islets and splenocyte-only groups resulted in the highest proliferation ($2x10^7$ and $3x10^7$, respectively) and both ROCKi$^{[+]}$ and ROCKi$^{[-]}$ coaggregates were of intermediate values ($4x10^6$ and $8x10^6$, respectively), which is indicative of immune suppression. To corroborate the cell count data, cell proliferation of the various types of aggregates exposed to activated splenocytes was assessed indirectly by examining the turbidity at day 5 both through qualitative inspection of dark-field images (data not shown) and spectrophotometric measurement of the absorbance at 750 *nm*. Absorbance-based turbidity measurements were used to estimate the stimulation indices (SIs) of the activated splenocytes and those cultured with islets, ROCKi$^{[+]}$ and ROCKi$^{[-]}$ coaggregates, and

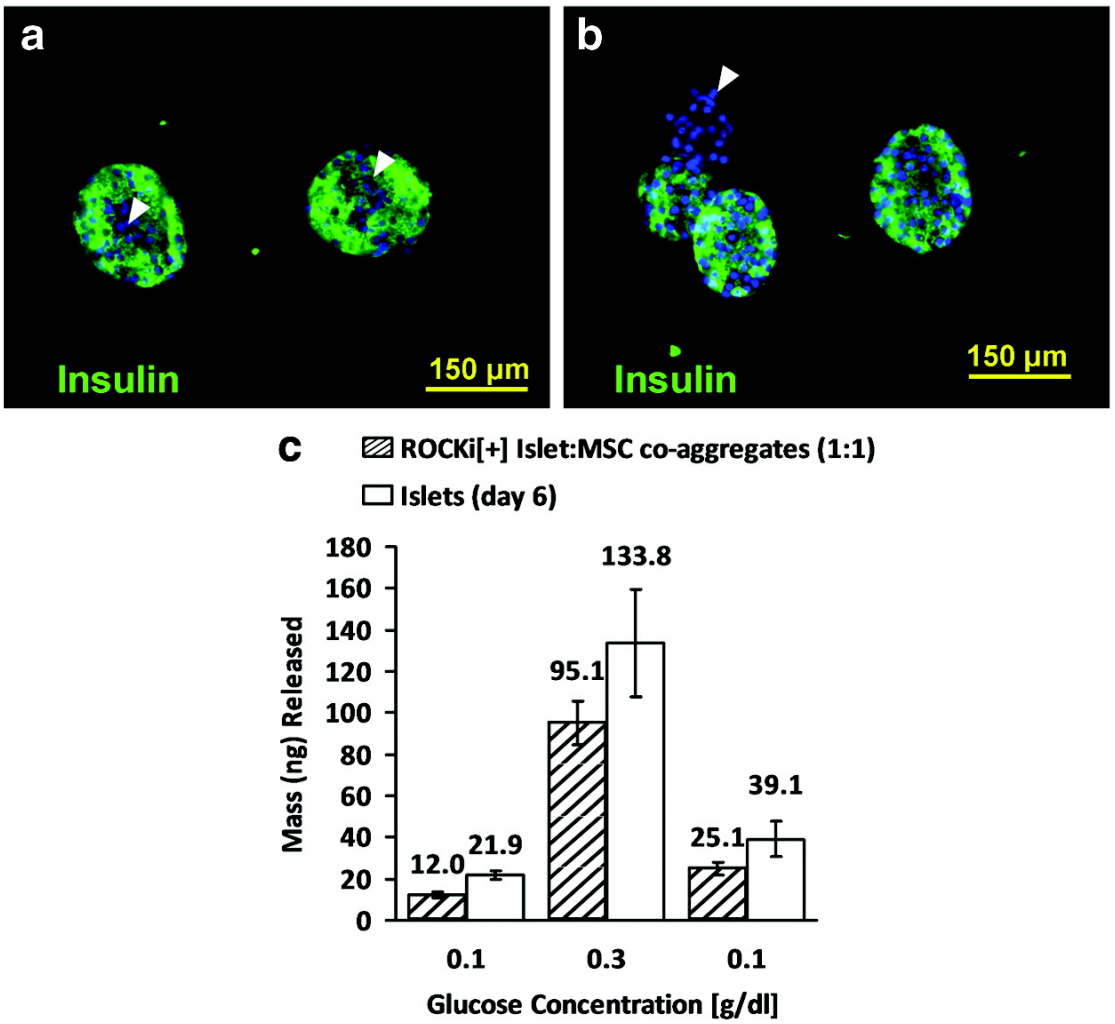

FIGURE 3.4: Functional evaluation of islet insulin secretion in ROCKi$^{[+]}$ coaggregates. (a) Immunostaining of insulin (green) and Hoechst (blue) of cryosections of ROCKi$^{[+]}$ coaggregates shows that insulin expression was limited to shell regions where islet cells were likely localized (20x magnification). Arrowheads indicate core regions. (b) Immunostaining of insulin (green) and Hoechst (blue) of ROCKi$^{[-]}$ coaggregates shows domains of Hoechst-expressing nuclei without insulin expression, indicating the regions containing nonislet-derived cells of MSC origin. Arrowhead indicates region of cells not expressing insulin. (c) Insulin expression during three-stage sequential glucose stimulation analyzed with ELISA. Exposure to low, high, and low-glucose-containing solutions was used to stimulate insulin secretion, which was not significant in ROCKi$^{[+]}$ coaggregates.

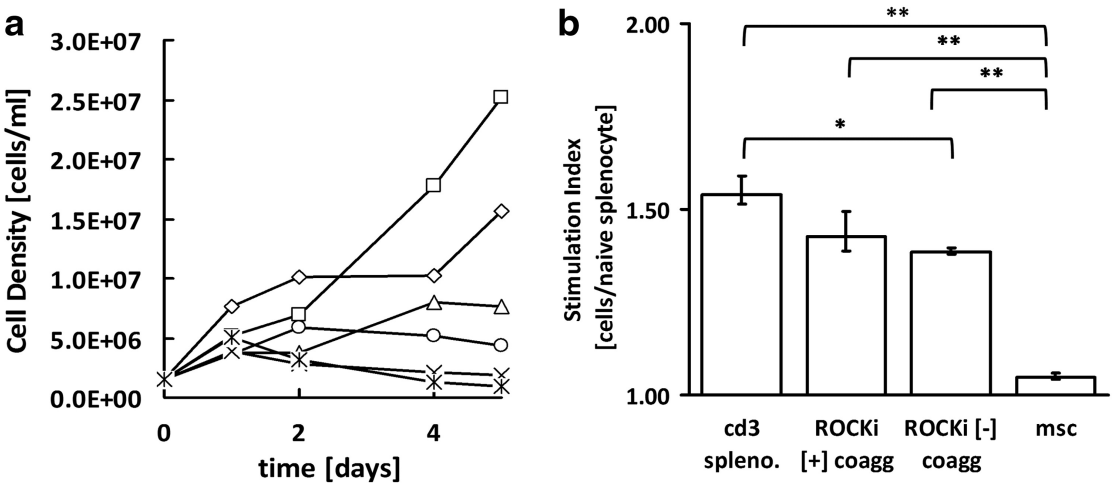

FIGURE 3.5: Evaluation of MSC immune-protective capacity of ROCKi$^{[+]}$ coaggregates and ROCKi$^{[-]}$ coaggregates. (a) Time course of cell proliferation in activated splenocyte cultures containing an equal proportion of cells residing in coaggregates. Anti-CD3-activated splenocytes (squares); 1:1 (cell:cell) coculture of islets and anti-CD3-activated splenocytes (diamonds); 1:1 (cell:cell) coculture of ROCKi$^{[-]}$ MSC/islet coaggregates and anti-CD3-activated splenocytes (triangles); 1:1 (cell:cell) coculture of ROCKi$^{[+]}$ MSC/islet coaggregates and anti-CD3-activated splenocytes (plus signs); 1:1 (cell:cell) coculture of MSC-only aggregates and anti-CD3-activated splenocytes (circles); naïve splenocytes only (asterisks). (b) Stimulation indices calculated based on turbidity measurements of splenocyte cultures at 6 days relative to naïve splenocytes. $*$ $p<0.05$, $**$ $p<0.005$ by ANOVA followed by Tukey-Kramer post hoc test.

MSC-only aggregates (Fig. 3.5b). These indices agree with the cell count data with the exception that SI value recorded for activated splenocytes cultured with islets (SI=2.48; ±SE·0.04) was much greater than activated splenocytes alone (SI=1.54; ±SE·0.03) due to additional turbidity from small debris of deteriorating islets that could not be manually removed as with aggregates in other conditions. For this reason, absorbance averages for coaggregates were compared statistically with MSC-only aggregates and activated splenocyte conditions. MSC-only aggregates were strong suppressors of the proliferative reaction (SI=1.048; ±SE·0.006), and ROCKi$^{[+]}$ and ROCKi$^{[-]}$ coaggregates exhibited intermediate SI values (SI=1.43; ±SE·0.04 and SI=1.384; ±SE·0.006, respectively).

To quantify the effects of Y-27632 concentration on aggregate conformation, day-4 confocal cross-sections were analyzed by manually tracing the contour formed between contacting intra-aggregate domains (GFP and non-GFP) and dividing it by the perimeter of the non-GFP-expressing domains to obtain the cross-sectional contact ratio (α). High values of α correspond to aggregates with greater contact between GFP and non-GFP domains, while lower values correspond to aggregates with low contact (Fig. 3.6a). Aggregates were formed at different concentrations of Y-27632, and α values were computed for each condition and were plotted as a function of Y-27632 concentration (Fig. 3.6b). α-Values can be divided into three categories: those representing aggregates of

high (α>0.7), low (α<0.3), and intermediate contact (0.3$\leq \alpha \leq$ 0.7) (SFig. A.6). Intermediate α values were uncommon; 10% of all calculated α values fell into this category for the range of Y-27632 concentrations tested. The switch from low values of α at low concentrations of Y-27632 to high values of α at high concentrations of Y-27632 suggests discrete concentration-dependent toggling of the state rather than continuous modulation.

To assess cohesive integrity of cellular aggregates, islets, ROCKi$^{[-]}$ coaggregates, and ROCKi$^{[+]}$ coaggregates were subjected to laminar fluid shear in 3-m-long tubing at constant flow rates (SFig. A.8). To observe losses in aggregate mass due to shear, images were captured before and after exposure to shear (Fig. 3.6c). GFP-expressing MSCs were employed to discriminate between MSCs and islet domains in both ROCKi$^{[+]}$ and ROCKi$^{[-]}$ coaggregates, and the projected areas of individual aggregate GFP and non-GFP domains were quantified so as to examine changes in islet-MSC ratio after shear. A change in islet-MSC ratio after 4800 s^{-1} mean shear rate was observed in the case of ROCKi$^{[-]}$ coaggregates (Fig. 3.6d) while changes in the case of ROCKi$^{[+]}$ coaggregates were small (Fig. 63.6e), indicating that the cohesion between islet and MSC portions was enhanced by formation in the presence of Y-27632. Since differences in MSC-islet cohesion could be attributed to either bond strength or contact area differences, the overall loss of coaggregate size was estimated by measuring projected cross-sectional areas for each coaggregate type as well as unmodified islets. Area-weighted average areas and the net changes due to shear exposure were determined for three mean shear rates: 4800, 2400, and 1200 s^{-1} (Fig. 3.6f). ROCKi$^{[+]}$ coaggregates exhibited resistance to shear surpassing that of unmodified islets, suggesting not only that contact areas were increased as a result of Y-27632 treatment, but that intercellular cohesion between islet cells also increased.

Timelapse confocal microscopy was employed in order to observe the dynamics of domain formation in both types of coaggregates (SMovies A.10 and A.11). In ROCKi$^{[-]}$ coaggregates, differing cell types quickly separated into local domains within 60 *min*, which remained separated as domains of the same cell type gradually become consolidated (Fig. 3.7a). Differing cell types in ROCKi$^{[+]}$ coaggregates exhibited a prolonged mixed distribution while the aggregate as a whole contracted and steadily sorted into core and shell domains (Fig. 3.7b).

Anti-pan-cadherin immunostaining and confocal fluorescence microscopy were used to image the distribution of cadherins in day-3 ROCKi$^{[-]}$ (Fig. 3.7c) and ROCKi$^{[+]}$ (Fig. 3.7f) coaggregates, and unmodified islets (Fig. 3.7h). Close inspection of ROCKi$^{[-]}$ coaggregates reveals that while islet domains contained clearly defined cadherin organization at cell boundaries (Fig. 3.7d), MSC regions were characterized by chaotic

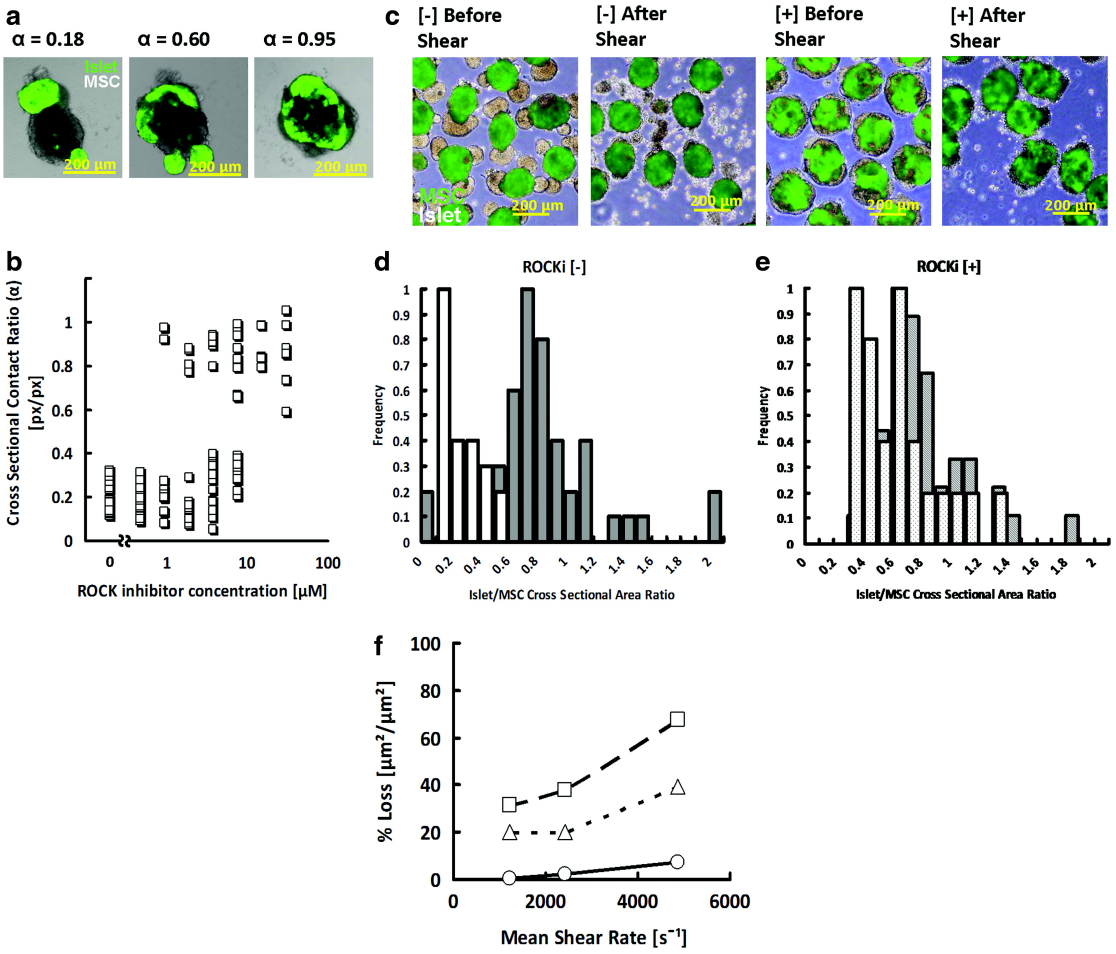

FIGURE 3.6: Image analysis of coaggregate cross-sections was used to quantify the cohesive interaction between islet cells and MSCs at varying concentrations of Y-27632. (a) Confocal cross-sections (cropped from 10x images) of day-5 MSC/GFP-islet coaggregates were analyzed to obtain the cross-sectional contact ratio (α), which was high in the case of core-shell configurations, low in the case of multisphere configurations, and intermediate for coaggregates exhibiting mixed configuration. (b) Individual values of cross-sectional contact ratio (α) plotted as a function of Y-27632 concentration. (c) Merged GFP/phase-contrast images of coaggregates subjected to laminar fluid shear. GFP-MSC/islet coaggregates before and after exposure to 4800 s^{-1} mean shear rate; right panes: ROCKi$^{[+]}$; left panes: ROCKi$^{[-]}$. (d) Distributions of the ratio of ROCKi$^{[-]}$ coaggregate cross-sectional GFP-MSC area to islet area before (gray bars) and after (white bars) being subjected to 4800 s^{-1} mean shear rate, normalized to peak frequency. (e) Distributions of the ratio of ROCKi$^{[+]}$ coaggregate cross-sectional GFP-MSC area to islet area before (striped bars) and after (speckled bars) being subjected to 4800 s^{-1} mean shear rate, normalized to peak frequency. (f) Plotted differences of before-shear and after-shear weighted mean cross-sectional areas at 1200, 2400, and 4800 s^{-1} mean shear rates for ROCKi$^{[-]}$ (squares) and ROCKi$^{[+]}$ (circles) coaggregates and unmodified islets (triangles).

cadherin distribution (Fig. 3.7e), whereas ROCKi$^{[+]}$ coaggregates had clear cadherin organization at their boundaries (Fig. 3.7g) comparable to those of the islet domains in ROCKi$^{[-]}$ coaggregates and unmodified islets (Fig. 3.7i).

We conducted immunostaining to examine the presence and localization of E-cadherin (Fig. 3.8a, b), as well as N-cadherin (Fig. 3.8c, d) in ROCKi$^{[-]}$ and ROCKi$^{[+]}$ co-aggregates. The coexistence of cytoplasmic N-cadherin-expressing (inset of Fig. 3.8c) and non-N-cadherin-expressing domains was observed only in the case of ROCKi$^{[-]}$ co-aggregates, while N-cadherin expression was not observed in ROCKi$^{[+]}$ coaggregates. Conversely, while coexisting domains of E-cadherin-expressing (inset of Fig. 3.8a) and non-E-cadherin-expressing cells were observed in ROCKi$^{[-]}$ coaggregates, in the case of ROCKi$^{[+]}$ coaggregates, the entirety of aggregates including core MSC regions expressed E-cadherin (Fig. 3.8b).

N-cadherin, associated with fibroblastic cell types, including MSCs, is a marker for a particular form of plasticity known as the epithelial-mesenchymal transition (EMT)[17] while de novo E-cadherin expression is an indicator of the reverse process, the mesenchymal-epithelial transition (MET)[18]. Beta-cells and alpha-cells, comprising the majority of islet cells, are known to express E-cadherin as their primary means of intercellular cohesion, a property that is closely tied to their health and function[19].

The switch to E-cadherin is suggestive of MET, so we stained for mesenchymal cell markers vimentin and CD44. ROCKi$^{[-]}$ coaggregates exhibited coexisting domains of CD44 and non-CD44 cells (Fig. 3.8e) and coexisting domains of both vimentin and nonvimentin cells (Fig. 3.8g). ROCKi$^{[+]}$ coaggregates had no observable CD44 (Fig. 3.8f) or vimentin (Fig. 3.8h).

3.4 Discussion

When Y-27632-containing media were used for preparing MSC/islet coaggregates, co-aggregates sorted into core-shell structures with islet-derived cells occupying the exterior while MSCs occupied the core. In contrast, ROCKi$^{[-]}$ coaggregates separated into two clearly defined spherical domains. Pan-cadherin cross-sections revealed that in ROCKi$^{[-]}$ coaggregates, cadherin expression was found in both MSC and islet domains.

[17] Wen-Ge Li and Xin Xiang Xu. "The expression of N-cadherin, fibronectin during chondrogenic differentiation of MSC induced by TGF-beta (1)." In: *Chinese journal of traumatology= Zhonghua chuang shang za zhi/Chinese Medical Association* 8.6 (2005), pp. 349–351.

[18] Ronghui Li et al. "A mesenchymal-to-epithelial transition initiates and is required for the nuclear reprogramming of mouse fibroblasts". In: *Cell stem cell* 7.1 (2010), pp. 51–63.

[19] Bosco, Rouiller, and Halban, "Differential expression of E-cadherin at the surface of rat β-cells as a marker of functional heterogeneity"; Parnaud et al., "Cadherin engagement protects human β-cells from apoptosis".

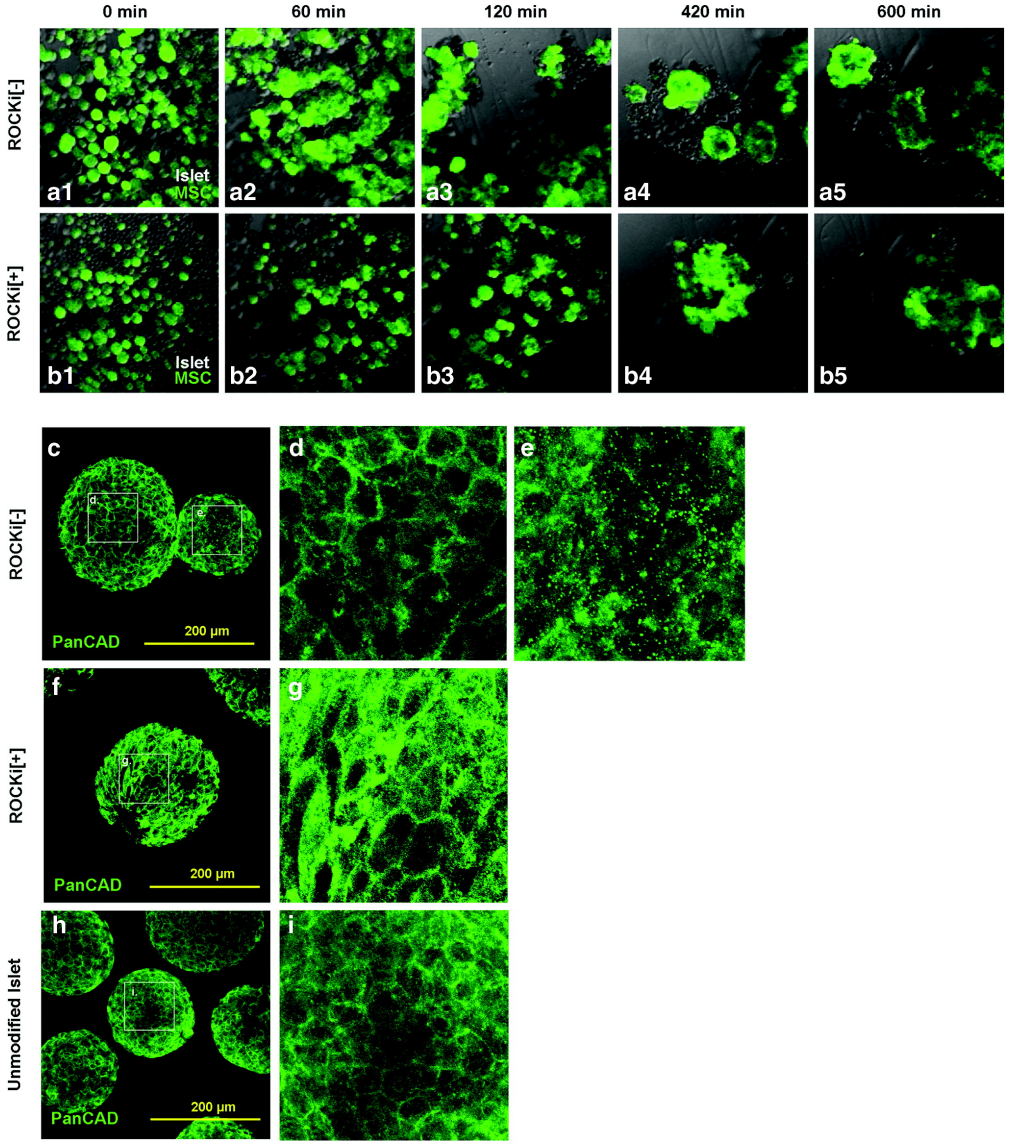

FIGURE 3.7: Examination of aggregate interactions by timelapse and pan-cadherin immunostaining. (a) Timelapse confocal microscopy of a ROCKi$^{[-]}$ coaggregate with GFP-MSCs and islet cells. Local clusters of GFP-MSCs can be seen within 60 *min*. Domain fusion can be observed 420 and 600 *min*, illustrating the process by which local domains of cells are gradually consolidated into fewer, larger clusters. (b) Timelapse confocal microscopy of ROCKi$^{[+]}$ coaggregate with GFP-MSCs and islet cells. The distribution of GFP and non-GFP cell types remains mixed even at 120 *min*. Unified coaggregate contraction can be observed between 120 and 420 *min*. Core-shell configuration begins to mature from 600 *min*. (c) Confocal section of pan-cadherin in a fixed ROCKi$^{[-]}$ coaggregate 72 *hr* after the initiation of aggregation. (d) Magnified inset of (b): the islet-dominated domain of a ROCKi$^{[-]}$ coaggregate revealing cadherin organization at cell boundaries. (e) Magnified inset of (b): the MSC-dominated domain of a ROCKi$^{[-]}$ coaggregate revealing a chaotic cadherin distribution. (f) Pan-cadherin in a ROCKi$^{[+]}$ coaggregate 72 *hr* after the initiation of aggregation. (g) Magnified inset of (f): ROCKi$^{[+]}$ coaggregate showing cadherin organization at cell boundaries. (h) Pan-cadherin in an unmodified islet. (i) Magnified inset of (h): unmodified islet with cadherin organization at cell boundaries.

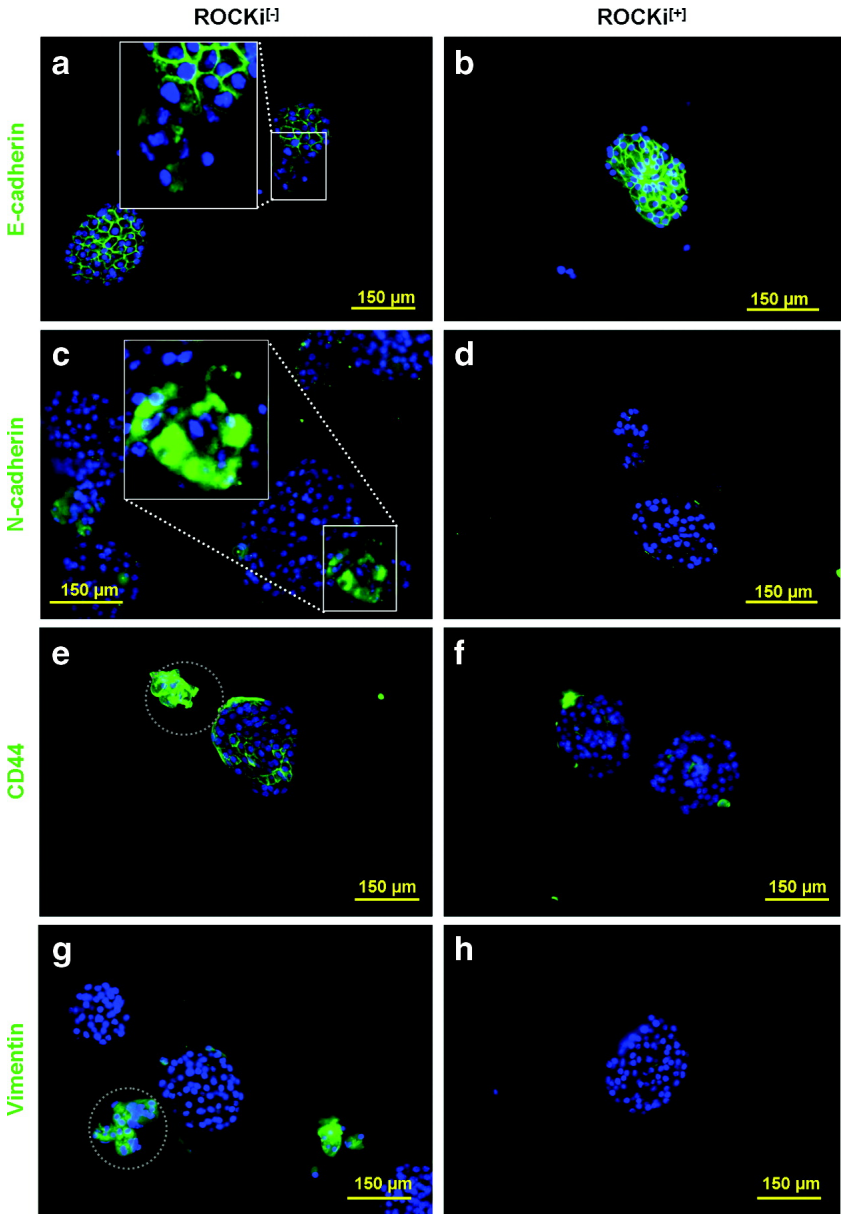

FIGURE 3.8: Immunostaining of coaggregate sections 4 days postaggregation shows a loss of mesenchymal marker expression and a switch to E-cadherin in ROCKi$^{[+]}$ coaggregates (blue regions correspond to Hoechst-stained nuclei). (a and inset) Immunostaining of E-cadherin in ROCKi$^{[-]}$ coaggregates shows expression of E-cadherin in domains of cells adjacent to nonexpressing domains likely indicating islet-dominated domains and MSC domains, respectively. (b) Immunostaining of E-cadherin in ROCKi$^{[+]}$ coaggregates shows clear expression of E-cadherin even in the core likely corresponding to MSC-derived cells. (c and inset) Immunostaining of N-cadherin in ROCKi$^{[-]}$ coaggregates shows expression of N-cadherin in domains of cells appended to nonexpressing adjacent domains likely indicating MSC-derived regions and islet regions, respectively. (d) Immunostaining of N-cadherin in ROCKi$^{[+]}$ coaggregates reveals no sign of N-cadherin even in the core. (e) Immunostaining of CD44 in ROCKi$^{[-]}$ coaggregates indicates domains containing MSC-derived cells. (f) Immunostaining of CD44 in ROCKi$^{[+]}$ coaggregates reveals little to no detectable expression even in the core. (g) Immunostaining of vimentin in ROCKi$^{[-]}$ coaggregates likely corresponds to domains containing MSC-derived cells. (h) Immunostaining of vimentin in ROCKi$^{[+]}$ coaggregates reveals little to no detectable expression even in the core.

However, only cadherins in islet domains were organized at cell borders. It is unlikely, therefore, that cadherins in the MSC domain are primary mediators of intercellular cohesion. This could explain the incompatibility between islet and MSC domains that led to separation. Conversely, expression of boundary-localized pan-cadherin in ROCKi$^{[+]}$ coaggregates could explain why these aggregates assumed single-sphere architecture, namely, that the introduction of a common adhesion mode through cadherin-mediated bonds permitted greater interaction between the two cell types. Timelapse microscopy showed that separation into local domains of cell types occurred early on in ROCKi$^{[-]}$ coaggregates, suggesting that a fundamental difference in adhesive compatibility exists between the two cell types, whereas cells within ROCKi$^{[+]}$ coaggregates contracted into a single domain before or in parallel with sorting out. Shear-based comparisons of aggregate cohesion also indicate that ROCKi$^{[+]}$ coaggregates are held together by stronger interactions not just as a result of increased contact area between MSCs and islets but also stronger interaction between like cells.

These observations are consistent with sorting via differential adhesion whereby cells with unlike cellcell adhesion molecules will arrange such as to minimize contact with each other while those with compatible cellcell adhesion molecules will maximize contact with each other leading to multispheroidal and monospheroidal conformations, respectively[20]. Core-shell conformations may arise from pairs of cohesively compatible cell types that either express like adhesion molecules in different proportions or cross-reactive differing adhesion molecules with weaker heterotypic interactions than homotypic[21], either of which may explain the arrangements adopted in ROCKi$^{[+]}$ coaggregates. The driving force of MSC aggregation was not determined in this study. Based on studies of MSC surface adhesion molecules, MSC cohesion might be driven by secreted ECM-integrin networks or CAM/immunoglobulin interaction[22].

Common mesenchymal markers found in native MSCs, such as vimentin (SFig. A.7c, d), CD44 (SFig. A.9), and N-cadherin, would normally be expected to serve as markers of MSC domains, and while these were identified in ROCKi$^{[-]}$ coaggregates, their absence in ROCKi$^{[+]}$ coaggregates coupled with the switch to E-cadherin in MSC domains is evidence of MET. Recent reports suggest that ROCK inhibition may have the potential to suppress EMT and possibly reverse it (MET) in combination with other signals[23].

[20] Foty and Steinberg, "The differential adhesion hypothesis: a direct evaluation"; Steinberg and Takeichi, "Experimental specification of cell sorting, tissue spreading, and specific spatial patterning by quantitative differences in cadherin expression".

[21] Duke Duguay, Ramsey A Foty, and Malcolm S Steinberg. "Cadherin-mediated cell adhesion and tissue segregation: qualitative and quantitative determinants". In: *Developmental biology* 253.2 (2003), pp. 309–323.

[22] Niehage et al., "The cell surface proteome of human mesenchymal stromal cells".

[23] Maria João Lima et al. "Suppression of epithelial-to-mesenchymal transitioning enhances ex vivo reprogramming of human exocrine pancreatic tissue toward functional insulin-producing β-like cells". In: *Diabetes* 62.8 (2013), pp. 2821–2833.

Several studies have also suggested that ROCK inhibition has a stabilizing effect on E-cadherin and that it has a protective effect on epithelial cells and embryonic or induced pluripotent stem cells[24]. It could be that, in addition to exposure to Y-27632, exposure to signals from neighboring islet-derived cells, including contact with E-cadherin-expressing beta and alpha cells, is a condition for the MET in this particular case.

The knockdown of stress fibers and acto-myosin forces resulting from ROCK inhibition is well established[25], and while natural cell sorting is a well-documented phenomenon generally attributed to differential adhesion, recent studies suggest that actomyosin cortical tension, polarity, and migration also contribute to cell sorting, and that differential adhesion may be insufficient to explain all sorting phenomena[26]. Since these properties are interrelated, it is important to recognize that cell sorting is an emergent characteristic of multicellular systems, and that manipulation of one or more cellcell interaction parameters could result in dramatic higher-order changes.

Because immunoprotection of islets may depend on close proximity or direct contact with protector cells, and in recognition of size-exclusion issues associated with intraportal transplantation, Iwata and colleagues demonstrated colocalization of protector cells and islets using membrane-tethered DNA strands[27]. Coating islets with MSCs by exposing the islet surface to suspended MSCs was demonstrated by Rasmusson et al.[28], and a similar procedure was demonstrated with the insulin-secreting MIN six-cell line by Bhaiji et al[29]. However, no study has yet provided an approach for uniformly coaggregated, temporally stable, and clearly integrated composites of MSCs and islets, and little attention has been given to the cohesive interaction between MSCs and islets.

The immune-suppressive capacity of MSCs was evaluated in vitro by incubating CD3-activated splenocytes with coaggregates. While the proliferation of activated splenocytes in the presence of both ROCKi$^{[+]}$ and ROCKi$^{[-]}$ coaggregates was significantly reduced

[24]Kroening et al., "Matrix-independent stimulation of human tubular epithelial cell migration by Rho kinase inhibitors"; Lili Wang et al. "Effects of ROCK inhibitor, Y-27632, on adhesion and mobility in esophageal squamous cell cancer cells". In: *Molecular biology reports* 37.4 (2010), pp. 1971–1977; Li et al., "The ROCK inhibitor Y-27632 enhances the survival rate of human embryonic stem cells following cryopreservation".

[25]Hassina Darenfed et al. "Molecular characterization of the effects of Y-27632". In: *Cell motility and the cytoskeleton* 64.2 (2007), pp. 97–109.

[26]M Lisa Manning et al. "Coaction of intercellular adhesion and cortical tension specifies tissue surface tension". In: *Proceedings of the National Academy of Sciences* 107.28 (2010), pp. 12517–12522; M Krieg et al. "Tensile forces govern germ-layer organization in zebrafish". In: *Nature cell biology* 10.4 (2008), pp. 429–436.

[27]Naohiro Takemoto, Yuji Teramura, and Hiroo Iwata. "Immobilization of Sertoli cells on islets of Langerhans". In: *Biomater. Sci.* 1.3 (2013), pp. 315–321.

[28]Ida Rasmusson Duprez et al. "Preparatory studies of composite mesenchymal stem cell islets for application in intraportal islet transplantation". In: *Upsala journal of medical sciences* 116.1 (2011), pp. 8–17.

[29]Tasneem Bhaiji, Zheng-Liang Zhi, and John C Pickup. "Improving cellular function and immune protection via layer-by-layer nanocoating of pancreatic islet β-cell spheroids cocultured with mesenchymal stem cells". In: *Journal of Biomedical Materials Research Part A* 100.6 (2012), pp. 1628–1636.

compared with those of activated splenocytes alone or with islets, the response was still greater than that of MSC-only aggregates. Lack of direct contact between MSCs and T-cells is an unlikely explanation for the difference, as similar surface areas of MSCs were available to ROCKi$^{[-]}$ coaggregates as were to MSC-only aggregates. The immunosuppressive effect was more likely due to the secretion of soluble factors that should be identified in future studies. The partial effect may be due to the response of activated splenocytes to allogenic islet cells leading to competing activation/suppression. The immunoprotective effect of MSCs in islet grafts will be carefully examined in future islet transplantation models. The effect of Y-27632 on MSC anti-inflammatory properties is likely to be significant and should be investigated, paralleling the ongoing question in the field of somatic cell reprogramming as to whether induced pluripotent stem cells, which undergo a stage of MET induction, are immunogenic or immunoprivileged[30].

In conclusion, we demonstrate that self-assembly of MSC-islet coaggregates can be manipulated in a way that greatly increases the contact between the two cell groups. We suggest a possible mechanism for the change in sorting behavior whereby MSC plasticity in the form of MET leads to expression of E-cadherin common to those of islet cells thus enabling contact between the different cell groups. We demonstrate that coaggregates retain basic insulin secretory function and splenocyte antiproliferative capability. Together these findings may provide insight for the design of engineered tissues, particularly those that employ the use of normally "immiscible" cells and may also serve as the basis for an islet therapy to be further explored in vivo.

[30] Shin Kaneko and Shinya Yamanaka. "To be immunogenic, or not to be: that's the iPSC question". In: *Cell stem cell* 12.4 (2013), pp. 385–386.

Chapter 4

Long term culture of cells patterned on glass via membrane-tethered oligonucleotides

---

"the chemical basis for the special properties of polymers that equip them for so many applications and functions, both in nature and in the artifacts of man, is not therefore to be sought in peculiarities of chemical bonding but rather in their macromolecular constitution, specifically, in the attributes of long molecular chains."

Paul J. Flory
1974 Nobel Lecture

4.1 Introduction

The possibility of arraying many types of cells in controlled two dimensional patterns is a promising tool for industrial drug screening and assays for functional analyses of genes[1]. In previous studies, cell arrays have been prepared by permitting cell adhesion through the binding of adhesive glycoproteins or antibodies to surface antigens patterned on culture substrates[2], while physically arranging cells using suction or microfluidic techniques[3], or restriction of adhesion area or path through lithography[4].

A wide variety of cell patterns can be achieved using such methods, but several key limitations remain. These limitations include non-specificity where co-culture of multiple cell types is hardly arranged in any meaningful pattern relative to each other and the need for time-consuming processes and expensive equipment. Previously, we reported a simple and rapid cell alignment method[5] whereby single stranded DNA (ssDNA) conjugated to poly(ethylene glycol) (PEG) and to a terminal phospholipid (ssDNA-PEG-lipid) was used for cell modification. The cells could then be attached to ssDNA'-modified surfaces through complementary DNA hybridization independently of cytoskeletal attachment through adhesive proteins, and an inkjet printer was employed to achieve higher resolution and control of cell arrangement[6]. However, one technical point remains to be overcome. A glass plate coated with a gold thin film was employed in our previous study to permit the immobilization of ssDNA-SH through the thiol-gold reaction. When cells were examined via optical microscopy, clear images of cells could hardly be captured due to the presence of a gold thin film and its characteristically high optical absorbance. The previous study was also limited to suspension cultured CCRF-CEM cells derived

[1] Dennise D Dalma-Weiszhausz et al. "[1] The Affymetrix GeneChip® Platform: An Overview". In: *Methods in enzymology* 410 (2006), pp. 3–28; Ricardo Macarrón and Robert P Hertzberg. "Design and implementation of high throughput screening assays". In: *High Throughput Screening*. Springer, 2002, pp. 1–29; Yoshihiro Ito and Masayuki Nogawa. "Preparation of a protein micro-array using a photo-reactive polymer for a cell-adhesion assay". In: *Biomaterials* 24.18 (2003), pp. 3021–3026.

[2] Hironobu Hatanaka, Tomoyuki Yasukawa, and Fumio Mizutani. "Detection of surface antigens on living cells through incorporation of immunorecognition into the distinct positioning of cells with positive and negative dielectrophoresis". In: *Analytical chemistry* 83.18 (2011), pp. 7207–7212; Chun Xiu Zhang et al. "Cell detection based on protein array using modified glass slides". In: *Electrophoresis* 24.18 (2003), pp. 3279–3283.

[3] Shuichi Takayama et al. "Patterning cells and their environments using multiple laminar fluid flows in capillary networks". In: *Proceedings of the National Academy of Sciences* 96.10 (1999), pp. 5545–5548; Wei Tan and Tejal A Desai. "Microfluidic patterning of cells in extracellular matrix biopolymers: effects of channel size, cell type, and matrix composition on pattern integrity". In: *Tissue engineering* 9.2 (2003), pp. 255–267.

[4] Stephan Rohr, Regula Flückiger-Labrada, and Jan P Kucera. "Photolithographically defined deposition of attachment factors as a versatile method for patterning the growth of different cell types in culture". In: *Pflügers Archiv* 446.1 (2003), pp. 125–132; Chen et al., "Micropatterned surfaces for control of cell shape, position, and function"; Roman Lutz et al. "Nano-stenciled RGD-gold patterns that inhibit focal contact maturation induce lamellipodia formation in fibroblasts". In: *PloS one* 6.9 (2011), e25459.

[5] Teramura et al., "Control of cell attachment through polyDNA hybridization".

[6] Sakurai, Teramura, and Iwata, "Cells immobilized on patterns printed in DNA by an inkjet printer".

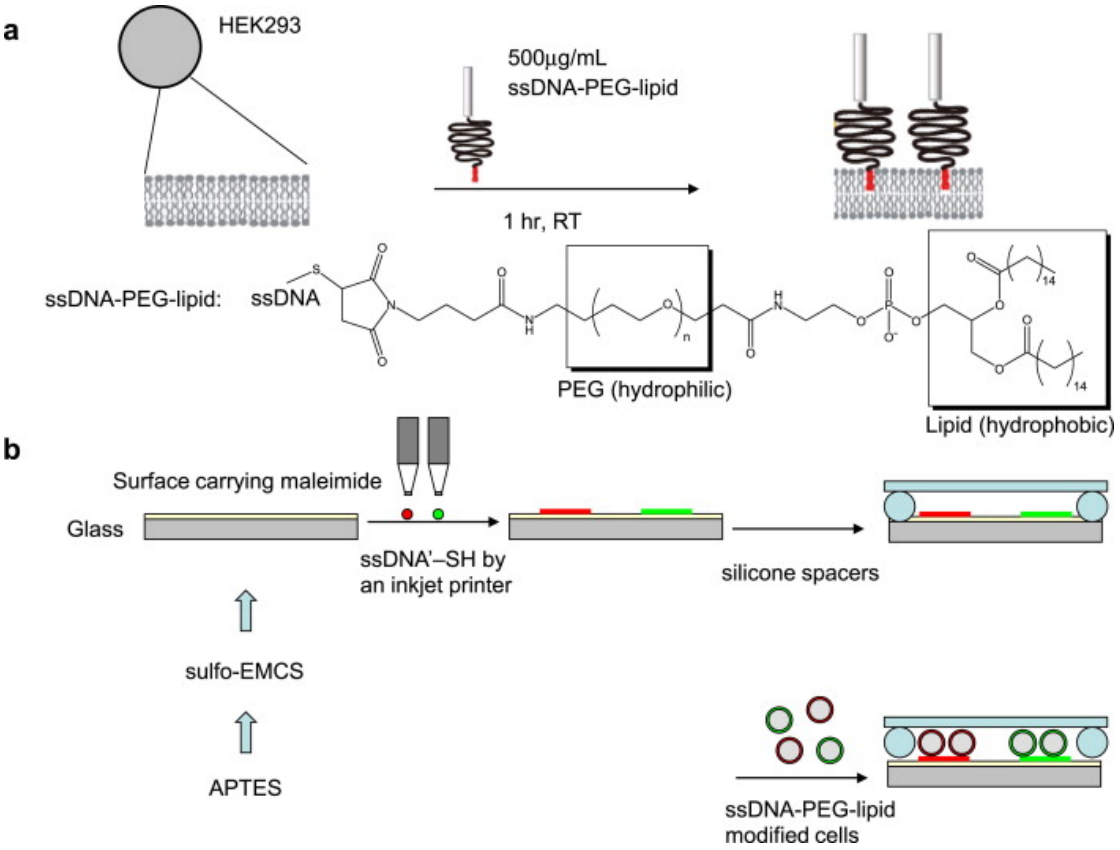

FIGURE 4.1: Schematic illustration of a method for cell immobilization on a pattern printed in DNA. (a) Immobilization of ssDNA with a specified sequence on the cell surface. ssDNA-PEG-lipid was immobilized on the cell surface through the hydrophobic interaction between lipid and the lipid bilayer of the cell membrane. (b) Printing a pattern in ssDNA'-SH with a complementary sequence of the ssDNA on a glass surface carrying maleimide by an inkjet printer. The ssDNA-PEG-lipidmodified cells were applied to the substrate and immobilized on the pattern

from T cell lymphoma and so did not address the use of any adhesive cells. The extent to which the membrane modification procedure affects natural cell processes remains to be elucidated. The consequences of an unnatural state of adhesion through membrane-based tethering may include cell death[7], inhibited cell motility[8], and altered cell fate[9]

[7]Marek Los and Spencer B Gibson. *Apoptotic pathways as targets for novel therapies in cancer and other diseases*. Springer, 2005; Mario Vitale et al. "Fibronectin Is Required to Prevent Thyroid Cell Apoptosis through an Integrin-Mediated Adhesion Mechanism 1". In: *The Journal of Clinical Endocrinology & Metabolism* 83.10 (1998), pp. 3673–3680; Zhouhua Zhang et al. "The alpha 5 beta 1 integrin supports survival of cells on fibronectin and up-regulates Bcl-2 expression". In: *Proceedings of the National Academy of Sciences* 92.13 (1995), pp. 6161–6165.

[8]Donald J Donaldson, James T Mahan, and Gerald N Smith. "Newt epidermal cell migration over collagen and fibronectin involves different mechanisms". In: *Journal of cell science* 90.2 (1988), pp. 325–333; Paul A DiMilla et al. "Maximal migration of human smooth muscle cells on fibronectin and type IV collagen occurs at an intermediate attachment strength". In: *The Journal of cell biology* 122.3 (1993), pp. 729–737; Brian S Spooner, Kenneth M Yamada, and Norman K Wessells. "Microfilaments and cell locomotion". In: *The Journal of cell biology* 49.3 (1971), pp. 595–613.

[9]Courtney M Williams et al. "Fibronectin expression modulates mammary epithelial cell proliferation during acinar differentiation". In: *Cancer research* 68.9 (2008), pp. 3185–3192; Robert P Stidwill and Miriam Christen. "Alteration of fibronectin affinity during differentiation modulates the in vitro migration velocities of Hydra nematocytes". In: *Cell motility and the cytoskeleton* 41.1 (1998), pp. 68–

as some of the potential consequences of not engaging cytoskeletal adhesion molecules.

In the present study, we developed a method for the immobilization of ssDNA-SH on glass plates without a gold thin film, and we characterized the behavior of adherent HEK293 cells patterned using ssDNA-PEG-lipid tethers using cellular indicators such as morphology, migration velocity, viability, and doubling time.

4.2 Materials & methods

4.2.1 Materials

α-N-hydroxysuccinimidyl-ω-maleimidyl poly(ethylene glycol) (NHS-PEG-Mal, MW:5000) and 1,2-dipalmitoyl-sn-glycerol-3-phosphatidylethanolamine (DPPE) were purchased from NOF Corporation (Tokyo, Japan). Dichloromethane, chloroform, diethyl ether, dimethyl sulfoxide (DMSO), triethylamine (TEA), mixed penicillin-streptomycin solution, paraformaldehyde, cell count reagent SF and Blocking One were purchased from Nacalai Tesque (Kyoto, Japan). Minimal essential medium was purchased from Gibco (Carlsbad, CA, USA). Fetal bovine serum (FBS) was purchased from BioWest (Miami, FL, USA), phosphate-buffered saline (PBS) from Nissui Pharmaceutical, Co., Ltd (Tokyo, Japan) and RPMI 1640 medium from Invitrogen (Carlsbad, CA, USA). Bovine serum albumin (BSA), PKH26 Red Fluorescent Cell Linker Kit, PKH67 Green Fluorescent Cell Linker Kit, L-α-phosphatidylcholine (Type XVI-E) from egg yolk (EggPC), oligo(deoxyadenosine phosphate)$_{20}$ $(dA)_{20}$, and oligo(deoxythymidine phosphate)$_{20}$ $(dT)_{20}$ carrying an SH group protected with 6-hydroxy-1-hexanethiol at the 5'-end (ssDNA-SH), and ssDNA ($(dT)_{20}$) carrying fluorescein isothiocyanate (FITC) at the 5' end were purchased from Sigma-Aldrich Chemical Co. (St. Louis, MO, USA). ssDNA-SH sequences designated as SeqA, SeqA', SeqB, and SeqB' and listed in Table 2 were also purchased from Sigma-Aldrich Chemical. Cover slips (22 x 26 mm, 0.12-0.17 mm thickness) and BK7 glass plates (refractive index: 1.515, size: 25 x 25 x 1 mm) were purchased from Matsunami Glass Ind., Ltd (Osaka, Japan) and Arteglass Associates Co. (Kyoto, Japan), respectively. Nitrocellulose membranes (pore size: 0.8 μm), Millex-GP 0.22 μm Filter Units, and Isopore Membrane Filters (0.1 μm) were purchased from Millipore Co. (MA, USA). The phospholipid C test kit, Triton-X, and polyoxyethylene sorbitan monolaurate (Tween 20) were purchased from Wako Pure Chemical Industries (Osaka, Japan). ϕ12 mm glass-bottom dishes were purchased from ASAHI GLASS Co., Ltd (Tokyo, Japan). 3-Aminopropyltriethoxysilane (APTES) was purchased from Shin-Etsu Chemical Co., Ltd (Tokyo, Japan). Propidium iodide staining solution was purchased

73; JP Van der Sluijs, MR Baert, and RE Ploemacher. "Differential adherence of murine hematopoietic stem cell subsets to fibronectin." In: *Experimental hematology* 22.13 (1994), pp. 1236–1243.

TABLE 4.1: Characteristics of modified surfaces at each stage of substrate preparation using water contact angle and XPS measurement.

Stage	Contact angle (mean ± SEM, n = 4)	Atomic composition [%]					
		C	O	S	P	Si	N
Glass	-	11.21	67.28	0.00	0.89	20.62	0.00
APTES	61.79 ± 2.63°	23.25	56.41	0.00	0.10	16.10	4.14
APTES-EMCS	52.76 ± 2.13°	42.88	39.84	0.00	0.23	10.18	6.87
APTES-oligo(dA)$_{20}$	44.36 ± 1.55°	47.99	35.43	0.03	1.72	1.97	12.85

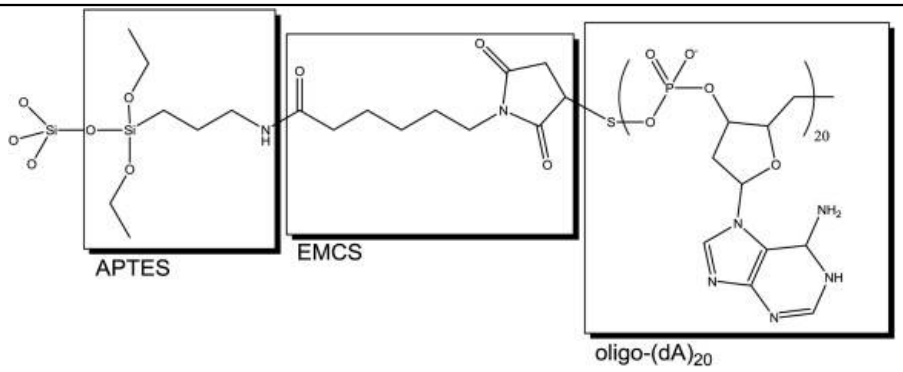

from BD Biosciences (New Jersey, USA). N-(ϵ-Maleimidocaproyloxy)sulfosuccinimide ester (sulfo-EMCS) was purchased from Thermo Fisher Scientific Inc. (Massachusetts, MS, USA). Anti-mouse vinculin, Alexa-594-conjugated phalloidin, Alexa-488-conjugated mouse anti-IgG, and Hoechst 33342 were purchased from Millipore Inc. (Billerica, MA, USA), Life Technologies Japan Ltd. (Tokyo, Japan), and Dojindo (Kumamoto, Japan), respectively.

4.2.2 Synthesis of ssDNA-PEG-lipid

ssDNA with a 5' end SH group (ssDNA-SH) was prepared by reduction of the disulfide bond at the 5' end with dithiothreitol according to the manufacturer's instructions. ssDNA-SH was conjugated with maleimide-PEG-lipid (Mal-PEG-lipid) as previously reported[10] (see Appendix Fig. A.13). Briefly, a Mal-PEG-lipid solution (300 μL, 1 mg/mL in PBS) and a ssDNA-SH solution (200 μL, 300 $\mu g/mL$ in PBS) were mixed and left for 12 h at RT to prepare ssDNA-PEG-lipids. Then the solution was diluted to 500 $\mu g/mL$ with PBS and stored at 4°C. ssDNA-PEG-lipids were used as prepared without further purification. In this study, three combinations of complementary DNA, oligo(dA)$_{20}$/oligo(dT)$_{20}$, SeqA/SeqA', and SeqB/SeqB', were used (Table 4.1).

[10]Teramura et al., "Control of cell attachment through polyDNA hybridization"; Sakurai, Teramura, and Iwata, "Cells immobilized on patterns printed in DNA by an inkjet printer".

4.2.3 Cell surface modification with ssDNA-PEG-lipid

HEK293 human embryonic kidney cells were obtained from Health Science Research Resources Bank (Osaka, Japan) and grown in minimal essential medium (MEM) containing 10% fetal bovine serum (FBS), 100 U/mL penicillin, and 0.1 mg/mL streptomycin at 37°C under 5% CO_2. The cells were harvested via trypsin treatment and washed twice with PBS by centrifugation (180 x g, 5 min, 25°C). 50 μL of a DNA-PEG-lipid solution (500 $\mu g/mL$ in PBS) was added to 50 μL of cell suspension (5.0 x 10^7 $cells/mL$) and incubated for 60 min at room temperature with gentle agitation. The cells were suspended in 3 mL PBS and washed with PBS by centrifugation (180 x g, 5 min, 25°C). The washing procedure was repeated twice. Cells modified with ssDNA-PEG-lipid will be hereafter referred to as ssDNA-PEG-cells. Non-adherent CCRF cells were modified with ssDNA using a similar method adapted for suspension cells described previously[11].

4.2.4 Preparation of ssDNA' immobilized culture substrates

(See Appendix Fig. A.14) Glass cell patterning substrates were prepared with ssDNA' sequences complementary to those inserted in cell membranes (ssDNA) for cell attachment through DNA hybridization. Glass cover slips were cleaned with piranha solution (a 7:3 mixture of concentrated sulfuric acid and 30% hydrogen peroxide) for 10 min, and rinsed three times with deionized water and three times with 2-propanol. After blow-drying with nitrogen gas, glass cover slips were immersed in 5% (v/v) APTES in H2O:EtOH (1:9, v/v) for 30 min at room temperature followed by washing with ethanol and water. Subsequently, glass cover slips were heated at 80°C in vacuo for 3 hr to complete condensation of APTES. Glass cover slips with amines on the surface were immersed in 500 $\mu g/mL$ aqueous sulfo-EMCS solution for 30 min at 37°C to introduce a maleimide group followed by rinsing with water. Then a ssDNA'-SH solution (300 $\mu g/mL$ in PBS) was printed by inkjet printer onto substrates and incubated at room temperature for 60 min to form a sulfide which was then followed by washing with water.

The sequentially modified substrate surfaces were characterized by water contact angle measurements, and surface atomic compositions were determined by X-ray photoelectron spectroscopy (XPS). Contact angles on each substrate were determined by the sessile drop method using a contact angle meter (CA-X, Kyowa Interface Science Co. Ltd., Saitama, Japan), and averages over four measurements were used. Atomic compositions of surfaces were determined using an ESCA-850V instrument (Shimadzu Co., Kyoto, Japan). A magnesium target was used with an electric current through the filament of 30 mA at 8 kV, and the base pressure of the analysis chamber was less than 1 x 10^{-5}

[11] Sakurai, Teramura, and Iwata, "Cells immobilized on patterns printed in DNA by an inkjet printer".

Pa. Sweeps were carried out for 600 *sec* with 0.100 eV steps. All spectra were corrected referring to the peak of Au 4f to 83.8 eV.

4.2.5 Cell attachment through DNA hybridization and subsequent culture

Before exposing cells to glass substrates modified with a DNA'-SH pattern, silicone rubber spacers (2 *cm* in length, 3 *cm* in width, 1 *mm* in thickness) were placed on opposite peripheral sides of the substrate, and a cover slip was then placed across the spacers to create a gap 1 *mm* thick between the two glass layers. A BSA solution (200 μL, 10 mg/mL) was injected into the chamber and incubated at room temperature for 20 *min*. Following rinsing with PBS, a ssDNA-PEG-cell suspension (200 μL, 2.5 x 10^7 $cells/mL$) was injected into the chamber. After incubation for 5 *min* at room temperature, the cover slip and the silicone slices were carefully separated with gentle shaking while the substrate was fully immersed in PBS. The substrate was then further shaken in PBS to gently wash away any non-binding cells. Note that it is critical that the substrate not be exposed to the air-liquid interface or else the cells on the substrate will be detached. To distinguish two groups of cells modified by different sequences of ssDNA, cells were labeled in advance with either PKH26 red or PKH67 green according to the manufacturer's instructions. Afterward, attachment of cells was observed using a fluorescence upright microscope (BX51, Olympus, Tokyo, Japan) and a stereoscopic microscope (MZF LIII, Leica, Solms, Germany). After adhesion, Minimal Essential Medium (MEM) supplemented with 10% FBS, 100 U/mL penicillin, and 100 $\mu g/mL$ streptomycin were added to the culture dish and incubated at 37°C under 5% CO_2.

4.2.6 Immunostaining for adhesive proteins of cells attached through DNA hybridization

Cells adhered to glass-base dishes through DNA hybridization were cultured for 2 *hr* in medium with or without FBS in the same manner as cells on glass substrates. Then cells were stained for F-actin and vinculin. Cultures were fixed with 4 percent paraformaldehyde for 15 *min*, permeabilized with 0.2 percent Triton-X for 15 *min*, blocked from non-specific binding with Blocking One for 1 *hr* and incubated with anti-mouse vinculin (1:500 dilution) 1 *hr* at room temperature. Then, they were washed with a 0.05% solution of Tween 20 for 15 *min* three times at room temperature and then treated with Alexa-594-conjugated phalloidin (1:40 dilution) for F-actin staining, Hoechst 33342 (1:500 dilution) for nucleus staining and Alexa-488-conjugated mouse anti-IgG (1:500 dilution) for vinculin staining, for 1 *hr* at room temperature. Next, fixed cultures were

washed with 0.05% solution of Tween 20 for 15 *min* thrice at room temperature. Imaging was performed using confocal laser scanning microscopy (Olympus, Tokyo, Japan).

4.2.7 Staining of double stranded DNA (dsDNA) acting as an adhesion molecule

To confirm that cells were anchored through DNA hybridization to the substrate, dsDNA was stained and observed. Cells were attached through DNA hybridization on glass-base dishes using ssDNA-PEG-lipid and then cultured in medium supplemented by 10% FBS. Following the application of cells, propidium iodide (PI), an intercalating agent used here as a DNA stain, was added to the medium at a concentration of 5 $\mu g/mL$ and incubated for 10 *min* at 37°C. dsDNA between cells and substrate was then observed by a confocal laser scanning microscopy. Subsequently, cells were cultured 6 *hr* in medium supplemented by 10% FBS without PI. PI was then added, and cells were observed in the same manner.

The membranes of cells dyed with PKH dyes were observed as well. Briefly, cells were harvested using trypsin and stained with PKH dye. They were then modified with ssDNA-PEG-lipid. The cells were seeded on ssDNA'-immobilized glass-base dishes and submerged in culture medium containing FBS. During culture, cells were observed via fluorescence microscopy.

4.2.8 Cell migration assay

Cell migration was measured through analysis of time-lapse motion picture. Cells adhered through DNA hybridization, ssDNA-PEG-lipid-modified cells seeded on non-complementary ssDNA-immobilized surfaces, and naked cells on glass substrates were analyzed. Each group of cells was seeded at 1.0 x 10^4 cells/dish and cultured in MEM supplemented with 10% FBS at 37°C. For an analysis of cell migration, cell images were captured every 10 *min* for 14 *hr* using an inverted phase contrast microscope (Cell-watcher; Corefront, Tokyo, Japan). Cell migration distance was evaluated by using ImageJ software.

4.2.9 Cell viability and growth rate

To examine the effects of short term and long term culture on cells adhered through DNA hybridization, cell viability and cell growth were tested. To determine cell viability, cultures were first exposed to PI to stain the nuclei of dead cells and were then observed

under a fluorescence microscope. Live cells were counted by subtracting PI-stained dead cells from bright field images in ImageJ. 5 pictures were taken per dish, and three-measurement averages were used. Additionally, growth rate was determined using a cell count reagent SF according to the manufacturer's instructions. Cell number was recorded after 1, 2, and 3 days of culture and subsequently used to calculate the doubling time.

4.2.10 Preparation of liposomes modified with ssDNA-PEG-lipid

EggPC (20 mg) was dissolved in chloroform (2 mL). Chloroform was removed from the Egg PC solution under reduced pressure to prepare a dry thin lipid film in a glass flask using a rotary evaporator. Two milliliters of PBS were added to the lipid film and stirred vigorously at 4°C for 1 day to prepare lipid vesicles (lipid concentration was 20 mg/mL). The suspension was then extruded through a series of membrane filters with a pore size of 0.8 μm, 0.22 μm (twice), and 0.1 μm (10 times) to form small unilamellar vesicles or liposomes (≈100 nm diameter). Lipid concentration was determined using the phospholipid C test kit. A ssDNA-PEG-liposome complex was prepared by incubation of a mixture of liposome suspension (500 μL of 8 mg/mL) and ssDNA-PEG-lipid solution (40 μL of 500 $\mu g/mL$) at 37°C for 60 min. ssDNA-PEG-liposome complex was used as prepared without further purification.

4.2.11 SPR analysis of adsorption of liposomes and adhesion proteins on ssDNA-immobilized surfaces

Surface interactions between oligo$(dT)_{20}$-PEG-liposomes and oligo$(dA)_{20}$-immobilized surfaces were examined by using a lab-made surface plasmon resonance (SPR) apparatus[12] to monitor the shift in resonance angle due to changes in surface adsorption. The substrates used in SPR measurements were gold-coated glass cover slips (a 1-nm chromium layer and a 49-nm gold layer). Prior to measurement, substrates were exposed to a solution of oligo$(dA)_{20}$-SH solution (50 $\mu g/mL$ in PBS) and allowed to react with the gold surface for 60 min at room temperature via the thiol-gold reaction. Flow chambers were then prepared by first placing the oligo$(dA)_{20}$-modified gold-coated glass cover slip on the prism of the SPR apparatus. PBS was then circulated at a flow rate of 4.0 mL/min into the flow chamber for 5 min. Either a complementary oligo$(dT)_{20}$-PEG-liposome suspension (10 $\mu g/mL$ in PBS) or non-complementary oligo$(dT)_{20}$-PEG-liposome was circulated over the oligo$(dA)_{20}$-immobilized surface for

[12] Yuji Teramura, Yusuke Arima, and Hiroo Iwata. "Surface plasmon resonance-based highly sensitive immunosensing for brain natriuretic peptide using nanobeads for signal amplification". In: *Analytical biochemistry* 357.2 (2006), pp. 208–215.

90 *min* to examine attachment due to hybridization. To account for refractive index changes of the oligo$(dT)_{20}$-PEG-liposome suspension, PBS was then circulated over the substrate for 5 *min*. To emulate cell culture conditions, each surface was then exposed to a 10% solution of FBS in PBS for 30 *min* again followed by 5 *min* circulation of PBS to account for a refractive index difference of the FBS solution.

Protein adsorption on ssDNA-immobilized surface was also examined using a lab-made surface plasmon resonance (SPR) apparatus. Oligo$(dT)_{20}$-modified gold-coated glass cover slips were set on the SPR apparatus, and PBS was circulated at a flow rate of 4.0 mL/min in the flow chamber for at least 5 *min*. Then, the surface of each glass cover slip was exposed to PBS containing 10% FBS (v/v). To examine whether adhesive proteins were among those that had been adsorbed, the antibody binding of 0.4% rabbit anti-bovine-vitronectin antiserum was monitored and compared with serum without anti-vitronectin.

4.3 Results

4.3.1 Surface characterization

Water contact angles of surfaces sequentially modified are summarized in Table 4.1. The contact angle of a bare glass substrate cleaned with piranha solution was too small to be determined. Contact angles of substrates increased to 61.8 ± 2.6° by APTES modification and slightly decreased to 52.8 ± 2.1° by EMCS modification. After oligo$(dT)_{20}$-SH immobilization, the contact angle decreased to 44.4 ± 1.6°.

Modified surfaces were analyzed for their atomic composition using X-ray photoelectron spectroscopy (XPS) via an ESCA-850V instrument. Table 4.1 shows the estimated atomic compositions of each stage in the manufacturing process calculated based on the integration of peak areas. The increase in atomic concentrations of phosphorous, carbon, nitrogen, and oxygen in the final stage of substrate preparation compared to preceding stages suggests that oligo-$(dA)_{20}$ was successfully conjugated to the surface.

4.3.2 Attachment of ssDNA-modified cells on a ssDNA'-modified surface

Cell patterning on glass cover slips was possible by applying ssDNA-PEG-cells on printed patterns of ssDNA' (complementary to the sequences attached to cell surfaces via ssDNA-PEG-lipid) as schematically shown in Fig. 4.1. Solutions of ssDNA'-SH were printed

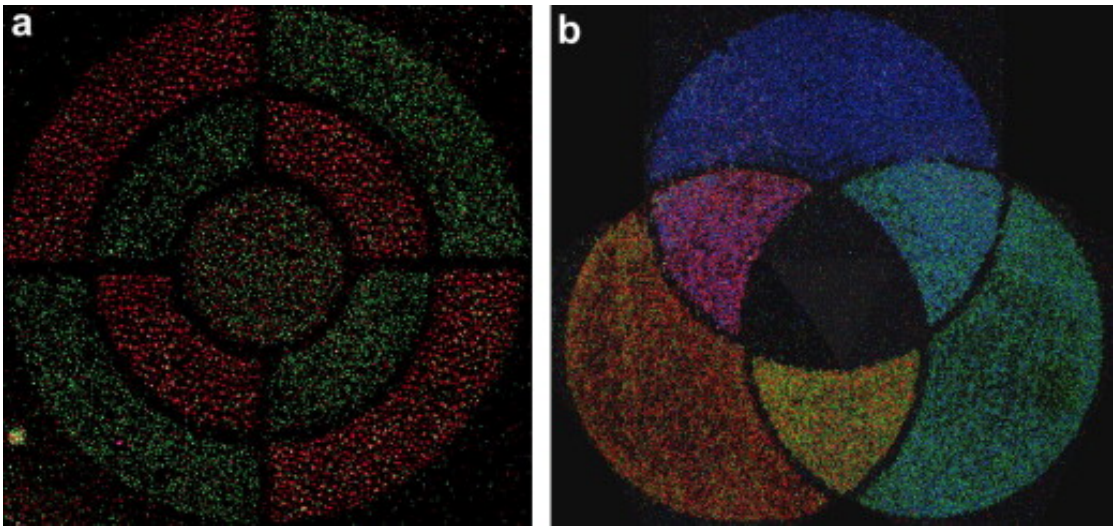

FIGURE 4.2: Fluorescence images of cells immobilized on patterns printed with an inkjet printer. (a): A dartboard pattern printed in a SeqA'-SH and SeqB'-SH solution using an inkjet printer. Solutions of SeqA'-SH and SeqB'-SH were separately loaded into each ink cartridge. A dartboard target pattern was printed using these solutions with the center circle of the target printed in both SeqA'-SH and SeqB'-SH solutions. A mixed suspension of HEK293 SeqA-PEG-cells (stained with PKH26 red) and SeqB-PEG-cells (stained with PKH67 green) was seeded over the surface. (b): Overlapping RGB colors patterned with CCRF cells. In addition to SeqA'-SH and SeqB'-SHloaded cartridges, a third color was achieved by including oligo$(dA)_{20}$-SH. The printed surface was then exposed to cells modified with the complementary counterparts of these three sequences and different dyes (PKH67, PKH26, or Hoechst 33342) to distinguish them.

with an inkjet printer onto glass cover slips presenting maleimide functional groups permitting ssDNA'-SH to be immobilized to substrates. Cells modified with ssDNA-PEG-lipid were applied to the ssDNA'-immobilized surface to induce cell attachment through the ssDNA-ssDNA' hybridization. In addition, ssDNA with variety of base sequences could be prepared allowing for distinctly different groups of cells to be simultaneously immobilized onto separate and overlapping regions of glass substrates. Fig. 4.2(a) shows a dartboard image created by the patterning two groups of HEK293 cells. The pattern was produced as follows: solutions of SeqA'-SH and SeqB'-SH were each added to different ink cartridges and printed via inkjet printer on maleimide presenting surfaces. After washing the glass cover slips, the surface was immersed in BSA to inhibit non-specific cell adhesion. Substrates were washed again with PBS, and then a mixed suspension of SeqA-PEG-cells and SeqB-PEG-cells were introduced. Green and red fluorescent staining of each cell group was used to distinguish the separate regions of the pattern, and green and red fluorescent images were overlaid in ImageJ to create a single image. This process can be expanded to three or more cell groups by using additional sequence pairs (Table 4.2). Fig. 4.2(b) shows the patterning on glass of suspension CCRF cells modified with ssDNA-PEG-lipid in the same manner as previously

TABLE 4.2: List of ssDNA sequences used in this study.

ssDNA Sequences	
Label 5'	3'
Oligo-dT_{20}	HS-TTT TTT TTT TTT TTT TTT TT
Oligo-dA_{20}	HS-AAA AAA AAA AAA AAA AAA AA
SeqA	HS-TGC GGA TAA CAA TTT CAC ACA
SeqA'	HS-TGT GTG AAA TTG TTA TCC GCA
SeqB	HS-TAG TAT TCA ACA TTT CCG TGT
SeqB'	HS-ACA CGG AAA TGT TGA ATA CTA

reported[13]. 3 separate groups of cells were each modified with one of 3 sequence pairs chosen from Table 4.2. To distinguish the three groups, PKH26 red, PKH67 green, or Hoechst 33342 were applied to the different cell groups. The pattern produced shows that combinations of the red, green, and blue (RGB) colors can be used to produce a complete range of colored images in the form of patterned cells.

4.3.3 Immunostaining for morphology of cells adhered through DNA hybridization

To study the effects of surface ssDNA' and attachment through DNA hybridization on cell behavior and morphology, ssDNA-PEG-cells were cultured in medium either with or without FBS for 2 *hr* after cells were introduced. Fig. 4.3 shows staining of F-actin, vinculin, and the nuclei of HEK293 cells. Vinculin, a membrane cytoskeletal protein which localizes at focal adhesions, acts as a linker between the actin cytoskeleton and integrins or cadherins. In the case of unmodified cells cultured on naked glass substrates in FBS-containing medium (Fig. 4.3(a)), vinculin was expressed in concentrated focal adhesions at the growing periphery of cells, and actin stress fibers elongated from these points spanning the cell. In contrast, cells attached by DNA hybridization and cultured in FBS-free medium were unable to take on the morphology observed on unmodified glass substrates. Instead, these cells assumed irregular geometry with elongated actin-fiber protrusions more characteristic of neurite or dendritic morphology. Vinculin expression was hardly visible and was uniformly distributed throughout the cell rather than being concentrated at focal adhesions (Fig. 4.3(b)). In contrast, when cells attached through DNA hybridization and were cultured in FBS-containing medium, they assumed similar geometries as the unmodified cells cultured on naked glass substrates. In this case, vinculin was expressed densely in focal adhesions at the growing periphery of cells, and actin stress fibers could be observed extending across the cell from the focal adhesions (Fig. 4.3(c)).

[13]Sakurai, Teramura, and Iwata, "Cells immobilized on patterns printed in DNA by an inkjet printer".

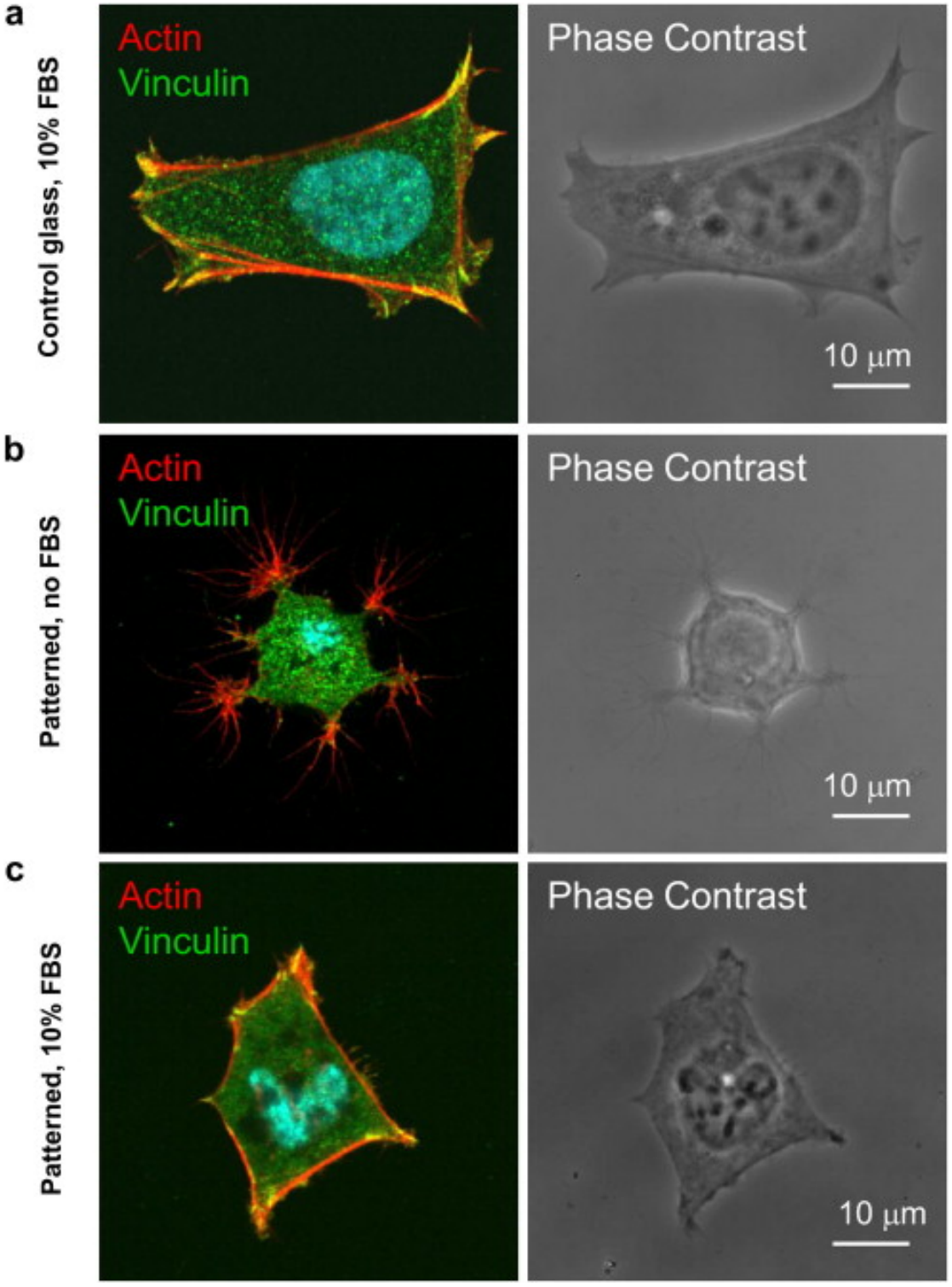

FIGURE 4.3: Immunostaining of F-actin, vinculin, and the nuclei of HEK293 cells. (a): Unmodified cell adhered on glass in a medium supplemented with 10% FBS. (b): ssDNA-PEG-cell adhered on a ssDNA' immobilized surface through DNA hybridization and then cultured in a medium without 10% FBS. (c): ssDNA-PEG-cell adhered on a ssDNA' immobilized surface through DNA hybridization and cultured in MEM supplemented with 10% FBS.

4.3.4 Characterization of double stranded DNA (dsDNA) located at the cell-glass interface

To track hybridized DNA engaged in cell attachment, dsDNA was stained with PI which acts as a fluorescent intercalator similar to ethidium bromide. A solution of PI was added to cells at various times following cell attachment. Cells and corresponding fluorescence images of intercalated PI are shown in Fig. 4.4(a) and (b). Following 10 *min* of cell attachment via DNA hybridization, the fluorescence of PI could be observed just underneath the cells. Cells were then cultured in PI-free medium with 10% FBS. Following 6 *hr* of culture, PI was added to culture medium and observed. After this extended culture time, cell migration was clearly observable with some cells seen to have departed from their original attachment locations (Fig. 4.4(b)). In these instances, the fluorescence of PI, revealing the existence of dsDNA, was observed at the same locations as those 6 *hr* prior. This indicates that dsDNA remained in its original location in spite of cell migration away from the original attachment point.

Cells with membranes stained with PKH67 green and attached through DNA hybridization were also cultured and observed under fluorescence microscopy (Fig. 4.4(c)). After 4 *hr* culture, cells migrated well away from their initial positions and left trails of fluorescence on and near their points of attachment. After 6 *hr* of culture, fluorescent trails were no longer observed in the wake of cell migration suggesting the possibility that initially inserted ssDNA-PEG-lipid was no longer present in the membrane and corresponding with the increased migration speed observed after 6 *hr* culture described in the following section.

4.3.5 Cell migration speed

In addition to qualitative observations of cell migration in the previous experiment, migration was also characterized quantitatively by measuring the speed. These results are shown as a box plot in Fig. 4.5. The magnitude of cell migration velocity immediately following attachment (Fig. 4.5(a)) through DNA hybridization was very low (median was 4.1 $\mu m/hr$; bottom and top of the box show the boundaries of the lower and upper quartiles which were 4.1 $\mu m/hr$ and 9.6 $\mu m/hr$ respectively). Although some outlier cells were observed to have migrated rapidly, the general tendency is for cells attached through DNA hybridization to exhibit a reduced migration speed. In contrast, migration velocities of cells adhered through adhesive proteins, regardless of whether cells were modified by non-complementary ssDNA-PEG-lipid or not modified, was high relative to cells adhered only by DNA. The median, lower quartile, and upper quartile values for migration speeds of cells modified with non-complementary ssDNA were 20.1 μm, 10.4

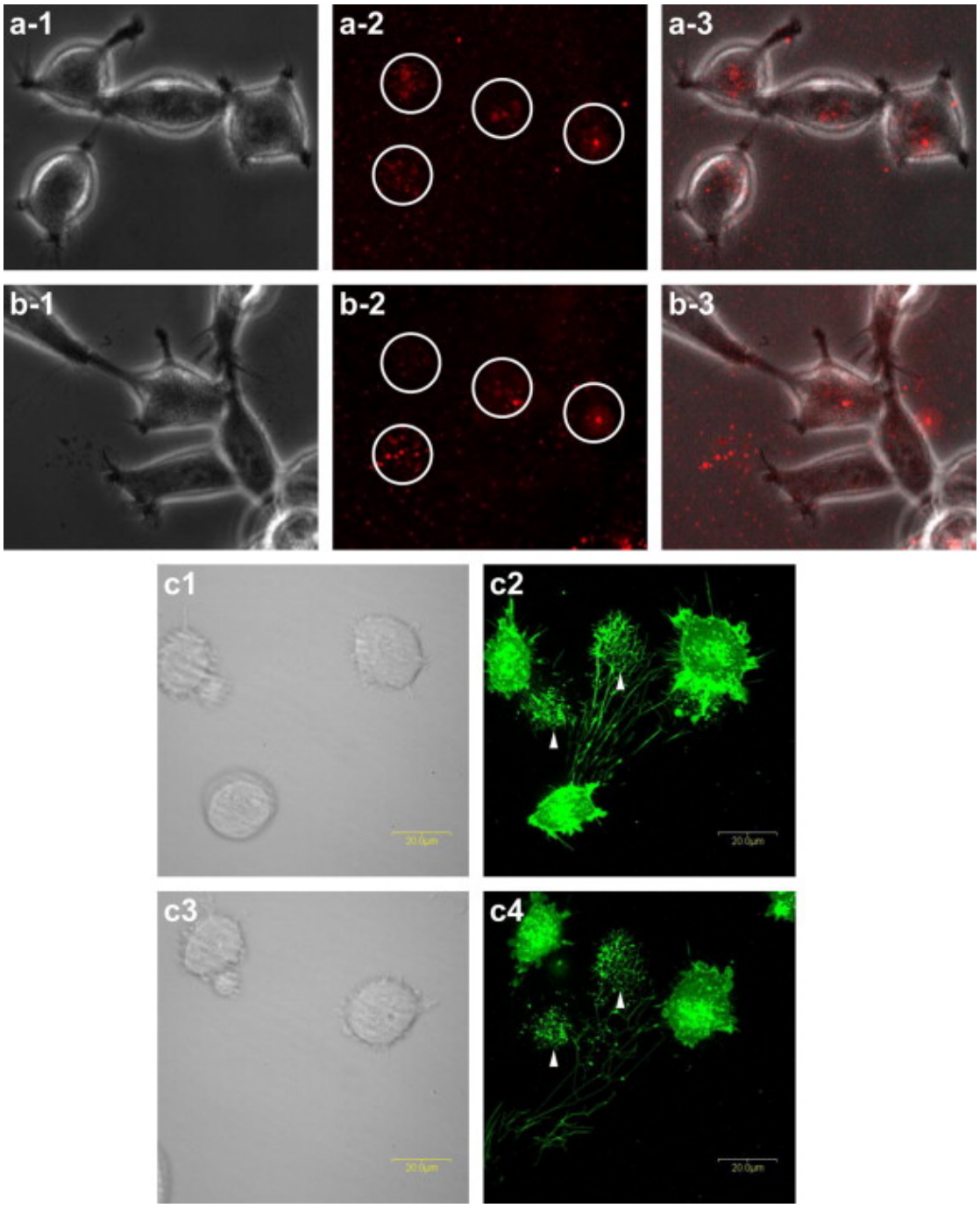

FIGURE 4.4: Characterization of ssDNA-PEG-cell morphology following seeding and verification of double stranded DNA (dsDNA) located at the cellglass interface. (a) and (b) show phase, fluorescence, and overlaid images of multiple instances of dsDNA located at the cellglass interface stained red with PI. (a): Cells cultured in MEM with 10% FBS 10 *min* after cell attachment via DNA hybridization, (b): 6 *hr* follow up of the cells cultured in (a). (c): Patterned cells with membranes stained using PKH67 green. (c-1) and (c-2): patterned cells at 10 *min* after cell attachment via DNA hybridization, (c-3) and (c-4): Patterned cells cultured in MEM with 10% FBS for 4 *hr*. White arrows indicate the locations of cell remnants which mark the points of initial attachment to the substrate.

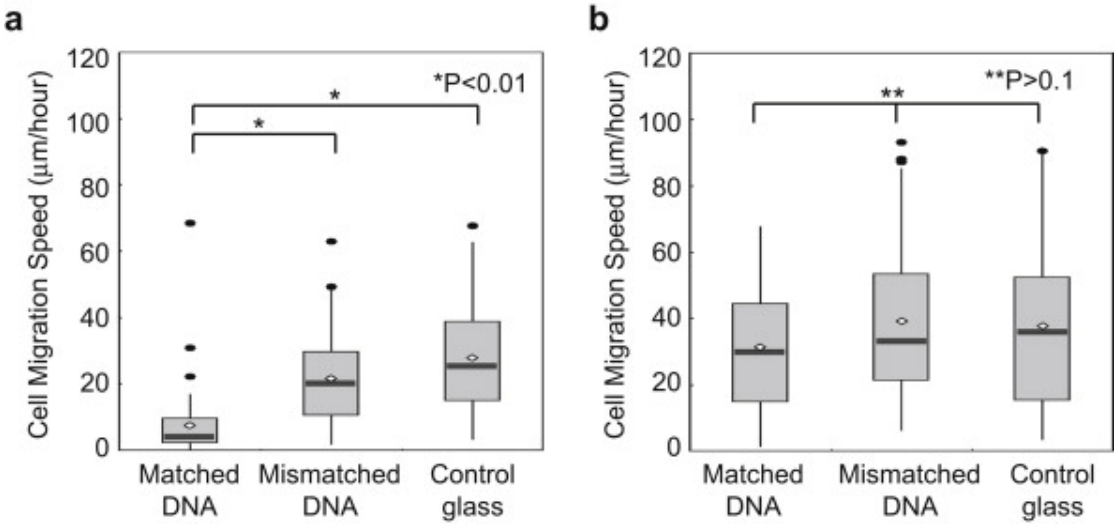

FIGURE 4.5: Cell migration. ssDNA-PEG-cells are seeded on either complementary or non-complementary ssDNA-immobilized surfaces while naked cells are seeded on glass substrates. In each condition, cells were cultured in MEM supplemented with 10% FBS at 37°C. Cell images were captured every 10 *min* for 14 *hr* using an inverted phase contrast microscope. Contour lengths of cell migration for 1 *hr* were evaluated using ImageJ software. (a): Distributions of migration distance measured during the first hour after initial seeding, (b): Distributions of migration measured for a 1 *hr* duration after 6 *hr* culture.

μm, and 29.7 μm respectively. Those of unmodified cells on naked glass substrates were 25.5 μm, 14.9 μm, and 38.8 μm respectively. Though attachment and spreading are accelerated using DNA-based inserts, the relative low migration after 1 *hr* compared to unmodified cells on glass substrates indicates that the attached inserts inhibit migration in the initial phase.

Migration speeds of cells after 6 *hr* of culture are also shown in Fig. 4.5(b). Migration speeds between each group of cells exhibited no significant differences; median, upper quartile, and lower quartile values of migration speed of cells modified with complementary ssDNA were 29.3 μm, 33.7 μm and 35.4 μm respectively, and p values calculated by t-test between any two groups were never less than 0.1.

4.3.6 Cell viability and growth rate

To further examine the influence of cell modification and attachment with DNA, the percent viability of cell cultures and associated doubling times were also measured (Fig. 4.6(a)) when the cells were cultured in medium with 10% FBS. Viabilities of cells attached through DNA hybridization and naked cells on glass substrates were both over 95% and did not exhibit a significant difference. These results did not change after 6 *hr* culture.

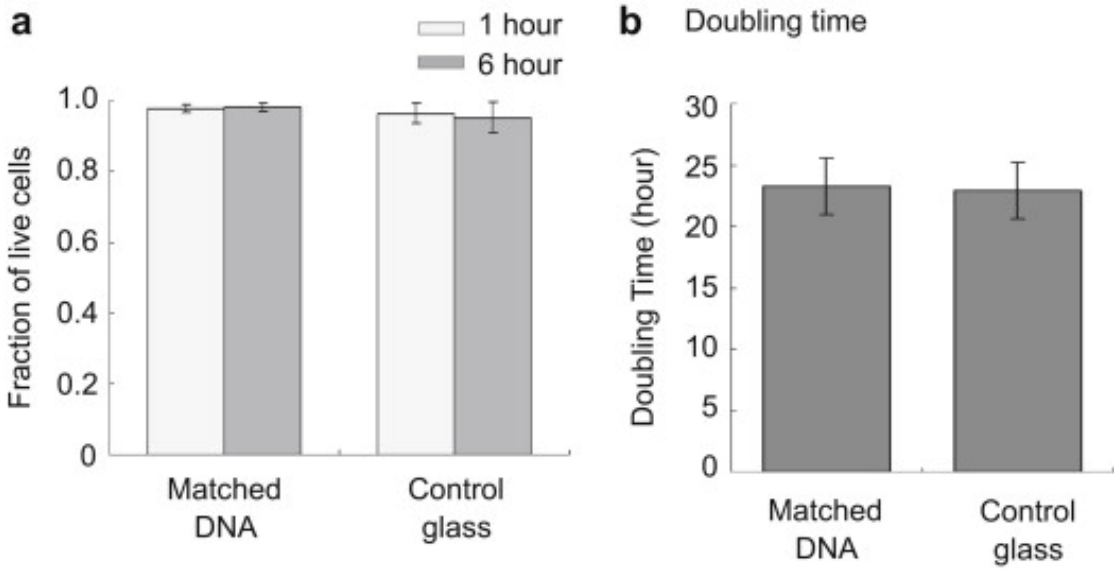

FIGURE 4.6: Viability and doubling times of HEK293 cells attached through DNA hybridization. Cells were cultured in MEM with 10% FBA. (a): Percent viability of patterned and unpatterned cell cultures at 1 and 6 *hr* (b): Cell doubling times of patterned and unpatterned cell cultures.

Growth rates characterized by doubling times exhibited no differences between each group (Fig. 4.6(b)). Doubling time of cells attached through DNA hybridization and naked cells were 23.3 ± 1.0 *hr* and 22.9 ± 1.0 *hr*, respectively, in medium with 10% FBS.

4.3.7 SPR measurement

Since precise quantitative surface adsorption measurements are difficult to perform with cell culture, ssDNA-SH immobilized on gold in the place of glass surfaces presenting maleimide functional groups along with a lab-made surface plasmon resonance (SPR) apparatus were employed to study the interaction between the ssDNA-modified substrates and complementary ssDNA'-PEG-liposomes. When a suspension of oligo$(dT)_{20}$-PEG-liposomes was introduced to the sensor surface, a large increase in the SPR angle was observed (Fig. 4.7(a)). On the other hand, no increase in the SPR angle was observed when oligo$(dA)_{20}$-PEG-liposomes were introduced (Fig. 4.7(b)). This indicates that the oligo$(dT)_{20}$-PEG-liposomes specifically bound to the oligo$(dA)_{20}$-immobilized surface through oligo$(dT)_{20}$-oligo$(dA)_{20}$ hybridization.

Adsorption of serum protein on these surfaces was also studied by exposing the hybridized substrate to PBS with 10% FBS. As shown in Fig. 4.7(a) and (b), a significant increase in the SPR angle was observed at this stage indicating that proteins contained in FBS adsorbed to the surfaces.

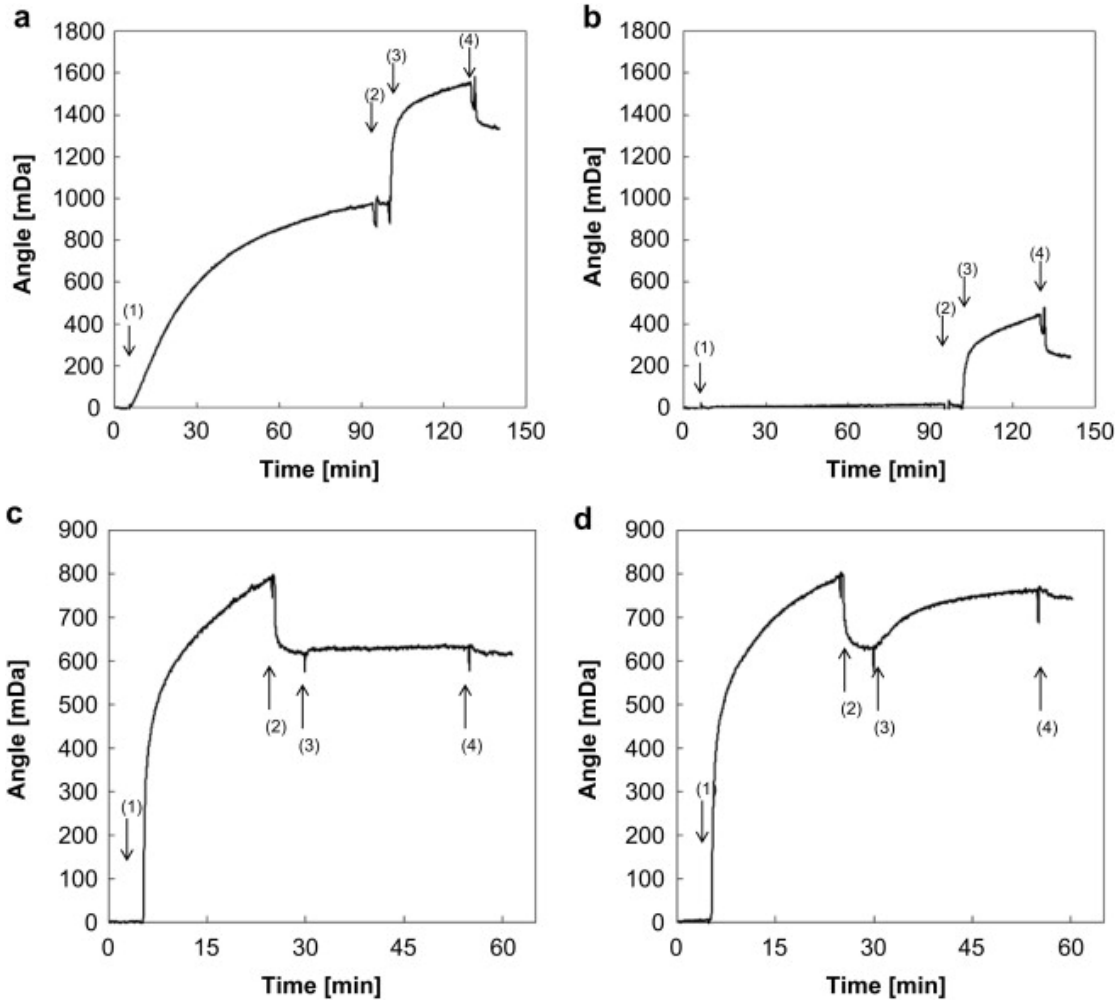

FIGURE 4.7: SPR analysis; shift in resonance angle versus time under different conditions. (a): oligo(dA)$_{20}$-treated surface exposed to (1) complementary oligo(dT)$_{20}$-PEG-liposomes, (2) PBS, (3) 10% FBS solution, (4) PBS. (b): oligo(dA)$_{20}$-treated surface exposed to (1) non-complementary oligo(dA)$_{20}$-PEG-liposomes, (2) PBS, (3) 10% FBS solution, (4) PBS. (c): oligo(dT)$_{20}$-treated surface exposed to (1) 10% FBS solution, (2) PBS, (3) 0.4% control serum (no antibody), (4) PBS. (d): oligo(dT)$_{20}$-treated surface exposed to (1) 10% FBS solution, (2) PBS, (3) 0.4% rabbit anti-bovine-vitronectin antiserum, (4) PBS.

The adsorption of serum proteins, particularly that of the cell adhesion protein vitronectin, was further studied using the SPR apparatus to examine the contribution of integrin mediated cell adhesion. As shown in Fig. 4.7(c) and (d), when the ssDNA-immobilized surface was exposed to 10% FBS, the SPR angle increased by over 600 mDA, indicating an approximate adsorption of 300 ng/cm^2 of serum proteins onto the ssDNA-immobilized surface. The surface was then exposed to solution containing anti-bovine vitronectin IgG. SPR angle shift was not observed when the surface was exposed to serum which did not contain anti-bovine vitronectin IgG (Fig. 4.7(a)), whereas SPR angle did increase when anti-bovine vitronectin antiserum was used. This indicates that vitronectin was present in the serum protein layer formed on the oligo(dT)$_{20}$-immobilized

surface (Fig. 4.7(b)).

4.4 Discussion

Membrane tethers do not engage the cytoskeleton, and previous studies have shown that failure to do so can result in apoptosis, a phenomenon known as anoikis[14]. By culturing cells in media with and without FBS (Fig. 4.3(a) and (b)), we show that cell morphology and extent of spreading are markedly different between the two conditions even amongst cells attached through DNA hybridization. This, taken in conjunction with SPR data (Fig. 4.7) showing that the addition of FBS leads to adsorption of adhesive serum proteins, suggests that patterned cells bind with adsorbed serum proteins via integrins in focal adhesions. In addition, cells patterned on substrates could be cultured for 24 *hr* (Fig. 4.6) and had a live/dead ratio and a proliferation rate comparable to control groups cultured on glass without modification. The ability for patterned cells to bind with adsorbed serum proteins and engage natural cytoskeletal adhesion proteins permits long term culture without anoikis.

Membrane tethering results in fast attachment since the kinetics of DNA hybridization greatly exceeds those of natural adhesion modes. Natural cell adhesion through adhesive glycoproteins can be viewed of as consisting of two stages: 1. the formation of immature focal contacts and 2. the maturation of focal contacts into focal adhesions[15]. In typical cell culture of adherent cell lines, this process can take 1-3 *hr* after the initial settling of cells onto the substrate and is followed by expansion of focal contacts from the cell pole to the peripheral regions of the cell marking the beginning of the feedback loop which characterizes spreading over rigid surfaces[16]. In addition to revealing concentrations of double stranded DNA, Fig. 4.4 shows that ssDNA-PEG-cells assumed a partially spread and elongated morphology indicating that attachment of ssDNA-PEG-cells occurred rapidly, within 10 *min* after exposure to the ssDNA-immobilized surface. This suggests that the initial process of focal contact formation and propagation was bypassed or accelerated by the close surface contact caused by DNA hybridization.

The cell patterning method presented here could be adapted for high-throughput screening assays for industrial pharmaceutical applications. In instances where heterotypic cell-cell interactions are of interest, close proximity of different cell types as well as a

[14] Helene Levrey Hadden and Craig A Henke. "Induction of lung fibroblast apoptosis by soluble fibronectin peptides". In: *American journal of respiratory and critical care medicine* 162.4 (2000), pp. 1553–1560.

[15] Lehnert et al., "Cell behaviour on micropatterned substrata: limits of extracellular matrix geometry for spreading and adhesion".

[16] David A Potter et al. "Calpain regulates actin remodeling during cell spreading". In: *The Journal of cell biology* 141.3 (1998), pp. 647–662.

high ratio of heterotypic to homotypic cell-cell contacts could be important for the efficiency and accuracy of implementing the assay. Due to the flexibility of inkjet printing, a variety of patterns incorporating heterotypic localization are possible. In contrast to previous techniques, the optical clarity of glass substrates employed in this process coupled with the potential for patterning of more than two groups of cells on a single substrate make this method a possible platform for the in vitro study of various cell behaviors. These studies may include cadherin-cadherin interactions, epithelial to mesenchymal transition, migration and cancer metastasis, or organization of mixed cell type tissues. The propensity for cells to migrate away from their initial locations could prove to be a limitation in applications where long term integrity of the initial pattern is needed. Therefore, this technology may be best suited for applications which depend on short term preservation of patterned cells rather than extended timelines.

4.5 Conclusions

We developed a new method for the patterning of different groups of cells over glass substrates via membrane-bound oligonucleotides. Optical transparency of the glass substrates enabled us to characterize the long term behavior of adherent cells patterned with this method. Membrane tethers using ssDNA-PEG-lipid cause fast cell attachment since the kinetics of DNA hybridization greatly exceed those of natural adhesion modes. The natural processes involved in cell adhesion and motility compete with the artificial attachment, and long term culture results in a transition from artificial to natural adhesion modes as surface adhesion proteins are engaged and up-regulated.

Chapter 5

Sequence-specific nuclease-mediated release of cells tethered by oligonucleotide phospholipids

---

"a simple inanimate device can achieve the same essential result as would be achieved by the intervention of intelligent beings. We have examined the 'biological phenomena' of a nonliving device and have seen that it generates exactly that quantity of entropy which is required by thermodynamics "

Leó Szilard
On the decrease of entropy in a thermodynamic system by the intervention of intelligent beings, 1923

5.1 Introduction

Techniques to control the spatiotemporal organization of cells are primarily limited to homogeneous cell populations, and technologies involving co-culture of different groups of cells would benefit from methods to control relative 2D and 3D arrangement. One approach for artificially introducing cell-cell and cell-substrate interactions is to modify cell surfaces with ligands of specific binding affinities. Unique chemistries can be introduced to cell surfaces through various means, for example by modifying native surface proteins[1] and glycans[2] or through exposure to synthetic lipids capable of associating with the cell membrane[3]. Cell surface modification can also be used to induce rapid cellular aggregate formation, a useful property for the enhancement of differentiation through heterotypic cell-cell stimulation or for accelerating wound healing in vitro as has been demonstrated using cell surface oxidation followed by modification with biotin/avidin chemistry[4]. We have previously explored synthetic single-stranded oligonucleotide-conjugated lipids (ssDNA-PEG-lipids) as a means to introduce artificial binding capacity to cells by exploiting specific hybridization of DNA[5], and this technology was extended to a variety of applications including the co-localization of unlike cell types[6] and printing of cell patterns on 2D substrates[7]. DNA has been recognized as an attractive ligand partly because of its specific binding affinity and the capacity for a practically unlimited variety of binding interaction schemes, which for example have been exploited to arrange nanoparticles into ordered lattice structures[8].

However, while this technology can be used to tether cells to a patterned surface or induce heterotypic cell-cell aggregation, the DNA linkages are effectively irreversible, a characteristic which inhibits downstream analysis or further experimentation on a captured cell group. One way to address this is by designing substrates with in situ release capability. For example, Shin et al used photolabile crosslinkers with exposed antibodies to first capture and then release CD4 antigen-bearing cells through UV-induced tether

[1] Matthias T Stephan and Darrell J Irvine. "Enhancing cell therapies from the outside in: Cell surface engineering using synthetic nanomaterials". In: *Nano today* 6.3 (2011), pp. 309–325.

[2] Eliana Saxon and Carolyn R Bertozzi. "Cell surface engineering by a modified Staudinger reaction". In: *Science* 287.5460 (2000), pp. 2007–2010.

[3] Keitaro Sou et al. "Poly (ethylene glycol)-modification of the phospholipid vesicles by using the spontaneous incorporation of poly (ethylene glycol)-lipid into the vesicles". In: *Bioconjugate chemistry* 11.3 (2000), pp. 372–379; Teramura, Kaneda, and Iwata, "Islet-encapsulation in ultra-thin layer-by-layer membranes of poly (vinyl alcohol) anchored to poly (ethylene glycol)–lipids in the cell membrane".

[4] De Bank et al., "Accelerated formation of multicellular 3-D structures by cell-to-cell cross-linking".

[5] Teramura et al., "Control of cell attachment through polyDNA hybridization".

[6] Teramura et al., "Control of cell attachment through polyDNA hybridization"; Teramura et al., "Microencapsulation of islets with living cells using polyDNA-PEG-lipid conjugate".

[7] Sakurai, Teramura, and Iwata, "Cells immobilized on patterns printed in DNA by an inkjet printer"; Kengo Sakurai, Ian T Hoffecker, and Hiroo Iwata. "Long term culture of cells patterned on glass via membrane-tethered oligonucleotides". In: *Biomaterials* 34.2 (2013), pp. 361–370.

[8] Robert J Macfarlane et al. "Nanoparticle superlattice engineering with DNA". in: *Science* 334.6053 (2011), pp. 204–208.

cleavage[9], and Zhu et al demonstrated that electrical stimulation could be used to trigger the release of cells attached to antibodies on alkane thiol gold monolayers[10]. In addition to temporary immobilization on a substrate it is conceivable that temporary aggregation or cell-cell contact may be desired. For example, stem cells at different stages of differentiation are sensitive to local signals, and a temporary stimulus from neighboring cells might trigger commitment to a certain lineage[11]. We sought, therefore, a means of severing the DNA-lipid hybridization connection common to both the cell-surface and cell-cell tethering schemes.

Because we are concerned with nucleic acid-based materials, we have at our disposal a unique set of tools largely developed for molecular biology and genetics. Employing a heterotypic single-stranded DNA (ssDNA) coupling method, we use endonucleases to cleave double stranded DNA (dsDNA) membrane tethers that connect cells to patterned 2D surfaces or to other cells in 3D aggregates. We utilize both nonspecific nuclease to indiscriminately cleave DNA tethers, and we demonstrate that selective excision of particular cell groups can be achieved using a sequence-specific restriction endonuclease. We expect this method to add an additional level of control to experiments involving heterotypic cell-cell assemblies or specific surface capture by permitting subsequent release or recovery of tethered cells.

5.2 Materials and Methods

5.2.1 Chemicals and reagents

α-N-hydroxysuccinimidyl-ω-maleimidyl poly(ethylene glycol) (NHS-PEG-Mal, MW:5000) and 1, 2-Dipalmitoyl-sn-glycerol-3-phosphatidylethanolamine (DPPE) were purchased from NOF Corporation (Tokyo, Japan). 2-Amino-2-hydroxymethyl-propane-1,3-diol (Tris-HCl), Sodium chloride, and Dithiothreitol (DTT) were purchased from Wako Pure Chemical (Osaka, JP). N-ϵ-Maleimidocaproyl-oxysulfosuccinimide ester (sulfo-EMCS) was purchased from Pierce, Thermo Fisher Scientific (Rockford, IL, USA). Triton X-100 (TX100), dichloromethane, chloroform, diethyl ether, triethylamine (TEA), mixed penicillin-streptomycin solution , propanol and ethanol (99.5%) were purchased from Nacalai Tesque (Osaka, JP). RPMI 1640 medium, fetal bovine serum (FBS), Hank's balanced salt solution (HBSS), CellTracker Orange CMTMR (5-(and-6)-(((4-chloromethyl)benzoyl)

[9] Shin et al., "Photolabile micropatterned surfaces for cell capture and release".

[10] Zhu, Yan, and Revzin, "Catch and release cell sorting: Electrochemical desorption of T-cells from antibody-modified microelectrodes".

[11] Myriam Hemberger, Wendy Dean, and Wolf Reik. "Epigenetic dynamics of stem cells and cell lineage commitment: digging Waddington's canal". In: *Nature reviews Molecular cell biology* 10.8 (2009), pp. 526–537.

amino)tetramethylrhodamine), CellTracker Green CMFDA (5-chloromethylfluorescein diacetate), and YOYO-1 Iodide (491509), and SYBR Green I Nucleic Acid Stain were purchased from Invitrogen (Carlsbad, CA, USA). Propidium iodide staining solution was purchased from BD Pharmagen (San Jose, CA, USA). Phosphate buffered saline (PBS) was purchased from Nissui Pharmaceutical Co. (Tokyo, JP). (3-Aminopropyl)triethoxysilane (APTES) was purchased from Shin Etsu Chemical Co. (Tokyo, JP). 10x RQ1 nuclease buffer solution was purchased from Promega (Fitchburg, WI, USA). Benzonase nuclease (25,000 U/mL) was purchased from Millipore (Billerica, MA, USA). BamHI-HF (100,000 U/mL), EcoRI-HF (100,000 U/mL) where one unit is defined as the amount of enzyme required to digest 1 μg of λ DNA in 1 hr at 37°C in a total reaction volume of 50 μL according to manufacturer specifications, and 10x NEBuffer 4 (B4) were purchased from New England Biolabs (Ipswitch, MA, USA). ssDNA was purchased from Greiner Bio-One Japan (Tokyo, JP).

5.2.2 Acquisition of DNA Melting Curves

Melting curve data was gathered with a StepOne Real Time PCR System (Applied Biosystems, Foster City, CA, USA). 1x SYBR Green I dye was used as the dsDNA reporter with 15 μL well volumes and 20 $\mu g/mL$ dsDNA concentration for each sequence. dsDNA was prepared by mixing protected disulfide-terminated ssDNA of complementary sequences in an equimolar amount. Normalized reporter values were obtained by first melting dsDNA at 95°C for 2 *min* followed by ramping temperature from 20°C to 95°C in 0.5°C increments (30 *sec* each) to gather fluorescence intensity as a function of temperature. Melting curve data was normalized [0,1] for comparison between sequences and enzyme treatments. The graph of the negative first derivative was obtained from normalized reporter values and smoothed by a moving average with a range of 4 data points.

5.2.3 Synthesis of DNA-PEG-lipids

(See Appendix Fig. A.13) rotected 5' disulfide-terminated ssDNA (ssDNA-SS) was reduced by reaction with dithiothreitol according to manufacturer's instructions to yield 5' thiol-terminated ssDNA (ssDNA-SH). Deprotected ssDNA was purified with an Illustra NAP-10 Sephadex Column, G-25 DNA grade (GE Healthcare, Buckinghamshire, UK) and again by centrifugal filtration 15000 x g, 3000 molecular weight cutoff (Amicon Ultra 0.5 ml Ultracell 3K, Millipore, Billerica, MA, USA). Enzyme cleavable and control sequences used in this study are summarized in Table 5.1. Maleimide-PEG-NHS was

used to crosslink ssDNA-SH with DPPE phospholipid as previously reported[12] yielding maleimide-PEG-lipid. Maleimide-peg-lipid was then reacted with ssDNA-SH in a 1:1 molar ratio for 12 hr RT yielding ssDNA-PEG-lipid. Solutions were adjusted to 200 $\mu g/mL$ in PBS and stored for up to one week at 4°C. ssDNA-PEG-lipids were used without further purification.

5.2.4 Cell surface Modification with ssDNA-PEG-lipid

CCRF-CEM cells were cultured in RPMI supplemented with 10% FBS and 1% penicillin/streptomycin solution (RPMI10). Cells were modified with ssDNA tethers according to the protocol described previously[13]. Briefly, CCRF-CEM cells were harvested from suspension culture and rinsed with HBSS and pelleted. In experiments requiring fluorescent identification of cell groups, pelleted cells were resuspended in either PKH67 for green labeling or PKH29 for red labeling (0.4% v/v PKH in Diluent C) and allowed to react for 3 min before quenching with RPMI10, and cells were subsequently rinsed with RPMI10 followed by centrifugation three times before proceeding. Approximately 10^7 cells were exposed to ssDNA-PEG-lipid solution (50 μL, 200 $\mu g/mL$) for 1 hr at RT with agitation every 15 min. ssDNA-PEG-lipid modified cells were rinsed thrice with RPMI10. Cells were resuspended at a concentration of 10^5 $cells/mL$ in RPMI10 prior to proceeding to patterned substrate exposure or aggregation with other modified cells.

5.2.5 Enzyme Treatment of Suspended Single Cells

For experiments involving single celled analysis of enzyme treatment, ssDNA-modifed cells suspended in RPMI10 were exposed to complementary ssDNA (protected disulfide terminated ssDNA) for > 1 min to induce hybridization. The nucleotide-intercalating and cell-impermeable fluorophore YOYO-1 was added (1000 times diluted from stock) to identify DNA modification. Confocal laser scanning microscopy was used to image cells before and after enzyme treatment (excitation 491 nm, emission 509 nm). BamHI solutions were prepared with 10,000 U/mL (10 times dilution of stock solution) with 1x B4 supplemented with NaCl (4.5 mg/mL) to maintain isotonicity without disrupting enzyme activity with a high concentration of monovalent cations. Benzonase solutions were prepared with 2500 U/mL (10 times dilution of stock solution) in 1x RQ1 DNase buffer supplemented with 4.5 mg/mL NaCl. dsDNA-bearing cells were pelleted and

[12] Teramura, Kaneda, and Iwata, "Islet-encapsulation in ultra-thin layer-by-layer membranes of poly (vinyl alcohol) anchored to poly (ethylene glycol)–lipids in the cell membrane".

[13] Teramura, Kaneda, and Iwata, "Islet-encapsulation in ultra-thin layer-by-layer membranes of poly (vinyl alcohol) anchored to poly (ethylene glycol)–lipids in the cell membrane".

rinsed once with HBSS before resuspending them in enzyme solution. BamHI reactions were carried out at 37°C for 10 *min* and Benzonase reactions at RT for 10 *min*. Reactions were quenched with RPMI10, pelleted, rinsed in RPMI10, pelleted, and finally resuspended in RPMI10 to be imaged with confocal microscopy. Confocal images of YOYO-1 fluorescence were analyzed by acquiring 1D intensity profiles in ImageJ. Statistical YOYO-1 fluorescence of treated and untreated cells was analyzed with flow cytometry (5000 cells, Guava Easy Cyte Mini, Millipore, Billerica, MA, USA). Flow cytometry data was analyzed with FlowJo software.

5.2.6 Grafting of ssDNA to glass surfaces

ssDNA sequences complementary to cell membrane ssDNA inserts were patterned on glass substrates as previously described[14]. Briefly, glass coverslips (22 *mm* x 26 *mm*, Matsunami, Osaka, JP) were oxidized by immersion in piranha solution (7:3 concentrated sulfuric acid : hydrogen peroxide) for 10 *min* followed by copious rinsing with deionized water. Coverslips were mounted on racks and rinsed twice with isopropanol and blow dried with compressed nitrogen gas. Coverslips were then immersed in 5% APTES in a 1:9 double distilled water : ethanol solution at 25°C for 30 *min* while shaking followed by rinsing thrice with 99% ethanol, thrice with deionized water, and blow drying with compressed nitrogen gas. APTES condensation was completed by heating at 80°C under vacuum for 3 *hr*. Amine functionalized glass coverslips were then transferred to aqueous sulfo-EMCS solution (500 $\mu g/mL$) for 20 *min* at 37°C while shaking. Substrates were rinsed with deionized water and blow-dried with compressed nitrogen gas. The resultant maleimide-modified glass substrates were then exposed to ssDNA-SH to graft ssDNA to the surface either by spotting or printing with a 7 *mm* x 7 *mm* latex rubber stamp (Tamaruinbo Shinkyogokuten, Kyoto, JP) followed by incubation at RT for 60 *min* in saturated atmosphere to prevent drying and premature inhibition of the reaction. Reacted substrates were then rinsed with deionized water and stored in a desiccator for up to 3 days.

5.2.7 Construction of flow cells and cell patterning of glass substrates

For stamp patterns, large flow cells were constructed by placing 22 *mm* x 4 *mm* x 0.5 *mm* silicone spacers (AsOne Corporation, Osaka, JP) on opposite sides of ssDNA-modified glass substrates forming a wide lane enclosing the pattern in between. A second coverglass 22 *mm* x 26 *mm* was placed on top bridging the spacers to form a 22 *mm* x

[14]Sakurai, Teramura, and Iwata, "Cells immobilized on patterns printed in DNA by an inkjet printer"; Sakurai, Hoffecker, and Iwata, "Long term culture of cells patterned on glass via membrane-tethered oligonucleotides".

18 mm chamber. Spotted substrates for quantitative measurement requiring controlled flow rate were made into flow cells by placing them under a rectangular silicone spacer 0.5 mm thick with an enclosed rectangular area cut away from the flow chamber (5 mm x 1 mm x 0.5 mm). On top of the spacer, an acrylic 10 mm x 25 mm x 2 mm block containing inlet and outlet holes spaced 5 mm apart and 1 mm in diameter each connected to silicone tubing 500 μm I.D. To prevent nonspecific cell attachment, 1% BSA solution was pipetted into both types of flow cells. ssDNA-cells suspended in serum-free RPMI were flowed into the chamber and allowed to settle and hybridize for 2 min. Flow cells were flushed with serum-free RPMI to remove unattached cells before proceeding to enzyme addition.

5.2.8 Detachment of patterned cells from substrates by endonuclease treatment

Cell patterned demo substrates were treated with enzyme solution by first rinsing the flow cell with the corresponding NaCl-supplemented enzyme buffer (RQ1 for Benzonase or NEBuffer 4 for BamHI and EcoRI). Benzonase stock solution was diluted to 2500 U/mL concentration in NaCl-supplmented RQ1 DNase buffer. BamHI stock solution was diluted to 10,000 U/mL in NaCl-supplemented NEBuffer 4. EcoRI stock solution, which contained Triton X-100, was first purified by centrifuge filtration (10,000 MWCO, 5,000 x g, 15 min x 3 repetitions). Solutions were prepared at 30,000 U/mL in NaCl-supplemented B4 In order to retain enzyme activity, Triton X-100 (TX100) was added back to formulated solutions at a reduced concentration of 0.115 mM conducive to cell maintenance and survival[15]. Buffer loaded in flow cells was then displaced by injecting enzyme solutions followed by incubation at 37°C for BamHI and EcoRI and RT for Benzonase. Demo substrates were flushed gently with 1 mL serum-free RPMI following incubation and imaged with confocal microscopy wide area scan. Spotted substrates were injected with 1 mL serum-free RPMI with a syringe pump (PHD2000, Harvard Apparatus, Kent, UK) at a flow rate of 50 $\mu L/sec$. Movies acquired during this process were taken with the Olympus IX73 firmware and Rylstim Screen Capture software (Sketchman Studios) at 30 fps.

[15]Dipankar Koley and Allen J Bard. "Triton X-100 concentration effects on membrane permeability of a single HeLa cell by scanning electrochemical microscopy (SECM)". in: *Proceedings of the National Academy of Sciences* 107.39 (2010), pp. 16783–16787.

5.2.9 Formation of cellular aggregates and dispersal with endonuclease

Cell aggregates were formed by modifying a group of cells with a given ssDNA sequence followed by exposing those cells to a separate group of cells modified with the complementary sequence. Cells were modified with ssDNA-PEG-lipid and resuspended in RPMI10 at a concentration of 10^5 $cells/mL$ as described earlier. Suspensions of complementary sequence-bearing cells were then pipetted into a single tube. Rapid aggregation limited by the rate of cell-cell collisions in suspension occurs in under 5 min and can be accelerated by briefly centrifuging the tubes to induce greater cell-cell contact. In order to visualize DNA content on cell surfaces, the membrane-impermeable ssDNA/dsDNA fluorescent label YOYO-1 was added to mixtures (1000 times diluted from stock) and allowed to complex with DNA at RT for 5 min. Clumps of aggregated cells were transferred by pipette to respective enzyme buffer solutions and then to enzyme containing solutions. Aggregates were visualized by pipetting 20 μL of solution containing cell aggregates onto glass bottom dishes and viewing them with confocal microscopy.

5.2.10 Cell viability

Viability was evaluated with propidium iodide (PI) and flow cytometry first by sampling from a suspension of ssDNA-modified cells in enzyme solutions (2,500 U/mL Benzonase in NaCl-supplemented RQ1, 10,000 U/mL BamHI in NaCl-supplemented B4, and 30,000 U/mL EcoRI in NaCl-supplemented B4 with 0.115 mM TX100). dsDNA-modified cells were not used to prevent a false positive by PI. 5000 cell samples were collected every 10 min from enzyme cell suspensions for a 40 min interval. Cells recovered from 10 min substrate treatment with the same formulations listed above were analyzed by suspending recovered cells in RPMI10 supplemented with PI and analyzing by flow cytometry (5000 cells).

5.2.11 Microscopy

Phase contrast, epifluorescence images, and movies were acquired via an Olympus IX73 epiflourescence microscope with a 10 x 0.30 NA objective and 20 x 0.45 NA objective. Confocal sections and wide area images were acquired with an Olympus Fluoview FVR10i scanning confocal microscope with a 60 x 1.35 NA objective.

TABLE 5.1: List of ssDNA sequences used in this study.

ssDNA Sequences		
Label	5'	3'
SeqA(BamHI)	HS-TGC GGA GGA TCC TTT CAC ACA	
SeqA'(BamHI)	HS-TGT GTG AAA GGA TCC TCC GCA	
SeqB(EcoRI)	HS-TAG TAT GAA TTC TTT CCG TGT	
SeqB'(EcoRI)	HS-ACA CGG AAA GAA TTC ATA CTA	
Oligo-dT_{20}	HS-TTT TTT TTT TTT TTT TTT TT	
Oligo-dA_{20}	HS-AAA AAA AAA AAA AAA AAA AA	

5.2.12 Statistics

Melt curve data were gathered in triplicate (3 wells prepared separately and analyzed simultaneously), and average T_m values and standard error of the mean ($S.E.M.$) were calculated. Derivative melt curve data was smoothed using a 4 point moving average of fine-grained $\frac{dF}{dT}$ data. Spot concentration curves were prepared by running experiments in triplicate (3 different substrates). Statistics on flow cytometry data including median YOYO-1 fluorescence and PI-positive percentages were computed with FlowJo software. Average dead cell percentages for cells recovered from substrate enzyme treatment were computed from triplicate experiments (3 different substrates), and dead cell percentages for suspension treatments were also performed in triplicate with error bars indicating standard deviation.

5.3 Results

We used ssDNA-PEG-lipid conjugates to modify cell membranes with sequence-specific affinity. By hybridizing ssDNA-modifications present on cell membranes with complementary freely suspended ssDNA, ssDNA grafted to 2D glass substrates, or ssDNA present on other modified cells we induced the formation of specific linkages to the cell membrane. Through exposure to endonucleases, both sequence-specific restriction enzymes BamHI and EcoRI as well as the nonspecific nuclease Benzonase, we show that the DNA linkages on cell membranes can be severed along with the subsequent cell linkage.

In order to utilize enzymes in the presence of living cells, NaCl was added to enzyme buffer solutions to prevent the deleterious effects on cells caused by hypotonicity. We expected that the presence of monovalent cations might reduce enzyme activity, so to verify that enzymes in this study retain their effectiveness under unique buffer conditions, we acquired the melting curves of dsDNA for each sequence without and after enzyme

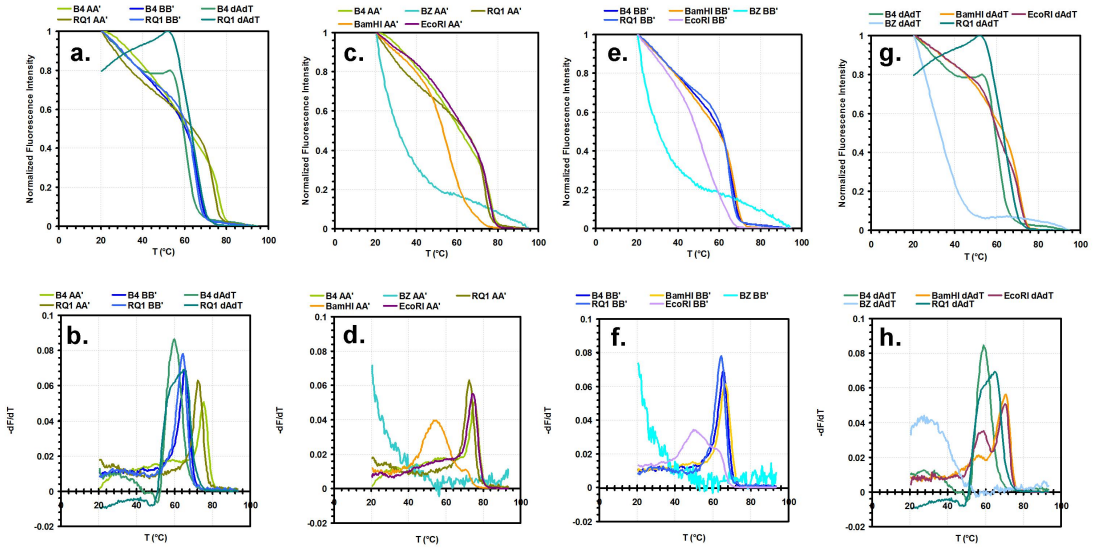

FIGURE 5.1: Melting curve analysis of the sequence pairs without and after enzyme reactions. Each curve's color corresponds to a particular combination of sequence pair (Sequence A and A':AA', sequence B and B':BB', oligo-dA_{20}/oligo-dT_{20}:dAdT) and enzyme (EcoRI, BamHI, Benzonase:BZ) or enzyme buffer (NEBuffer 4:B4, RQ1 DNAse buffer:RQ1). (a) Normalized reporter curves of sequences in NaCl-supplemented buffers without any enzyme treatment. (b) Derivative of normalized fluorescence with respect to time for sequences in NaCl-supplemented buffers. (c) Comparison of sequence AA' containing the BamHI-recognition sequence under each enzyme treatment condition. (d) Comparison of derivatives of normalized fluorescence with respect to time for sequence AA' under each treatment condition. (e) Comparison of sequence BB' containing the BamHI-recognition sequence under each enzyme treatment condition. (f) Comparison of derivatives of normalized fluorescence with respect to time for sequence BB' under each treatment condition. (g) Comparison of oligo-dA_{20}/oligo-dT_{20} containing the BamHI-recognition sequence under each enzyme treatment condition. (h) Comparison of derivatives of normalized fluorescence with respect to time for sequence oligo-dA_{20}/oligo-dT_{20} under each treatment condition. n=3 runs for each condition.

treatment (Fig. 5.1) to obtain average melting points (T_m) summarized in Table 5.2. Normalized reporter curves (Fig. 5.1a, c, e, & g) and computed derivative curves (Fig. 5.1b, d, f, & h) for sequence A hybridized to sequence A', sequence B to sequence B', and oligo-dA_{20} to oligo-dT_{20} in NaCl-containing buffer solutions NEBuffer 4 (B4) and RQ1 DNase buffer (RQ1) (Fig. 5.1a & b) indicate that T_m values for untreated sequences are all between 60°C and 80°C. A comparison of the sequence A/sequence A' pair (AA')(Fig. 5.1c & d), shows that 10 *min* treatment with EcoRI at 37°C resulted in a derivative maximum corresponding to a T_m of 75.21°C ± 0.00 *S.E.M.*, a negligible change compared to control conditions (eg. $T_m = 76.20$°C ± 0.00 *S.E.M.* in B4) whereas 10 *min* treatment with BamHI at 37°C resulted in a decreased T_m of 55.70°C ± 0.08 *S.E.M.* reflecting that of the halved products, and treatment with Benzonase resulted in an even further decreased $T_m = 22.66$°C ± 0.14. *S.E.M.* Conversely, a comparison of the sequence B/sequence B' pair (BB')(Fig. 5.1e & f) shows a negligible change from B4

TABLE 5.2: Average DNA melting points (T_m) and standard error of the mean for each sequence pair and enzyme/enzyme buffer treatment condition: n=3.

Condition	Average T_m	SEM
B4 AA'	76.20	0.00
RQ1 AA'	73.13	0.17
BamHI AA'	55.70	0.08
EcoRI AA'	75.21	0.00
BZ AA'	22.66	0.14
B4 BB'	66.41	0.08
RQ1 BB'	65.00	0.00
BamHI BB'	67.40	0.08
EcoRI BB'	51.47	0.08
BZ BB'	22.50	0.17
B4 dAdT	60.35	0.22
RQ1 dAdT	63.59	0.88
BamHI dAdT	70.97	0.14
EcoRI dAdT	70.72	0.00
BZ dAdT	29.05	0.65

(T_m=66.41°C ± 0.08 *S.E.M.*) to post BamHI-treated (T_m=67.40°C ± 0.08 *S.E.M.*), while post EcoRI-treated was significantly lower (T_m=51.47°C ± 0.08 *S.E.M.*), and post Benzonase treated even more so (T_m=22.50°C ± 0.17 *S.E.M.*). These results indicate that enzyme activity is retained in solutions containing NaCl. Sequences of oligo-dA_{20} hybridized to oligo-dT_{20} (dAdT) (Fig. 5.1g & h) which does not contain an enzyme recognition sequence for either BamHI or EcoRI, did not exhibit reduced T_m for either restriction enzyme (T_m=60.35°C ± 0.22 *S.E.M.* in B4; T_m=70.97°C ± 0.14 *S.E.M.* after BamHI; T_m=70.72°C ± 0.00 *S.E.M.* after EcoRI) and had the expected reduced T_m resulting from Benzonase treatment (T_m=29.05°C ± 0.65 *S.E.M.*). The derivative melting curve (Fig. 5.1h) identifies a multimodal distribution in the range of 60°C to 80°C, for dAdT in B4 and RQ1 exhibits irregularity compared to AA' and BB' possibly as a result of higher order structures or aggregation that are inherently possible for poly(base) sequences.

We probed the effect of nucleases on DNA bound to membranes of freely suspended cells modified with ssDNA-PEG-lipid (Fig. 5.2a) and hybridized to unbound complementary ssDNA (disulfide protected). Fig. 5.2b schematically shows how BamHI and Benzonase can be used to sever dsDNA bound to the cell membrane. After modifying cells with ssDNA-PEG-lipid and subsequently exposing them to unbound ssDNA-SS, we used the cell impermeable DNA intercalating fluorophore YOYO-1 to visualize the DNA itself. The dye binds both ssDNA and dsDNA, though the latter is associated with greater emission intensity. Confocal images of dsDNA-bearing cells labeled with YOYO-1 in NaCl-supplemented buffers prior to enzyme exposure are shown in Fig. 5.2c, i, & o

TABLE 5.3: Summary of flow cytometry measurements of YOYO-1 fluorescence for dsDNA-bearing cells treated with nucleases.

Conditions	Median YOYO-1 Fluorescence	Healthy YOYO-1 (%age) Positive Pop
AA' Cells Before BamHI Treatment	8.82	86.8
AA' Cells After BamHI Treatment	3.01	0.72
BB' Cells Before BamHI Treatment	14.50	89.64
BB' Cells After BamHI Treatment	8.62	80.36
AA' Cells Before Benzonase Treatment	21.20	77.34
AA' Cells After Benzonase Treatment	4.14	20.24

and at 360x magnification in Fig. 5.2e, k, & q. AA'-bearing cells exposed to BamHI (10,000 U/mL, 10 min, 37°C) (Fig. 5.2d & f) showed near-complete extinction in detectable fluorescence whereas BB'-bearing cells were relatively unaffected by identical conditions (Fig. 5.2j & l). Near-complete extinction of detectable YOYO-1 fluorescence was observed for AA'-bearing cells exposed to Benzonase (2,500 U/ml, 10 min, RT) (Fig. 5.2p & r). Line profiles taken from the high magnification confocal cross sections (Fig. 5.2e, f, k, l, q, & r) are shown in Fig. 5.2g, h, m, n, s, & t respectively and show quantitatively the absence of peak YOYO-1 fluorescence at cell peripheries after BamHI and Benzonase treatment contrasted with prior to treatment as well as BB'-bearing cells both before and after treatment.

We also examined YOYO-1-labeled cell suspensions before and after enzyme treatment by flow cytometry. A majority population of YOYO-1-positive cells were present in AA' samples before BamHI or Benzonase treatment (Fig. 5.2u-w, black curve). BB' samples contained a majority population of YOYO-1-positive cells both before and after BamHI treatment (Fig. 5.2v), and AA' samples under these conditions exhibited a clear absence of detectable YOYO-1-positive cells (Fig. 5.2u, blue curve). AA' cells treated with Benzonase exhibited a significant drop in detected YOYO-1 fluorescence (Fig. 5.2w)). Median YOYO-1 fluorescence statistics and the percentages of YOYO-1 positive cells (gated by nominal side-scatter/forward-scatter distribution for healthy population) are summarized for different conditions in Table 5.3.

We tethered ssDNA-modifed cells to 2D substrates with grafted complementary ssDNA (Fig. 5.3a) in order to determine whether enzyme cleavage could sever physical linkages in practice. To demonstrate the selectivity of restriction enzyme removal of cells patterned on glass with DNA-tethers, we fabricated patterns of DNA on glass such that control patches of sequence B, BamHI-cleavable patches of sequence A, were on a single substrate (illustrated schematically in Fig. 5.3b). Subsequent treatment with sequence specific restriction enzymes (Fig. 5.3c) or nonspecific nuclease (Fig. 5.3d) would demonstrate whether selective and nonselective removal of tethered cells could be achieved. We

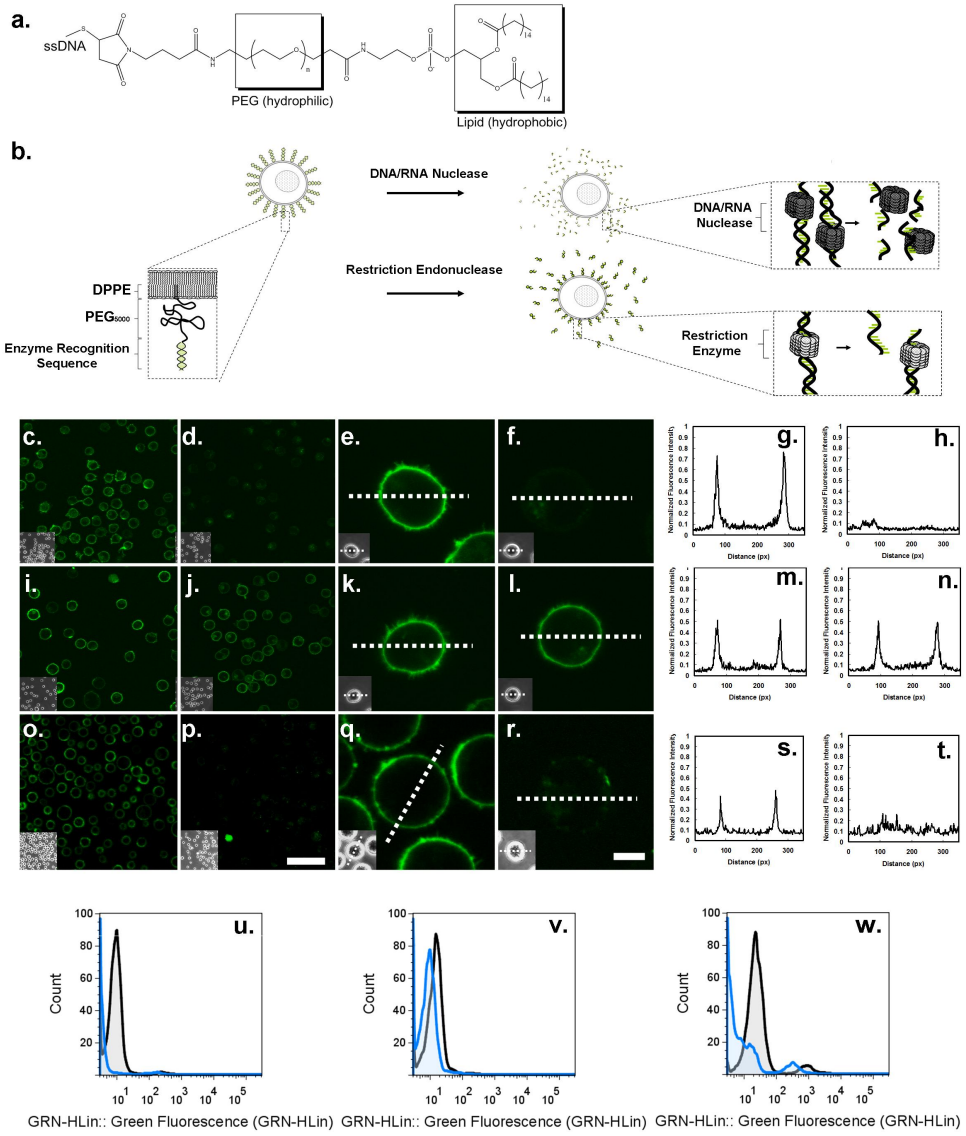

FIGURE 5.2: Enzyme cleavage of DNA bound to freely suspended cells. (a) Molecular structure of ssDNA-PEG-lipid used to modify cell membranes. (b) Schematic of enzyme treatment. dsDNA bound to the cell surface is cleaved by either sequence-specific restriction endonuclease or nonspecific nuclease. (c, e) YOYO-1-labeled AA'-bearing cells prior to BamHI treatment. (d, f) AA'-cells after BamHI treatment. (g, h) YOYO-1 fluorescence line profiles from the AA'-cells shown in e and f respectively. (i, k) YOYO-1-labeled BB'-bearing cells prior to BamHI treatment (j, l) BB'-cells after BamHI treatment. (m, n) YOYO-1 fluorescence line profiles from the BB'-cells shown in k and l respectively. (o, q) YOYO-1-labeled AA'-bearing cells prior to Benzonase treatment (p, r) AA'-cells after Benzonase treatment. (s, t) YOYO-1 fluorescence line profiles from the AA'-cells shown in q and r respectively. Scale bars: 30 μm and 5 μm respectively. (u) Flow cytometry measurement of YOYO-1 fluorescence on AA'-cells prior to (black) and after (blue) BamHI treatment. (v) Flow cytometry measurement of YOYO-1 fluorescence on BB'-cells prior to (black) and after (blue) BamHI treatment. (w) Flow cytometry measurement of YOYO-1 fluorescence on AA' cells prior to (black) and after (blue) Benzonase treatment.

constructed a flow chamber out of ssDNA-patterned substrates and injected a 1:1 mixed suspension of sequence B'-modified cells and sequence A'-modified cells. To distinguish sequence A'-cells from sequence B'-cells, we labeled the cell groups respectively with cell tracker green and cell tracker orange. After rinsing the flow chamber, we could obtain a clear cell-on-glass pattern with separate BB'-cell patches (red), AA'-cell patches (green), and mixed patches (red and green) (Fig. 5.4a & d). High sequence specificity could be observed by noting the separation of green cells (Fig. 5.4g) from red cells (Fig. 5.4m) on AA' and BB' patches respectively, as well as the equal proportions of red and green cells in mixed patches (Fig. 5.4j).

We then treated the cell patterns with BamHI (10,000 U/mL, 10 min, 37°C) followed by gently flushing the cell with 1 mL serum-free RPMI, yielding patterns (Fig. 5.4b & e) that had qualitatively fewer AA' cells in both the exclusive AA'-cell patch (Fig. 5.4h) and the mixed patch (Fig. 5.4k) while BB' patches remained constant in cell density (Fig. 5.4n) demonstrating that sequence-specific removal of patterned cells can be accomplished with this method.

BamHI treatment was followed with Benzonase (2,500 U/mL, 10 min, 37°C) to release remaining patterned cells (Fig. 5.4c & f). followed by 1 mL gentle flushing with serum-free RPMI, yielding substrates where the remaining BB' cell patches (Fig. 5.4o), AA'-cell patches (Fig. 5.4i), and mixed patches (Fig. 5.4l) were mostly devoid of cells. We similarly treated substrates patterned with oligo-dT_{20}, sequence B, and mixed patches and complementary oligo-dA_{20} and sequence B'-modified cells with EcoRI solution (30,000 U/mL purged of TX100 and readjusted to 0.115 mM, 10 min, 37°C, x3 rounds of incubation and flushing) and afterwards Benzonase solution (2,500 U/mL, 10 min, 37°C) to obtain equivalent results (SFig. A.17). These conditions were less effective than BamHI and thus required consecutive treatments to obtain selective release comparable to that of the BamHI-treated substrate.

The enzyme solutions, though supplemented with NaCl to prevent hypotonicity, may nonetheless stress cells over long durations due to the presence of other factors such as DTT (1 mM in 1x B4) and glycerol present in stock enzyme solution (5% v/v final concentration in 10,000 U/mL BamHI and 2,500 U/mL formulations used in the majority of experiments). Moreover, TX100 added to EcoRI solutions at 0.115 mM to maintain enzyme activity is damaging to cells in higher concentration ranges (0.17-0.2 mM[16]). We examined the viability of cells with PI labeling and flow cytometry for both free suspensions as well as cells recovered from 2D substrates after enzyme treatment and flushing. Fig. 5.5a shows a representative side scatter versus forward scatter plot of

[16]Koley and Bard, "Triton X-100 concentration effects on membrane permeability of a single HeLa cell by scanning electrochemical microscopy (SECM)".

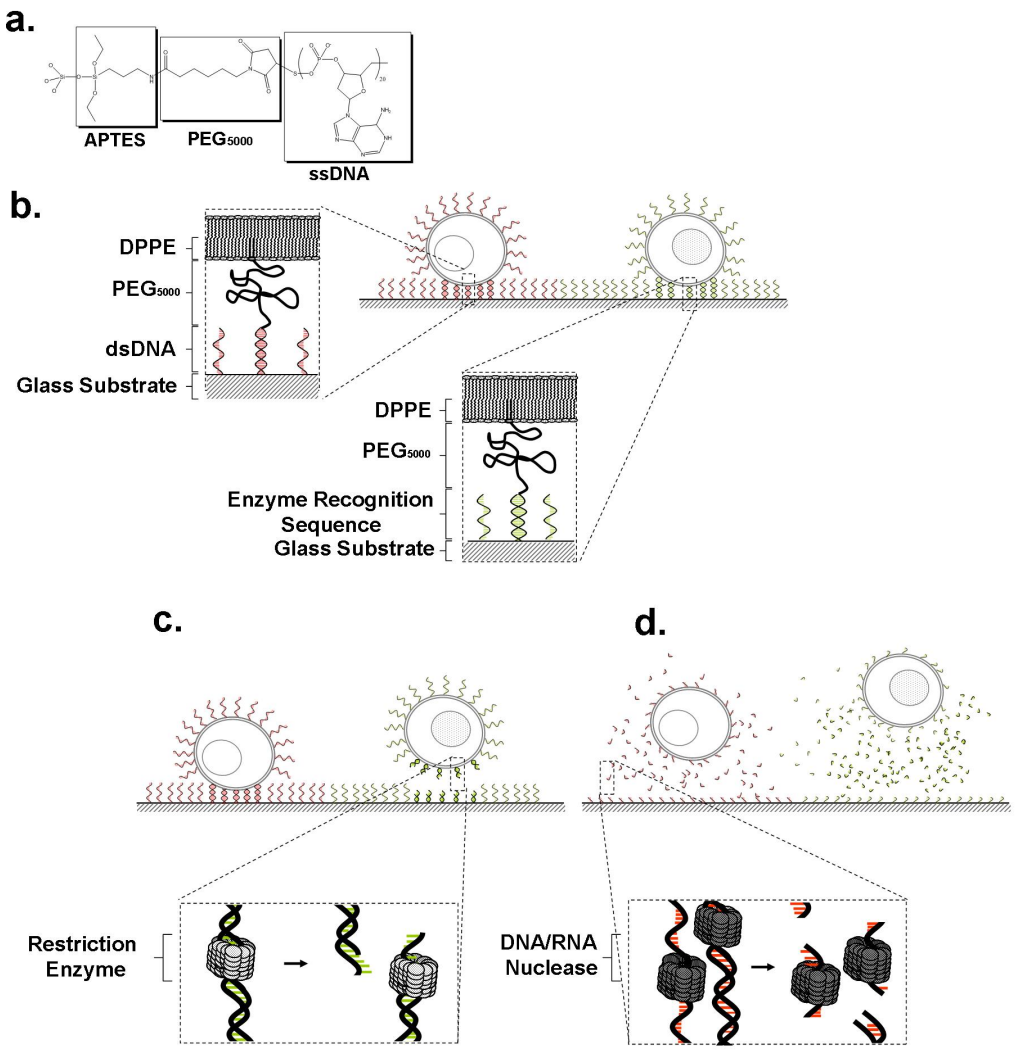

FIGURE 5.3: Schematic of cell surface tethering and release with nucleases. (a) Molecular structure of ssDNA grafted to glass substrate (b) ssDNA-modified cells are tethered to ssDNA-modified surfaces through hybridization of complementary strands (c) Sequence-specific restriction enzymes cleave dsDNA recognition sequences releasing target cells. (d) Nonspecific nucleases indiscriminately digest ssDNA and dsDNA releasing all DNA-tethered cells.

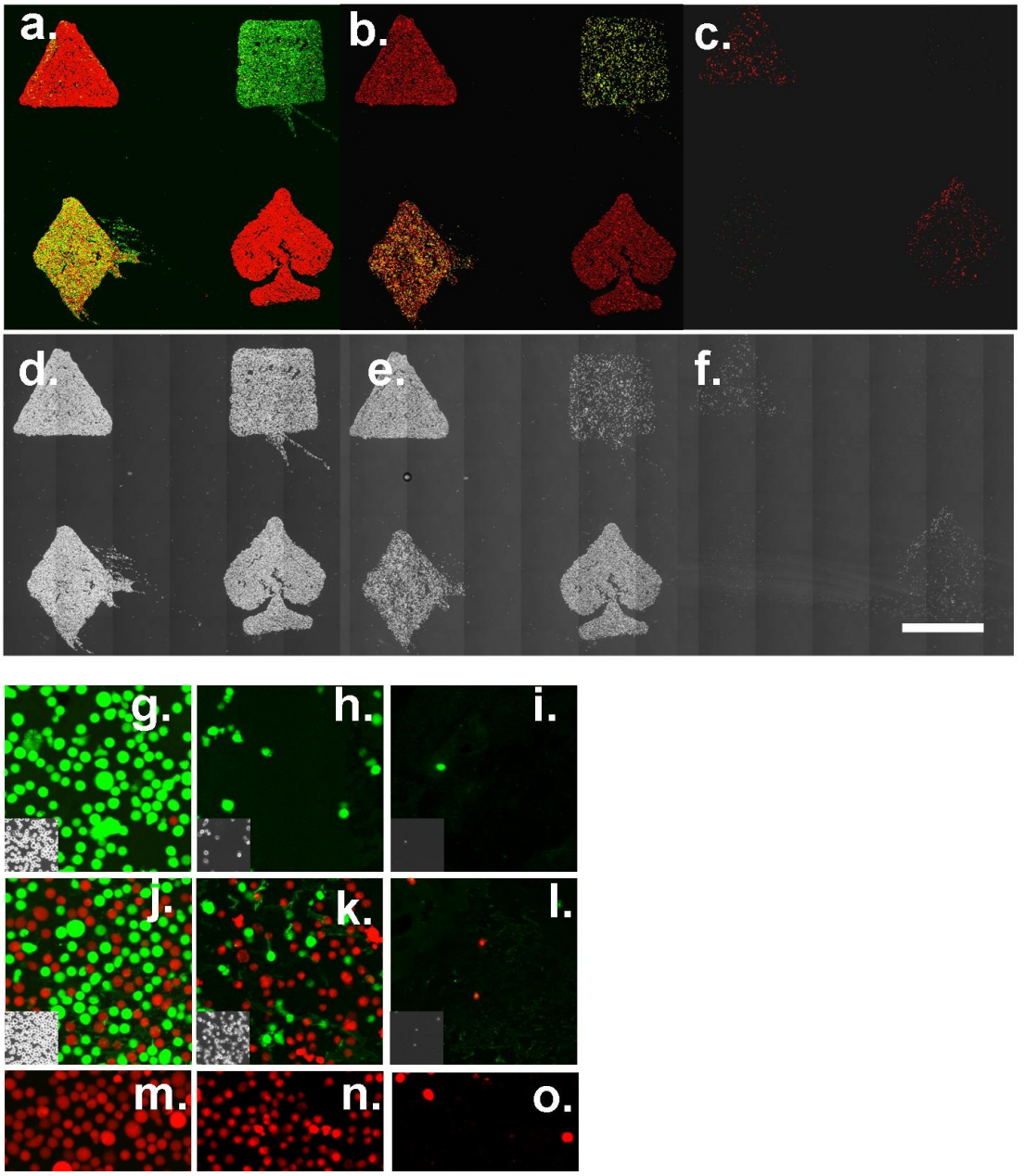

FIGURE 5.4: Sequential treatment of cell patterns with BamHI and Benzonase. (a) Substrate patterned with BB'-cells (red), AA'-cells (green), and mixed patches of BB' and AA'-cells prior to enzyme treatment. (b) Cell-patterned substrate after BamHI exposure and flushing to recover detached cells. (c) Cell-patterned substrate after Benzonase exposure and flushing to recover detached cells. (d-f) Phase contrast images of a-c respectively. Scale bar: 1.5 mm (g-i) High magnification images of AA' patch corresponding to a-c respectively. (j-l) High magnification images of mixed patch corresponding to a-c respectively. (m-o) High magnification images of BB' patch corresponding to a-c respectively. Scale bar: 50 μm

TABLE 5.4: Summary of average PI-positive cell (dead cell) fractions and standard error of the mean values for recovered cells.

Conditions	Mean Percentage of PI Positive Cells	SEM
AA'-tethered Recovered by BamHI	22.31	0.71
BB'-tethered Recovered by EcoRI	35.78	0.67
dAdT-tethered Recovered by Benzonase	15.03	0.52

control cells (modified with ssDNA-PEG-lipid) in serum-free RPMI. Red fluorescence profiles are shown for control cells in serum-free RPMI (Fig. 5.5b), cells in BamHI solution (10,000 U/mL, 37°C) after 40 min incubation (Fig. 5.5c), cells in EcoRI solution (30,000 U/mL purged of TX100 and readjusted to 0.115 mM, 40 min, 37°C) (Fig. 5.5d), and cells in Benzonase solution (2,500 U/mL, RT) after 40 min incubation (Fig. 5.5e). Measurements of the proportion of the dead cells taken in 10 min intervals is shown in Fig. 5.5f. Red fluorescence profiles are shown 2D substrate immobilized AA' cells recovered with BamHI (10,000 U/mL, 10 min, 37°C) in Fig. 5.5g, BB' cells recovered with EcoRI (30,000 U/mL purged of TX100 and readjusted to 0.115 mM, 10 min, 37°C, x3 rounds of incubation and flushing) in Fig. 5.5h, and dAdT cells recovered with Benzonase (2,500 U/mL, 10 min, 37°C) in Fig. 5.5i. The mean proportion of dead cells recovered from 2D substrate experiments are summarized in Table 5.4.

To demonstrate the rapid rate of fluid shear-driven cell recovery after incubation phases, we captured movie data of a mixed BB' and AA' cell spot labeled red and green respectively while undergoing a single flush with serum-free RPMI via syringe pump after BamHI treatment (10,000 U/mL, 10 min, 37°C) (SMovie 1) as well as a movie captured during flushing after Benzonase treatment (2,500 U/mL, 10 min, RT)(SMovie 2). BamHI-treated substrates exhibited rapid detachment and removal of green AA' cells while the majority of red BB' control cells remain in place. Benzonase treated substrates exhibited an indiscriminant loss of both green AA' cells and red BB' cells.

Next we employed nuclease cleavage to disperse cells aggregated via ssDNA-PEG-lipid bonds. We produced aggregated cell clusters by modifying two separate groups of cells: one bearing the ssDNA-PEG-lipids of a particular sequence and the other bearing the corresponding complementary sequence. Mixing the two groups of cells resulted in rapid formation of cell clusters occurring on the order of seconds to minutes. YOYO-1 was again employed to visualize both the ssDNA-modification on cell membranes and the dsDNA contacts formed between aggregating cells. Halos of YOYO-1 fluorescence were visible around ssDNA-modified cells and clear dsDNA mediated contacts between aggregated cells could be identified by confocal microscopy (Fig. 5.6a).

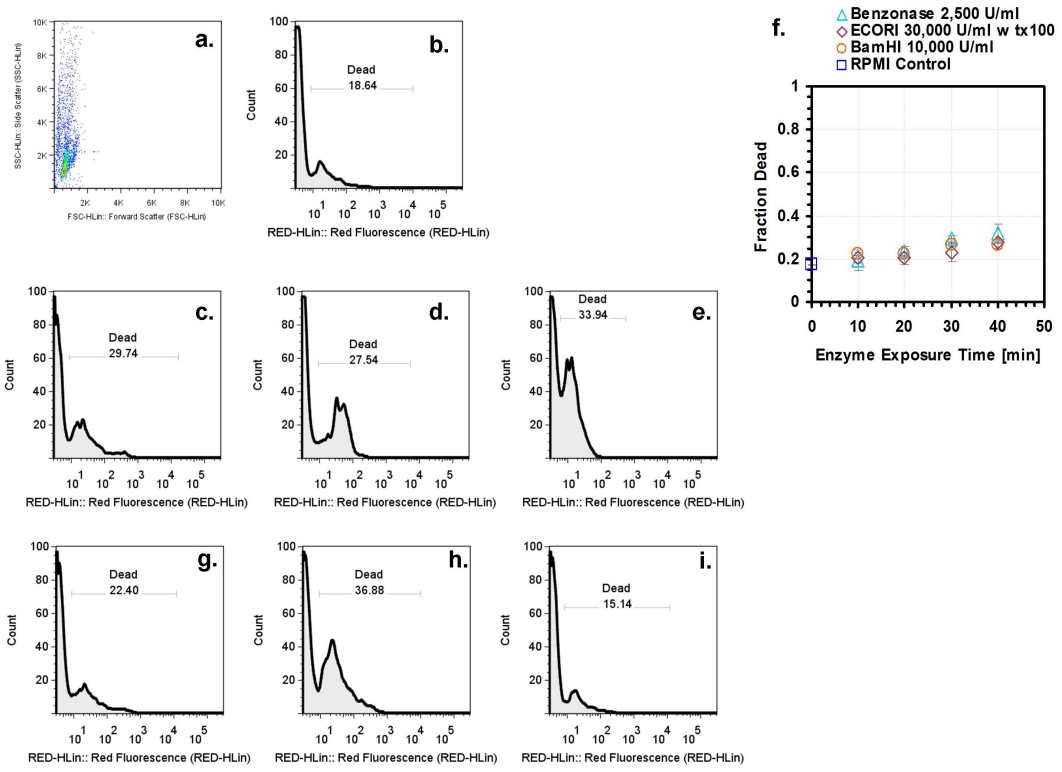

FIGURE 5.5: Viability tests on cells exposed to enzyme treatments. (a) Flow cytometry dot plot of side scatter versus forward scatter. (b) PI fluorescence profile of ssDNA-modified cells in serum-free RPMI. (c) PI profiles of cells suspended in BamHI solution for 40 *min* (d) PI profiles of cells suspended in EcoRI solution for 40 *min*. (e) PI profiles of cells suspended in Benzonase solution for 40 *min*. (f) Plot of dead cell fraction estimated by peak area at each stage of incubation for the various enzymes (g) PI profile of AA'-cells recovered from glass substrates after BamHI treatment. (h) PI profile of BB'-cells recovered from glass substrates after 3 consecutive EcoRI treatments. (i) PI profile of dAdT-cells recovered from glass substrates after Benzonase treatment.

To examine the effectiveness of site-specific restriction endonucleases for digestion of DNA crosslinks holding cellular aggregates together and subsequent dispersal of those clusters into single cells (shown schematically in Fig. 5.6b), we formed aggregates connected by seqA and seqA' ssDNA containing the BamHI cleavage site and labeled cells comprising these aggregates with red PKH-26 dye (AA' aggregates). The contact area between the cells can be identified by boundaries that appear yellow in color, that is overlapping fluorescence of green YOYO-1 and red PKH-26 dye. Control aggregates were formed from seqB/seqB'-cell mixtures (BB' aggregates) and were left unlabeled to distinguish them from AA' aggregates (Fig. 5.6c & f). Aggregates were then immersed in BamHI solution (10,000 U/mL, 10 *min*, 37°C). Red labeled BamHI-specific cells after treatment had significantly attenuated YOYO-1 fluorescence around their periphery (Fig. 5.6d & g) compared to untreated aggregates and those treated with enzyme buffer only (Sfig. A.18). The contact points between cells in enzyme treated populations had

qualitatively reduced YOYO-1, and the little yellow fluorescence observed was discontinuous in confocal sections, apparently aggregated into punctate clusters. In contrast, strong bands of green YOYO-1 fluorescence on cells unlabeled with red PKH-26 could still be observed indicating that dsDNA junctions holding BB'-aggregates together were unaffected by incubation with BamHI.

Independently, we subjected AA' and BB' aggregates to Benzonase (2,500 U/mL, 10 min, RT) and observed near-complete extinction of detectable YOYO-1 fluorescence irrespective of aggregate type (Fig. 5.6e & h). Single cells were numerous compared to before treatment indicating that even in the absence of any external forces or agitation, aggregates were dispersed into single cells. We similarly treated mixtures of dAdT-aggregates and BB'-aggregates with EcoRI (30,000 U/mL purged of TX100 and readjusted to 0.115 mM, 20 min, 37°C) as well as Benzonase treatment (2,500 U/mL, 10 min, RT) and obtained equivalent results (SFig A.18).

5.4 Discussion

ssDNA-PEG-lipid was used to modify cell membranes and engineer artificial physical interactions between single cells and dissolved ssDNA, cells tethered to 2D glass substrates, and cells linked to other ssDNA-modified cells to form 3D aggregates. YOYO-1 was used to clearly identify DNA on cell membranes. It was anticipated that this fluorescence would be mostly extinguished by treatment with Benzonase, which digests both ssDNA and dsDNA into 2-5 base-long parts. Melting curve analysis confirmed this prediction, identifying the melting points of all sequences to be below room temperature. The extinction of fluorescence observed by confocal microscopy and flow cytometry after Benzonase therefore coincided with these expectations.

Nearly identical results were obtained for AA' cells treated with BamHI, a restriction endonuclease which cleaves only at the recognition site on dsDNA. The AA' sequence is 21 bases long, and when cleaved, would theoretically partition into 7 base and 10 base long dsDNA strands with 4 base long ssDNA ends. Based on melting curve measurements of DNA in enzyme buffer conditions containing NaCl, the melting point after BamHI treatment is above 37°C, potentially prohibiting the notion that the cleaved products are below the hybridization limit. A key difference between the melting point measurements and the confocal images and flow cytometry data gathered is the concentration of cations such as Na^+ and Mg^{2+}, which are different in the serum-free RPMI that was used to quench the enzyme reaction. It is possible that while the melting point of cleaved AA' DNA is higher than 37°C under the conditions of the melt curve analysis, in the context of DNA-PEG-lipid inserted into the cell membrane and immersed in RPMI

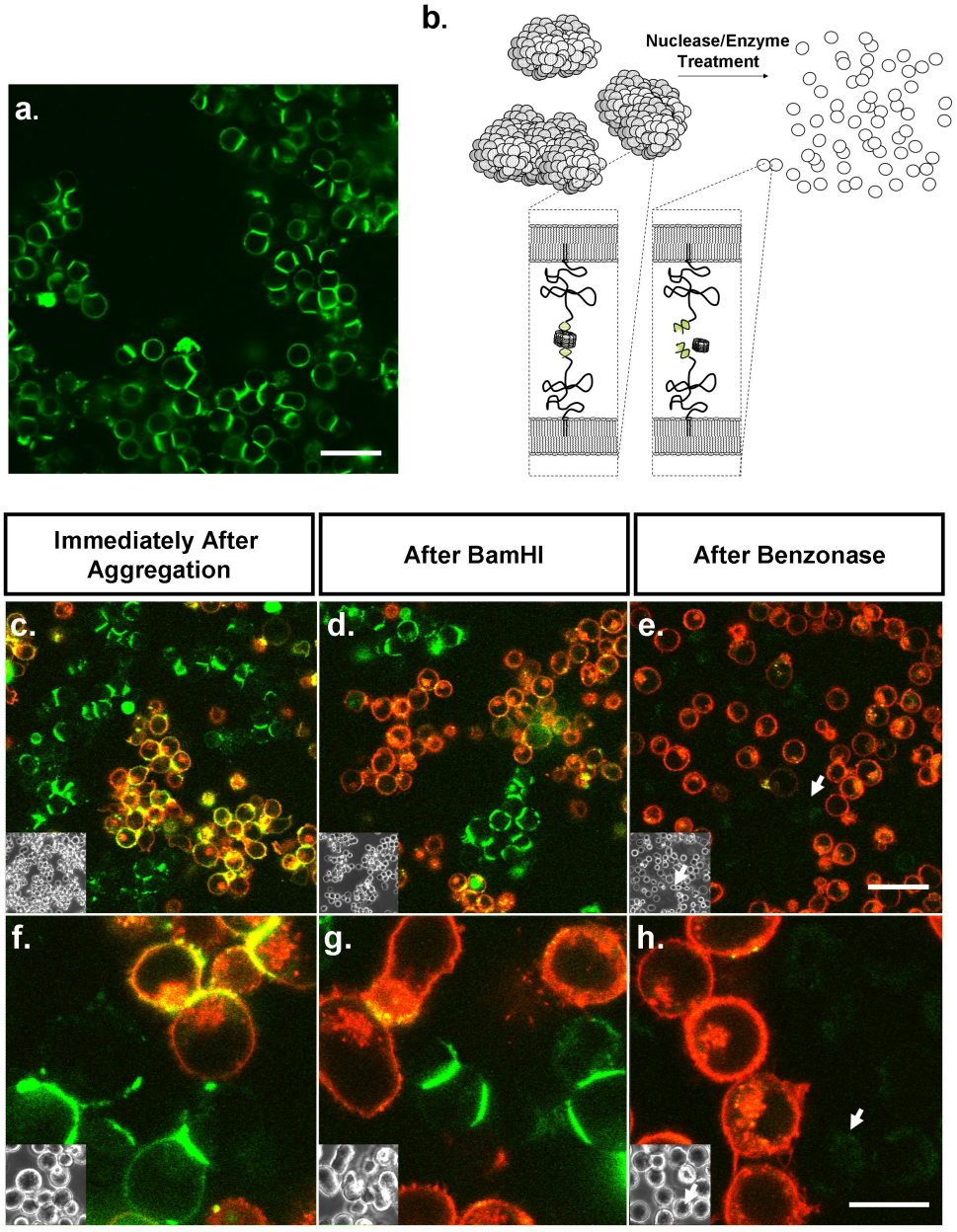

FIGURE 5.6: DNA-mediated cellular aggregates treated with nucleases. (a) Example confocal image of oligo-dA_{20}-modified cells tethered to oligo-dT_{20}-modified cells to form dsDNA contact edges between (YOYO-1-labeled). Scale bar: 25 μm (b) Schematic of aggregate treatment with nucleases. Aggregates are held together by complementary DNA complexes which can be severed by treatment with nucleases. (c, f) Images of juxtaposed AA'-aggregates (membrane-labeled with PKH26 red and DNA-labeled with YOYO-1) and BB' aggregates (YOYO-1-labeled only) prior to enzyme treatment. (d, g) Images of juxtaposed AA'-aggregates (membrane-labeled with PKH26 red and DNA-labeled with YOYO-1) and BB' aggregates (YOYO-1-labeled only) after BamHI treatment. (e, h) Images of juxtaposed AA'-aggregates (membrane-labeled with PKH26 red and DNA-labeled with YOYO-1) and BB' aggregates (YOYO-1-labeled only) after Benzonase treatment. (Insets of c-h are the corresponding phase contrast images) Scale bars: 25 μm and 10 μm respectively. White arrows indicate locations of cells not visible by fluorescence.

medium, either the association of YOYO-1 with remaining fragments or the melting temperature of the remaining fragments are such that YOYO-1 fluorescence is too low to distinguish from background noise. An alternative explanation could be that interaction between the enzyme and labeled DNA is sufficient to cause a sequence specific disruption of YOYO-1 intercalation which persists even after the enzyme is quenched in RPMI medium. Though this point remains unclear, we nevertheless interpret the dependence of post-BamHI YOYO-1 fluorescence on sequence as evidence of specific enzyme activity.

BamHI was used to selectively recover AA' cells immobilized to 2D substrates while leaving BB'-immobilized cells tethered. This was demonstrated to be possible for cells sharing the same substrate as well as immediate proximity as demonstrated by the selective removal of green AA' cells from mixed AA'/BB' patches in Fig. 5.4 and SMovie1. The capability to colocalize different groups of cells using ssDNA-PEG-lipids with the added option of selectively removing one group of cells could prove useful in a variety of applications such as in the induction of stem cell differentiation by exposure to other cells or the activation of immune-reactive cells by local secretion of cytokines or surface contact.

Decoupling adjacent cells from one another is not limited to 2D substrates, and we showed that aggregated groups of cells linked by the complementary ssDNA-PEG-lipid relationship could also be severed with nuclease exposure (Fig. 5.6). As with single celled treatment, the obvious contrast in YOYO-1 fluorescence between juxtaposed BB' and AA' aggregates treated with BamHI supports the notion that specific enzyme activity is responsible for the decreased fluorescence in AA' aggregates, though details of the molecular mechanism leading to this sharp decline are still unclear. It is worth noting here that BamHI-treated AA' aggregates (Fig. 5.6d & g) displayed residual fluorescence due to YOYO-1 at certain cell-cell boundaries, significantly reduced in size of coverage and intensity compared to before treatment, but nonetheless observable in contrast to the near-complete extinction in fluorescence observed with single cell treatment. One possible explanation for this is that fluorescence at the contact surfaces of untreated dsDNA-linked cell pairs is far more intense than the thin halos observed around dsDNA-bearing single cells of Fig. 5.2, a phenomenon worthy of attention in and of itself, and that the amount of DNA to be cleaved by enzyme could be much greater at these concentrated surfaces. Yet another possibility is that the junction between cells is tight enough to prevent the infiltration of enzyme molecules resulting in kinetics limited to the reaction at the extreme perimeter of contact surfaces. Future studies examining the dynamics of enzyme activity for different spatial arrangements may be useful for practical adaptations of the concepts presented here.

In this study, we investigated the action of 3 enzymes on membrane-tethered nucleotides. Of these, BamHI and Benzonase fulfilled their expected roles, BamHI selectively cleaving AA' dsDNA and Benzonase digesting bonds irrespective of sequence. At the concentrations tested, the reaction of EcoRI with the BB' sequence pair was successful in the absence of cells as evidenced by the clear change in melting curves. However, the presence of TX100 in stock solutions in concentrations above the cell viability threshold required that solutions be purged before exposure to cells, and readjusted to concentrations below that threshold. It is possible that the process of ultracentrifugation or the reduction in TX100 led to reduced activity due to denaturation or adsorption of enzyme, and concentration dependence analysis of cell recovery from 2D substrates showed a markedly reduced efficiency of EcoRI acting on BB' than BamHI on AA'. Though less efficient than BamHI in this study, a positive, sequence specific activity was observed in all cases tested for EcoRI, demonstrating that the technique of cleaving DNA tethers with specific restriction enzymes is not limited to a single system. We anticipate therefore, that provided conditions conducive to cell survival and sufficient enzyme activity, other enzyme-sequence pairs could be employed in place of those used in this study. This option opens up the possibility of complex culture schemes involving multiple cells groups, sequence pairs, enzymes, and exposure timings.

5.5 Conclusions

In this study, we showed that the restriction enzyme BamHI and nonspecific endonuclease Benzonase could be used to cleave engineered DNA linkages present on cell membranes. ssDNA-PEG-lipid conjugates inserted in CCRF-CEM cells enabled us to develop three model cases: free-floating ssDNA hybridized to ssDNA-modified single cells, DNA-mediated cell patterns on 2D glass substrates, and 3D aggregates of cells tethered heterotypically via complementary sequences. Sequence pairs encoded with the BamHI recognition sequence could be exploited for targeted digestion of the engineered physical bonds in each of the three cases, and complete digestion irrespective of sequence could be executed by exposure to Benzonase. This technique is broadly applicable to any fields involving controlled positioning and timed exposure of cells relative to other structures and cells.

5.6 Acknowledgements

This study was supported by a Grant-in-Aid for Scientific Research on Innovative Areas "Nanomedicine Molecular Science" (No. 2306) and the Monbukagakusho Scholarship

for graduate studies from the Ministry of Education, Culture, Sports, Science, and Technology (MEXT) of Japan.

Chapter 6

Estimation of Cell-Cell Adhesion Energy Mediated by DNA-Lipid Bonds

---

"Of all the social interactions between cells in a multicellular organism, the most fundamental are the those that hold the cells together. Cells may cling to one another through direct cell-cell junctions, or they may be bound together by extracellular materials that they secrete; but by one means or another, they must cohere if they are to form an organized multicellular structure."

Bruce Alberts
Molecular Biology of the Cell, Chapter 19

6.1 Introduction

Cell-cell adhesion is central to the maintenance and dynamics of tissues. Cytoskeletally-linked cell behaviors are integrally related to cell-cell adhesion in multicellular contexts. Cell migration is influenced by cell-cell contact and the expression of cadherin cell-cell adhesion proteins[1]. Patterns that emerge during the collective migration of cells such as long range polarity or the leader-follower phenomenon depend upon the propagation of interactions of many cells connected through cell-cell adhesion molecules[2].Differential cell-cell adhesion is implicated as one of the driving forces of cell sorting, a process central to the organization of tissues in embryos and during organogenesis[3].

Cell-cell adhesion is manifested as mechanical energy provided by chemical bonds, serving to maintain the geometry, spacing, and arrangement of cells in multicellular contexts. Natural cell adhesion molecules such as cadherins are connected to the internal cytoskeleton and are thus chemically and physically linked to many processes occurring in the cytosol. Any artificial changes introduced to cell-cell adhesive contacts mediated by cadherins will be have consequences on the cytoskeleton and related processes including differentiation, apoptosis, and proliferation[4]. Steinberg and Takeichi used L-cells transfected with cadherins to create unique sorting patterns experimentally[5], and Hoffecker and Iwata showed that a conformational change in MSC-islet sorting patterns could be induced using ROCK inhibition, affecting both cadherin membrane residence time and cytoskeletal contraction[6].

The interdependence of cytoskeleton and cell-cell adhesion can be a confounding factor when a process of interest can only be controlled by manipulating coupled variables such

[1] Paulina Niewiadomska, Dorothea Godt, and Ulrich Tepass. "DE-Cadherin is required for intercellular motility during Drosophila oogenesis". In: *The Journal of cell biology* 144.3 (1999), pp. 533–547; Eric Theveneau et al. "Collective chemotaxis requires contact-dependent cell polarity". In: *Developmental cell* 19.1 (2010), pp. 39–53.

[2] Vedula et al., "Emerging modes of collective cell migration induced by geometrical constraints"; Dhananjay T Tambe et al. "Collective cell guidance by cooperative intercellular forces". In: *Nature materials* 10.6 (2011), pp. 469–475; Friedl and Gilmour, "Collective cell migration in morphogenesis, regeneration and cancer".

[3] François Graner and James A Glazier. "Simulation of biological cell sorting using a two-dimensional extended Potts model". In: *Physical review letters* 69.13 (1992), p. 2013; Steinberg and Takeichi, "Experimental specification of cell sorting, tissue spreading, and specific spatial patterning by quantitative differences in cadherin expression".

[4] Nastaran Zahir and Valerie M Weaver. "Death in the third dimension: apoptosis regulation and tissue architecture". In: *Current opinion in genetics & development* 14.1 (2004), pp. 71–80; Michelle L Hermiston and Jeffrey I Gordon. "In vivo analysis of cadherin function in the mouse intestinal epithelium: essential roles in adhesion, maintenance of differentiation, and regulation of programmed cell death." In: *The Journal of cell biology* 129.2 (1995), pp. 489–506; Celeste M Nelson and Christopher S Chen. "VE-cadherin simultaneously stimulates and inhibits cell proliferation by altering cytoskeletal structure and tension". In: *Journal of cell science* 116.17 (2003), pp. 3571–3581.

[5] Steinberg and Takeichi, "Experimental specification of cell sorting, tissue spreading, and specific spatial patterning by quantitative differences in cadherin expression".

[6] Ian T Hoffecker and Hiroo Iwata. "Manipulation of Cell Sorting Within Mesenchymal Stromal Cell–Islet Cell Multicellular Spheroids". In: *Tissue Engineering Part A* 20.11-12 (2014), pp. 1643–1653.

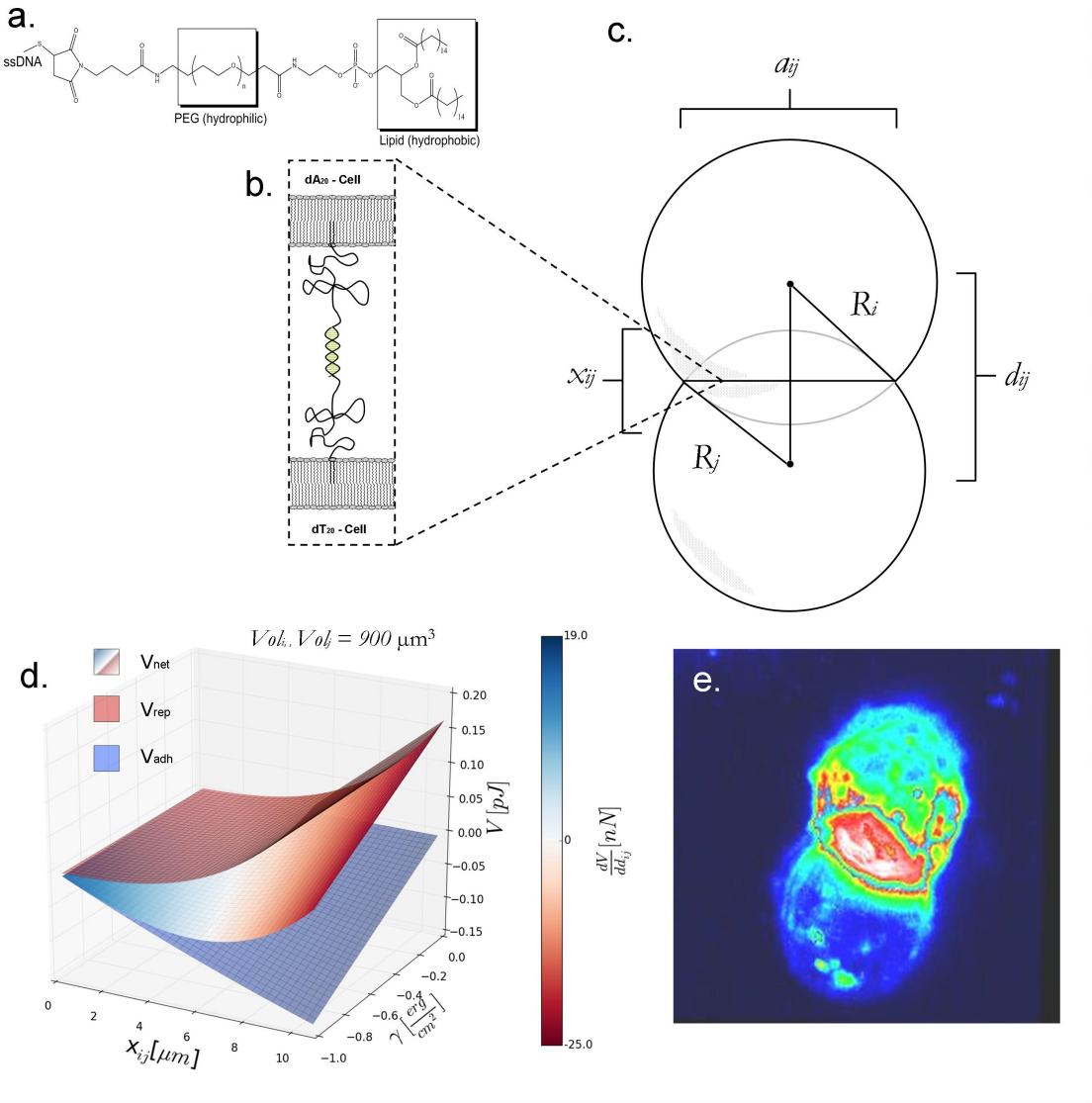

FIGURE 6.1: (a) Molecular structure of ssDNA-PEG-lipid molecule. (b) Depiction of the cell-cell interface mediated by adjacent hybridized ssDNA-PEG-lipid molecules residing in cell membranes (c) Geometric representation of a cell doublet including variables names used in this study. (d) Theoretical interfacial potential energies V (blue/red), V_{Rep} (red), and V_{Adh} (blue) [pJ] as a function of indentation depth x_{ij} $[\mu m]$ and γ $[erg/cm^2]$ for fixed values of isolated single cell radii $Vol_i = Vol_j = 900\ \mu m^3$. The value of the derivative $\frac{dV}{dd_{ij}}$ is shown as a color map where white corresponds to the potential energy minimum. (c) 3D image of cell doublet constructed tomographically from YOYO-1 fluorescence confocal image slices, heat map-colored to show the intensity distribution and the circular shape of the cell-cell contact region.

as in the case of cell sorting which depends not only on differential adhesive interactions between two groups of cells but also cytoskeletal contraction. Indeed, a controversy still remains as to the role of cytoskeletal forces in cell sorting due to the difficulty associated with separating the two variables experimentally[7].

ssDNA-conjugated lipids cross-linked with polyethylene glycol (ssDNA-PEG-lipid)(Fig. 6.1a) able to associate with the cell membrane have been used to artificially engineer cell-cell adhesion even in the absence of cadherins or other natural cell-cell adhesion molecules as is the case with the CCRF-CEM lymphoblast-like cell line[8]. Cells modified with a particular oligonucleotide sequence can specifically bind to cells modified with the complementary sequence via DNA hybridization leading to a heterotypic adhesive interaction between cells (Fig. 6.1b). This artificially-induced form of cell-cell adhesion has its own associated adhesion energy capable of resisting the migration of cells as was demonstrated with adherent-type cells modified with ssDNA-PEG-lipids and plated on substrates bearing both fibronectin and complementary ssDNA ligands[9]. The capability of retarding cell migration and generating artificial cell-cell adhesion independently of the cytoskeleton could be a powerful tool in the study of the cytoskeleton itself as well as in tissue engineering applications, however neither quantitative measurement nor precise modulation of the adhesion energy associated with ssDNA-PEG-lipid-mediated adhesion has yet to be demonstrated.

Adhesion energy drives the maximization of adhesive contact between cohering cell membranes, which in turn is opposed by cellular interfacial tension[10]. The primary contributor to cellular interfacial tension is contractile actomyosin tension generated from the cell cortex which is subsequently responsible for maintaining the spherical shape of cells in isolation[11]. By measuring the deformation of cell doublets adhered through ssDNA-PEG-lipids, we estimate the interfacial energy and cohesion (energy per unit contact area) through the inference that adhesion energy must balance elastic energy at steady state. We show that by modulating either the determinants of cohesion strength through

[7] Manning et al., "Coaction of intercellular adhesion and cortical tension specifies tissue surface tension"; Albert K Harris. "Is cell sorting caused by differences in the work of intercellular adhesion? A critique of the Steinberg hypothesis". In: *Journal of Theoretical Biology* 61.2 (1976), pp. 267–285.

[8] Teramura et al., "Control of cell attachment through polyDNA hybridization".

[9] Sakurai, Hoffecker, and Iwata, "Long term culture of cells patterned on glass via membrane-tethered oligonucleotides".

[10] Manning et al., "Coaction of intercellular adhesion and cortical tension specifies tissue surface tension"; Jos Käfer et al. "Cell adhesion and cortex contractility determine cell patterning in the Drosophila retina". In: *Proceedings of the National Academy of Sciences* 104.47 (2007), pp. 18549–18554.

[11] Krieg et al., "Tensile forces govern germ-layer organization in zebrafish"; Thomas Lecuit and Pierre-Francois Lenne. "Cell surface mechanics and the control of cell shape, tissue patterns and morphogenesis". In: *Nature Reviews Molecular Cell Biology* 8.8 (2007), pp. 633–644; E Evans and A Yeung. "Apparent viscosity and cortical tension of blood granulocytes determined by micropipet aspiration". In: *Biophysical journal* 56.1 (1989), pp. 151–160.

the number of available cell-cell adhesion molecules or the elastic repulsion by pharmacologically disrupting the cytoskeleton, it is possible to affect the size of the contact area formed between cell doublets.

6.2 Materials and Methods

6.2.1 Experimental Methods

α-N-hydroxysuccinimidyl-ω-maleimidyl poly(ethylene glycol) (NHS-PEG-Mal, MW 5000) and 1,2-dipalmitoyl-sn-glycerol-3-phosphatidylethanolamine (DPPE) were purchased from NOF Corporation (Tokyo, JP). Fetal bovine serum (FBS), Hanks Balanced Salt Solution (HBSS), and RPMI 1640 medium were purchased from Invitrogen, Co. (Carlsbad, CA, USA). Cytochalsin D was purchased from Sigma Aldrich(St. Louis, MO, USA).

The cells used in this experiment were CCRF-CEM cells, the human T-cell lymphoblast-like cell line, a non-adherent cell type used in previous ssDNA-PEG-lipid experiments[12]. ssDNA-PEG-lipids[13] and methoxy-PEG-lipids[14] were synthesized as previously described. Cells were modified with ssDNA-PEG-lipids by incubation for 1 hr, RT, in a solution of ssDNA-PEG-lipid at a concentration of 200 $\mu g/mL$. This was followed thrice with rinsing in HBSS and pelleting. Doublets were formed by mixing complementary ssDNA-PEG-lipid-bearing cell groups into a single glass bottom dish during observation with confocal microscopy. Labeling was performed with YOYO-1 intercalating fluorescent dye at a concentration 1000x diluted from stock.

To form cell doublets, a group of CEM cells modified with oligo-dA_{20}-PEG-lipid was exposed to a complementary group of CEM cells modified with oligo-dT_{20}-PEG-lipid. Complementary cell groups were exposed to each other over a glass bottom dish during imaging by confocal laser scanning microscopy and allowed to settle and reach steady state over the course of 15 min. Doublets were identified manually out of a population also containing single cells, triplets, and larger aggregates.

For cells modified to exhibit reduced cohesion, methoxy-PEG-lipid was added to the ssDNA-PEG-lipid solutions during the cell modification stage in a 10:1 molar ratio. Methoxy-PEG-lipid/ssDNA-PEG-lipid-modified cells were combined to form a mixture of varied aggregate sizes including doublets and were imaged according to the same procedure applied to normal ssDNA-PEG-lipid-modified cells.

[12] Teramura et al., "Control of cell attachment through polyDNA hybridization".
[13] Teramura et al., "Control of cell attachment through polyDNA hybridization".
[14] Mitsuaki Toda, Yusuke Arima, and Hiroo Iwata. "Complement activation on degraded polyethylene glycol-covered surface". In: *Acta biomaterialia* 6.7 (2010), pp. 2642–2649.

For cells treated pharmacologically to exhibit reduced elastic repulsion, cytochalasin D (1 mg/mL in DMSO) was added to cell suspensions during the 1 hr ssDNA-PEG-lipid modification for a final concentration of 2 $\mu g/mL$[15], and cells observed with confocal microscopy were kept in medium containing 2 $\mu g/mL$ cytochalasin D.

6.2.2 Model and Data Analysis

Cells i and j interact with a total energy given by

$$V = V_{Rep} + V_{Adh}, \tag{6.1}$$

where V_{Rep} is the potential energy contribution due to elastic repulsion and V_{Adh} is the potential energy contribution resulting from adhesion over the surface of contact.

To estimate the adhesion energy, we have chosen to model the cell repulsive energy due to elastic deformation by the Hertz-model applied to two compressed elastic spheres described in Landau and Lifschitz's Theory of Elasticity[16] shown schematically in Fig. 6.1c. Two cells i and j of unequal spherical radii R_i and R_j are bound by a contact surface $A_{contact}$ with radius $\frac{a_{ij}}{2}$. The two cell centers of curvature are separated by a distance d_{ij}, and the truncated caps due to adhesion are together of length x_{ij} referred to as the indentation depth. The contribution to interfacial energy due to repulsion is given as

$$V_{Rep} = \frac{2}{15}(R_i + R_j - d_{ij})^{5/2}\Big(\frac{1-\nu^2}{\tilde{E}}\Big)^{-1}\sqrt{\frac{R_i R_j}{R_i + R_j}} \tag{6.2}$$

where $\tilde{E}$ and ν are the Young's modulus and Poisson's ratio respectively defined for both cells i and j.

We assume that the radii of curvature of cells can be represented by spherical radii. We imported the Young's modulus, which we assume for simplicity to be constant in the Hertz model, from Rosenbluth et al. ($E = 855 \pm 670\ Pa$ for HL60 leukemia myeloid cells, and likewise assumed a Poisson's ratio of 0.5 as was done so by Rosenbluth et al[17].

[15] Bruce R Stevenson and David A Begg. "Concentration-dependent effects of cytochalasin D on tight junctions and actin filaments in MDCK epithelial cells". In: *Journal of Cell Science* 107.3 (1994), pp. 367–375.

[16] Heinrich Hertz. "Ueber die Berührung fester elastischer Körper." In: *Journal für die reine und angewandte Mathematik* 92 (1882), pp. 156–171; Lev D Landau and EM Lifshitz. "Theory of Elasticity, vol. 7". In: *Course of Theoretical Physics* 3 (1986).

[17] Michael J Rosenbluth, Wilbur A Lam, and Daniel A Fletcher. "Force microscopy of nonadherent cells: a comparison of leukemia cell deformability". In: *Biophysical journal* 90.8 (2006), pp. 2994–3003.

The adhesive contribution to potential energy is given by

$$V_{Adh} = \gamma A_{contact} \tag{6.3}$$

where γ is the cohesion represented in units of energy per unit area. The contact area can be rewritten as a function of R_i, R_j, and d_{ij} such that the potential due to adhesion becomes

$$V_{Adh} = \gamma\pi\left(R_i^2 - \frac{(d_{ij}^2 - R_j^2 + R_i^2)^2}{4d_{ij}^2}\right). \tag{6.4}$$

Thus, given values of R_i, R_j, and γ, the total interfacial energy between cells i and j can be determined as a function of d_{ij} or x_{ij}. Fig. 6.1d shows a plot of potential energies V (magenta), V_{Rep} (red), and V_{Adh} (blue) as a function of indentation depth x_{ij} and cohesion γ for a hypothetical pair of fixed volumes $Vol_i = Vol_j = 900\ \mu m^3$.

The minimum of V can also be determined by the roots of its derivative with respect to separation distance which is given by

$$\frac{dV}{dd_{ij}} = \frac{-\gamma\pi}{2d_{ij}^3}\left(d_{ij}^4 - (R_i^2 - R_j^2)^2\right) - \frac{1}{3}\left(\frac{1-\nu^2}{\tilde{E}}\right)^{-1}\sqrt{\frac{R_iR_j}{R_i+R_j}}(R_i + R_j - d_{ij})^{3/2}, \tag{6.5}$$

and is shown in Fig. 6.1d as the color map. For values of γ sufficient to overcome thermal and convective noise, a potential energy well exists for V such that $x_{ij} > 0$ and cell adhesion occurs. This region is indicated by white on the color map in Fig. 6.1d. The roots of the derivative equation can be rearranged to solve for cohesion:

$$\gamma = -\frac{2}{3\pi}\sqrt{\frac{R_iR_j}{R_i+R_j}}\left(\frac{1-\nu^2}{\tilde{E}}\right)^{-1}\frac{d_{ij}^3(R_i + R_j - dij)^{3/2}}{d_{ij}^4 - (R_i^2 - R_j^2)^2}, \qquad \frac{dV}{dd_{ij}} = 0. \tag{6.6}$$

Theoretical computations on the interfacial energies and contact areas were implemented in a custom Python-based program using the Matplotlib, Scipy, and Numpy libraries. A numerical algorithm was used to identify the roots of the derivative $\frac{dV}{dd_{ij}}$ and relate those to the steady state contact area. Volume of the cell was assumed to be conserved, so to account for the change of cell radius that occurs with increasing contact area and adhesion, an optimization algorithm (minimization of volume discrepancy via Nelder Mead downhill simplex) was included to numerically adjust each radius involved in

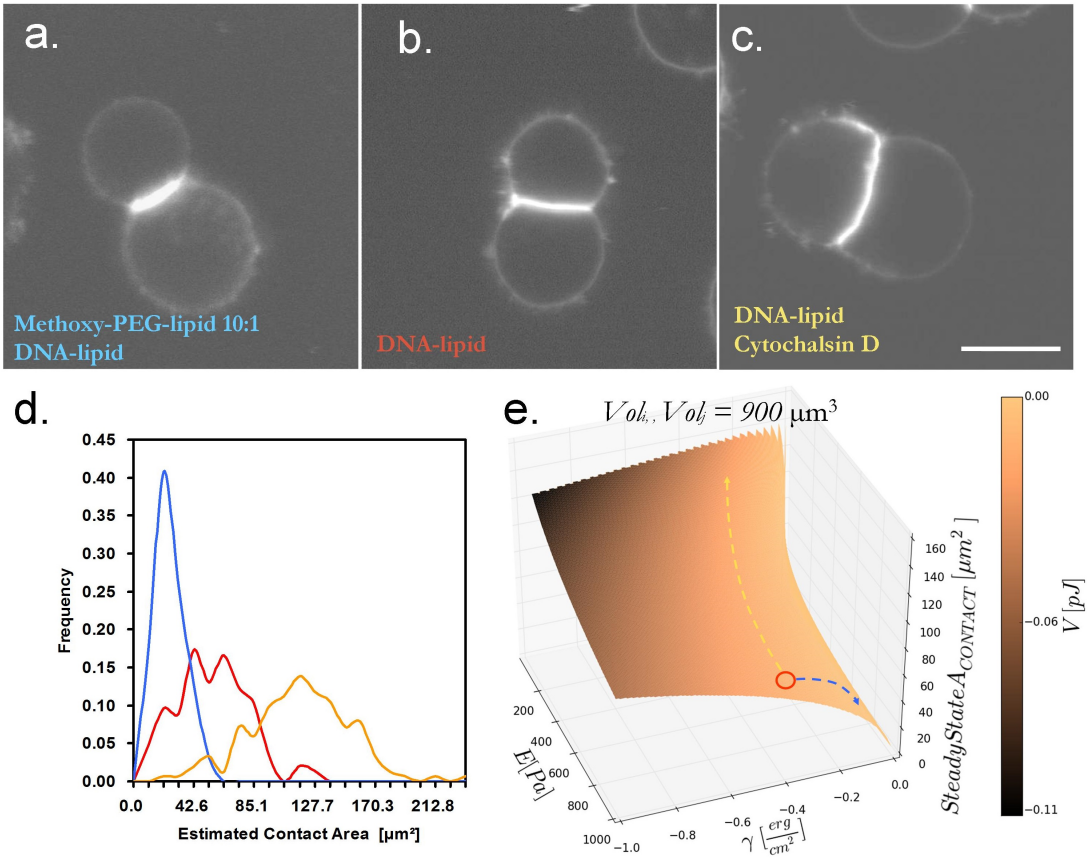

FIGURE 6.2: (a) Confocal fluorescence image of YOYO-1-labeled cell doublets exhibiting the reduced contact characteristic of cells bearing methoxy-PEG-lipids in addition to dA_{20}/dT_{20}-PEG-lipids. (b) Confocal fluorescence image of YOYO-1-labeled cell doublet with adhesion mediated by hybridization between dA_{20}- and dT_{20}-PEG-lipids. (c) Confocal fluorescence image of YOYO-1-labeled cell doublets exhibiting the increased contact characteristic of cells treated with cytochalsin D prior to cohering via dA_{20}/dT_{20}-PEG-lipids. Scale bar = 10 μm (d) Histogram of contact areas calculated based on geometric measurements of confocal images. Curves correspond to treatment conditions in a-c: meo/dAdT doublets (blue) (n=125), normal dAdT doublets (red) (n=145), and cytD/dAdT doublets (yellow) (n=152). (e) Surface plot of the contact area at steady state calculated as a function of the Young's modulus (E) and cohesion (γ). Red circle indicates approximate point corresponding dAdT doublets, the yellow line indicates Young's modulus reduction via cytochalsin D and its corresponding effect on area, and the blue line indicates modulation of cohesion by addition of methoxy-PEG-lipid.

energy and area calculations. This way, all points on surface plots correspond to a single pair of cell volumes.

Images of doublets were manually analyzed by drawing circles conforming to the radius of curvature of the cell periphery opposite the contact surface to obtain values for the radii (R_i and R_j) and the positions of circles used to calculate d_{ij}. The analytical expressions for cohesion and interfacial energy were solved in terms of the measured geometric data.

6.2.3 Statistics

Distributions of estimated cohesion values were assessed by evaluating the skew and kurtosis. Distributions were compared by unpaired, unequal variance t-test and by Wilcoxon rank sum test. Error bars/uncertainties of calculated adhesion energies were determined based on the propagation of error due to random error in the literature parameter values used (Poisson's ratio and Young's modulus) according to the variance equation for variables with independent random errors[18].

6.3 Results

6.3.1 Formation of Doublets with and without Methoxy-PEG-lipids

To estimate the adhesion energy of cell-cell bonds formed with ssDNA-PEG-lipids, we prepared mixtures of oligo-dA_{20}-PEG-lipid-modified CEM cells and exposed them in a 1:1 ratio with a suspension of oligo-dT_{20}-PEG-lipid-modified CEM cells. Suspensions of cells were observed in glass bottom dishes with confocal laser scanning microscopy. To visualize ssDNA and dsDNA, the intercalating dye YOYO-1 was added to the cell suspension.

Rapid formation of cellular doublets, triplets, and larger aggregates was observed with confocal microscopy. After 20 minutes of settling by gravity and stablization of nascent doublets and aggregates, images of doublets could be captured. A stack of images reconstructed tomographically in 3 dimensions is shown in Fig. 6.1e. YOYO-1 fluorescence intensity, which is greater for dsDNA than ssDNA, is distinguishable as a circular disc at the contact surface between the two cells, in agreement with the assumption made in our model of two intersecting spheres with a circular contact area.

145 crosssectional images of separate oligo-dA_{20}/oligo-dT_{20} doublets (hereafter referred to as dAdT doublets) were gathered at 360x magnification (Fig. 6.2b). Doublets were characterized by a high intensity band of YOYO-1 fluorescence at their surface of contact, which in the majority of cases was observed as a straight line in cross-sectional images. A thin YOYO-1 fluorescence halo of lesser intensity indicating the un-bonded ssDNA at the periphery of the rest of the cell could be observed in most cases as well. Qualitative deviation from spherical curvature was observed in some instances, however the majority of doublets were qualitatively in agreement with the geometric assumptions of Fig. 6.1c.

[18] HH Ku. "Notes on the use of propagation of error formulas". In: *Journal of Research of the National Bureau of Standards* 70.4 (1966).

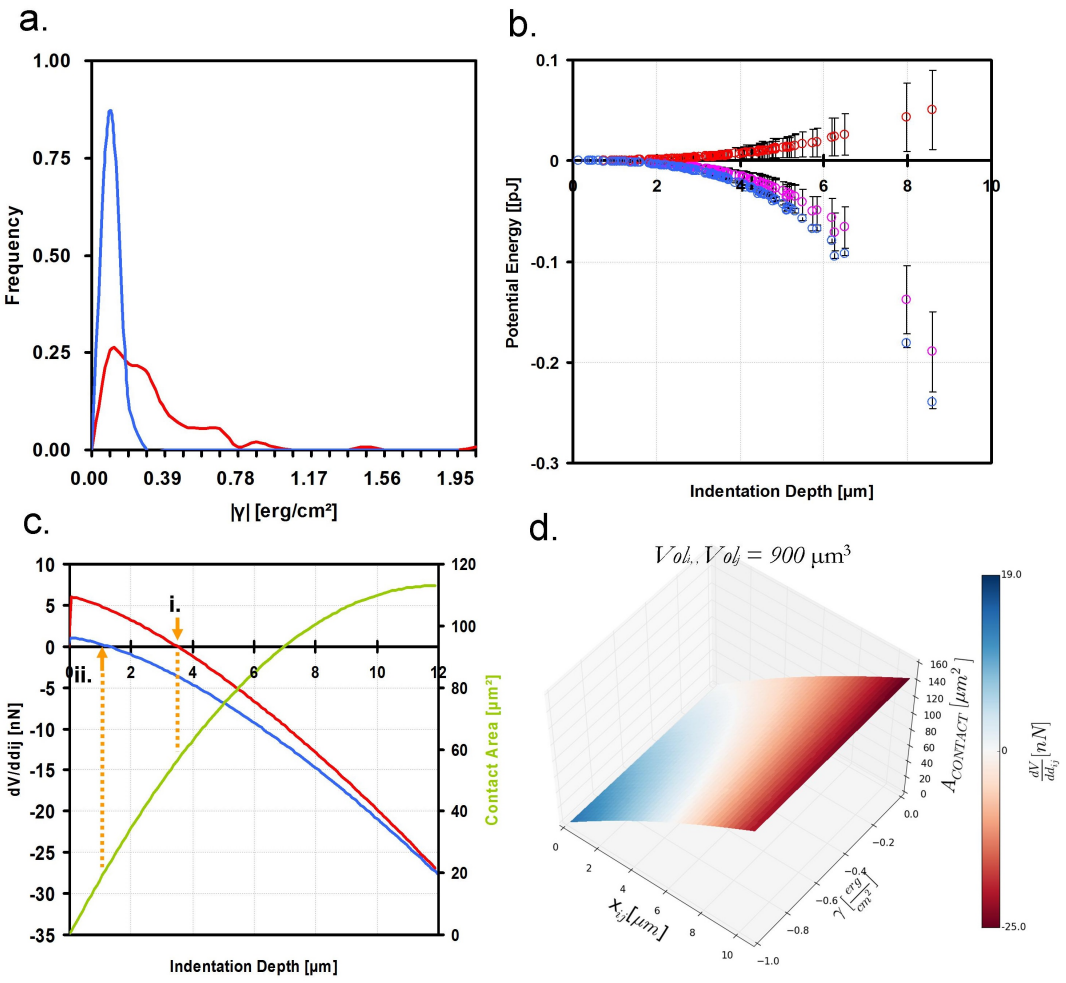

FIGURE 6.3: (a) Histogram of cohesion values estimated using the Hertz model. Cells decorated with methoxy-PEG-lipids in addition to ssDNA-PEG-lipids (blue) had a narrower distribution and lower peak value as compared to cells without methoxy-PEG-lipids (red). (b) Potential energies V (magenta), V_{Rep} (red), and V_{Adh} (blue) (pJ) calculated from R_i, R_j, and d_{ij} measurements plotted as a function of indentation depth x_{ij} (μm). Error bars were calculated using the variance formula to account for propagation of uncertainties in Poisson's ratio and Young's modulus. (c) Left vertical axis: the derivative $\frac{dV}{dd_{ij}}$ of net potential energy with respect to separation distance (nN) plotted as a function of indentation depth x_{ij}. Right vertical axis: contact area $A_{contact}$ as a function of indentation depth x_{ij}. Given Vol_i, Vol_j, and γ, the roots of $\frac{dV}{dd_{ij}}$ correspond to the expected x_{ij} at steady state. The roots of $\frac{dV}{dd_{ij}}$ assuming the average cohesion values determined for cell doublets with (ii) and without (i) methoxy-PEG-lipids ($\gamma = -0.055$ erg/cm^2 $\pm$ 0.046 *S.D.* and -0.32 erg/cm^2 $\pm$ 0.31 *S.D.* respectively) correspond to steady state values of $d_{ij} = 1.4$ μm and 3.7 μm and $A_{contact} = 25$ μm^2 and 60 μm^2 respectively. (d) Surface plot of contact area $A_{contact}$ as a function of indentation depth x_{ij} and cohesion γ. Color map corresponds to the magnitude of the derivative $\frac{dV}{dd_{ij}}$ as a function of indentation depth x_{ij} and cohesion γ, and white regions correspond to expected contact area at steady state given cell volumes of Vol_j and Vol_i = 900 μm^3 when in isolation.

Cells modified with methoxy-PEG-lipid in addition to ssDNA-PEG-lipid (exposed 10:1 methoxy-PEG-lipid:ssDNA-PEG-lipid concentration) were subjected to the same analysis as the doublets exposed to ssDNA-PEG-lipids without methoxy-PEG-lipids. 125 confocal cross-sectional images were again gathered for this condition (Fig. 6.2a). Methoxy-PEG-lipid/ssDNA-PEG-lipid doublets (hereafter referred to as Meo/dAdT doublets) had a qualitatively lower incidence of highly deformed doublets, and contact surfaces were consistently observed to be smaller than those of dAdT doublets.

We hypothesized that actin cortical tension contributes to the cell Young's modulus, increasing the repulsive term in the energy equation, and opposing the adhesion to reduce contact area. To test this, we added cytochalsin D to cell suspensions during the insertion reaction of ssDNA-PEG-lipid and to medium used during observation. Cytochalsin D, which binds to the rapidly growing barbed ends of actin filaments thus inhibiting polymerization, was hypothesized to lead to reduced Young's modulus, permitting larger deformations to satisfy adhesion energy. Fig. 6.2c shows a cohering dAdT doublet after 1 hr treatment with and in the presence of cytochalsin D (2 $\mu g/mL$) (cytD/dAdT doublet). Contact areas were notably larger for cytochalsin D doublets, as shown as a histogram in Fig. 6.2d which compares the distributions of contact areas calculated from geometric measurements for normal dAdT doublets, meo/dAdT doublets, and cytD/dAdT doublet.

In order to map the space of possible doublet conformations as a function of Young's modulus and cohesion, a custom program was implemented in Python for identifying the roots of the derivative $\frac{dV}{dd_{ij}}$ and corresponding contact area. Fig. 6.2e shows this as a plot, and specific doublet-forming conditions in Fig. 6.2a-c can be represented as points on this surface. Cytochalasin D treatment corresponds to a decrease in Young's modulus and a movement along that axis (yellow arrow), resulting in larger contact area at steady state. Conversely, doublet formation with methoxy-PEG-lipid corresponds to a reduction in cohesion strength and movement on that axis (blue arrow), orthogonal to the Young's modulus axis and leading to a decrease in the contact area at steady state.

The cohesion γ, a function of (R_i, R_j, and d_{ij}) was then found for each cell doublet in both the case of dAdT doublets and meo/dAdT doublets, calculated from geometric variables measured during image analysis. The distribution of γ values are summarized in Fig. 6.3a. The mean cohesion values of dAdT doublets ($\bar{\gamma} = 0.32$ erg/cm^2 $\pm$ 0.31 *S.D.*) was significantly greater (two sample T-test, unequal variances: $t(151) = 10.1$, $p = 1.3\ x10^{-18}$) than that of meo/dAdT doublets ($\bar{\gamma} = 0.055$ erg/cm^2 $\pm$ 0.046 *S.D.*).

The distributions of γ values determined for dAdT were skewed and highly leptokurtic (skewness = 2.67, excess kurtosis = 11.98) while distributions of γ values determined for meo/dAdT were skewed but comparatively mesokurtic (skewness = 0.94, excess kurtosis

= 1.32). To account for skewed samples, we further tested the sameness of $\bar{\gamma}$ for the two populations by Wilcoxon Rank Sum Test: $w_{dAdT} = 26239; w_{meo/dAdT} = 10364$; $\mu_{dAdT} = 16937$; $p(w_{dAdT} \leq \mu_{dAdT}) = 1.6x10^{-136}$.

Potential energies V (magenta), V_{Rep} (red), and V_{Adh} (blue) (pJ), shown in Fig. 6.3b for dAdT doublets, were determined based on the values of R_i, R_j, and d_{ij} obtained from image analysis. Sensitivity to random error in the parameter values used for Young's modulus and the Poisson's ratio was estimated by applying the variance equation[19] for independent variables (See Appendix). Error bars in Fig. 6.3b represent the propagated standard deviation of potential based on random error in ν and $\tilde{E}$.

Obtaining an average value of cohesion for a population of ssDNA-modified cells $\bar{\gamma}$ allows one to solve numerically for the expected separation distance d_{ij}, indentation depth x_{ij}, and contact area $A_{contact}$ for two cells given known radii R_i and R_j. This is shown in Fig. 6.3c for $Vol_i = Vol_j = 900\mu m^3$ where the plot of $\frac{dV}{dd_{ij}}$ is plotted for two different average values of cohesion: $\gamma = -0.055$ erg/cm^2 (blue, meo/dAdT doublets) and -0.32 erg/cm^2 (red, dAdT doublets). The roots of these curves are equal to the indentation depths x_{ij} that correspond to the minimum total interfacial energy which can subsequently define the corresponding contact area $A_{contact}$(green). This curve is represented as a function of γ in Fig. 6.3d, where the color map indicates the value of $\frac{dV}{dd_{ij}}$, and the white line corresponds to steady state values of contact area.

6.4 Discussion

In this study, we examined the deformation of cell membranes caused by ssDNA-PEG-lipid-modified CEM cells adhered through complementary DNA hybridization. By assuming cells to be elastic intersecting spheres, the Hertz model was used to infer quantitatively the cohesion γ, or energy required to support a unit area of contact surface, based on the observed deformation. The validity of the inference rests on several factors, the first being the legitimacy of simplifying assumptions made in order to apply the Hertz model. We assumed a spherical radius of curvature of cells. At particularly high deformations, this assumption breaks down and cell curvature qualitatively deviates from spherical curvature. The Hertz model also assumes constant Young's modulus and Poisson's ratio, and thus a linear relationship between stress and strain. Due to the heterogeneous organization of the cytosol, the potential for the redistribution of organelles and the impact this may have on actin cortex, it is likely that the Young's modulus is not constant at certain time scales. For this reason as well, the model is most valid for small deformations. Sensitivity of γ to these sources of systematic error were not investigated,

[19] Ku, "Notes on the use of propagation of error formulas".

as the bulk of the γ distribution was concentrated around small indentation depths in the dAdT doublet case and particularly so in the meo/dAdT doublet case.

The addition of methoxy-PEG-lipid to the ssDNA-PEG-lipid membrane insertion reaction was used to reduce the final average cohesion. The high insertion concentrations and long 1 hour incubation times were used to ensure saturation of the cell surface with PEG-lipids. Rather than modulate the insertion concentrations to achieve surface densities below saturation levels, a process which could be involve a nonlinear dependence on solution concentrations due to the complex surface characteristics of cells, cohesion modulation was approached by selecting conditions of competitive insertion with non-adhesive methoxy-PEG-lipids. The significant decrease in average contact area and subsequently estimated cohesion agrees with the expected reduction in available adhesive ligands as a consequence of the methoxy-PEG-lipids. Measurement of average cohesion for a given condition enables estimation of a steady state contact area and indentation depth for a given pair of cells by numerically determining the roots of the derivative of potential.

Adding cytochalsin D to affect the actin cortex had the anticipated effect of increasing contact area. This is in agreement with the Hertz model interpretation of contact area as an indicator of the balance between repulsive and adhesive force. A reduction in actin cortex integrity would reduce the Young's modulus of the cell, lowering the repulsive energy term, and permitting a larger surface contact between the cells for an identical surface adhesion energy density.

In summary, the average cohesion due to ssDNA-PEG-lipid bonds can be estimated according to their elastic deformation. The Hertz model applied in this study predicted reduced deformation for lesser cohesion values. This was experimentally tested by modulating the cohesion by the introduction of adhesively neutral methoxy-PEG-lipids during the insertion phase of ssDNA-PEG-lipids. Additionally, pharmacological inhibition of actin polymerization by cytochalasin D was expected to reduce Young's modulus and had the predicted effect of increasing the contact area at steady state. We expect that the approach of tuning tuning the characteristics of artificially adhered cells may be useful in controlling and quantitatively characterizing cohesion between cells mediated by natural cell-cell adhesion modes such as adherens junctions.

Appendix A

Supplementary Data

A.1 Appendix Figures

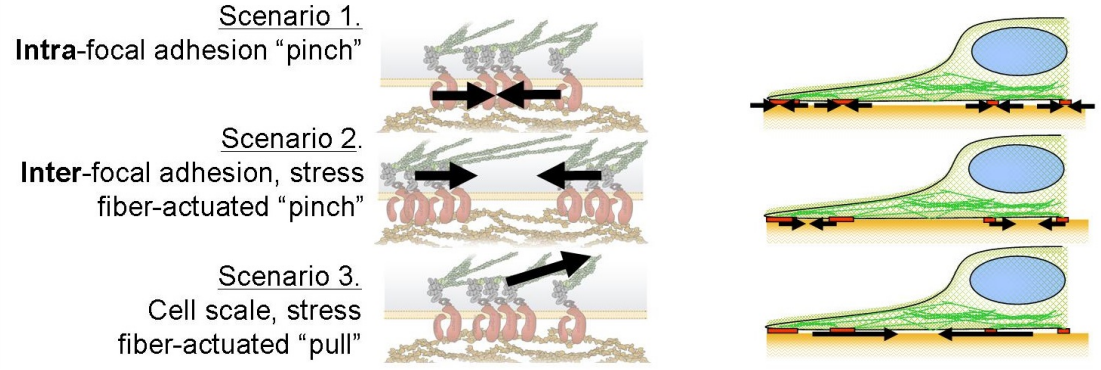

FIGURE A.1: Possible mechanisms of rigidity sensing. (top) Intra-focal adhesion sensing of rigidity would respond to deformations at sub micrometer scale. (middle) Inter-focal adhesion rigidity sensing could occur between local clusters of focal adhesions. (bottom) Cell-scale or cytoskeletal scale force sensing could occur across the body of the cell.

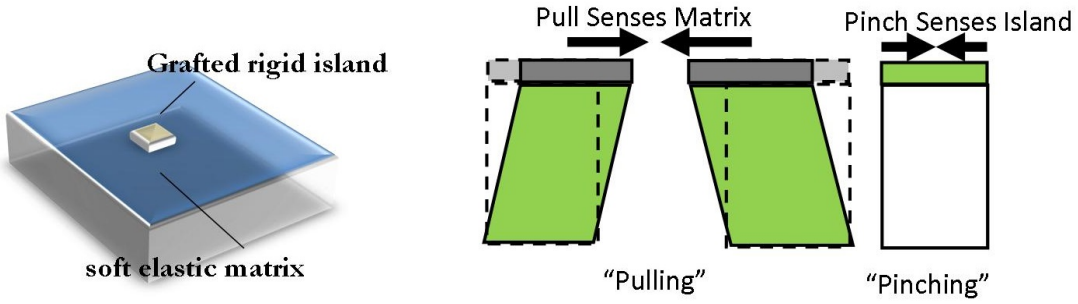

FIGURE A.2: Experimental design for detecting rigidity sensing scale. (left) An island feature made from an intrinsically high rigidity material grafted to a soft elastic matrix could either be "pulled" or "pinched" leading to assessment of either the gel rigidity or the island rigidity respectively. (right) The spacing and size of islands dictates the resolution of force sensing. Forces acting on islands relative to each other deforms the soft elastic matrix whereas fine resolution forces exerted between one point on the island and another deforms only the rigid island without affecting the gel.

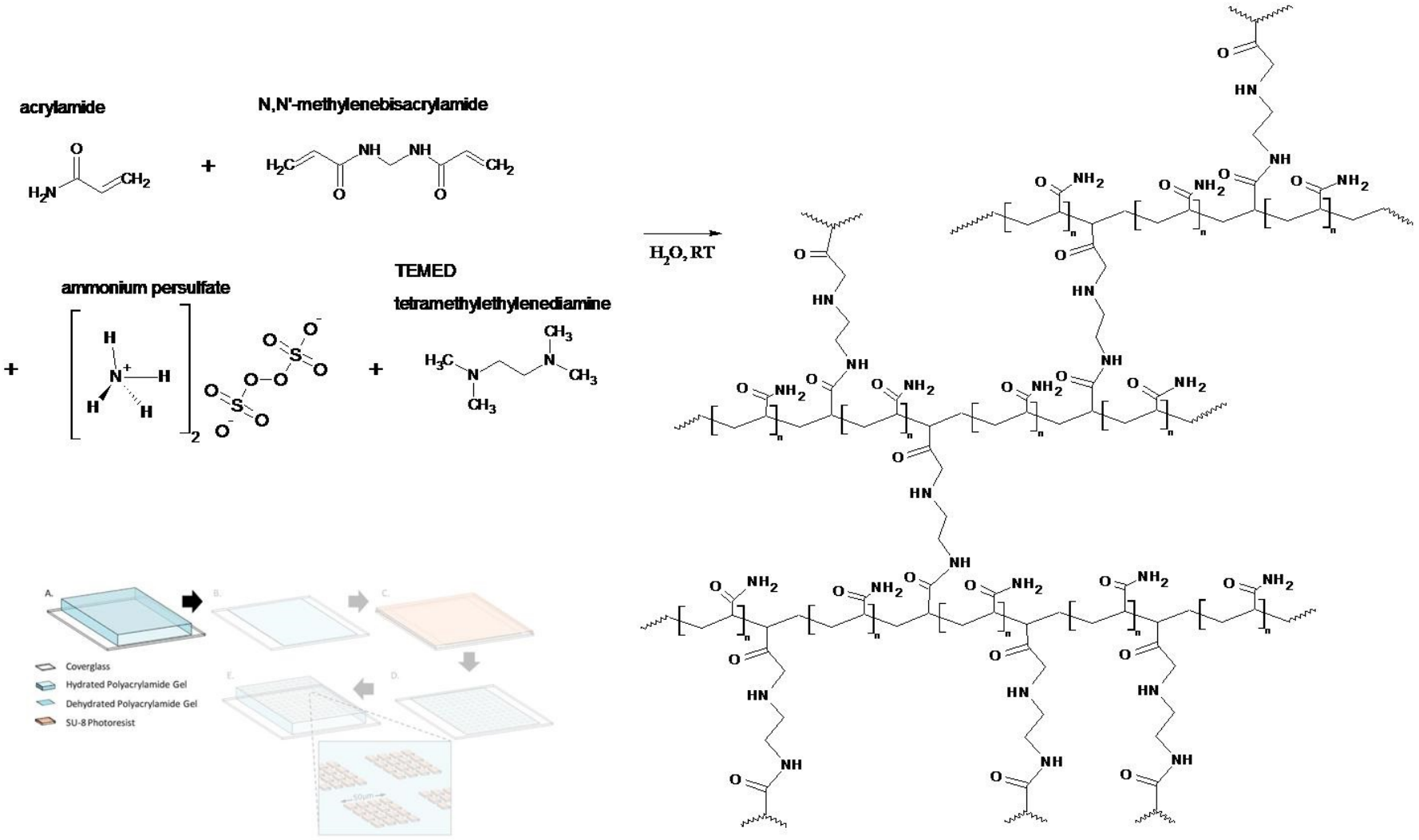

FIGURE A.3: The concentration of acrylamide monomer and the ratio of acrylamide monomer to bisacrylamide cross-linker can be modulated to tune the rigidity of elastic hydrogels.

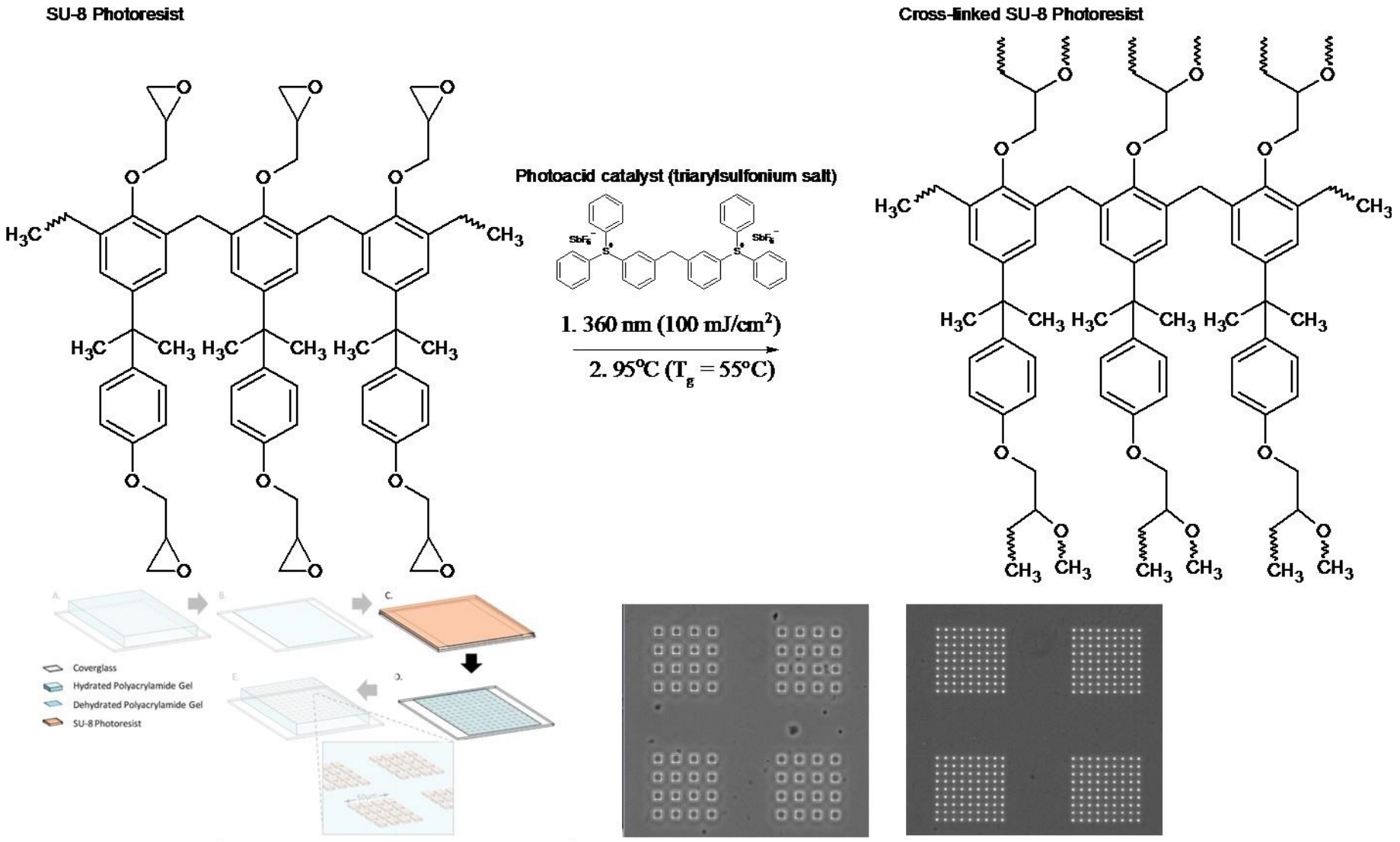

FIGURE A.4: The epoxy-based photoresist SU-8 undergoes a photoacid-catalyzed ring-opening polymerization upon UV exposure and forms a cross-linked network which does not dissolve upon the addition of organic developer solution allowing patterns to be designed using a photomask.

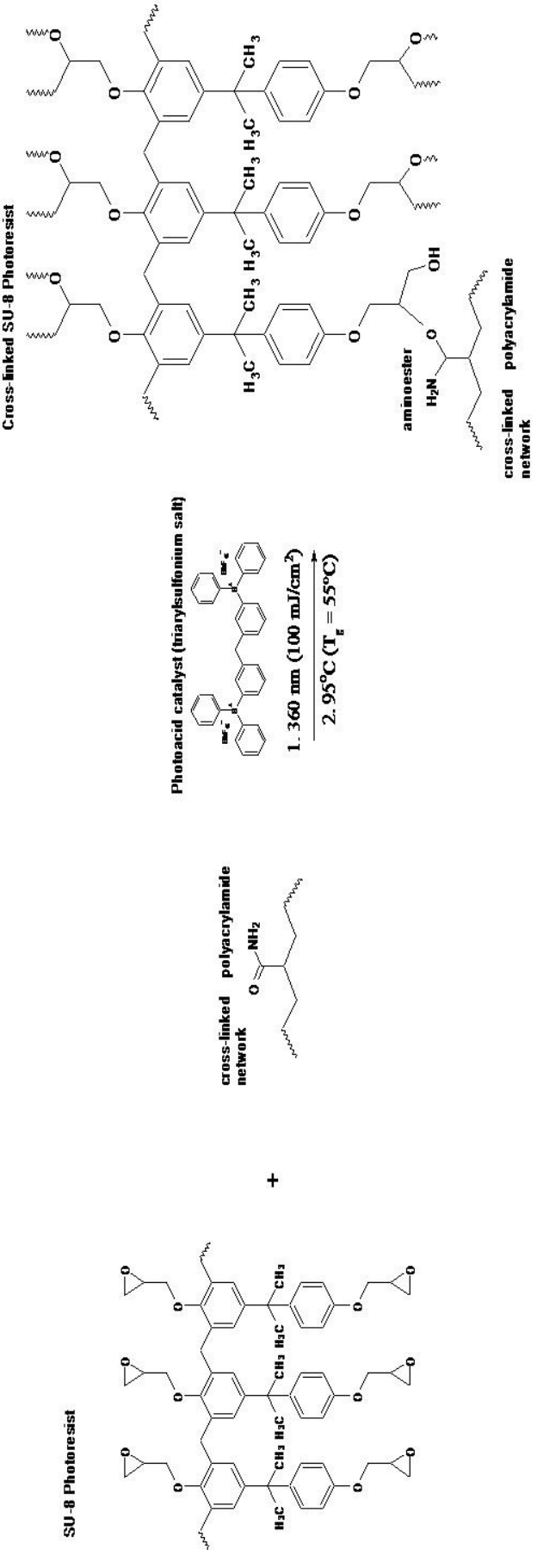

FIGURE A.5: It is possible that the grafting between SU-8 and the dehydrated polyacrylamide network is a covalent coupling. Under acidic conditions and high T, amides act as a weak nucleophile on oxonium ions, undergoing O-alkylation at the carbonyl oxygen to produce an alkylamino ester. (weak nucleophile will add to the more substituted carbon)

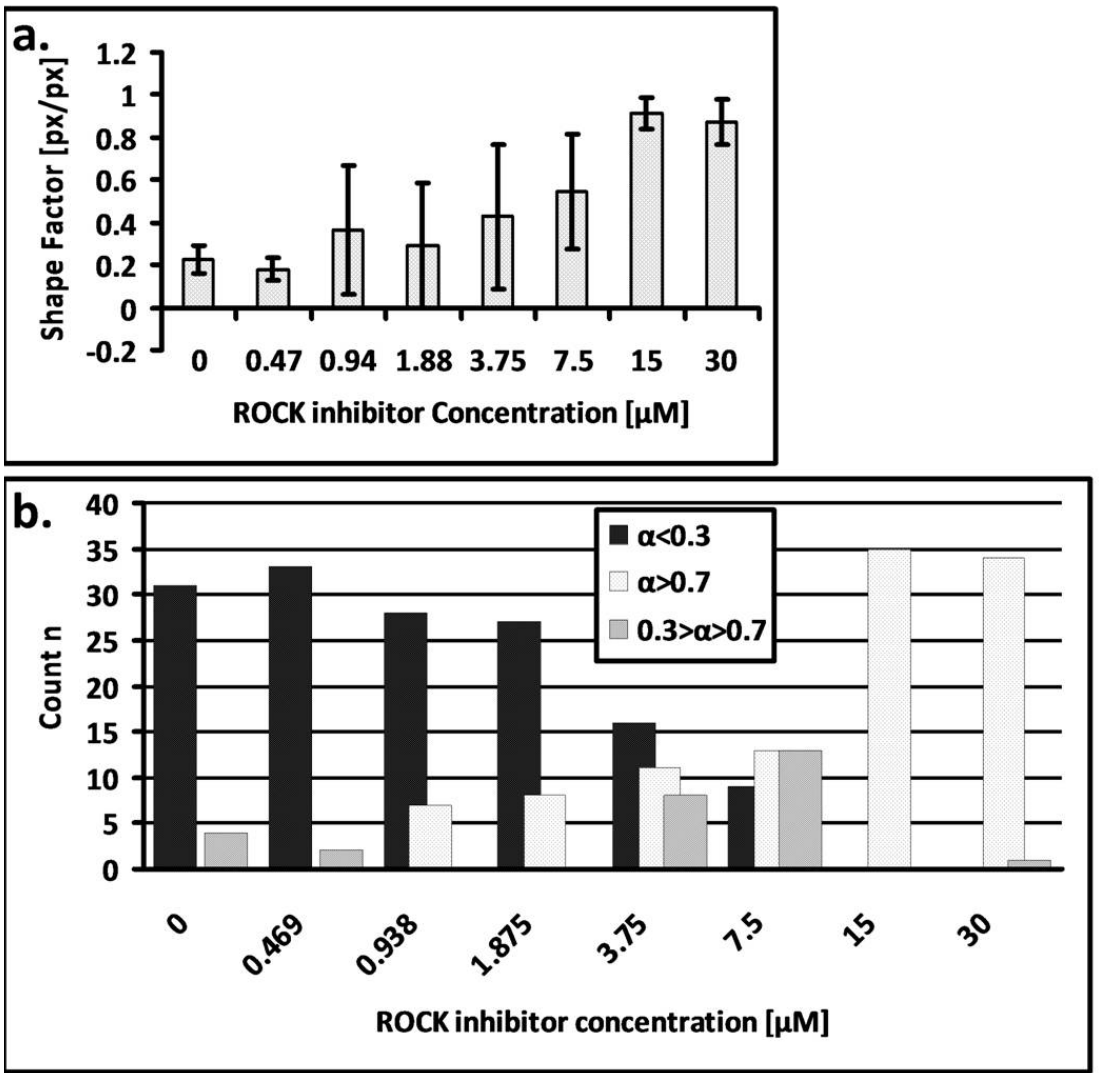

FIGURE A.6: Image analysis of confocal cross sections was used to quantify the cohesive interaction between islet cells and MSC's at varying concentrations of Y-27632. (a) Average cross-sectional contact ratio (α) at different values of Y-27632 concentration (b) Concentration dependence of co-aggregates with α values less than 0.3, greater than 0.7, and those that fall between 0.3 and 0.7 reveals low incidences of intermediate α values at any concentration.

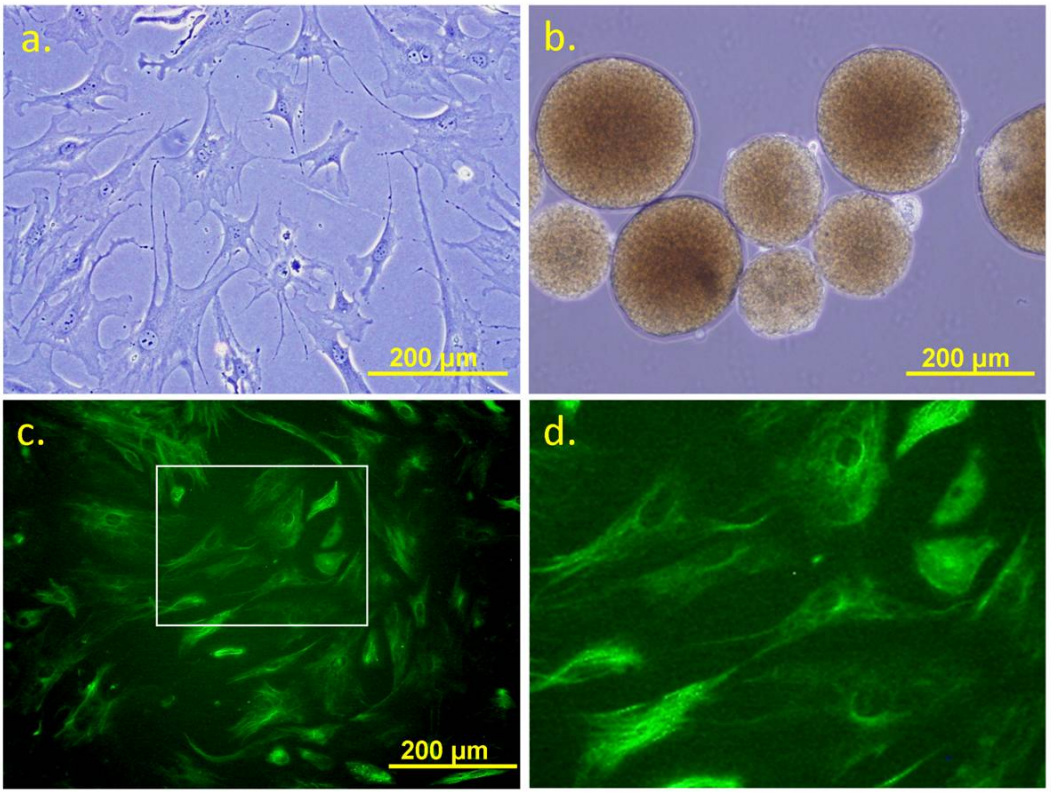

FIGURE A.7: (a) Phase contrast image of MSC's before aggregation (passage 6). (20x magnification) (b). Phase contrast image of isolated islets (day 1). (10x magnification) (c) Vimentin staining of fixed MSC's. (d) Inset of c. Vimentin filaments can be observed extending across the length of spread cells.

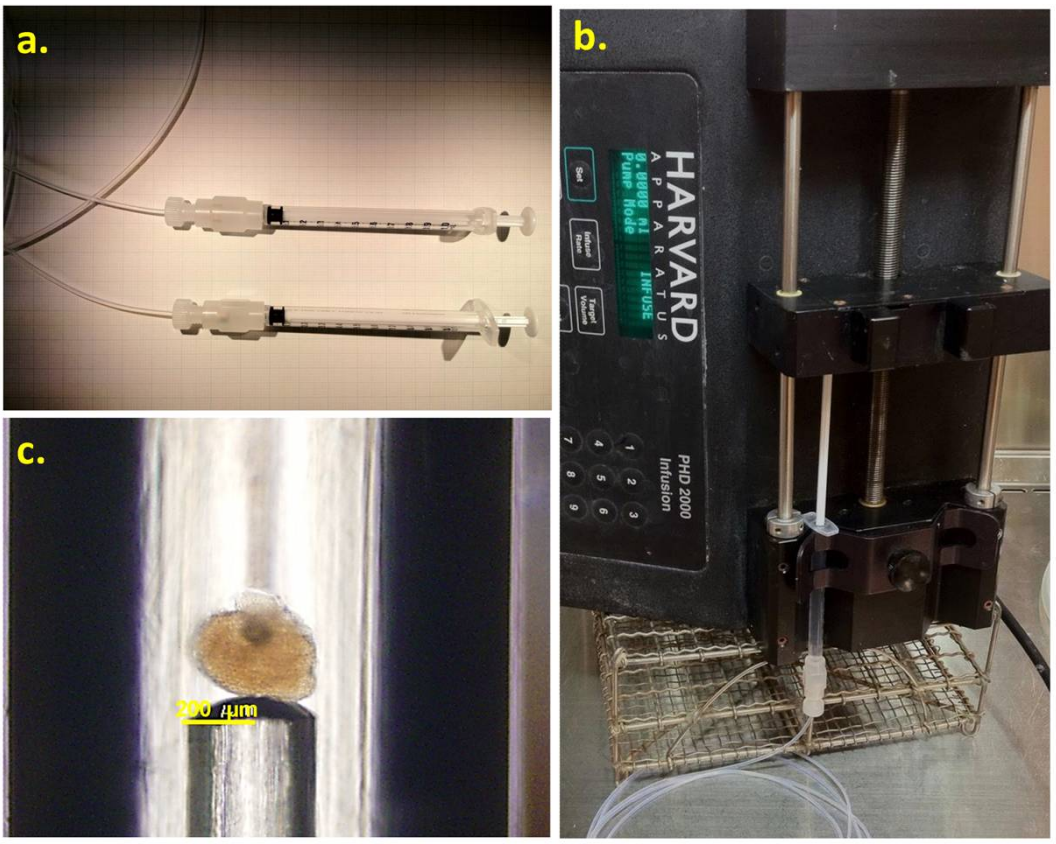

FIGURE A.8: Apparatus for producing laminar fluid shear on cellular aggregates. (a) 5 mm ID 1 mL syringes x2 were connected by 3 m long 400 μm ID polyethylene HPLC tubing. (b) A syringe pump was used to create constant laminar flow through the tubing and exert shear on cell aggregates. (c) A single islet of critical diameter loaded into the tubing. 200 μm scale bar is aligned to show the inner radius.

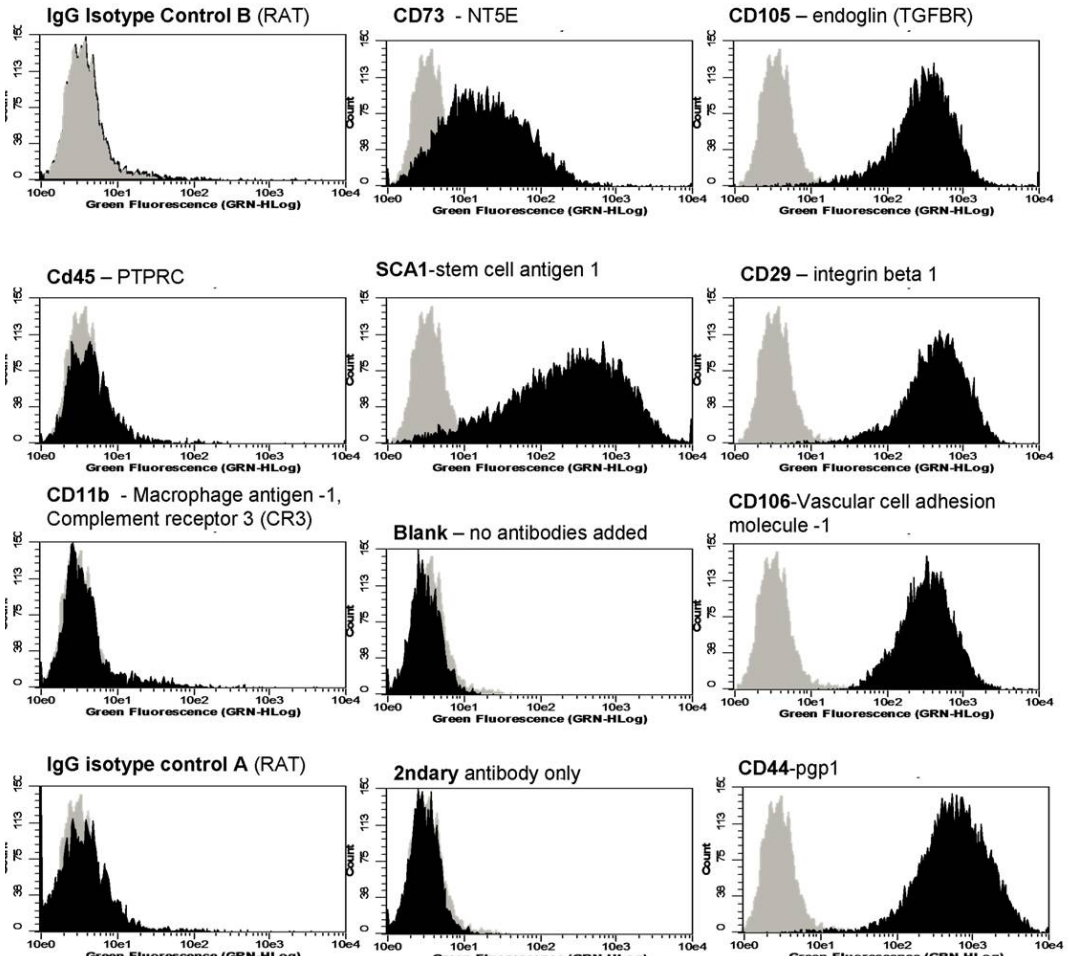

FIGURE A.9: Flow cytometry of MSC's tagged with surface markers. MSC's were cultured for no more than 10 passages and were assessed for their multipotency and purity based on the positive expression of MSC markers CD44, CD29, CD73, CD105, CD106, and Sca-1, and negative expression of CD45 and CD11b. Quality of assessment was verified by negative expression of IgG isotype control A, IgG isotype control B, a secondary antibody-only condition, and a blank with no antibody.

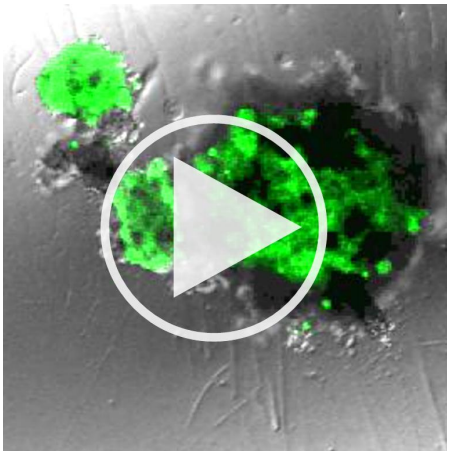

FIGURE A.10: 16 *hr* timelapse of aggregation of a ROCKi$^{[-]}$ co-aggregate. GFP-MSC's and non-GFP islet cells.

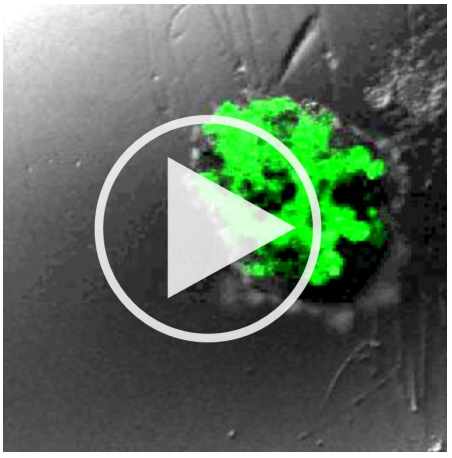

FIGURE A.11: 16 *hr* timelapse of aggregation of a ROCKi$^{[+]}$ co-aggregate. GFP-MSC's and non-GFP islet.

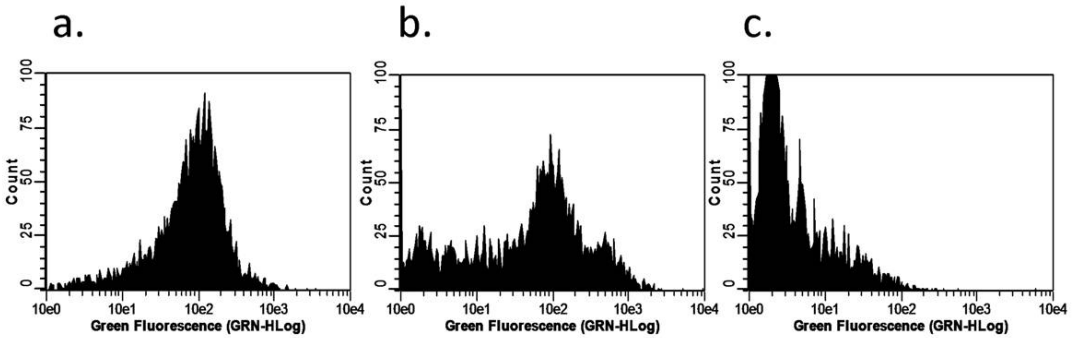

FIGURE A.12: Flow cytometry results for cell proliferation analysis. BrdU was used to verify efficacy of the T-cell/splenocyte proliferation assay. 1 μM bromodeoxyuridine (BrdU) was added to (a) anti-CD3 activated splenocytes, (b) naïve splenocytes, and (c) proliferation-inhibited mitomycin C treated splenocytes. Incubation was carried out for 24 hr, and then cells were washed and fixed with paraformaldehyde, permeabilized by exposure to cold methanol, stained with fluorescently tagged anti-BrdU antibodies, and analyzed via flow cytometry. Activated splenocytes had a larger percentage of BrdU-positive cells indicating proliferation greater than that of naïve splenocytes.

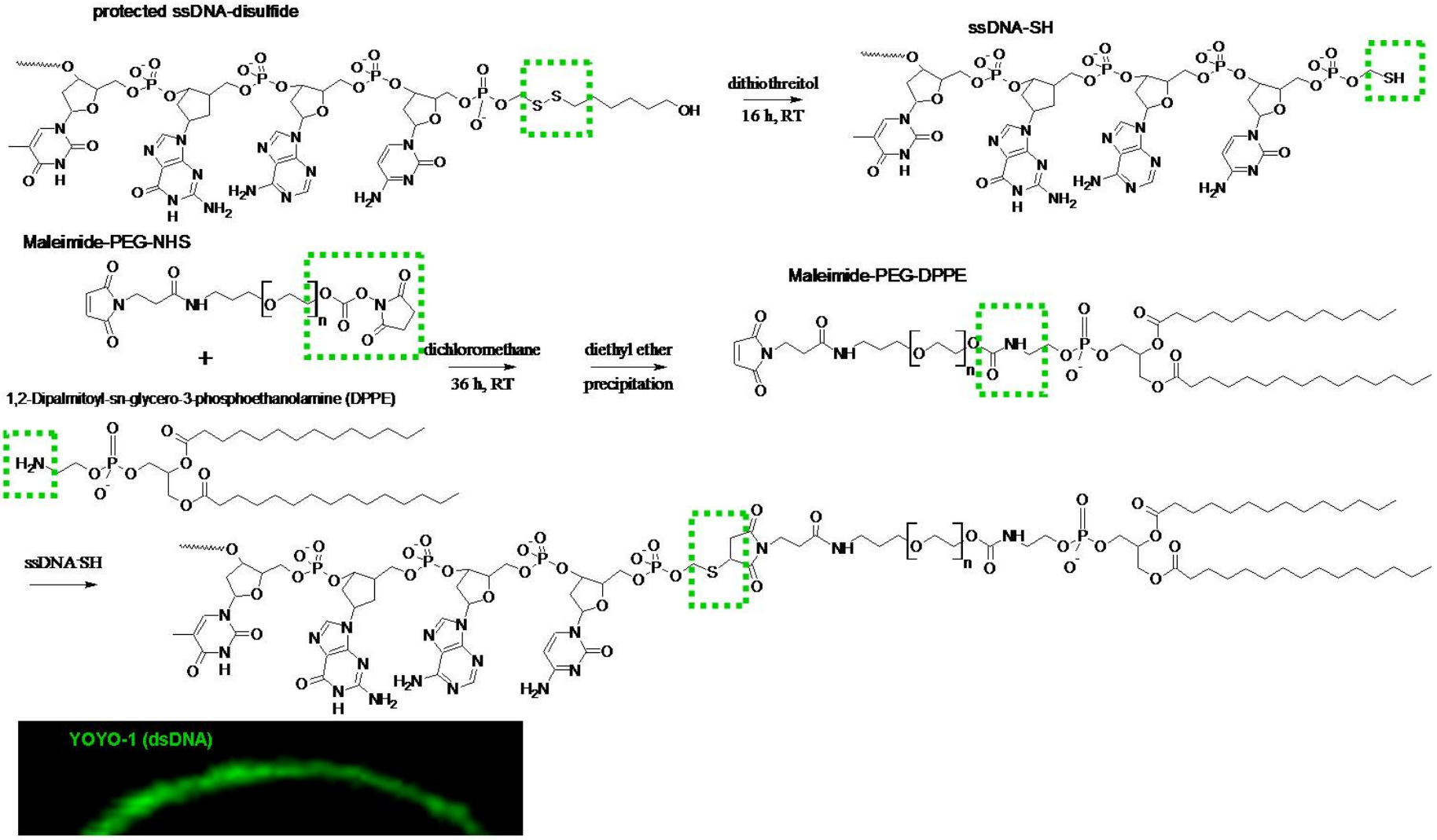

FIGURE A.13: ssDNA-PEG-lipid synthesis process. An example of a cell membrane (via confocal microscopy and YOYO-1 nucleotide dye) modified with ssDNA-PEG-lipid.

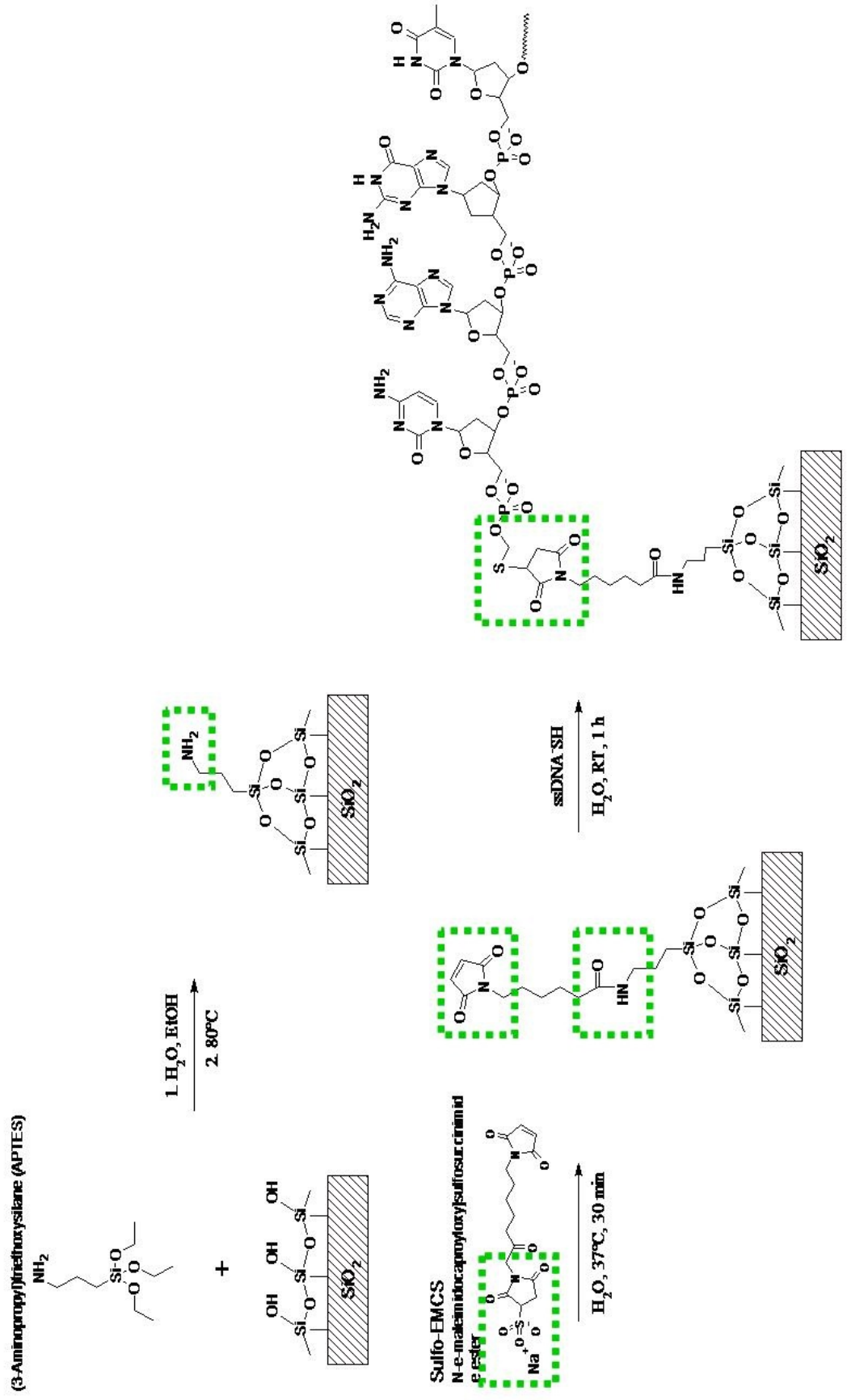

FIGURE A.14: ssDNA grafting to glass surface synthesis procedure.

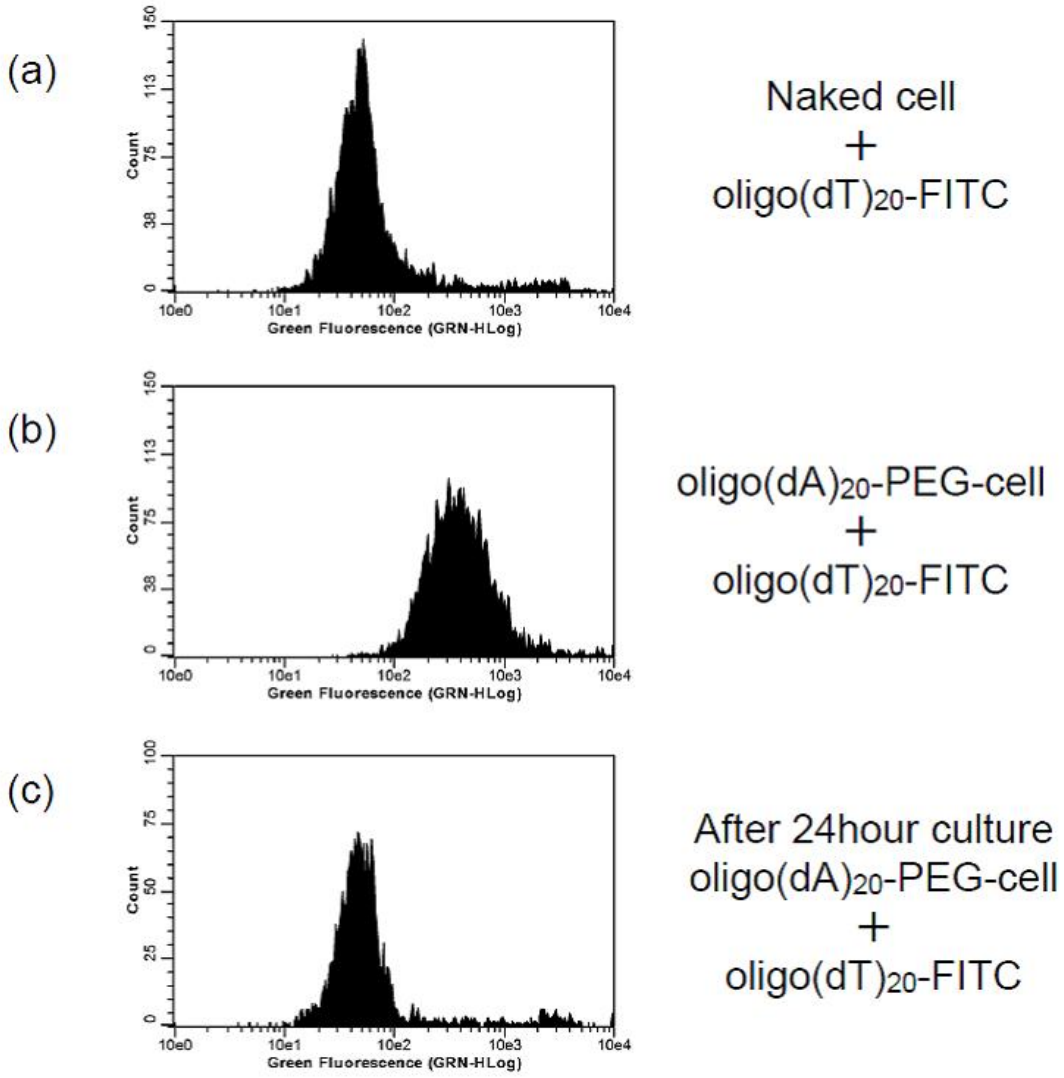

FIGURE A.15: Retention of FITC-labeled oligo-dT_{20} on the cell surface. Cells treated with oligo-dT_{20}-FITC were analyzed by flow cytometry. (a) Naked cells were treated with oligo-dT_{20}-FITC, (b) Oligo-dA_{20}-PEG-cells were analyzed just after treatment with oligo-dT_{20}-FITC, (c) Oligo-dA_{20}-PEG-cells were analyzed at 24 *hr* after treatment with oligo-dT_{20}-FITC.

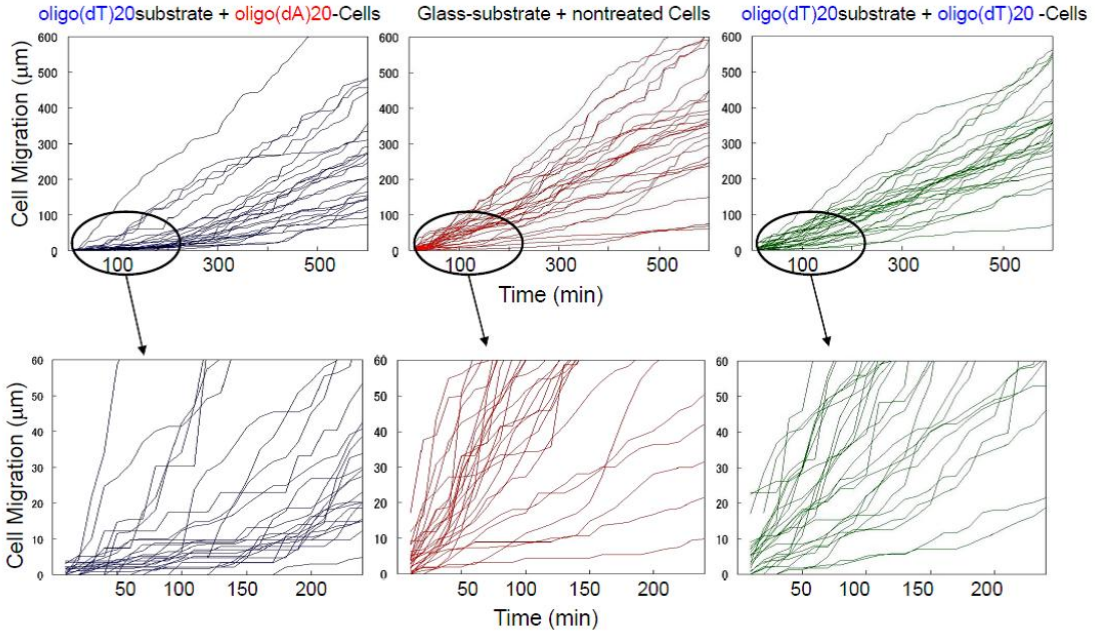

FIGURE A.16: Contour length of cell migration. ssDNA-PEG-cells are seeded on complementary or non-complementary ssDNA-immobilized surfaces, and naked cells are seeded on glass substrates, and they cultured in MEM supplemented with 10% FBS at 37°C. Cell images were captured every 10 *min* for 14 *hr* using an inverted phase contrast microscope. 10 *min* migration contour lengths for each cell were measured and accumulated.

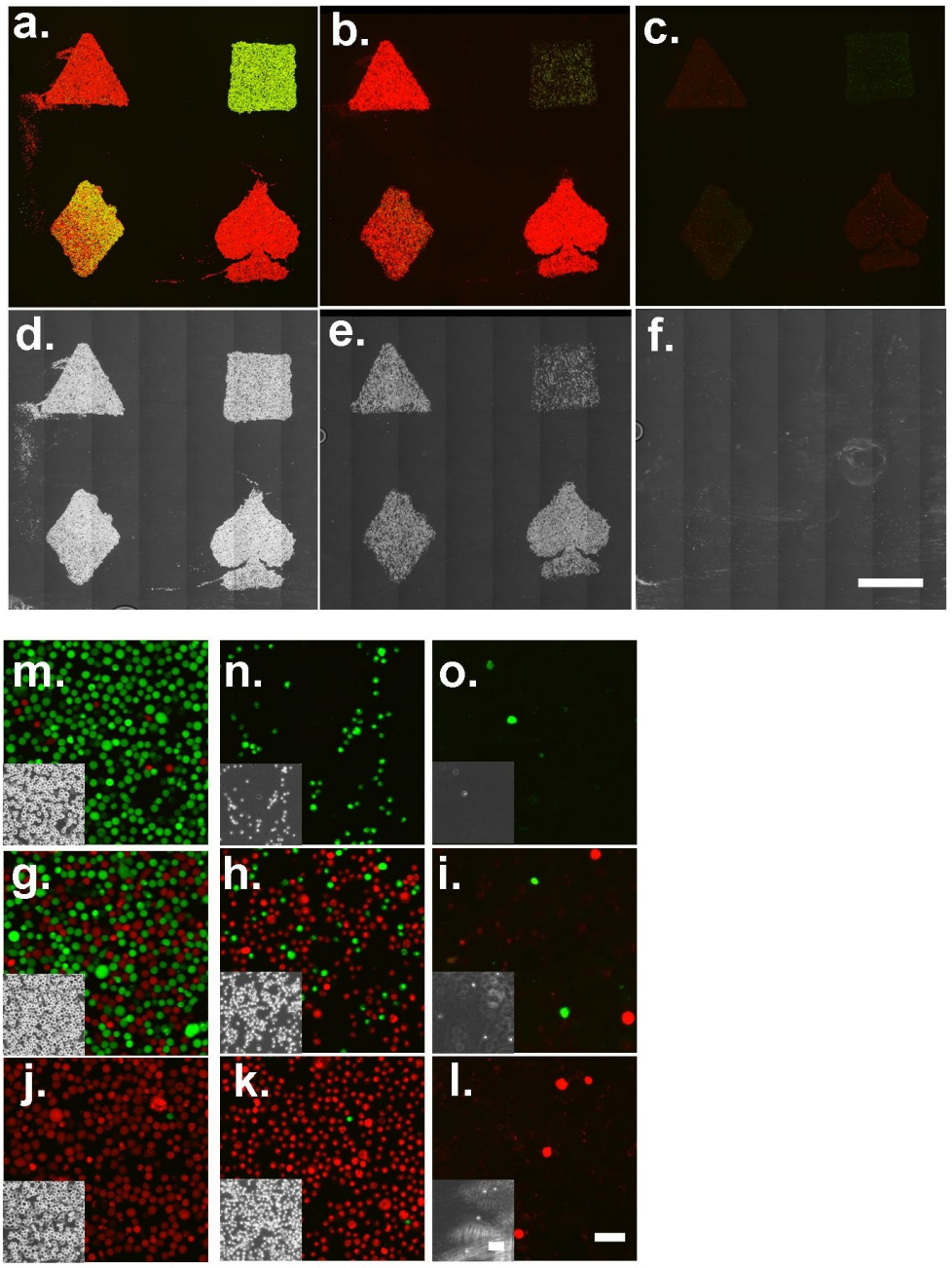

FIGURE A.17: Demo pattern with consecutive EcoRI treatment. (a) Substrate patterned with BB'-cells (green), dAdT-cells (red), and mixed patches of BB' and dAdT-cells prior to enzyme treatment. (b) Cell-patterned substrate after EcoRI exposure and flushing to recover detached cells. (c) Cell-patterned substrate after Benzonase exposure and flushing to recover detached cells. Scale bar: 1.5 *mm* (d-f) Phase contrast images of a-c respectively. (g-i) High magnification images of BB' patch corresponding to a-c respectively. (j-l) High magnification images of mixed patch corresponding to a-c respectively. (m-o) High magnification images of dAdT patch corresponding to a-c respectively. Scale bar: 50 μm.

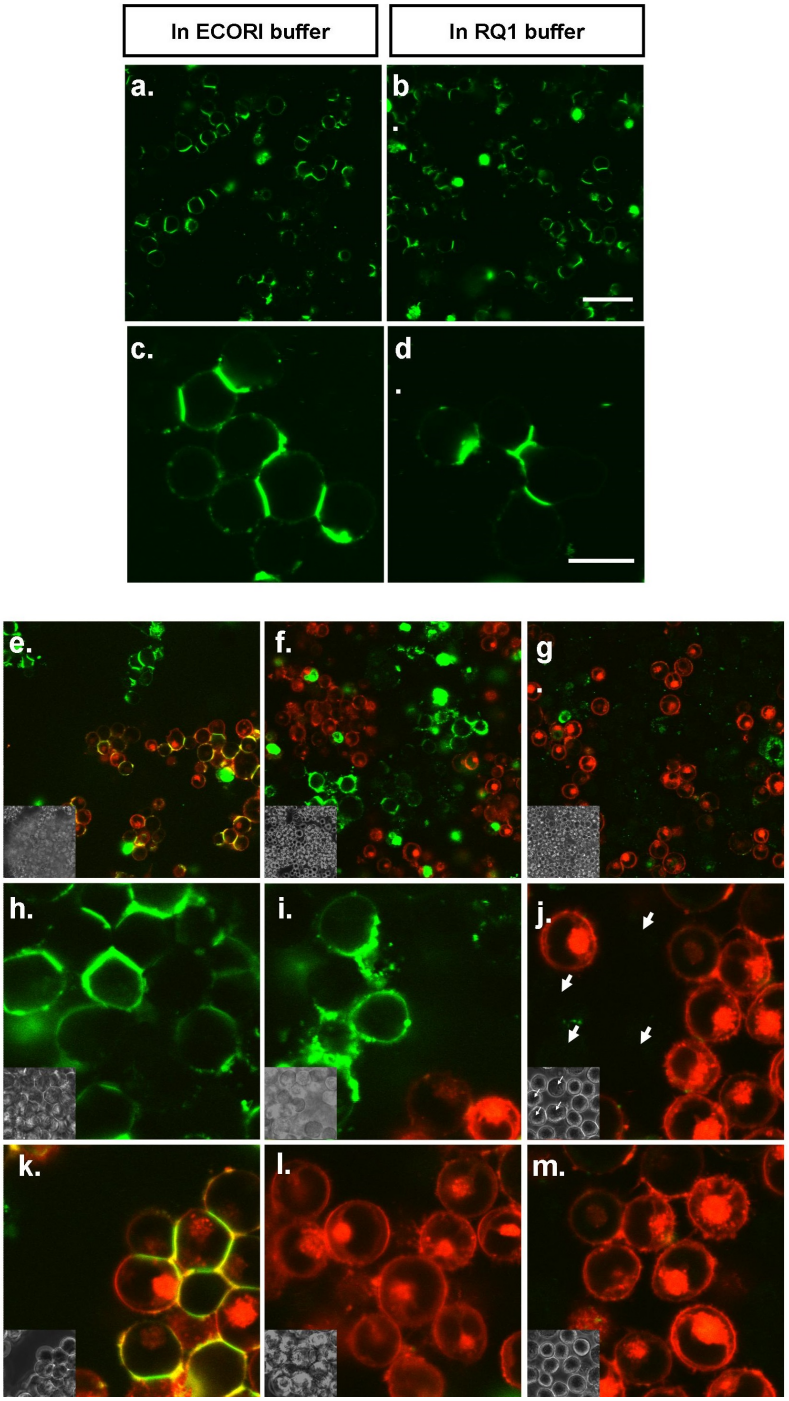

FIGURE A.18: BB'-mediated cellular aggregates treated with nucleases. (a, b) Aggregates subjected to EcoRI incubation conditions and buffer with no EcoRI enzyme. Scale bars: 25 μm and 10 μm respectively (c, d) Aggregates subjected to Benzonase incubation conditions and buffer with no Benzonase enzyme. (e, f, g) Juxtaposed dAdT (YOYO-1 only) and BB' (red PKH-labeled in addition to YOYO-1) aggregates without any nuclease exposure. (h, i, j) Juxtaposed dAdT (YOYO-1 only) and BB' (red PKH-labeled in addition to YOYO-1) aggregates after EcoRI exposure. (k, l, m) Juxtaposed dAdT (YOYO-1 only) and BB' (red PKH-labeled in addition to YOYO-1) aggregates after Benzonase exposure.

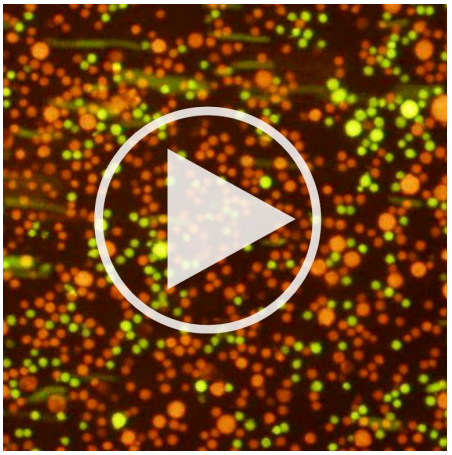

FIGURE A.19: AA' cells (green) are separated from BB' cells (red) by flushing flow chamber following BamHI treatment.

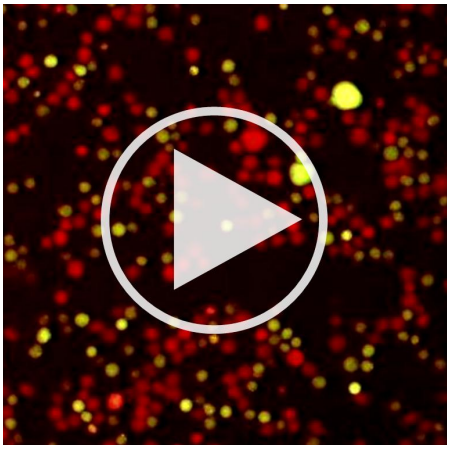

FIGURE A.20: AA' cells (green) and BB' cells (red) are removed at the same time by flushing flow chamber following Benzonase treatment.

A.2 Chapter 3: Supplementary Materials and Methods

A.2.1 Purchased chemicals and antibodies

Complete MSC medium was prepared with 40% (v/v) MCDB 201 medium with L-glutamine (Sigma-aldrich; St Louis, MO, USA), 60% (v/v) minimum essential medium alpha (MEMα 1X) (Life technologies Corporation; Grand Island, NY, USA), 1% insulin transferring selenium solution (Life technologies Corporation; Grand Island, NY, USA), 2 ng/mL PDGF-BB, Human, Recombinant (WAKO Chemicals ltd.; Richmond, VA, USA), 1 ng/mL FGF (WAKO Chemicals ltd.; Richmond, VA, USA), 10 ng/mL EGF (Sigma-aldrich; St Louis, MO, USA), 100 U/mL penicillin and 100 $\mu g/mL$ streptomycin (Nacalai Tesque; Osaka, JP). HBSS(1X) without calcium or magnesium and RPMI medium 1640 1X were purchased from Life Technologies Corporation (Grand Island, NY, USA). 0.25% trypsin/1 mM EDTA solution and 0.05 g/l trypsin/0.53 $mmol/L$ EDTA with phenol red solution were both purchased from Nacalai Tesque (Osaka, JP). Krebs-Ringer buffer solutions containing glucose were prepared with 115 mM NaCl (WAKO Fine Chemicals; Richmond VA, USA), 5.9 mM KCl, 1.2 mM MgCl2, 1.2 mM NaH_2PO_4, 1.2 mM Na_2SO_4, 2.5 mM $CaCl_2$, 25 mM $NaHCO_3$ (Nacalai Tesque; Osaka, JP), 1 g/L bovine serum albumin (Sigma-aldrich; St Louis, MO, USA), and 0.3 or 0.1 g/dL D-(+)-glucose (Nacalai Tesque; Osaka, JP), with pH adjusted to 7.4. Primary antibodies Rat IgG2A isotype control, Rat IgG2B isotype control, rat-anti-mouse Sca-1 mAB, rat-anti-mouse CD106 mAB, rat-anti-mouse CD105 mAB, rat-anti-mouse CD73 mAB, rat-anti-mouse CD29 monoclonal antibody (mAB), rat-anti-mouse CD44 mAB, rat-anti-mouse CD11b mAB, rat-anti-mouse CD45 mAB were purchased from R&D Systems, Inc. (Minneapolis, MN, USA), rabbit-anti-mouse vimentin (D21H3) XP mAB and rabbit-anti-mouse E-cadherin (24E10) mAB were both purchased from Cell Signaling Technology (Boston, MA, USA), and rat-anti-mouse N-cadherin mAB was purchased from abcam (Cambrige, MA, USA), and polyclonal guinea pig-anti-swine insulin was purchased from DAKO (Carpinteria, CA, usa). Polyclonal rabbit-anti-pan-cadherin was purchased from abcam (Cambrige, MA, USA). Secondary antibodies goat-anti-guinea pig Alexa 488, goat-anti-rabbit Alexa 488, donkey-anti-rat Alexa 488, goat-anti-mouse Alexa 488 were purchased from Life Technologies (Grand Island, NY, USA). Hamster-anti-mouse CD3 mAB was purchased from BD Biosciences (San Jose, CA, USA).

A.2.2 Isolation of MSC's

Animal experiments were conducted in accordance with standards approved by the Kyoto University Animal Care Committee. Bone marrow derived mesenchymal stromal cells (MSC's) were isolated according to common protocols[1]. Bone marrow cells were isolated from C57BL/6 mice (Japan SLC, Inc., Shizuoka, Japan) by flushing the tibias and femurs of 8 week-old mice with DMEM containing 10% FBS. Bone marrow cells depleted of erythrocytes by red blood cell lysis buffer (Sigma-aldrich, St Louis, MO, USA) were plated at a density of 5106 cells per cm^2 in complete MSC medium on non tissue culture-treated plates (IWAKI AGT; Tokyo, JP). Non-adherent cells were removed after 48 hours by rinsing gently with HBSS and replacing with complete MSC medium. The cells were grown for 1 week until nearly confluent and then removed using 0.25% trypsin-EDTA solution, diluted 1:2, and seeded on tissue culture treated plates (IWAKI AGT; Tokyo, JP). Media was replaced every 2 days, and the cells were passaged several times at a density of 5,000 cells per cm^2 and were used between 4 and 8 passages. MSC's were analyzed for surface markers using immunohistochemistry and flow cytometry on passage 6 (SFig. A.9).

A.2.3 Isolation of Islets

Islet isolation was carried out as described previously[2]. Islets were isolated from the pancreases of C57BL/6 mice (Japan SLC, Inc., Shizuoka, Japan) using collagenase digestion. Islets were separated from digested pancreas material using discontinuous Ficoll/Conray solutions[3]. Islets were maintained in RPMI 1640 supplemented with 10% FBS, 100 U/mL penicillin, and 100 $\mu g/mL$ streptomycin for 1 day prior to use.

A.2.4 Isolation of Splenocytes

Splenocytes containing multiple immune-associated cell types were isolated from 8 week-old male BALB/c mice. Spleens were crushed between two glass slides with frosted surfaces and collected in RPMI medium. The resulting tissue was filtered thrice through 40 μm cell strainers (BD Biosciences; San Jose, CA, USA) and then depleted of red blood cells using lysis buffer. The splenocytes were resuspended and cultured in RPMI

[1] Alexandra Peister et al. "Adult stem cells from bone marrow (MSCs) isolated from different strains of inbred mice vary in surface epitopes, rates of proliferation, and differentiation potential". In: *Blood* 103.5 (2004), pp. 1662–1668.

[2] Nguyen Minh Luan, Yuji Teramura, and Hiroo Iwata. "Immobilization of the soluble domain of human complement receptor 1 on agarose-encapsulated islets for the prevention of complement activation". In: *Biomaterials* 31.34 (2010), pp. 8847–8853.

[3] Paul E Lacy and Mery Kostianovsky. "Method for the isolation of intact islets of Langerhans from the rat pancreas". In: *Diabetes* 16.1 (1967), pp. 35–39.

containing 10% FBS, 100 U/mL penicillin, and 100 $\mu g/mL$ streptomycin. Experiments were performed within 24 hr of splenocyte isolation.

A.2.5 Flow Cytometry and Surface Marker Verification

10^6 MSC's were treated with trypsin after 6 passages and separated into groups corresponding to each antibody, washed, and each pelleted. Pellets were dispersed in primary antibody-containing solutions at concentrations according to manufacturers' instructions. The antibody reaction was carried out at 4°C for 45 min in 10% FBS containing RPMI 1640. Cells were washed 3 times and repelleted. Cells were resuspended in secondary antibody containing solutions according to the manufacturers' instructions and incubated at 4°C for 45 min in 10% FBS containing RPMI 1640. Cells were finally washed 3 times and resuspended in 400 μL RPMI with 10% FBS. Cell suspensions were analyzed using a Guava Easy-cyte mini flow cytometer (Millipore; Billerica, MA, USA) according to manufacturer instructions.

A.2.6 Immunostaining

Aggregates were first fixed in 4% paraformaldehyde solution, rinsed in HBSS, and concentrated at the bottom of a PCR tube containing heat activated 2.5% agarose (SeaKem GTG Agarose; Camrex Bio Science Rockland Inc.; Rockland, ME, USA) solution maintained at 37°C. Cones of agarose-containing aggregates were chilled and suspended in Tissue-Tek embedding medium (Sakura Finetek USA; Torrance, CA, USA) and frozen at -30°C. Samples were cryo-sectioned into 6 μm sections. Slides were then stained for E-cadherin, N-cadherin, insulin, vimentin, and CD-44 expression. Briefly, slides were blocked in a Blocking 1 solution (Nacalai Tesque; Osaka, JP) for 1 hr. Slides were then immunostained with primary antibodies (100x dilution in Blocking 1 solution) overnight at 4°C. After primary antibody incubation, slides were rinsed twice and immunostained secondary antibodies (200x dilution in Blocking 1 solution) for 1 hr at RT. Slides were then counterstained with nuclear Hoechst 33258 (Dojindo Laboratories; Kumamoto, JP) and imaged with an Olympus BX51 non-inverted fluorescence microscope (Olympus; Tokyo, JP). Pan-cadherin staining was applied to PFA-fixed whole aggregates. Aggregates were stained with pan-cadherin antibody solution (100x dilution in Blocking 1 solution) and then secondary antibody solution (200x dilution in Blocking 1 solution) for 1 hour each with sequential rinses in between each stage. Fixed, stained aggregates were then imaged with confocal microscopy.

A.2.7 Timelapse Confocal Microscopy

A microscope-objective-sized 2x2 well square was cut from a non-tissue culture treated 96 well U- bottom plate (Becton Dickinson, FR) and then treated with 150 $\mu L/well$ sterile PLURONIC F-127 (Sigma) 2% solution in PBS overnight at 37°C. PLURONIC solution was aspirated and wells were washed five times sequentially with PBS (200 $\mu L/rinse$). Cell suspensions of dispersed islets and trypsinized MSC's were prepared as described in the materials and methods section of this manuscript. A final cell suspension of 150 μL was pipetted into a single well to be imaged. The 2x2 square was then centrifuged at 200 x g for 5 min and placed over the 10x objective of a laser scanning Olympus IX81 confocal microscope (Olympus, Tokyo, JP) and covered in a humidified, 37°C incubated chamber with 5% CO_2. Images were captured every 2 min for 16 hr.

A.3 Chapter 6: Code for Theoretical Computations

A.3.1 Code for producing Fig. 6.1d and Fig. 6.3d

```
from __future__ import division
import numpy as np
import math as math
import matplotlib.pyplot as plt
import scipy.optimize as optimize
from matplotlib import cm
from matplotlib import colors
from mpl_toolkits.mplot3d import Axes3D
from matplotlib.ticker import LinearLocator, FormatStrFormatter
# Description: This program produces three plots:

### fig4: [V, Vrep, Vadh vs xij vs Gamma](heatmap = dV/ddij) ;
### fig6: [Asteadystate vs gamma vs xij](heatmap = dV/ddij) ;
### fig7: [dVddij(heatmap) vs xij vs gamma ]

# the program fixes the volume of the cell based on the radius of a cell in isolation (Ri_value) and (Rj_value)
# if they are set to 6 um, then this corresponds roughly to a cell of 900 um3 volume
# the nelder mead downhill simplex algorithm (optimize.fmin) is used to adjust the radius of the cell doublet
# if this is not done, then the radius will not change with different levels of deformation,
# and volume will not be conserved



######### PARAMETER VALUES ################
Ri_value = 6e-6 #meters #the radius of an isolated cell of interest eg: 6 um
Rj_value = 6e-6 #meters #the radius of
Youngs_Modulus = 855 #pascal
Poissons_Ratio = 0.5 #unitless
Gammalimit = -1e-3
squaresize = 40 #minimum size is 40, maximum (due to computation time limt) around 300, nominal size either 100 or 200
dij = np.linspace(3e-6, (Ri_value+Rj_value), num=squaresize)

def pp(x, y): #defines a power function that accepts nan without returning math domain value error aka pow with nan
    try:
      return math.pow(x, y)
    except ValueError:
      return float(0)


def vol_error(radii): ######### volume error calculator function to be minimized ######
    radiusi = radii[0]
    radiusj = radii[1]
    chordaij = (1/dij[row])*pp((4*pp(dij[row], 2)*pp(radiusi, 2)-pp((pp(dij[row], 2)-pp(radiusj, 2)+pp(radiusi, 2)), 2)), 0.5)
    heighti = radiusj-pp((pp(radiusj, 2)-pp((chordaij/2), 2)), 0.5)
    heightj = radiusi-pp((pp(radiusi, 2)-pp((chordaij/2), 2)), 0.5)
    Volumei = (4/3)*np.pi*pp(radiusi, 3)
    Volumej = (4/3)*np.pi*pp(radiusj, 3)
    Volumei_cap = (1/3) *np.pi * pp(heighti, 2)*(3*radiusi - heighti)
    Volumej_cap = (1/3) *np.pi * pp(heightj, 2)*(3*radiusj - heightj)
    Volumei_cell = Volumei - Volumei_cap
    Volumej_cell = Volumej - Volumej_cap
    Volumei_target = (4/3)*np.pi*pp(Ri_value, 3)
    Volumej_target = (4/3)*np.pi*pp(Rj_value, 3)
    Volume_error = pp((Volumei_cell - Volumei_target), 2) + pp((Volumej_cell - Volumej_target), 2)
    return Volume_error


#THE MASTER LOOP! FOR CALCULATING A ROUND OF ACONTACT, ENERGIES, COHESION GIVEN RI RJ and DIJ
Gamma = np.linspace(Gammalimit, 0, num=len(dij)) #a range of cohesion values in SI
Gammaerg = np.linspace(Gammalimit*1000, 0, num=len(dij))

########################## COORDINATE ARRAYS ##############################
xs = np.zeros(len(dij)*len(Gamma))
ys = np.zeros(len(dij)*len(Gamma))
zsr = np.zeros(len(dij)*len(Gamma))
zsa = np.zeros(len(dij)*len(Gamma))
zsn_neg = np.zeros(len(dij)*len(Gamma))
zsn_pos = np.zeros(len(dij)*len(Gamma))
zsdVddij_neg = np.zeros(len(dij)*len(Gamma))
zsdVddij_pos = np.zeros(len(dij)*len(Gamma))
zsacontact_neg = np.zeros(len(dij)*len(Gamma))
zsacontact_pos = np.zeros(len(dij)*len(Gamma))
zdVroot = np.zeros(len(dij)*len(Gamma))

#surface plot vectors
```

```
    Zsr = np.zeros(shape=(len(Gamma),len(dij)))
    Zsa = np.zeros(shape=(len(Gamma),len(dij)))
    Zsn_neg = np.zeros(shape=(len(Gamma),len(dij)))
    Zsn_pos = np.zeros(shape=(len(Gamma),len(dij)))
    Zsn = np.zeros(shape=(len(dij),len(dij)))
    ZsdVddij_neg = np.zeros(shape=(len(Gamma),len(dij)))
    ZsdVddij_pos = np.zeros(shape=(len(Gamma),len(dij)))
    Zsacontact_neg = np.zeros(shape=(len(Gamma),len(dij)))
    Zsacontact_pos = np.zeros(shape=(len(Gamma),len(dij)))
    ZdVroot = np.zeros(shape=(len(Gamma),len(dij)))
    ZV_net_pj = np.zeros(len(Gamma))
    ZAcontactequil = np.zeros(len(Gamma))

    xderivative =  np.zeros(len(Gamma))
    yderivative =  np.zeros(len(Gamma))
    Zacontact = np.zeros(shape=(len(Gamma),len(dij)))
    ZdVddij = np.zeros(shape=(len(Gamma),len(dij)))
    normZdVddij = np.zeros(shape=(len(Gamma),len(dij)))


    ##### ROOT STORAGE ARRAYS - arrays of zeros and 1 value per gamma corresponding to the energy derivative root
     #####
    Aequil_um = np.zeros(len(dij)*len(Gamma))
    dVddijequil_nN = np.zeros(len(dij)*len(Gamma))
    V_net_pj_equil = np.zeros(len(dij)*len(Gamma))
    Ri_equil = np.zeros(len(Gamma))
    Rj_equil = np.zeros(len(Gamma))
    #Ri0_error = np.zeros(len(Gamma))
    #Rj0_error = np.zeros(len(Gamma))
    #Ri_guess=np.empty(len(Gamma)); Ri_guess.fill(Ri_value)
    #Rj_guess=np.empty(len(Gamma)); Rj_guess.fill(Rj_value)
    #zsdVddijlog = np.zeros(len(dij)*len(Gamma))
    index = 0

    ######################### GAMMA LOOP define several arrays that will vary with gamma
     ##############################

    for col in range(0, len(Gamma)):
        Ri = np.zeros(len(dij))
        Ri_um = np.zeros(len(dij))
        Rj = np.zeros(len(dij))
        Rj_um = np.zeros(len(dij))
        aij = np.zeros(len(dij))
        aij_um = np.zeros(len(dij))
        xij = np.zeros(len(dij))
        xij_um = np.zeros(len(dij))
        V_rep = np.zeros(len(dij)) #joules - repulsive term of interfacial energy Hertz model, Landau and Lifshitz 1986
        V_rep_pj = np.zeros(len(dij)) #picojoules
        A_contact = np.zeros(len(dij)) # the area of the contact surface in m2
        A_contact_um = np.zeros(len(dij)) #um2
        V_adh = np.zeros(len(dij))
        V_adh_pj = np.zeros(len(dij))
        V_net = np.zeros(len(dij))
        V_net_pj = np.zeros(len(dij))
        dVddij = np.zeros(len(dij))
        dVddij_nN = np.zeros(len(dij))
        hi = np.zeros(len(dij))
        #hi_um = np.zeros(len(dij))
        hj = np.zeros(len(dij))
        #hj_um = np.zeros(len(dij))
        Voli = np.zeros(len(dij))
        Volj = np.zeros(len(dij))
        Voli_cap = np.zeros(len(dij))
        Volj_cap = np.zeros(len(dij))
        Voli_cell = np.zeros(len(dij))
        Volj_cell = np.zeros(len(dij))
        #Ri_0 = np.zeros(len(dij))
        #Rj_0 = np.zeros(len(dij))

        ######################### dij LOOP ##############################

        for row in range(0, len(dij)):
            Rs_guess = np.array([Ri_value, Rj_value])
            Rs = optimize.fmin(vol_error, Rs_guess, xtol = 1e-10)
            Ri[row] = Rs[0] #populate Ri array with a fixed radius value
            Rj[row] = Rs[1]
            Ri_um[row] = Ri[row]*10**6
```

```
        Rj_um[row] = Rj[row]*10**6

        aij_row = (1/dij[row])*pp((4*pp(dij[row], 2)*pp(Ri[row], 2)-pp((pp(dij[row], 2)-pp(Rj[row], 2)+pp(Ri[row], 2)), 2)), 0.5)
        aij[row] = aij_row
        aij_um[row] = aij_row*10**6

        xij[row] = Ri[row]+Rj[row]-dij[row] #the indentation depth - aka the penetration of the intersecting spehres
        xij_um[row] = xij[row]*10**6 #microns

        V_rep_row = (2/15)*pp((Ri[row]+Rj[row]-dij[row]), (2.5))*pp(((1-Poissons_Ratio)/Youngs_Modulus), (-1))*pp(((Ri[row]*Rj
    [row])/(Ri[row]+Rj[row])), (1/2))
        V_rep[row] = V_rep_row
        V_rep_pj[row] = V_rep_row*10**12

        A_contact[row] = math.pi*pp((aij_row/2), 2)
        A_contact_um[row] = A_contact[row]*10**12

        V_adh[row] = Gamma[col]*A_contact[row]
        V_adh_pj[row] = V_adh[row]*10**12

        V_net[row] = V_adh[row]+V_rep[row]
        V_net_pj[row] = V_net[row]*10**12

        dVddij[row] = ((-Gamma[col]*math.pi)/(2*pp(dij[row], 3)))*(pp(dij[row], 4)-pp((pp(Ri[row], 2)-pp(Rj[row], 2)), 2))-(1/3)*(
    Youngs_Modulus/(1-pp(Poissons_Ratio, 2)))*pp(((Ri[row]*Rj[row])/(Ri[row]+Rj[row])), 0.5)*pp((Ri[row]+Rj[row]-dij[row]), 1.5)
        dVddij_nN[row] = dVddij[row]*10**9

        ############### Optional VOLUME CALCULATIONS ############################
        hi[row] = Rj[row]-pp((pp(Rj[row], 2)-pp((aij[row]/2), 2)), 0.5)
        hj[row] = Ri[row]-pp((pp(Ri[row], 2)-pp((aij[row]/2), 2)), 0.5)
        Voli[row] = (4/3)*np.pi*pp(Ri[row], 3)
        Volj[row] = (4/3)*np.pi*pp(Rj[row], 3)
        Voli_cap[row] = (1/3) *np.pi * pp(hi[row], 2)*(3*Ri[row] - hi[row])
        Volj_cap[row] = (1/3) *np.pi * pp(hj[row], 2)*(3*Rj[row] - hj[row])
        Voli_cell[row] = Voli[row] - Voli_cap[row]
        Volj_cell[row] = Volj[row] - Volj_cap[row]


        ##################AXIS ARRAYS FOR PLOTTING IN TERMS OF UNIQUE INDEX FOR EACH STATE (IE STATE
    ID)#################
        xs[index] = xij_um[row]
        ys[index] = Gammaerg[col]
        zsr[index] = V_rep_pj[row]
        zsa[index] = V_adh_pj[row]
        if dVddij[row] < 0:
            zsdVddij_neg[index] = dVddij_nN[row]
            zsacontact_neg[index] = A_contact_um[row]
            normZdVddij[col,row] = (ZdVddij[col,row])/-(np.min(ZdVddij))
        else:
            zsdVddij_pos[index] = dVddij_nN[row]
            zsacontact_pos[index] = A_contact_um[row]
            normZdVddij[col,row] = (ZdVddij[col,row])/(np.max(ZdVddij))

        if V_net_pj[row]<0:
            zsn_neg[index] = V_net_pj[row]
        else:
            zsn_pos[index] = V_net_pj[row]




        ##### DERIVATIVE ROOT LOCATOR TEST ###############
        if abs(dVddij[row-1]) != dVddij[row-1] and abs(dVddij[row]) == dVddij[row]:
            Aequil_um[index] = A_contact_um[row]
            dVddijequil_nN[index] = dVddij_nN[row]

            ZV_net_pj[col] = V_net_pj[row] #vectors by column for the derivative root tracing line in all plots
            xderivative[col] = xij_um[row]
            yderivative[col] = Gammaerg[col]
            ZAcontactequil[col] = A_contact_um[row]

            V_net_pj_equil[index] = V_net_pj[row]
            Ri_equil[col] = Ri[row]
            Rj_equil[col] = Rj[row]
```

```
        index = index + 1 #this makes a unique state ID for every point in the 2D space of gamma and  dij

        Zsr[col,row] = V_rep_pj[row] #2D matrices containing energies for the surface plot
        Zsa[col,row] = V_adh_pj[row]
        Zsn[col,row] = V_net_pj[row]
        Zacontact[col,row] = A_contact_um[row]
        ZdVddij[col,row] = dVddij_nN[row]




for col in range(0, len(Gamma)):
    for row in range(0, len(dij)):
        if dVddij[row] < 0:
            normZdVddij[col,row] = (ZdVddij[col,row])/-(np.min(ZdVddij))
        else:
            normZdVddij[col,row] = (ZdVddij[col,row])/(np.max(ZdVddij))
        normZdVddij[col,row] = (normZdVddij[col,row]+1)/2

Zsn_pos[Zsn_pos == 0.0] = np.nan #removing zeros in the surface plot energy matrices
Zsn_neg[Zsn_neg == 0.0] = np.nan
Zsr[Zsr == 0.0] = np.nan
Zsa[Zsa == 0.0] = np.nan
Zsn[Zsn == 0.0] = np.nan
Zacontact[Zacontact == 0.0] = np.nan


Xs = np.linspace(xij_um[0], xij_um[len(dij)-1], num=squaresize)
Ys = np.linspace(Gammaerg[0],Gammaerg[len(Gammaerg)-1], num=squaresize)
Xs, Ys = np.meshgrid(Xs, Ys)


########################## REMOVE ZEROS FOR PLOTS otherwise you get plateaus and cliffs
 ##############################
Aequil_um[Aequil_um == 0.0] = np.nan
dVddijequil_nN[dVddijequil_nN == 0.0] = np.nan
V_net_pj_equil[V_net_pj_equil == 0.0] = np.nan
zsn_pos[zsn_pos == 0.0] = np.nan
zsn_neg[zsn_neg == 0.0] = np.nan
xs[xs < 0] = np.nan
zsr[zsr == 0.0] = np.nan
zsdVddij_neg[zsdVddij_neg == 0.0] = np.nan
zsdVddij_neg[zsdVddij_neg < -5e1] = np.nan
zsdVddij_pos[zsdVddij_pos == 0.0] = np.nan
zsacontact_neg[zsacontact_neg == 0.0] = np.nan
zsacontact_pos[zsacontact_pos == 0.0] = np.nan



########################## PLOTS ##############################


cdict = {'red':   ((0,    0, 0),  #i.e. at value 0, red component is 0. First parameter is the value, second is the color component.
Ignore the third parameter, it is for discontinuities.
                   (.5,  1, 1),  #     at value 0.5, red component is 1.
                   (1,    1, 1)), #     at value 1, red component is 1
         'green': ((0,    0, 0),
                   (.5,  1, 1),
                   (1,    0, 0)),
         'blue':  ((0,    1, 1),
                   (.5,  1, 1),
                   (1,    0, 0))}

cmap1 = colors.LinearSegmentedColormap('UWR',cdict,256)
cm.register_cmap(name='UWR', cmap=cmap1)
UWR = cm.get_cmap('UWR')

#############################################################################

# Create a variable for the colorbar
m = cm.ScalarMappable(cmap='RdBu')
m.set_array(ZdVddij)
fig6 = plt.figure()
# ax8 = fig6.add_subplot()
```

```
ax6 = fig6.add_subplot(111, projection='3d')
# ax8 = fig6.gca(projection='3d')
ax6.set_xlabel(r'x$_{ij} $[$\mu m$]')
ax6.set_ylabel(r'$\gamma$ $[ \frac{erg}{cm^2} ]$')
ax6.set_zlabel(r'$A_{CONTACT}$ $[\mu m^2]$')
ax6.set_xlim(0,xij_um[0])
ax6.plot_surface(Xs, Ys, Zacontact, rstride=int(squaresize/40), cstride=int(squaresize/40), alpha=1,facecolors=cm.RdBu(
normZdVddij), linewidth=.1, antialiased=False, shade=False)
# ax8.plot(xderivative, yderivative, ZAcontactequil, ls="-", ms=0,lw=2, c="#FF9933")
cbar = fig6.colorbar(m, ticks=[np.min(ZdVddij),((abs(np.min(ZdVddij))+abs(np.max(ZdVddij)))/2)+np.min(ZdVddij),np.max(
ZdVddij)], shrink=0.85)
cbar.set_label(r'$\frac{dV}{dd_{ij}} [nN]$',size=30)
cbar.ax.tick_params(labelsize=15)
cbar.set_ticklabels([round(np.min(ZdVddij),0),0,round(np.max(ZdVddij),0)])
for item in ([ax6.title, ax6.xaxis.label, ax6.yaxis.label, ax6.zaxis.label] +
        ax6.get_xticklabels() + ax6.get_yticklabels() + ax6.get_zticklabels()):
    item.set_fontsize(30)
for item in (ax6.get_xticklabels() + ax6.get_yticklabels() + ax6.get_zticklabels()):
    item.set_fontsize(15)

fig4 = plt.figure()
ax4 = fig4.add_subplot(111, projection='3d')
# ax5 = fig4.gca(projection='3d')
ax4.set_xlabel(r'x$_{ij} $[$\mu m$]')
ax4.set_ylabel(r'$\gamma$ $[ \frac{erg}{cm^2} ]$')
ax4.set_zlabel(r'$V$ $[pJ]$')
ax4.set_xlim(0,xij_um[0])
ax4.plot_surface(Xs, Ys, Zsa, rstride=int(squaresize/40), cstride=int(squaresize/40), alpha=.5,color='#3366FF',linewidth=.1,
antialiased=True, vmin=-.15,vmax=.15)
ax4.plot_surface(Xs, Ys, Zsn, rstride=int(squaresize/40), cstride=int(squaresize/40), alpha=1,facecolors=cm.RdBu(
normZdVddij),linewidth=0, antialiased=True, vmin=-.15,vmax=.15, shade=False)
# ax5.plot(xderivative, yderivative, ZV_net_pj, ls="-", ms=0,lw=2, c="#FF9933")
ax4.plot_surface(Xs, Ys, Zsr, rstride=int(squaresize/40), cstride=int(squaresize/40), alpha=.5,color='#CC3333',linewidth=.1,
antialiased=True, vmin=-.15,vmax=.15)
cbar4 = fig4.colorbar(m, ticks=[np.min(ZdVddij),((abs(np.min(ZdVddij))+abs(np.max(ZdVddij)))/2)+np.min(ZdVddij),np.max(
ZdVddij)], shrink=0.85)
cbar4.set_label(r'$\frac{dV}{dd_{ij}} [nN]$',size=30)
cbar4.ax.tick_params(labelsize=15)
cbar4.set_ticklabels([round(np.min(ZdVddij),0),0,round(np.max(ZdVddij),0)])
for item in ([ax4.title, ax4.xaxis.label, ax4.yaxis.label, ax4.zaxis.label] +
        ax4.get_xticklabels() + ax4.get_yticklabels() + ax4.get_zticklabels()):
    item.set_fontsize(30)
for item in (ax4.get_xticklabels() + ax4.get_yticklabels() + ax4.get_zticklabels()):
    item.set_fontsize(15)


fig7 = plt.figure()
ax7 = fig7.add_subplot(111, projection='3d')
# ax7 = fig7.gca(projection='3d')
ax7.set_xlabel(r'x$_{ij} $[$\mu m$]')
ax7.set_ylabel(r'$\gamma$ $[ \frac{erg}{cm^2} ]$')
ax7.set_zlabel(r'$\frac{dV}{dd_{ij}} [nN]$')
ax7.set_xlim(0,xij_um[0])
ax7.plot_surface(Xs, Ys, ZdVddij, rstride=int(squaresize/40), cstride=int(squaresize/40), alpha=1,cmap='UWR', vmin=-20,
vmax=20,linewidth=.1, antialiased=True)#, vmin=min(A_contact_um),vmax=max(A_contact_um))
#ax6.plot(xderivative, yderivative, ZAcontactequil, ls="-", ms=0,lw=2, c="#FF9933")
for item in ([ax7.title, ax7.xaxis.label, ax7.yaxis.label, ax7.zaxis.label] +
        ax7.get_xticklabels() + ax7.get_yticklabels() + ax7.get_zticklabels()):
    item.set_fontsize(30)
for item in (ax7.get_xticklabels() + ax7.get_yticklabels() + ax7.get_zticklabels()):
    item.set_fontsize(15)


plt.show()
```

A.3.2 Code for producing Fig. 6.2e

```
from __future__ import division
import numpy as np
import math as math
import matplotlib.pyplot as plt
import scipy.optimize as optimize
from matplotlib import cm
from matplotlib import colors
import matplotlib as mpl
from mpl_toolkits.mplot3d import Axes3D
from matplotlib.ticker import LinearLocator, FormatStrFormatter
import time

# Description: This program produces a single plot:
### fig9:[SteadStateAContact vs Gamma vs YoungsModulus]
# Instead of fixing Youngs Modulus as a parameter value and calculating energy or Acontact as a fn of indentation depth,
# a point on this plot corresponds to the minimum energy well (dVddij = 0) of Acontact, thus it plots the steadystate
# Warning - the parameter value for "squaresize" has a major impact on computation time. 20 takes about 30 seconds
# But squaresize = 100 or 200 will require running overnight to complete and will produce much smoother plots

start_time = time.time()

######### PARAMETER VALUES ################
Ri_value = 6e-6 #meters #the radius of an isolated cell of interest eg: 6 um
Rj_value = 6e-6 #meters #the radius of
Poissons_Ratio = 0.5 #unitless
Gammalimit = -1e-3
squaresize = 20 #minimum size is 20, maximum (due to computation time limitations) around 300, nominal size either 100 or
 200
dij = np.linspace(3e-6, (Ri_value+Rj_value), num=squaresize)

def pp(x, y): #defines a power function that accepts nan without returning math domain value error aka pow with nan
    try:
      return math.pow(x, y)
    except ValueError:
      return float(0)


def vol_error(radii): ######### volume error calculator function to be minimized ######
    radiusi = radii[0]
    radiusj = radii[1]
    chordaij = (1/dij[row])*pp((4*pp(dij[row], 2)*pp(radiusi, 2)-pp((pp(dij[row], 2)-pp(radiusj, 2)+pp(radiusi, 2)), 2)), 0.5)
    heighti = radiusj-pp((pp(radiusj, 2)-pp((chordaij/2), 2)), 0.5)
    heightj = radiusi-pp((pp(radiusi, 2)-pp((chordaij/2), 2)), 0.5)
    Volumei = (4/3)*np.pi*pp(radiusi, 3)
    Volumej = (4/3)*np.pi*pp(radiusj, 3)
    Volumei_cap = (1/3) *np.pi * pp(heighti, 2)*(3*radiusi - heighti)
    Volumej_cap = (1/3) *np.pi * pp(heightj, 2)*(3*radiusj - heightj)
    Volumei_cell = Volumei - Volumei_cap
    Volumej_cell = Volumej - Volumej_cap
    Volumei_target = (4/3)*np.pi*pp(Ri_value, 3)
    Volumej_target = (4/3)*np.pi*pp(Rj_value, 3)
    Volume_error = pp((Volumei_cell - Volumei_target), 2) + pp((Volumej_cell - Volumej_target), 2)
    return Volume_error

Youngs = np.linspace(1,1000, num=squaresize)
YoungsAequil = np.zeros(shape=(squaresize,squaresize))
YoungsVnet = np.zeros(shape=(squaresize,squaresize))
normYoungsVnet = np.zeros(shape=(squaresize,squaresize))
for stack in range(0,len(Youngs)):

    #THE MASTER LOOP! FOR CALCULATING A ROUND OF ACONTACT, ENERGIES, COHESION GIVEN RI RJ and DIJ
    Gamma = np.linspace(Gammalimit, 0, num=len(dij)) #a range of cohesion values in SI
    Gammaerg = np.linspace(Gammalimit*1000, 0, num=len(dij))

    ########################## COORDINATE ARRAYS ##############################
    xs = np.zeros(len(dij)*len(Gamma))
    ys = np.zeros(len(dij)*len(Gamma))
    zsr = np.zeros(len(dij)*len(Gamma))
    zsa = np.zeros(len(dij)*len(Gamma))
    zsn_neg = np.zeros(len(dij)*len(Gamma))
    zsn_pos = np.zeros(len(dij)*len(Gamma))
    zsdVddij_neg = np.zeros(len(dij)*len(Gamma))
    zsdVddij_pos = np.zeros(len(dij)*len(Gamma))
    zsacontact_neg = np.zeros(len(dij)*len(Gamma))
    zsacontact_pos = np.zeros(len(dij)*len(Gamma))
    zdVroot = np.zeros(len(dij)*len(Gamma))
```

```
    #surface plot vectors
    Zsr = np.zeros(shape=(len(Gamma),len(dij)))
    Zsa = np.zeros(shape=(len(Gamma),len(dij)))
    Zsn_neg = np.zeros(shape=(len(Gamma),len(dij)))
    Zsn_pos = np.zeros(shape=(len(Gamma),len(dij)))
    Zsn = np.zeros(shape=(len(dij),len(dij)))
    ZsdVddij_neg = np.zeros(shape=(len(Gamma),len(dij)))
    ZsdVddij_pos = np.zeros(shape=(len(Gamma),len(dij)))
    Zsacontact_neg = np.zeros(shape=(len(Gamma),len(dij)))
    Zsacontact_pos = np.zeros(shape=(len(Gamma),len(dij)))
    ZdVroot = np.zeros(shape=(len(Gamma),len(dij)))
    ZV_net_pj = np.zeros(len(Gamma))
    ZAcontactequil = np.zeros(len(Gamma))

    xderivative =  np.zeros(len(Gamma))
    yderivative =  np.zeros(len(Gamma))
    Zacontact = np.zeros(shape=(len(Gamma),len(dij)))
    ZdVddij = np.zeros(shape=(len(Gamma),len(dij)))
    normZdVddij = np.zeros(shape=(len(Gamma),len(dij)))


    ##### ROOT STORAGE ARRAYS - arrays of zeros and 1 value per gamma corresponding to the energy derivative root
  #####
    Aequil_um = np.zeros(len(dij)*len(Gamma))
    dVddijequil_nN = np.zeros(len(dij)*len(Gamma))
    V_net_pj_equil = np.zeros(len(dij)*len(Gamma))
    Ri_equil = np.zeros(len(Gamma))
    Rj_equil = np.zeros(len(Gamma))
    index = 0

    ########################## GAMMA LOOP define several arrays that will vary with gamma
  ##############################

    for col in range(0, len(Gamma)):
        Ri = np.zeros(len(dij))
        Ri_um = np.zeros(len(dij))
        Rj = np.zeros(len(dij))
        Rj_um = np.zeros(len(dij))
        aij = np.zeros(len(dij))
        aij_um = np.zeros(len(dij))
        xij = np.zeros(len(dij))
        xij_um = np.zeros(len(dij))
        V_rep = np.zeros(len(dij)) #joules - the repulsive term of cell interfacial energy based on Hertz model, Landau and
 Lifshitz 1986
        V_rep_pj = np.zeros(len(dij)) #picojoules
        A_contact = np.zeros(len(dij)) # the area of the contact surface in m2
        A_contact_um = np.zeros(len(dij)) #um2
        V_adh = np.zeros(len(dij))
        V_adh_pj = np.zeros(len(dij))
        V_net = np.zeros(len(dij))
        V_net_pj = np.zeros(len(dij))
        dVddij = np.zeros(len(dij))
        dVddij_nN = np.zeros(len(dij))
        hi = np.zeros(len(dij))
        hj = np.zeros(len(dij))
        Voli = np.zeros(len(dij))
        Volj = np.zeros(len(dij))
        Voli_cap = np.zeros(len(dij))
        Volj_cap = np.zeros(len(dij))
        Voli_cell = np.zeros(len(dij))
        Volj_cell = np.zeros(len(dij))

        ########################## dij LOOP ##############################

        for row in range(0, len(dij)):
            Youngs_Modulus = Youngs[stack]
            Rs_guess = np.array([Ri_value, Rj_value])
            Rs = optimize.fmin(vol_error, Rs_guess, xtol = 1e-10)
            Ri[row] = Rs[0] #populate Ri array with a fixed radius value
            Rj[row] = Rs[1]
            Ri_um[row] = Ri[row]*10**6
            Rj_um[row] = Rj[row]*10**6

            aij_row = (1/dij[row])*pp((4*pp(dij[row], 2)*pp(Ri[row], 2)-pp((pp(dij[row], 2)-pp(Rj[row], 2)+pp(Ri[row], 2)), 2)), 0.5)
            aij[row] = aij_row
            aij_um[row] = aij_row*10**6
```

```
        xij[row] = Ri[row]+Rj[row]-dij[row] #the indentation depth - aka the penetration of the intersecting spehres
        xij_um[row] = xij[row]*10**6 #microns

        V_rep_row = (2/15)*pp((Ri[row]+Rj[row]-dij[row]), (2.5))*pp(((1-Poissons_Ratio)/Youngs_Modulus), (-1))*pp(((Ri[row]*
Rj[row])/(Ri[row]+Rj[row])), (1/2))
        V_rep[row] = V_rep_row
        V_rep_pj[row] = V_rep_row*10**12

        A_contact[row] = math.pi*pp((aij_row/2), 2)
        A_contact_um[row] = A_contact[row]*10**12

        V_adh[row] = Gamma[col]*A_contact[row]
        V_adh_pj[row] = V_adh[row]*10**12

        V_net[row] = V_adh[row]+V_rep[row]
        V_net_pj[row] = V_net[row]*10**12

        dVddij[row] = ((-Gamma[col]*math.pi)/(2*pp(dij[row], 3)))*(pp(dij[row], 4)-pp((pp(Ri[row], 2)-pp(Rj[row], 2)), 2))-(1/3)*(
Youngs_Modulus/(1-pp(Poissons_Ratio, 2)))*pp(((Ri[row]*Rj[row])/(Ri[row]+Rj[row])), 0.5)*pp((Ri[row]+Rj[row]-dij[row]), 1.5)
        dVddij_nN[row] = dVddij[row]*10**9

        ############### Optional VOLUME CALCULATIONS ##########################
        hi[row] = Rj[row]-pp((pp(Rj[row], 2)-pp((aij[row]/2), 2)), 0.5)
        hj[row] = Ri[row]-pp((pp(Ri[row], 2)-pp((aij[row]/2), 2)), 0.5)
        Voli[row] = (4/3)*np.pi*pp(Ri[row], 3)
        Volj[row] = (4/3)*np.pi*pp(Rj[row], 3)
        Voli_cap[row] = (1/3) *np.pi * pp(hi[row], 2)*(3*Ri[row] - hi[row])
        Volj_cap[row] = (1/3) *np.pi * pp(hj[row], 2)*(3*Rj[row] - hj[row])
        Voli_cell[row] = Voli[row] - Voli_cap[row]
        Volj_cell[row] = Volj[row] - Volj_cap[row]

        ##################AXIS ARRAYS FOR PLOTTING IN TERMS OF UNIQUE INDEX FOR EACH STATE (IE
STATE ID)#################
        xs[index] = xij_um[row]
        ys[index] = Gammaerg[col]
        zsr[index] = V_rep_pj[row]
        zsa[index] = V_adh_pj[row]
        if dVddij[row] < 0:
            zsdVddij_neg[index] = dVddij_nN[row]
            zsacontact_neg[index] = A_contact_um[row]
            normZdVddij[col,row] = (ZdVddij[col,row])/-(np.min(ZdVddij))
        else:
            zsdVddij_pos[index] = dVddij_nN[row]
            zsacontact_pos[index] = A_contact_um[row]
            normZdVddij[col,row] = (ZdVddij[col,row])/(np.max(ZdVddij))

        if V_net_pj[row]<0:
            zsn_neg[index] = V_net_pj[row]
        else:
            zsn_pos[index] = V_net_pj[row]


        ##### DERIVATIVE ROOT LOCATOR TEST ###############
        if abs(dVddij[row-1]) != dVddij[row-1] and abs(dVddij[row]) == dVddij[row]:
            Aequil_um[index] = A_contact_um[row]
            dVddijequil_nN[index] = dVddij_nN[row]

            ZV_net_pj[col] = V_net_pj[row] #vectors by column for the derivative root tracing line in all plots
            xderivative[col] = xij_um[row]
            yderivative[col] = Gammaerg[col]
            ZAcontactequil[col] = A_contact_um[row]

            ######################## For the 3rd loop - Aequil vs Youngs vs Gamma
            YoungsAequil[col, stack] = A_contact_um[row]
            YoungsVnet[col, stack] = V_net_pj[row]

            V_net_pj_equil[index] = V_net_pj[row]
            Ri_equil[col] = Ri[row]
            Rj_equil[col] = Rj[row]

        index = index + 1 #this makes a unique state ID for every point in the 2D space of gamma and  dij

        Zsr[col,row] = V_rep_pj[row] #2D matrices containing energies for the surface plot
        Zsa[col,row] = V_adh_pj[row]
        Zsn[col,row] = V_net_pj[row]
        Zacontact[col,row] = A_contact_um[row]
```

```
            ZdVddij[col,row] = dVddij_nN[row]



for stack in range(0, len(Youngs)):
    for col in range(0, len(Gamma)):
        normYoungsVnet[col,stack] = (YoungsVnet[col,stack]+abs(np.min(YoungsVnet)))/np.max(YoungsVnet+abs(np.min(
YoungsVnet)))


for col in range(0, len(Gamma)):
    for row in range(0, len(dij)):
        if dVddij[row] < 0:
            normZdVddij[col,row] = (ZdVddij[col,row])/-(np.min(ZdVddij))
        else:
            normZdVddij[col,row] = (ZdVddij[col,row])/(np.max(ZdVddij))
        normZdVddij[col,row] = (normZdVddij[col,row]+1)/2

Zsn_pos[Zsn_pos == 0.0] = np.nan #removing zeros in the surface plot energy matrices
Zsn_neg[Zsn_neg == 0.0] = np.nan
Zsr[Zsr == 0.0] = np.nan
Zsa[Zsa == 0.0] = np.nan
Zsn[Zsn == 0.0] = np.nan
YoungsAequil[YoungsAequil == 0.0] = np.nan
# xderivative[xderivative <= 0] = np.nan
Zacontact[Zacontact == 0.0] = np.nan


Xs = np.linspace(xij_um[0], xij_um[len(dij)-1], num=squaresize)
Ys = np.linspace(Gammaerg[0],Gammaerg[len(Gammaerg)-1], num=squaresize)
Xs, Ys = np.meshgrid(Xs, Ys)

Qs = np.linspace(Youngs[0],Youngs[len(Youngs)-1], num=squaresize)
Ws = np.linspace(Gammaerg[0],Gammaerg[len(Gammaerg)-1], num=squaresize)
Qs, Ws = np.meshgrid(Qs, Ws)


######################### REMOVE ZEROS FOR PLOTS otherwise you get plateaus and cliffs
 ##############################
Aequil_um[Aequil_um == 0.0] = np.nan
dVddijequil_nN[dVddijequil_nN == 0.0] = np.nan
V_net_pj_equil[V_net_pj_equil == 0.0] = np.nan
zsn_pos[zsn_pos == 0.0] = np.nan
zsn_neg[zsn_neg == 0.0] = np.nan
xs[xs < 0] = np.nan
zsr[zsr == 0.0] = np.nan
zsdVddij_neg[zsdVddij_neg == 0.0] = np.nan
zsdVddij_neg[zsdVddij_neg < -5e1] = np.nan
zsdVddij_pos[zsdVddij_pos == 0.0] = np.nan
zsacontact_neg[zsacontact_neg == 0.0] = np.nan
zsacontact_pos[zsacontact_pos == 0.0] = np.nan

######################### PLOTS ##############################

cdict = {'red':   ((0,    0, 0),  #i.e. at value 0, red component is 0. First parameter is the value, second is the color component.
Ignore the third parameter, it is for discontinuities.
                   (.5,  1, 1),  #     at value 0.5, red component is 1.
                   (1,    1, 1)), #     at value 1, red component is 1
         'green': ((0,    0, 0),
                   (.5,  1, 1),
                   (1,    0, 0)),
         'blue':  ((0,    1, 1),
                   (.5,  1, 1),
                   (1,    0, 0))}
cmap1 = colors.LinearSegmentedColormap('UWR',cdict,256)
cm.register_cmap(name='UWR', cmap=cmap1)
UWR = cm.get_cmap('UWR')

############################


m2 = cm.ScalarMappable(cmap='copper')
m2.set_array(YoungsVnet)
fig9 = plt.figure()
ax9 = fig9.add_subplot(111, projection='3d')
ax9.set_xlabel(r'$E [Pa]$')
```

```
    ax9.set_ylabel(r'$\gamma$ $[ \frac{erg}{cm^2} ]$')
    ax9.set_zlabel(r'$Steady State A_{CONTACT}$ $[\mu m^2]$')
    ax9.set_xlim(Youngs[0],Youngs[squaresize-1])
    ax9.plot_surface(Qs, Ws, YoungsAequil, rstride=int(1), cstride=int(1), alpha=1,facecolors=cm.copper(normYoungsVnet),
    linewidth=.1, antialiased=True, shade=False)#, vmin=min(A_contact_um),vmax=max(A_contact_um))
    cbar2 = fig9.colorbar(m2, ticks=[round(np.min(YoungsVnet), 2),round(np.min(YoungsVnet)/2, 2),0], shrink=0.85)#, label=r'
    $V$ $[pJ]$')
    cbar2.set_label('$V$ $[pJ]$',size=30)
    cbar2.ax.tick_params(labelsize=15)
    for item in ([ax9.title, ax9.xaxis.label, ax9.yaxis.label, ax9.zaxis.label] +
                 ax9.get_xticklabels() + ax9.get_yticklabels() + ax9.get_zticklabels()):
        item.set_fontsize(30)
    for item in (ax9.get_xticklabels() + ax9.get_yticklabels() + ax9.get_zticklabels()):
        item.set_fontsize(15)

    elapsed_time = time.time() - start_time
    print elapsed_time

    plt.show()
```

Bibliography

Alenghat, Francis J and Donald E Ingber. "Mechanotransduction: all signals point to cytoskeleton, matrix, and integrins". In: *Science Signaling* 2002.119 (2002), pe6.

Almany, Liora and Dror Seliktar. "Biosynthetic hydrogel scaffolds made from fibrinogen and polyethylene glycol for 3D cell cultures". In: *Biomaterials* 26.15 (2005), pp. 2467–2477.

Altman, Meghan O et al. "Modifying cellular properties using artificial aptamer-lipid receptors". In: *Scientific reports* 3 (2013).

Arima, Yusuke and Hiroo Iwata. "Effect of wettability and surface functional groups on protein adsorption and cell adhesion using well-defined mixed self-assembled monolayers". In: *Biomaterials* 28.20 (2007), pp. 3074–3082.

Augello, Andrea et al. "Bone marrow mesenchymal progenitor cells inhibit lymphocyte proliferation by activation of the programmed death 1 pathway". In: *European journal of immunology* 35.5 (2005), pp. 1482–1490.

Augello, Andrea et al. "Cell therapy using allogeneic bone marrow mesenchymal stem cells prevents tissue damage in collagen-induced arthritis". In: *Arthritis & Rheumatism* 56.4 (2007), pp. 1175–1186.

Austrup, Frank et al. "P-and E-selectin mediate recruitment of T-helper-1 but not T-helper-2 cells into inflamed tissues". In: (1997).

Baddoo, Melody et al. "Characterization of mesenchymal stem cells isolated from murine bone marrow by negative selection". In: *Journal of cellular biochemistry* 89.6 (2003), pp. 1235–1249.

Balaban, Nathalie Q et al. "Force and focal adhesion assembly: a close relationship studied using elastic micropatterned substrates". In: *Nature cell biology* 3.5 (2001), pp. 466–472.

Ball, Lynne M et al. "Cotransplantation of ex vivo–expanded mesenchymal stem cells accelerates lymphocyte recovery and may reduce the risk of graft failure in haploidentical hematopoietic stem-cell transplantation". In: *Blood* 110.7 (2007), pp. 2764–2767.

Bartholomew, Amelia et al. “Mesenchymal stem cells suppress lymphocyte proliferation in vitro and prolong skin graft survival in vivo”. In: *Experimental hematology* 30.1 (2002), pp. 42–48.

Behrens, Jiirgen et al. “Loss of epithelial differentiation and gain of invasiveness correlates with tyrosine phosphorylation of the E-cadherin/beta-catenin complex in cells transformed with a temperature-sensitive v-SRC gene.” In: *The Journal of cell biology* 120.3 (1993), pp. 757–766.

Bell, George I. “Models for the specific adhesion of cells to cells”. In: *Science* 200.4342 (1978), pp. 618–627.

Beningo, Karen A, Chun-Min Lo, and Yu-Li Wang. “Flexible polyacrylamide substrata for the analysis of mechanical interactions at cell-substratum adhesions”. In: *Methods in cell biology* 69 (2002), pp. 325–339.

Berendt, AR et al. “Intercellular adhesion molecule-1 is an endothelial cell adhesion receptor for Plasmodium falciparum”. In: *Nature* 341.6237 (1989), pp. 57–59.

Berman, Dora M et al. “Mesenchymal stem cells enhance allogeneic islet engraftment in nonhuman primates”. In: *Diabetes* 59.10 (2010), pp. 2558–2568.

Bhaiji, Tasneem, Zheng-Liang Zhi, and John C Pickup. “Improving cellular function and immune protection via layer-by-layer nanocoating of pancreatic islet β-cell spheroids cocultured with mesenchymal stem cells”. In: *Journal of Biomedical Materials Research Part A* 100.6 (2012), pp. 1628–1636.

Bitterman, Peter B et al. “Role of fibronectin as a growth factor for fibroblasts.” In: *The Journal of cell biology* 97.6 (1983), pp. 1925–1932.

Bosco, Domenico, Dominique G Rouiller, and Philippe A Halban. “Differential expression of E-cadherin at the surface of rat β-cells as a marker of functional heterogeneity”. In: *Journal of endocrinology* 194.1 (2007), pp. 21–29.

Bryant, Stephanie J et al. “Crosslinking density influences chondrocyte metabolism in dynamically loaded photocrosslinked poly (ethylene glycol) hydrogels”. In: *Annals of biomedical engineering* 32.3 (2004), pp. 407–417.

Butler, James P et al. “Traction fields, moments, and strain energy that cells exert on their surroundings”. In: *American Journal of Physiology-Cell Physiology* 282.3 (2002), pp. C595–C605.

Carter, Stephen B. “Haptotaxis and the mechanism of cell motility”. In: *Nature* 213 (1967), pp. 256–260.

Chandra, Ravi A et al. “Programmable cell adhesion encoded by DNA hybridization”. In: *Angewandte Chemie* 118.6 (2006), pp. 910–915.

Chang, Stephanie S et al. “Guidance of cell migration by substrate dimension”. In: *Biophysical journal* 104.2 (2013), pp. 313–321.

Chen, Christopher S et al. “Geometric control of cell life and death”. In: *Science* 276.5317 (1997), pp. 1425–1428.

Chen, Christopher S et al. "Micropatterned surfaces for control of cell shape, position, and function". In: *Biotechnology Progress* 14.3 (1998), pp. 356–363.

Chen, Hao, Yuji Teramura, and Hiroo Iwata. "Immobilization of anticoagulant-loaded liposomes on cell surfaces by DNA hybridization". In: *Biomaterials* 32.31 (2011), pp. 7971–7977.

Cheresh, David A. and R.P. Mecham. *Integrins: Molecular and Biological Responses to the Extracellular Matrix*. Biology of extracellular matrix. Academic Press, 1994. ISBN: 9780121711603.

Choquet, Daniel, Dan P Felsenfeld, and Michael P Sheetz. "Extracellular matrix rigidity causes strengthening of integrin–cytoskeleton linkages". In: *Cell* 88.1 (1997), pp. 39–48.

Chrzanowska-Wodnicka, Magdalena and Keith Burridge. "Rho-stimulated contractility drives the formation of stress fibers and focal adhesions." In: *The Journal of cell biology* 133.6 (1996), pp. 1403–1415.

Claessens, Mireille MAE et al. "Actin-binding proteins sensitively mediate F-actin bundle stiffness". In: *Nature materials* 5.9 (2006), pp. 748–753.

Dalma-Weiszhausz, Dennise D et al. "[1] The Affymetrix GeneChip® Platform: An Overview". In: *Methods in enzymology* 410 (2006), pp. 3–28.

Darenfed, Hassina et al. "Molecular characterization of the effects of Y-27632". In: *Cell motility and the cytoskeleton* 64.2 (2007), pp. 97–109.

De Bank, Paul A et al. "Accelerated formation of multicellular 3-D structures by cell-to-cell cross-linking". In: *Biotechnology and bioengineering* 97.6 (2007), pp. 1617–1625.

De Bank, Paul A et al. "Surface engineering of living myoblasts via selective periodate oxidation". In: *Biotechnology and bioengineering* 81.7 (2003), pp. 800–808.

Delanoë-Ayari, H, JP Rieu, and M Sano. "4D traction force microscopy reveals asymmetric cortical forces in migrating Dictyostelium cells". In: *Physical review letters* 105.24 (2010), p. 248103.

Dembo, Micah and Yu-Li Wang. "Stresses at the cell-to-substrate interface during locomotion of fibroblasts". In: *Biophysical journal* 76.4 (1999), pp. 2307–2316.

Dillon, George P et al. "The influence of physical structure and charge on neurite extension in a 3D hydrogel scaffold". In: *Journal of Biomaterials Science, Polymer Edition* 9.10 (1998), pp. 1049–1069.

DiMilla, Paul A et al. "Maximal migration of human smooth muscle cells on fibronectin and type IV collagen occurs at an intermediate attachment strength". In: *The Journal of cell biology* 122.3 (1993), pp. 729–737.

Discher, Dennis E, Paul Janmey, and Yu-li Wang. "Tissue cells feel and respond to the stiffness of their substrate". In: *Science* 310.5751 (2005), pp. 1139–1143.

Donaldson, Donald J, James T Mahan, and Gerald N Smith. "Newt epidermal cell migration over collagen and fibronectin involves different mechanisms". In: *Journal of cell science* 90.2 (1988), pp. 325–333.

Doxzen, Kevin et al. "Guidance of collective cell migration by substrate geometry". In: *Integrative Biology* 5.8 (2013), pp. 1026–1035.

Du Roure, Olivia et al. "Force mapping in epithelial cell migration". In: *Proceedings of the National Academy of Sciences of the United States of America* 102.7 (2005), pp. 2390–2395.

Duguay, Duke, Ramsey A Foty, and Malcolm S Steinberg. "Cadherin-mediated cell adhesion and tissue segregation: qualitative and quantitative determinants". In: *Developmental biology* 253.2 (2003), pp. 309–323.

Dunn, Graham A and Julian P Heath. "A new hypothesis of contact guidance in tissue cells". In: *Experimental cell research* 101.1 (1976), pp. 1–14.

Duprez, Ida Rasmusson et al. "Preparatory studies of composite mesenchymal stem cell islets for application in intraportal islet transplantation". In: *Upsala journal of medical sciences* 116.1 (2011), pp. 8–17.

Dustin, Michael L et al. "Induction by IL 1 and interferon-gamma: tissue distribution, biochemistry, and function of a natural adherence molecule (ICAM-1)." In: *The Journal of Immunology* 137.1 (1986), pp. 245–254.

Elices, Mariano J et al. "VCAM-1 on activated endothelium interacts with the leukocyte integrin VLA-4 at a site distinct from the VLA-4/fibronectin binding site". In: *Cell* 60.4 (1990), pp. 577–584.

Engl, W et al. "Actin dynamics modulate mechanosensitive immobilization of E-cadherin at adherens junctions". In: *Nature cell biology* 16.6 (2014), pp. 587–594.

Evans, E and A Yeung. "Apparent viscosity and cortical tension of blood granulocytes determined by micropipet aspiration". In: *Biophysical journal* 56.1 (1989), pp. 151–160.

Foty, Ramsey A and Malcolm S Steinberg. "The differential adhesion hypothesis: a direct evaluation". In: *Developmental biology* 278.1 (2005), pp. 255–263.

Franck, Christian et al. "Three-dimensional traction force microscopy: a new tool for quantifying cell-matrix interactions". In: *PLoS One* 6.3 (2011), e17833.

Friedl, Peter and Darren Gilmour. "Collective cell migration in morphogenesis, regeneration and cancer". In: *Nature reviews Molecular cell biology* 10.7 (2009), pp. 445–457.

Froehner, S.C. and V. Bennett. *Cytoskeletal Regulation of Membrane Function: Society of General Physiologists 50th Annual Symposium, Marine Biological Laboratory, Woods Hole, Massachusetts, 5-7 September 1996*. Annual symposium. Rockefeller University Press, 1997. ISBN: 9780874700596.

Fujita, Takayuki, Kazusuke Maenaka, and Yoichiro Takayama. "Dual-axis MEMS mirror for large deflection-angle using SU-8 soft torsion beam". In: *Sensors and Actuators A: Physical* 121.1 (2005), pp. 16–21.

Galbraith, Catherine G, Kenneth M Yamada, and Michael P Sheetz. "The relationship between force and focal complex development". In: *The Journal of cell biology* 159.4 (2002), pp. 695–705.

Garanger, Elisabeth et al. "Multivalent RGD synthetic peptides as potent α V β 3 integrin ligands". In: *Organic & biomolecular chemistry* 4.10 (2006), pp. 1958–1965.

Gardel, Margaret L et al. "Elastic behavior of cross-linked and bundled actin networks". In: *Science* 304.5675 (2004), pp. 1301–1305.

Gaudet, Christianne et al. "Influence of type I collagen surface density on fibroblast spreading, motility, and contractility". In: *Biophysical journal* 85.5 (2003), pp. 3329–3335.

Gjorevski, Nikolce, Eline Boghaert, and Celeste M Nelson. "Regulation of epithelial-mesenchymal transition by transmission of mechanical stress through epithelial tissues". In: *Cancer Microenvironment* 5.1 (2012), pp. 29–38.

Graner, François and James A Glazier. "Simulation of biological cell sorting using a two-dimensional extended Potts model". In: *Physical review letters* 69.13 (1992), p. 2013.

Green, Kathleen J and Cory L Simpson. "Desmosomes: new perspectives on a classic". In: *Journal of Investigative Dermatology* 127.11 (2007), pp. 2499–2515.

Grinnell, Frederick and Marian K Feld. "Fibronectin adsorption on hydrophilic and hydrophobic surfaces detected by antibody binding and analyzed during cell adhesion in serum-containing medium." In: *Journal of Biological Chemistry* 257.9 (1982), pp. 4888–4893.

Groves, Jay T, Lara K Mahal, and Carolyn R Bertozzi. "Control of cell adhesion and growth with micropatterned supported lipid membranes". In: *Langmuir* 17.17 (2001), pp. 5129–5133.

Guvendiren, Murat and Jason A Burdick. "The control of stem cell morphology and differentiation by hydrogel surface wrinkles". In: *Biomaterials* 31.25 (2010), pp. 6511–6518.

Hadden, Helene Levrey and Craig A Henke. "Induction of lung fibroblast apoptosis by soluble fibronectin peptides". In: *American journal of respiratory and critical care medicine* 162.4 (2000), pp. 1553–1560.

Halbleib, Jennifer M and W James Nelson. "Cadherins in development: cell adhesion, sorting, and tissue morphogenesis". In: *Genes & development* 20.23 (2006), pp. 3199–3214.

Harris, Albert K. "Is cell sorting caused by differences in the work of intercellular adhesion? A critique of the Steinberg hypothesis". In: *Journal of Theoretical Biology* 61.2 (1976), pp. 267–285.

Harris, Albert K, Patricia Wild, and David Stopak. "Silicone rubber substrata: a new wrinkle in the study of cell locomotion". In: *Science* 208.4440 (1980), pp. 177–179.

Harris, Andrew R, Alicia Daeden, and Guillaume T Charras. "Formation of adherens junctions leads to the emergence of a tissue-level tension in epithelial monolayers". In: *Journal of cell science* 127.11 (2014), pp. 2507–2517.

Hatanaka, Hironobu, Tomoyuki Yasukawa, and Fumio Mizutani. "Detection of surface antigens on living cells through incorporation of immunorecognition into the distinct positioning of cells with positive and negative dielectrophoresis". In: *Analytical chemistry* 83.18 (2011), pp. 7207–7212.

Hatta, Kohei et al. "Cloning and expression of cDNA encoding a neural calcium-dependent cell adhesion molecule: its identity in the cadherin gene family." In: *The Journal of cell biology* 106.3 (1988), pp. 873–881.

Hemberger, Myriam, Wendy Dean, and Wolf Reik. "Epigenetic dynamics of stem cells and cell lineage commitment: digging Waddington's canal". In: *Nature reviews Molecular cell biology* 10.8 (2009), pp. 526–537.

Herman, B, MA Langevin, and DF Albertini. "The effects of taxol on the organization of the cytoskeleton in cultured ovarian granulosa cells." In: *European journal of cell biology* 31.1 (1983), pp. 34–45.

Hermiston, Michelle L and Jeffrey I Gordon. "In vivo analysis of cadherin function in the mouse intestinal epithelium: essential roles in adhesion, maintenance of differentiation, and regulation of programmed cell death." In: *The Journal of cell biology* 129.2 (1995), pp. 489–506.

Hertz, Heinrich. "Ueber die Berührung fester elastischer Körper." In: *Journal für die reine und angewandte Mathematik* 92 (1882), pp. 156–171.

Hinz, Boris and Giulio Gabbiani. "Mechanisms of force generation and transmission by myofibroblasts". In: *Current opinion in biotechnology* 14.5 (2003), pp. 538–546.

Hoffecker, Ian T and Hiroo Iwata. "Manipulation of Cell Sorting Within Mesenchymal Stromal Cell–Islet Cell Multicellular Spheroids". In: *Tissue Engineering Part A* 20.11-12 (2014), pp. 1643–1653.

Huang, Sui and Donald E Ingber. "Shape-dependent control of cell growth, differentiation, and apoptosis: switching between attractors in cell regulatory networks". In: *Experimental cell research* 261.1 (2000), pp. 91–103.

Huber, F et al. "Emergent complexity of the cytoskeleton: from single filaments to tissue". In: *Advances in Physics* 62.1 (2013), pp. 1–112.

Huen, Arthur C et al. "Intermediate filament–membrane attachments function synergistically with actin-dependent contacts to regulate intercellular adhesive strength". In: *The Journal of cell biology* 159.6 (2002), pp. 1005–1017.

Hynes, Richard O and Kenneth M Yamada. "Fibronectins: multifunctional modular glycoproteins." In: *The Journal of cell biology* 95.2 (1982), pp. 369–377.

Inohara, Hidenori and Avraham Raz. "Functional evidence that cell surface galectin-3 mediates homotypic cell adhesion". In: *Cancer research* 55.15 (1995), pp. 3267–3271.

Ito, Yoshihiro and Masayuki Nogawa. "Preparation of a protein micro-array using a photo-reactive polymer for a cell-adhesion assay". In: *Biomaterials* 24.18 (2003), pp. 3021–3026.

Iwata, Hiroo. "Cell LEGO". In: *Optical MEMS and Nanophotonics (OMN), 2013 International Conference on*. IEEE. 2013, pp. 75–76.

Janmey, Paul A, Penelope C Georges, and Søren Hvidt. "Basic rheology for biologists". In: *Methods in cell biology* 83 (2007), pp. 1–27.

Jaynes, Edwin T. *Probability theory: the logic of science*. Cambridge university press, 2003.

Jin, Yonghui et al. "Mesenchymal stem cells cultured under hypoxia escape from senescence¡ i¿ via¡/i¿ down-regulation of p16 and extracellular signal regulated kinase". In: *Biochemical and biophysical research communications* 391.3 (2010), pp. 1471–1476.

Käfer, Jos et al. "Cell adhesion and cortex contractility determine cell patterning in the Drosophilaretina". In: *Proceedings of the National Academy of Sciences* 104.47 (2007), pp. 18549–18554.

Kaneko, Shin and Shinya Yamanaka. "To be immunogenic, or not to be: that's the iPSC question". In: *Cell stem cell* 12.4 (2013), pp. 385–386.

Kasai, Michiki, Hirotaka Kawashima, and Fumio Oosawa. "Structure of F–actin solutions". In: *Journal of Polymer Science* 44.143 (1960), pp. 51–69.

Kedrin, Dmitriy et al. "Cell motility and cytoskeletal regulation in invasion and metastasis". In: *Journal of mammary gland biology and neoplasia* 12.2-3 (2007), pp. 143–152.

Koch, Thorsten M et al. "3D Traction forces in cancer cell invasion". In: *PLoS One* 7.3 (2012), e33476.

Koga, Tomoyo et al. "Rho-associated protein kinase inhibitor, Y-27632, induces alterations in adhesion, contraction and motility in cultured human trabecular meshwork cells". In: *Experimental eye research* 82.3 (2006), pp. 362–370.

Koley, Dipankar and Allen J Bard. "Triton X-100 concentration effects on membrane permeability of a single HeLa cell by scanning electrochemical microscopy (SECM)". In: *Proceedings of the National Academy of Sciences* 107.39 (2010), pp. 16783–16787.

Korbutt, Gregory S, John F Elliott, and Ray V Rajotte. "Cotransplantation of allogeneic islets with allogeneic testicular cell aggregates allows long-term graft survival without systemic immunosuppression". In: *Diabetes* 46.2 (1997), pp. 317–322.

Kovács, Mihály et al. "Mechanism of blebbistatin inhibition of myosin II". In: *Journal of Biological Chemistry* 279.34 (2004), pp. 35557–35563.

Krieg, M et al. "Tensile forces govern germ-layer organization in zebrafish". In: *Nature cell biology* 10.4 (2008), pp. 429–436.

Kroening, Sven et al. "Matrix-independent stimulation of human tubular epithelial cell migration by Rho kinase inhibitors". In: *Journal of cellular physiology* 223.3 (2010), pp. 703–712.

Ku, HH. "Notes on the use of propagation of error formulas". In: *Journal of Research of the National Bureau of Standards* 70.4 (1966).

Lacy, Paul E and Mery Kostianovsky. "Method for the isolation of intact islets of Langerhans from the rat pancreas". In: *Diabetes* 16.1 (1967), pp. 35–39.

Landau, Lev D and EM Lifshitz. "Theory of Elasticity, vol. 7". In: *Course of Theoretical Physics* 3 (1986).

Lawrence, Michael B and Timothy A Springer. "Leukocytes roll on a selectin at physiologic flow rates: distinction from and prerequisite for adhesion through integrins". In: *Cell* 65.5 (1991), pp. 859–873.

Leckband, Deborah and Anil Prakasam. "Mechanism and dynamics of cadherin adhesion". In: *Annu. Rev. Biomed. Eng.* 8 (2006), pp. 259–287.

Lecuit, Thomas and Pierre-Francois Lenne. "Cell surface mechanics and the control of cell shape, tissue patterns and morphogenesis". In: *Nature Reviews Molecular Cell Biology* 8.8 (2007), pp. 633–644.

Lee, Kuen Yong et al. "Nanoscale adhesion ligand organization regulates osteoblast proliferation and differentiation". In: *Nano Letters* 4.8 (2004), pp. 1501–1506.

Legant, Wesley R et al. "Multidimensional traction force microscopy reveals out-of-plane rotational moments about focal adhesions". In: *Proceedings of the National Academy of Sciences* 110.3 (2013), pp. 881–886.

Lehnert, Dirk et al. "Cell behaviour on micropatterned substrata: limits of extracellular matrix geometry for spreading and adhesion". In: *Journal of cell science* 117.1 (2004), pp. 41–52.

Li, Ronghui et al. "A mesenchymal-to-epithelial transition initiates and is required for the nuclear reprogramming of mouse fibroblasts". In: *Cell stem cell* 7.1 (2010), pp. 51–63.

Li, Wen-Ge and Xin Xiang Xu. "The expression of N-cadherin, fibronectin during chondrogenic differentiation of MSC induced by TGF-beta (1)." In: *Chinese journal of traumatology= Zhonghua chuang shang za zhi/Chinese Medical Association* 8.6 (2005), pp. 349–351.

Li, Xiangyun et al. "The ROCK inhibitor Y-27632 enhances the survival rate of human embryonic stem cells following cryopreservation". In: *Stem cells and development* 17.6 (2008), pp. 1079–1086.

Lima, Maria João et al. "Suppression of epithelial-to-mesenchymal transitioning enhances ex vivo reprogramming of human exocrine pancreatic tissue toward functional insulin-producing β-like cells". In: *Diabetes* 62.8 (2013), pp. 2821–2833.

Litvinov, Sergey V et al. "Epithelial cell adhesion molecule (Ep-CAM) modulates cell–cell interactions mediated by classic cadherins". In: *The Journal of cell biology* 139.5 (1997), pp. 1337–1348.

Lo, Chun-Min et al. "Cell movement is guided by the rigidity of the substrate". In: *Biophysical journal* 79.1 (2000), pp. 144–152.

Los, Marek and Spencer B Gibson. *Apoptotic pathways as targets for novel therapies in cancer and other diseases*. Springer, 2005.

Lu, L. and Washington University in St. Louis. *Mechanical Properties of Actin Stress Fibers*. Washington University in St. Louis, 2008. ISBN: 9780549646426.

Lu, Yanrong et al. "Mesenchymal stem cells protect islets from hypoxia/reoxygenation-induced injury". In: *Cell biochemistry and function* 28.8 (2010), pp. 637–643.

Luan, Nguyen Minh, Yuji Teramura, and Hiroo Iwata. "Immobilization of the soluble domain of human complement receptor 1 on agarose-encapsulated islets for the prevention of complement activation". In: *Biomaterials* 31.34 (2010), pp. 8847–8853.

Lutz, Roman et al. "Nano-stenciled RGD-gold patterns that inhibit focal contact maturation induce lamellipodia formation in fibroblasts". In: *PloS one* 6.9 (2011), e25459.

Macarrón, Ricardo and Robert P Hertzberg. "Design and implementation of high throughput screening assays". In: *High Throughput Screening*. Springer, 2002, pp. 1–29.

Macfarlane, Robert J et al. "Nanoparticle superlattice engineering with DNA". In: *Science* 334.6053 (2011), pp. 204–208.

Mader, Christopher C, Edward H Hinchcliffe, and Yu-li Wang. "Probing cell shape regulation with patterned substratum: requirement of myosin II-mediated contractility". In: *Soft Matter* 3.3 (2007), pp. 357–363.

Maheshwari, Gargi et al. "Cell adhesion and motility depend on nanoscale RGD clustering". In: *Journal of cell science* 113.10 (2000), pp. 1677–1686.

Manning, M Lisa et al. "Coaction of intercellular adhesion and cortical tension specifies tissue surface tension". In: *Proceedings of the National Academy of Sciences* 107.28 (2010), pp. 12517–12522.

Markman, Maurie and Tarek M Mekhail. "Paclitaxel in cancer therapy". In: *Expert opinion on pharmacotherapy* 3.6 (2002), pp. 755–766.

Marlin, Steven D and Timothy A Springer. "Purified intercellular adhesion molecule-1 (ICAM-1) is a ligand for lymphocyte function-associated antigen 1 (LFA-1)". In: *Cell* 51.5 (1987), pp. 813–819.

Martìn-Padura, Inés et al. "Junctional adhesion molecule, a novel member of the immunoglobulin superfamily that distributes at intercellular junctions and modulates monocyte transmigration". In: *The Journal of cell biology* 142.1 (1998), pp. 117–127.

McBeath, Rowena et al. "Cell shape, cytoskeletal tension, and RhoA regulate stem cell lineage commitment". In: *Developmental cell* 6.4 (2004), pp. 483–495.

Meisel, Roland et al. “Human bone marrow stromal cells inhibit allogeneic T-cell responses by indoleamine 2, 3-dioxygenase–mediated tryptophan degradation”. In: *Blood* 103.12 (2004), pp. 4619–4621.

Miller, Karol et al. “Mechanical properties of brain tissue in-vivo: experiment and computer simulation”. In: *Journal of biomechanics* 33.11 (2000), pp. 1369–1376.

Miranti, Cindy K and Joan S Brugge. “Sensing the environment: a historical perspective on integrin signal transduction”. In: *Nature cell biology* 4.4 (2002), E83–E90.

Miura, Suguru, Yuji Teramura, and Hiroo Iwata. “Encapsulation of islets with ultra-thin polyion complex membrane through poly (ethylene glycol)-phospholipids anchored to cell membrane”. In: *Biomaterials* 27.34 (2006), pp. 5828–5835.

Miyake, Yuka et al. “Actomyosin tension is required for correct recruitment of adherens junction components and zonula occludens formation”. In: *Experimental cell research* 312.9 (2006), pp. 1637–1650.

Morton, Walter M, Kathryn R Ayscough, and Paul J McLaughlin. “Latrunculin alters the actin-monomer subunit interface to prevent polymerization”. In: *Nature cell biology* 2.6 (2000), pp. 376–378.

Nelea, Valentin, Yukiko Nakano, and Mari T Kaartinen. “Size distribution and molecular associations of plasma fibronectin and fibronectin crosslinked by transglutaminase 2”. In: *The protein journal* 27.4 (2008), pp. 223–233.

Nelson, Celeste M and Christopher S Chen. “VE-cadherin simultaneously stimulates and inhibits cell proliferation by altering cytoskeletal structure and tension”. In: *Journal of cell science* 116.17 (2003), pp. 3571–3581.

Niehage, Christian et al. “The cell surface proteome of human mesenchymal stromal cells”. In: *PLoS One* 6.5 (2011), e20399.

Niewiadomska, Paulina, Dorothea Godt, and Ulrich Tepass. “DE-Cadherin is required for intercellular motility during Drosophila oogenesis”. In: *The Journal of cell biology* 144.3 (1999), pp. 533–547.

Nose, Akinao, Akira Nagafuchi, and Masatoshi Takeichi. “Expressed recombinant cadherins mediate cell sorting in model systems”. In: *Cell* 54.7 (1988), pp. 993–1001.

Omary, M Bishr, Pierre A Coulombe, and WH Irwin McLean. “Intermediate filament proteins and their associated diseases”. In: *New England Journal of Medicine* 351.20 (2004), pp. 2087–2100.

Osakada, Fumitaka et al. “Stepwise differentiation of pluripotent stem cells into retinal cells”. In: *Nature protocols* 4.6 (2009), pp. 811–824.

Osta, Walid A et al. “EpCAM is overexpressed in breast cancer and is a potential target for breast cancer gene therapy”. In: *Cancer research* 64.16 (2004), pp. 5818–5824.

Palazzo, Alexander F et al. “Localized stabilization of microtubules by integrin-and FAK-facilitated Rho signaling”. In: *Science* 303.5659 (2004), pp. 836–839.

Palecek, Sean P et al. “Integrin-ligand binding properties govern cell migration speed through cell-substratum adhesiveness”. In: *Nature* 385.6616 (1997), pp. 537–540.

Pankov, Roumen and Kenneth M Yamada. “Fibronectin at a glance”. In: *Journal of cell science* 115.20 (2002), pp. 3861–3863.

Parker, Kevin Kit et al. “Directional control of lamellipodia extension by constraining cell shape and orienting cell tractional forces”. In: *The FASEB Journal* 16.10 (2002), pp. 1195–1204.

Parnaud, Géraldine et al. “Cadherin engagement protects human β-cells from apoptosis”. In: *Endocrinology* 152.12 (2011), pp. 4601–4609.

PaszeK, Matthew J et al. “Tensional homeostasis and the malignant phenotype”. In: *Cancer cell* 8.3 (2005), pp. 241–254.

Peglion, Florent, Flora Llense, and Sandrine Etienne-Manneville. “Adherens junction treadmilling during collective migration”. In: *Nature cell biology* 16.7 (2014), pp. 639–651.

Peister, Alexandra et al. “Adult stem cells from bone marrow (MSCs) isolated from different strains of inbred mice vary in surface epitopes, rates of proliferation, and differentiation potential”. In: *Blood* 103.5 (2004), pp. 1662–1668.

Pelham, Robert J and Yu-li Wang. “Cell locomotion and focal adhesions are regulated by substrate flexibility”. In: *Proceedings of the National Academy of Sciences* 94.25 (1997), pp. 13661–13665.

Perez-Moreno, Mirna, Colin Jamora, and Elaine Fuchs. “Sticky business: orchestrating cellular signals at adherens junctions”. In: *Cell* 112.4 (2003), pp. 535–548.

Plestant, Charlotte et al. “Adhesive interactions of N-cadherin limit the recruitment of microtubules to cell–cell contacts through organization of actomyosin”. In: *Journal of cell science* 127.8 (2014), pp. 1660–1671.

Plow, Edward F et al. “Ligand binding to integrins”. In: *Journal of Biological Chemistry* 275.29 (2000), pp. 21785–21788.

Pokutta, Sabine and William I Weis. “Structure and mechanism of cadherins and catenins in cell-cell contacts”. In: *Annu. Rev. Cell Dev. Biol.* 23 (2007), pp. 237–261.

Pollard, Thomas D and Gary G Borisy. “Cellular motility driven by assembly and disassembly of actin filaments”. In: *Cell* 112.4 (2003), pp. 453–465.

Pollard, Thomas D, William C Earnshaw, and Jennifer Lippincott-Schwartz. *Cell biology*. Elsevier Health Sciences, 2007.

Potter, David A et al. “Calpain regulates actin remodeling during cell spreading”. In: *The Journal of cell biology* 141.3 (1998), pp. 647–662.

Qureshi, Khalid M et al. “Human amniotic epithelial cells induce localized cell-mediated immune privilege in vitro: implications for pancreatic islet transplantation”. In: *Cell transplantation* 20.4 (2011), pp. 523–534.

Rajagopalan, Padmavathy et al. "Direct comparison of the spread area, contractility, and migration of balb/c 3T3 fibroblasts adhered to fibronectin-and RGD-modified substrata". In: *Biophysical journal* 87.4 (2004), pp. 2818–2827.

Rape, Andrew D, Wei-hui Guo, and Yu-li Wang. "The regulation of traction force in relation to cell shape and focal adhesions". In: *Biomaterials* 32.8 (2011), pp. 2043–2051.

Rape, Andrew, Wei-hui Guo, and Yu-li Wang. "Microtubule depolymerization induces traction force increase through two distinct pathways". In: *Journal of cell science* 124.24 (2011), pp. 4233–4240.

Redmer, Torben et al. "E-cadherin is crucial for embryonic stem cell pluripotency and can replace OCT4 during somatic cell reprogramming". In: *EMBO reports* 12.7 (2011), pp. 720–726.

Reinhart-King, Cynthia A, Micah Dembo, and Daniel A Hammer. "The dynamics and mechanics of endothelial cell spreading". In: *Biophysical journal* 89.1 (2005), pp. 676–689.

Revenu, Céline et al. "Quantitative cell polarity imaging defines leader-to-follower transitions during collective migration and the key role of microtubule-dependent adherens junction formation". In: *Development* 141.6 (2014), pp. 1282–1291.

Riveline, Daniel et al. "Focal contacts as mechanosensors externally applied local mechanical force induces growth of focal contacts by an mdia1-dependent and rock-independent mechanism". In: *The Journal of cell biology* 153.6 (2001), pp. 1175–1186.

Roeder, Blayne A et al. "Tensile mechanical properties of three-dimensional type I collagen extracellular matrices with varied microstructure". In: *Journal of biomechanical engineering* 124.2 (2002), pp. 214–222.

Rohr, Stephan, Regula Flückiger-Labrada, and Jan P Kucera. "Photolithographically defined deposition of attachment factors as a versatile method for patterning the growth of different cell types in culture". In: *Pflügers Archiv* 446.1 (2003), pp. 125–132.

Rosenbluth, Michael J, Wilbur A Lam, and Daniel A Fletcher. "Force microscopy of non-adherent cells: a comparison of leukemia cell deformability". In: *Biophysical journal* 90.8 (2006), pp. 2994–3003.

Russell, David et al. "Mechanical stress induces profound remodelling of keratin filaments and cell junctions in epidermolysis bullosa simplex keratinocytes". In: *Journal of cell science* 117.22 (2004), pp. 5233–5243.

Saez, Alexandre et al. "Is the mechanical activity of epithelial cells controlled by deformations or forces?" In: *Biophysical journal* 89.6 (2005), pp. L52–L54.

Sakurai, Kengo, Ian T Hoffecker, and Hiroo Iwata. "Long term culture of cells patterned on glass via membrane-tethered oligonucleotides". In: *Biomaterials* 34.2 (2013), pp. 361–370.

Sakurai, Kengo, Yuji Teramura, and Hiroo Iwata. "Cells immobilized on patterns printed in DNA by an inkjet printer". In: *Biomaterials* 32.14 (2011), pp. 3596–3602.

Samson, Susan L and Lawrence Chan. "Gene therapy for diabetes: reinventing the islet". In: *Trends in Endocrinology & Metabolism* 17.3 (2006), pp. 92–100.

Sato, Kazuya et al. "Nitric oxide plays a critical role in suppression of T-cell proliferation by mesenchymal stem cells". In: *Blood* 109.1 (2007), pp. 228–234.

Saxon, Eliana and Carolyn R Bertozzi. "Cell surface engineering by a modified Staudinger reaction". In: *Science* 287.5460 (2000), pp. 2007–2010.

Schliwa, Manfred. "Action of cytochalasin D on cytoskeletal networks." In: *The Journal of cell biology* 92.1 (1982), pp. 79–91.

Schober, Markus et al. "Focal adhesion kinase modulates tension signaling to control actin and focal adhesion dynamics". In: *The Journal of cell biology* 176.5 (2007), pp. 667–680.

Schwarz, Ulrich S et al. "Calculation of forces at focal adhesions from elastic substrate data: the effect of localized force and the need for regularization". In: *Biophysical journal* 83.3 (2002), pp. 1380–1394.

Sefah, Kwame et al. "Development of DNA aptamers using Cell-SELEX". In: *Nature protocols* 5.6 (2010), pp. 1169–1185.

Shapiro, AM James et al. "Islet transplantation in seven patients with type 1 diabetes mellitus using a glucocorticoid-free immunosuppressive regimen". In: *New England Journal of Medicine* 343.4 (2000), pp. 230–238.

Sheetz, Michael P. "Cell control by membrane–cytoskeleton adhesion". In: *Nature Reviews Molecular Cell Biology* 2.5 (2001), pp. 392–396.

Shin, Dong-Sik et al. "Photolabile micropatterned surfaces for cell capture and release". In: *Chemical Communications* 47.43 (2011), pp. 11942–11944.

Sikanen, Tiina et al. "Dynamic coating of SU-8 microfluidic chips with phospholipid disks". In: *Electrophoresis* 31.15 (2010), pp. 2566–2574.

Silva Meirelles, Lindolfo da, Pedro Cesar Chagastelles, and Nance Beyer Nardi. "Mesenchymal stem cells reside in virtually all post-natal organs and tissues". In: *Journal of cell science* 119.11 (2006), pp. 2204–2213.

Solari, Mario G et al. "Marginal mass islet transplantation with autologous mesenchymal stem cells promotes long-term islet allograft survival and sustained normoglycemia". In: *Journal of autoimmunity* 32.2 (2009), pp. 116–124.

Sordi, Valeria and Lorenzo Piemonti. "Mesenchymal stem cells as feeder cells for pancreatic islet transplants". In: *The review of diabetic studies: RDS* 7.2 (2010), p. 132.

Sou, Keitaro et al. "Poly (ethylene glycol)-modification of the phospholipid vesicles by using the spontaneous incorporation of poly (ethylene glycol)-lipid into the vesicles". In: *Bioconjugate chemistry* 11.3 (2000), pp. 372–379.

Spooner, Brian S, Kenneth M Yamada, and Norman K Wessells. "Microfilaments and cell locomotion". In: *The Journal of cell biology* 49.3 (1971), pp. 595–613.

Steinberg, Malcolm S and Masatoshi Takeichi. "Experimental specification of cell sorting, tissue spreading, and specific spatial patterning by quantitative differences in cadherin expression". In: *Proceedings of the National Academy of Sciences* 91.1 (1994), pp. 206–209.

Stephan, Matthias T and Darrell J Irvine. "Enhancing cell therapies from the outside in: Cell surface engineering using synthetic nanomaterials". In: *Nano today* 6.3 (2011), pp. 309–325.

Stevenson, Bruce R and David A Begg. "Concentration-dependent effects of cytochalasin D on tight junctions and actin filaments in MDCK epithelial cells". In: *Journal of Cell Science* 107.3 (1994), pp. 367–375.

Stidwill, Robert P and Miriam Christen. "Alteration of fibronectin affinity during differentiation modulates the in vitro migration velocities of Hydra nematocytes". In: *Cell motility and the cytoskeleton* 41.1 (1998), pp. 68–73.

Stracke, Mary L et al. "Cytoskeletal agents inhibit motility and adherence of human tumor cells". In: *Kidney international* 43 (1993), pp. 151–151.

Sumi, Chikayoshi, Akifumi Suzuki, and Kiyoshi Nakayama. "Estimation of shear modulus distribution in soft tissue from strain distribution". In: *Biomedical Engineering, IEEE Transactions on* 42.2 (1995), pp. 193–202.

Svitkina, Tatyana M and Gary G Borisy. "Arp2/3 complex and actin depolymerizing factor/cofilin in dendritic organization and treadmilling of actin filament array in lamellipodia". In: *The Journal of cell biology* 145.5 (1999), pp. 1009–1026.

Szabo, Balint et al. "Phase transition in the collective migration of tissue cells: experiment and model". In: *Physical Review E* 74.6 (2006), p. 061908.

Takayama, Shuichi et al. "Patterning cells and their environments using multiple laminar fluid flows in capillary networks". In: *Proceedings of the National Academy of Sciences* 96.10 (1999), pp. 5545–5548.

Takeichi, Masatoshi. "Cadherin cell adhesion receptors as a morphogenetic regulator". In: *Science* 251.5000 (1991), pp. 1451–1455.

– "Cadherins: a molecular family important in selective cell-cell adhesion". In: *Annual review of biochemistry* 59.1 (1990), pp. 237–252.

– "The cadherins: cell-cell adhesion molecules controlling animal morphogenesis". In: *Development* 102.4 (1988), pp. 639–655.

Takemoto, Naohiro, Yuji Teramura, and Hiroo Iwata. "Immobilization of Sertoli cells on islets of Langerhans". In: *Biomater. Sci.* 1.3 (2013), pp. 315–321.

– "Islet surface modification with urokinase through DNA hybridization". In: *Bioconjugate chemistry* 22.4 (2011), pp. 673–678.

Tambe, Dhananjay T et al. “Collective cell guidance by cooperative intercellular forces”. In: *Nature materials* 10.6 (2011), pp. 469–475.

Tan, John L et al. “Cells lying on a bed of microneedles: an approach to isolate mechanical force”. In: *Proceedings of the National Academy of Sciences* 100.4 (2003), pp. 1484–1489.

Tan, Wei and Tejal A Desai. “Microfluidic patterning of cells in extracellular matrix biopolymers: effects of channel size, cell type, and matrix composition on pattern integrity”. In: *Tissue engineering* 9.2 (2003), pp. 255–267.

Tanner, Kandice et al. “Coherent angular motion in the establishment of multicellular architecture of glandular tissues”. In: *Proceedings of the National Academy of Sciences* 109.6 (2012), pp. 1973–1978.

Teramura, Yuji, Yusuke Arima, and Hiroo Iwata. “Surface plasmon resonance-based highly sensitive immunosensing for brain natriuretic peptide using nanobeads for signal amplification”. In: *Analytical biochemistry* 357.2 (2006), pp. 208–215.

Teramura, Yuji and Hiroo Iwata. “Bioartificial pancreas: microencapsulation and conformal coating of islet of Langerhans”. In: *Advanced drug delivery reviews* 62.7 (2010), pp. 827–840.

– “Islets surface modification prevents blood-mediated inflammatory responses”. In: *Bioconjugate chemistry* 19.7 (2008), pp. 1389–1395.

– “Surface modification of islets with PEG-lipid for improvement of graft survival in intraportal transplantation”. In: *Transplantation* 88.5 (2009), pp. 624–630.

Teramura, Yuji, Yoshihiro Kaneda, and Hiroo Iwata. “Islet-encapsulation in ultra-thin layer-by-layer membranes of poly (vinyl alcohol) anchored to poly (ethylene glycol)–lipids in the cell membrane”. In: *Biomaterials* 28.32 (2007), pp. 4818–4825.

Teramura, Yuji et al. “Behavior of synthetic polymers immobilized on a cell membrane”. In: *Biomaterials* 29.10 (2008), pp. 1345–1355.

Teramura, Yuji et al. “Control of cell attachment through polyDNA hybridization”. In: *Biomaterials* 31.8 (2010), pp. 2229–2235.

Teramura, Yuji et al. “Microencapsulation of islets with living cells using polyDNA-PEG-lipid conjugate”. In: *Bioconjugate chemistry* 21.4 (2010), pp. 792–796.

Terranova, Victor P, David H Rohrbach, and George R Martin. “Role of laminin in the attachment of PAM 212 (epithelial) cells to basement membrane collagen”. In: *Cell* 22.3 (1980), pp. 719–726.

Theveneau, Eric et al. “Collective chemotaxis requires contact-dependent cell polarity”. In: *Developmental cell* 19.1 (2010), pp. 39–53.

Tibbitt, Mark W and Kristi S Anseth. “Hydrogels as extracellular matrix mimics for 3D cell culture”. In: *Biotechnology and bioengineering* 103.4 (2009), pp. 655–663.

Tilghman, Robert W et al. “Matrix rigidity regulates cancer cell growth and cellular phenotype”. In: *PLoS One* 5.9 (2010), e12905.

Toda, Mitsuaki, Yusuke Arima, and Hiroo Iwata. "Complement activation on degraded polyethylene glycol-covered surface". In: *Acta biomaterialia* 6.7 (2010), pp. 2642–2649.

Tse, William T et al. "Suppression of allogeneic T-cell proliferation by human marrow stromal cells: implications in transplantation". In: *TRANSPLANTATION-BALTIMORE-* 75.3 (2003), pp. 389–397.

Van der Sluijs, JP, MR Baert, and RE Ploemacher. "Differential adherence of murine hematopoietic stem cell subsets to fibronectin." In: *Experimental hematology* 22.13 (1994), pp. 1236–1243.

Vasioukhin, Valeri et al. "Desmoplakin is essential in epidermal sheet formation". In: *Nature cell biology* 3.12 (2001), pp. 1076–1085.

Vedula, Sri Ram Krishna et al. "Emerging modes of collective cell migration induced by geometrical constraints". In: *Proceedings of the National Academy of Sciences* 109.32 (2012), pp. 12974–12979.

Vitale, Mario et al. "Fibronectin Is Required to Prevent Thyroid Cell Apoptosis through an Integrin-Mediated Adhesion Mechanism 1". In: *The Journal of Clinical Endocrinology & Metabolism* 83.10 (1998), pp. 3673–3680.

Wang, Lili et al. "Effects of ROCK inhibitor, Y-27632, on adhesion and mobility in esophageal squamous cell cancer cells". In: *Molecular biology reports* 37.4 (2010), pp. 1971–1977.

Wang, Ning and Donald E Ingber. "Control of cytoskeletal mechanics by extracellular matrix, cell shape, and mechanical tension". In: *Biophysical journal* 66.6 (1994), pp. 2181–2189.

Wehrle-Haller, Bernhard and Beat A Imhof. "The inner lives of focal adhesions". In: *Trends in cell biology* 12.8 (2002), pp. 382–389.

Williams, Courtney M et al. "Fibronectin expression modulates mammary epithelial cell proliferation during acinar differentiation". In: *Cancer research* 68.9 (2008), pp. 3185–3192.

Witke, Walter et al. "Hemostatic, inflammatory, and fibroblast responses are blunted in mice lacking gelsolin". In: *Cell* 81.1 (1995), pp. 41–51.

Xiong, Xiangling et al. "DNA Aptamer-Mediated Cell Targeting". In: *Angewandte Chemie International Edition* 52.5 (2013), pp. 1472–1476.

Yang, Hua and James R Wright Jr. "Co-Encapsulation of Sertoli Enriched Testicular Cell Fractions Further Prolongs Fish-to-Mouse Islet Xenograft Survival1". In: *Transplantation* 67.6 (1999), pp. 815–820.

Yang, Junwei, Chunsun Dai, and Youhua Liu. "Hepatocyte growth factor gene therapy and angiotensin II blockade synergistically attenuate renal interstitial fibrosis in mice". In: *Journal of the American Society of Nephrology* 13.10 (2002), pp. 2464–2477.

Yeung, Tony et al. "Effects of substrate stiffness on cell morphology, cytoskeletal structure, and adhesion". In: *Cell motility and the cytoskeleton* 60.1 (2005), pp. 24–34.

Yilmaz, Mahmut and Gerhard Christofori. "EMT, the cytoskeleton, and cancer cell invasion". In: *Cancer and Metastasis Reviews* 28.1-2 (2009), pp. 15–33.

Yousaf, Muhammad N, Benjamin T Houseman, and Milan Mrksich. "Using electroactive substrates to pattern the attachment of two different cell populations". In: *Proceedings of the National Academy of Sciences* 98.11 (2001), pp. 5992–5996.

Zahir, Nastaran and Valerie M Weaver. "Death in the third dimension: apoptosis regulation and tissue architecture". In: *Current opinion in genetics & development* 14.1 (2004), pp. 71–80.

Zhang, Chun Xiu et al. "Cell detection based on protein array using modified glass slides". In: *Electrophoresis* 24.18 (2003), pp. 3279–3283.

Zhang, Zhouhua et al. "The alpha 5 beta 1 integrin supports survival of cells on fibronectin and up-regulates Bcl-2 expression". In: *Proceedings of the National Academy of Sciences* 92.13 (1995), pp. 6161–6165.

Zhu, He, Jun Yan, and Alexander Revzin. "Catch and release cell sorting: Electrochemical desorption of T-cells from antibody-modified microelectrodes". In: *Colloids and Surfaces B: Biointerfaces* 64.2 (2008), pp. 260–268.

List of Papers

- Chapter 2
  Hoffecker, Ian T., Wei-hui Guo, and Yu-li Wang. "Assessing the spatial resolution of cellular rigidity sensing using a micropatterned hydrogelphotoresist composite." *Lab on a Chip* 11, no. 20 (2011): 3538-3544.

- Chapter 3
  Hoffecker, Ian T., and Hiroo Iwata. "Manipulation of Cell Sorting Within Mesenchymal Stromal CellIslet Cell Multicellular Spheroids." *Tissue Engineering Part A* 20, no. 11-12 (2014): 1643-1653.

- Chapter 4
  Sakurai, Kengo, Ian T. Hoffecker, and Hiroo Iwata. "Long term culture of cells patterned on glass via membrane-tethered oligonucleotides." *Biomaterials* 34, no. 2 (2013): 361-370.

- Chapter 5
  Hoffecker, Ian T., Takemoto N., Arima Y., Iwata H. "Sequence-specific nuclease-mediated release of cells tethered by oligonucleotide phospholipids" Submitted Sept. 2014.

- Chapter 6
  Hoffecker, Ian T., and Hiroo Iwata. "Estimation of Cell-Cell Adhesion Energy Mediated by DNA-Lipid Bonds" In Preparation.

  Other papers not included as part of this thesis:

- Wong, Stephanie, W. H. Guo, Ian T. Hoffecker, and Y. L. Wang. "Preparation of a micropatterned rigid-soft composite substrate for probing cellular rigidity sensing." *Methods in cell biology* 121 (2013): 3-15.

- LaNasa, Stephanie M., Ian T. Hoffecker, and Stephanie J. Bryant. "Presence of pores and hydrogel composition influence tensile properties of scaffolds fabricated from welldefined sphere templates." *Journal of biomedical materials research part b*: applied biomaterials 96, no. 2 (2011): 294-302.

Acknowledgements

I wish to express my sincerest gratitude to my advisor Prof. Hiroo Iwata, for his continuous support over the course of my studies. His patience, enthusiasm, knowledge, creativity, and passion for science have been a never ending source of motivation. I could not be happier with the experience I have had at Kyoto University, and I owe so much of this to him.

In addition, I wish to thank my Masters thesis advisor at Carnegie Mellon University, Prof. Yu-Li Wang, whose influence over the way I think as a scientist has long out-lived the time I spent under his supervision.

I thank my mentors Prof. Yusuke Arima, Dr. Weihui Guo, Dr. Minh Luan, and Dr. Naohiro Takemoto, who have each spent countless hours at their expense training me and helping me solve the hardest problems.

I thank Monbukagakusho and Kyoto University Department of Polymer Science for my admission into the International Doctoral Program and its funding without which I would not be here today. I thank Prof. Detlev Helmig and Prof. Stephanie Bryant, my first advisors who introduced me to scientific research as an undergraduate at the University of Colorado, Boulder.

Finally, I thank my family Adam Tatsuo Hoffecker, Lilian Takahashi Hoffecker, and John Frank Hoffecker for their limitless support which I have been privileged to my entire life.